LINE IDENTIFICATION INCLUDING OFF-AXIS SPECTRA WITH THE *HERSCHEL* SPIRE SPECTROMETER

CHRIS S. BENSON
Bachelor of Science, University of Lethbridge, 2018

A Thesis
Submitted to the School of Graduate Studies
of the University of Lethbridge
in Partial Fulfillment of the
Requirements for the Degree

MASTER OF SCIENCE
in

PHYSICS

Department of Physics and Astronomy
University of Lethbridge
LETHBRIDGE, ALBERTA, CANADA

LINE IDENTIFICATION INCLUDING OFF-AXIS SPECTRA WITH THE *HERSCHEL* SPIRE SPECTROMETER

CHRIS S. BENSON

Date of Defence: January 7, 2020

Dr. Locke Spencer Supervisor	Associate Professor	Ph.D.
Dr. David Naylor Committee Member	Professor	Ph.D.
Dr. Paul Hazendonk Committee Member	Associate Professor	Ph.D.
Dr. Chad Povey Chair, Thesis Examination Committee	Instructor	Ph.D.

Dedication

To Anna, whose laughter and joy makes all of this possible. I also wish to dedicate this thesis to all inquiring minds who seek to shed light on the incredible Universe that we call our home.

Abstract

The European Space Agency (ESA) *Herschel* Mission concluded observation of the Far-infrared (FIR) Universe in 2013, providing a wealth of observations of the interstellar medium and distant galaxies. The Spectral and Photometric Imaging Receiver (SPIRE), one of *Herschel*'s three instruments, consists of an imaging photometer and an imaging Fourier Transform Spectrometer (FTS). The SPIRE team has developed an automated routine to extract spectral features from all SPIRE FTS observations.

This thesis introduces FIR astronomy and instrumentation, and the legacy of FIR space telescopes through to *Herschel*. The SPIRE instrument and the Feature Finder are introduced. This thesis includes the methods by which the molecular and atomic transitions of the lines extracted from SPIRE FTS observations are identified, and presents these identification results. The application of the feature finder to SPIRE FTS off-axis detectors is also detailed and presented. The thesis concludes with a brief discussion of future FIR instrumentation.

Acknowledgements

First and foremost I must thank Prof. Locke Spencer for making this opportunity possible. His efforts to provide opportunities to connect with members of the European Space Agency and the SPIRE instrument team have provided me with opportunities I never thought could be available to me. Most of all I must thank him for his constant encouragement for me to reach my higher potential. I still remember being a nervous second-year undergraduate student enjoying his phenomenal astronomy lectures (that were full of obscure references to "A New Hope") when he offered me the opportunity to work with him and get my hands on real astronomical data from *Herschel*. Thank you, Locke, for providing so much mentoring, encouragement, and patient advice throughout this journey.

Words can only begin to express my deepest gratitude towards my beautiful wife, Anna, who has supported me through every step of my journey. Her constant care, understanding, and laughter is a massive part of what makes all of this possible. It really does take a special person to make you laugh during the stressful writing process by sharing bizarre Christmas raps about cats. Thank you Anna, for the countless things you do to make the world a brighter and happier place.

I also want to thank my parents, Lawrence and Debbie Benson, for teaching me to be diligent, ambitious, and caring in all my endeavors. Their enduring support and encouragement of my curiosity will always be something I am thankful for. I must also thank my brother David. Not many people can endure the waves of jargon that wash out when people ask me about my work, let alone ask questions after drowning in it. I also want to thank Eric Dumouchel and Josie Macfarlane for their willingness to accept me into their lives and the blessing that it has been. It has never been a mystery to me as to where Anna found her wonderful and quirky sense of humour, she learned from the best. I also owe many thanks to my grandmother, Glenda Benson, who has always believed me capable of wonderful accomplishments and encouraged me to reach them.

Contents

List of Tables

List of Figures

List of Abbreviations

AGB Asymptotic Giant Branch
ALMA Atacama Large Millimeter/submillimeter Array
BSM Beam Steering Mirror
CASSIS Centre d'Analyse Scientifique de Spectres Instrumentaux et Synthétiques
CDMS Cologne Database for Molecular Spectroscopy
Dec Declination
ESA European Space Agency
FF *Herschel* SPIRE FTS Spectral Feature Finder
FFT Fast Fourier Transform
FIR Far-Infrared
FIRI Far Infrared Interferometer
FOV Field of View
FTS Fourier Transform Spectrometer
FWHM Full Width at Half Maximum
HIFI Heterodyne Instrument for the Far Infrared
HIPE Herschel Interactive Processing Environment
HPDP Highly Processed Data Product
HR High Resolution
HSA Herschel Science Archive
ILS Instrumental Line Shape
IR Infrared
IRAS Infrared Astronomical Satellite
ISM Interstellar Medium
ISO Infrared Space Observatory
JPL NASA Jet Propulsion Laboratory
LIGO Laser Interferometer Graviational-wave Observatory
LR Low Resolution

LTE Local Thermodynamic Equilibrium

MR Medium Resolution

MZ Mach-Zehnder

NED NASA/IPAC Extragalactic Database

NIST National Institute of Standards and Technology

NRAO National Radio Astronomy Observatory

OPD Optical Path Difference

PACS Photodetector Array Camera and Spectrometer

PSW Photometer Short Wavelength

RA Right Ascencion

rms root mean square

SAFECAT the SPIRE Automated Feature Extraction Catalogue

SCAL Spectrometer Calibrator

SIMBAD Set of Identifications and Bibliography for Astronomical Data

SLW Spectrometer Long Wavelength Array

SMEC Spectrometer Mirror Mechanism

SNR Signal to Noise Ratio

SPICA Space Infrared Telescope for Cosmology and Astrophysics

SPIRE Spectral and Photometric Imaging Receiver

SPIRIT Space Infrared Interferometric Telescope

SSW Spectrometer Short Wavelength Array

ZPD Zero Path Difference

Notes on Format

The following style conventions were selected:

Reference Parenthetic citation was utilized for references to external works by other authors (e.g., [1-3,7] refers to citations 1,2,3 and 7). Internal references to different chapters/appendices and sections are denoted by *chapter/appendix.section.subsection*. Figure, table and equation numbers are denoted by *chapter/appendix.value*, where value is the incremental numerical value of the figure, table or equation.

Equations Units are provided for every numbered equation, presented in square brackets (e.g., [$\mu m\, s^{-1}$] indicates micrometres per second). If the units are not provided, the equation is unitless unless it is otherwise explained in the text of the thesis. Units are provided in the standard International System of Units (SI), unless otherwise noted.

Frequency and Wavelength In far-infrared astronomy it is fairly common to use both wavelength (λ) and frequency (ν) to represent the spectral content of electromagnetic radiation. Both are related by $c = \nu\lambda$ where c is the speed of light in vacuum. Both frequency and wavelength will be used in this way throughout this thesis.

Isotopes It is standard for isotopes in an atom to be marked by a super-script when it is not the most abundant isotope e.g., ^{13}CO marks the less abundant isotope of carbon while the oxygen atom which is the most abundant isotope (^{16}O). Sometimes the isotope number is included in molecules even when a particular atom is the most abundant isotope for emphasis.

Variables The Greek letter σ is used in this thesis to both represent wavenumber, $\sigma = 1/\lambda$, and the statistical quantity, standard deviation. To distinguish between both cases, standard deviation will be represented by a $\boldsymbol{\sigma}$ character while wavenumber will use the σ character. In this thesis the Greek character, ν, is used to represent frequency while the Latin character v is used for velocity. In some fonts these characters are very similar, here I note their difference. Also as a note, the non italicized Latin character v is used to denote vibrational quantum states when labelling molecular transitions.

Astronomical and Physical Constants

Table 1: See Carol and Ostlie [1] and P. J. Mohr and B. N. Taylor, (2003) Searchable Bibliography on the Constants (version 3.0), National Institute of Standards and Technology

Gravitational constant	$G = 6.674 \times 10^{-11}$ m^3 kg^{-1}s^{-2}
Speed of light	$c = 2.99792458 \times 10^5$ km s^{-1}
Planck's constant	$h = 6.62607015 \times 10^{-34}$ J s
	$\hbar = h/2\pi$
Boltzmann's constant	$k = 1.380649 \times 10^{-23}$ J K^{-1}
Atomic hydrogen mass	$m_H = 1.6735 \times 10^{-27}$ kg
Electron Volt	$1\,\mathrm{eV} = 1.602176634 \times 10^{-19}$ J
Astronomical Unit	$1\,\mathrm{AU} = 1.4960 \times 10^8$ km

Chapter 1

Introduction

> I cleave the heavens and soar to the infinite. And while I rise from my own globe to others and penetrate ever further through the eternal field, that which others saw from afar, I leave far behind me.
>
> –Giordano Bruno (1584)

The pursuit of a greater understanding of the Universe around us has been an inspiration and motivation for the human race throughout history. This endless search for our place in the vastness of space has lead humanity to its first steps on the moon 50 years ago, to send Voyageur [2] out into the reaches of interstellar space and beyond (continuing its mission, to date more than 143 times further out from the sun than Earth) [2], and to construct the 16 km^2 LIGO interferometers [3] looking for the faintest of signals. Indeed, it seems that the majesty and wonder one experiences when looking up at a starry night sky is one of the things that is common to all of humanity.

Our search for knowledge concerning the Universe around us is not without difficulties. Due to the vastness and nature of the large scale Universe, direct experimentation of most systems in astronomy and astrophysics is for the most part beyond our reach. One cannot simply travel to the nearest star and put a thermometer in it nor can we arrange for a convenient viewing of a stellar birth in a laboratory environment. As such, almost all of the information available to us about these distant systems comes in the form of light. The careful cataloguing of the information contained in this light has always played an important role in astronomy and astrophysics. Even from the ancient works of ‘Abd al-Rahman ibn

‘Umar al-Sufi [4] and Chinese astronomers [5] (964, 1054 A.D.), cataloguing astronomical observations has played an important role in advancing our understanding of the Universe. In spite of the enormous quantities of data available to us today, most of the Universe is still not understood and we are limited by both current technology and current theoretical models. Advancements in both of these areas are highly contingent on data from previous generations of instruments and astronomers making it an important work to extract all useful information from each and every observation.

In this first chapter I will give a brief overview of major scientific goals in the field of Far-Infrared (FIR) astronomy and the unique challenges faced by instruments designed to observe FIR wavelengths. As part of this discussion I will summarize the legacy of space telescopes that have been launched to observe the IR and FIR Universe leading to the development of the *Herschel* space observatory and one of its three focal plane instruments, the Spectral and Photometric Imaging Receiver (SPIRE). Through this discussion, I hope that the reader will begin to appreciate how the SPIRE instrument represents decades of past knowledge and experience culminating in a truly unique and specialized instrument to further our understanding of how stars form and how galaxies evolve. As the SPIRE instrument houses a Fourier Transform Spectrometer (FTS), I will provide an overview of Fourier Transform Spectroscopy techniques and design. This discussion will include an introduction to Fourier analysis, the optical design of FTS instruments and their mathematical framework, and how spectral information is retrieved from an FTS. This overview is far from exhaustive on the subject but provides the foundation knowledge required for the following chapters.

In the second chapter of this thesis I will introduce the Spectral and Photometric Imaging Receiver (SPIRE) FTS instrument and the development of the *Herschel* SPIRE FTS Spectral Feature Finder (FF) algorithm and line catalogue. My discussion of the SPIRE

FTS will include technical details of the SPIRE instrument concerning optical design, observational modes, and SPIRE FTS data products that are necessary for an understanding of SPIRE FTS spectral observations. An accessible technical description of the entire instrument written for an observer's perspective can be found in the SPIRE observers manual (Valtchanov et al. [6]). The FF is an archival work by the SPIRE instrument team to develop a computer automated routine to extract all prominent spectral information from SPIRE FTS spectra and present it in a publicly available user-searchable catalogue for astronomers [7]. In this chapter I will present a summary of my contributions to the overarching project and provide an overview of the automated routine. My goal in this discussion is to provide the reader with the technical details, nomenclature, and conventions employed by the FF that will be necessary for the discussion of my largest contributions to the project.

The third and fourth chapters of this thesis present my largest contributions to the FF project. Chapter 3 discusses the formulation of a template comprised of spectral features that are important to FIR astronomy and are commonly found in SPIRE FTS spectra. Using this template, I match the prominent spectral features extracted by the FF routine with the energy transitions in molecules and atoms. Also included is a description of a routine I developed that uses the information from line identification to address low SNR features contained in SPIRE FTS observations that can be missed by the FF. The results of both routines after being applied to all publicly available SPIRE FTS observations are presented in this section. Through this identification routine, the FF is expanded to include information concerning the chemical and atomic composition of astronomical sources observed by the SPIRE FTS .

In the fourth chapter of this thesis, I present my work to extend the FF to include all 56 operational detectors of the SPIRE FTS for sparsely sampled single-pointing observations. These observations make up the majority of the SPIRE FTS catalogue and, up to now, only the two central detectors of the FTS are nominally considered by the FF. The results from applying the FF to off-axis detectors in these observations are presented and the utility that the extracted spectral features provide is also discussed. To complement these results, I have developed postcard images that are used in the FF catalogue to provide at-a-glance summaries of the information contained in the off-axis detectors in sparsely sampled single-pointing observations. The work presented in this chapter provides a significant contribution of spectral features observed by the SPIRE FTS to be included in the FF catalogue for its upcoming third public release.

I use the fifth and final chapter of this thesis to summarize all that has been presented in this thesis and discuss its contribution to the archival stage that finalizes the mission of the SPIRE instrument. In this section I also discuss the future of FIR astronomy as a whole as it progresses towards future missions by building on the *Hesrchel* Space Observatory and SPIRE instrument legacy.

1.1 Far-Infrared Astronomy

> *Coelorum perrupit claustra.* He broke through the barriers of the skies.
> –William Herschel's Epitaph

Observing the Universe at different wavelengths provides a completely different view. As we peer into longer wavelengths, the emission from nearby stars fades into the background and the emission from distant galaxies and the cold dusty regions of the Interstellar Medium (ISM) become more apparent. Throughout this thesis I will refer to FIR radiation as corresponding to wavelengths of light ranging ~ 100–$1000\,\mu$m which corresponds to the peak blackbody radiation from sources of temperatures between ~ 30 and $3\,$K, respectively. It is particularly important to note that modern research has shown that nearly half of all the spectral energy ever emitted by stars in galaxies would be observed in FIR and IR frequencies [8]. In this section, I will describe the unique systems that FIR light allows astronomers to study and the unique challenges faced by those wishing to study these frequencies of light.

1.1.1 Star Formation

Stars and planetary systems can be considered to be a constituent building block in the structure of the Universe. Observations of star formation in the FIR were first enabled by the development of the infrared bolometer in the early 1960s by Low, F [9, 10, 11, 12]. The field has matured to the point that we now have obtained broad spectral observations of the FIR from multiple space observatories. Understanding the origin of stars and planetary systems has become an active area of study [13] with many recent discoveries. Despite finding their origins in the diffuse ISM ($\leq 6 \times 10^{-21}\,\mathrm{kg\,m^{-3}}$), stars often achieve densities in excess of $10^{3}\,\mathrm{kg\,m^{-3}}$, which is no simple task [14]. We will see through a simple model that the cold dense regions of the ISM that are bright at FIR frequencies are the ideal locations for stars to form.

We begin with a spherically symmetric self-gravitating cloud of monatomic gas that is only under the forces of self-gravity and internal pressure. We will ignore any pressure from surrounding gas allowing us to write the equilibrium condition, using the virial theorem [15], as

$$2\mathcal{T} + \Omega = 0 \quad [\mathrm{J}] \tag{1.1}$$

where $\mathcal{T}$ is the thermal energy content of the cloud and Ω is the gravitational self-energy (for a full derivation see Appendix D.1). Equation 1.1 demonstrates the battle between thermal pressure (encoded in $\mathcal{T}$) and gravity (Ω); if the pressure term dominates the cloud expands but if the gravity term dominates it will collapse. It should be noted that this treatment of star formation has not accounted for the effects of magnetic fields [16, 17] and turbulence [18] in the ISM which are known to play an important role in star formation processes. This discussion is, however, sufficient to demonstrate the utility of FIR wavelengths for studying star formation.

If we assume that the cloud is of uniform pressure and density we can write the condition for collapse in terms of the cloud's pressure P_c, radius R_c, and mass M_c. With

$$2\mathcal{T} = 3P_cV_c = 4\pi R_c^3 P_c \quad [\mathrm{J}] \tag{1.2}$$

and

$$\Omega = -\int_0^{M_c} \frac{GM(r)\,dM}{r} = -\frac{16\pi^2}{3}\rho_c^2 G \int_0^{R_c} r^4\,dr = -\frac{3}{5}\frac{GM_c^2}{R_c} \quad [\mathrm{J}], \tag{1.3}$$

we require

$$\frac{3}{5}\frac{GM_c^2}{R_c} \gtrsim 4\pi R_c^2 P_c \quad [\mathrm{J}] \tag{1.4}$$

for the successful collapse of the cloud. From the ideal gas law and Equation 1.4, we obtain

$$P_c = \frac{3M_ckT_c}{4\pi R_c^3 m_H \mu} \quad [\mathrm{Pa}], \tag{1.5}$$

where T_c is the temperature of the cloud, k is the Boltzmann constant, m_H is the mass of hydrogen, and μ is the mean molecular weight ($\mu = 1$ for a neutral atomic hydrogen gas, $\mu = 0.5$ if the hydrogen is ionized). Equation 1.5 allows us to write our collapse condition as,

$$\frac{GM_c}{5R_c} \gtrsim \frac{kT_c}{\mu m_H} \quad [\mathrm{J}]. \tag{1.6}$$

If we write R_c in terms of the cloud's mass density, ρ_c,

$$R_c = \left(\frac{3M_c}{4\pi\rho_c}\right)^{1/3} \quad [\mathrm{m}], \tag{1.7}$$

and arrange our condition for the mass of the cloud, we obtain Jean's criterion [19, 1]:

$$M_c \gtrsim \left(\frac{5kT}{G\mu m_H}\right)^{3/2} \left(\frac{3}{4\pi\rho_c}\right)^{1/2} \quad \text{[kg]}. \tag{1.8}$$

This criterion is often referred to as the limiting mass required for a cloud to collapse, or the Jean's mass. Similarly we can solve for the minimum radius required for collapse,

$$R_J \simeq \left(\frac{15kT}{4\pi G\mu m_H \rho_0}\right)^{1/2} \quad \text{[m]}, \tag{1.9}$$

known as the Jean's length.

Through Jean's criterion, we see that the ideal environments for clouds in the ISM to collapse and form stars are cold and dense regions since they require smaller and less massive density enhancements. This is supported by overwhelming observational evidence that stars form from cold molecular clouds in the ISM that provide the required cooling mechanisms for density enhancements to collapse [13, 14]. These cold molecular clouds are particularly bright at sub-mm and FIR wavelengths. For this reason, FIR light is particularly useful for probing systems where stars collapse and begin their earliest proto-star stages [20, 21, 22].

1.1.2 Distant Galaxies

Perhaps one of the most profound discoveries about the nature of the Universe from the previous century is Edwin Hubble's characterization of the expanding Universe [23, 24]. An observer looking out into the Universe in all directions will find, perhaps to their surprise, that the light from almost all extragalactic objects experiences a shift to lower frequencies, or a redshift, that indicates that they are moving away from us and that the further away an object is, the faster it moves away from us. This universal redshift phenomena has come to be known as Hubble's Law [1]:

$$v = H_0 d \quad [\mathrm{km\,s^{-1}}], \tag{1.10}$$

where v is the radial velocity of a given source, d is the distance from observer and H_0 is the Hubble constant. Hubble's law shows us that the light from distant objects is observed in FIR wavelengths [1]. A more complete discussion of redshift can be found in Section 2.2.5 of this Thesis.

It is well understood that due to the fixed speed of light in vacuum, when an observer receives light from a distant object they are seeing the object as it existed in the past [1]. Let us consider a simple example; Andromeda (or M31) is the closest spiral galaxy to our own, being a seemingly enormous $\sim 2.4 \times 10^{19}$ km away from us (more than ten orders of magnitude greater than Earth's separation from the Sun) [25]. Ignoring any interactions with matter that may occur along the line of sight, the light we receive from Andromeda was emitted from the stars in that galaxy ~ 2.5 million years ago. Thus as we study highly redshifted (distant) FIR galaxies we are able to see them in their infancy. Recent surveys have shown that IR luminous galaxies are responsible for at least half of the light in the Universe ever emitted by stars with many of these galaxies at large distances such that their light is now observable at FIR frequencies [8, 26].

1.1.3 Challenges

Though FIR light allows the study of unique systems that provide important insights for cosmology and astrophysics, there are certain instrumental design challenges that make observation at these frequencies particularly difficult. Some obstacles faced by FIR instruments for astrophysical observation are atmospheric absorption, angular resolution, thermal emission from instrument optics, and the sensitivity of the associated FIR detectors.

The atmosphere of Earth contains large quantities of water and other molecules that are optically active at FIR frequencies and for the most part absorb all of the light at these frequencies. With the exception of high altitude or antarctic ground based observatories (see Soifer and Pipher [27]), the atmosphere is considered to be mostly opaque to FIR astronomers (Figure 1.1) and the most effective broad band FIR observatories are by necessity space-borne missions.

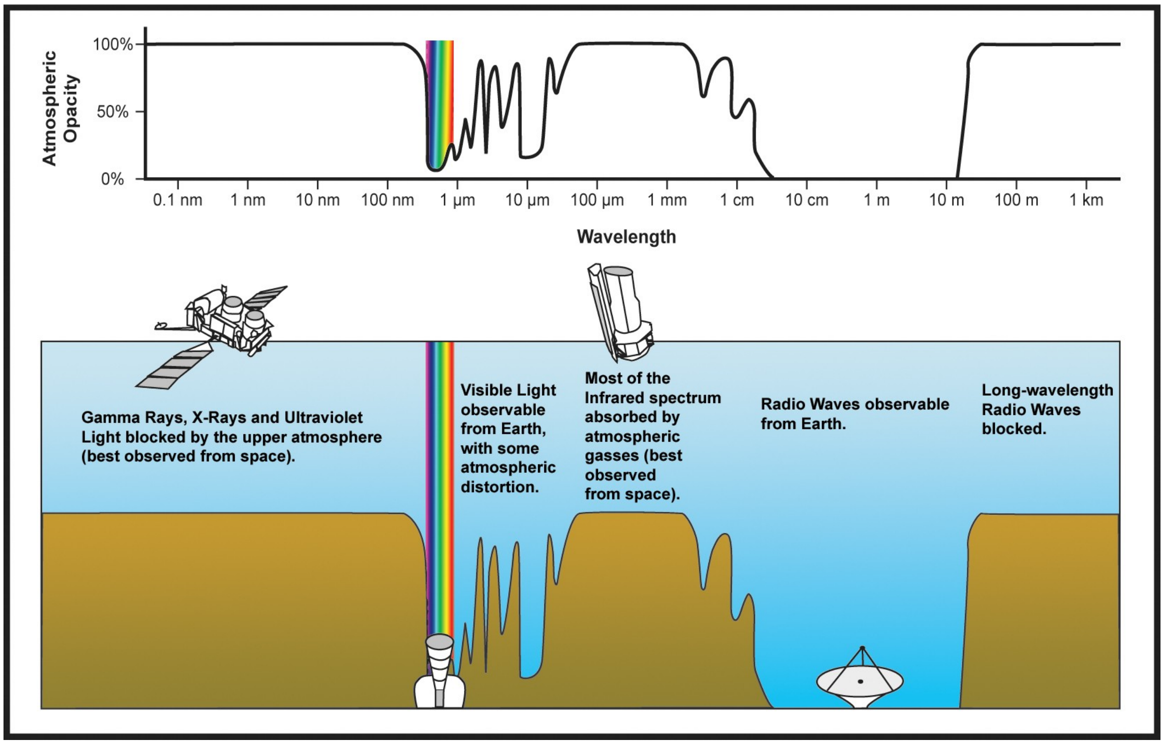

Figure 1.1: The opacity of Earth's atmosphere for different wavelengths of light. Courtesy of NASA, `http://coolcosmos.ipac.caltech.edu/cosmic_classroom/ir_tutorial/irwindows.html`.

If we consider an instrument with a circular aperture, the Rayleigh criterion [28] for resolving two point sources is

$$\theta = 1.220\frac{\lambda}{D}, \tag{1.11}$$

where θ is the angular resolution of the instrument, λ is the wavelength of light observed, and D is the diameter of the aperture [1]. From Equation 1.11, we see that to observe the longer FIR wavelengths a larger aperture (i.e., telescope mirror) is required. For a simple example, consider the nearby star forming region, Serpens South, at a distance of ~ 1400 light-years [29]. In order to resolve two massive bodies separated by ~ 1 AU (say a young stellar object and a newly forming planetary mass) an angular resolution of ~ 0.06 arcseconds is required. At a wavelength of $200\,\mu$m this resolution corresponds to a telescope with a primary mirror that has a diameter of ~ 14 m.

The thermal emission from the telescope itself becomes a major obstacle when observing FIR light. As we discussed previously, blackbody radiation which peaks at FIR wavelengths corresponds to objects of very low temperatures ($\sim$ 3–30 K) and thus objects at temperatures of even just a few kelvin may be significant sources of radiation to detectors that are sensitive to FIR wavelengths.

The atmospheric opacity, thermal background from the instrument itself, and the size requirements of the primary aperture give rise to the unique situation of FIR astronomy. The sensitivity of the detector must be well coupled to the system optical design while the FIR instruments must balance a budget of size, cryogenics, and height above the Earth's atmosphere. We see that the ideal FIR observatory would be a large space-based instrument that is cooled to cryogenic temperatures but the size of the primary mirror and weight of the cryogens is then limited by rocket fuel, durability, and the dimensions of the rocket. The history of space-based FIR telescopes is a progression of instruments with increasing lifetimes as these three budgets of size, cooling, and rocket fuel are all balanced.

1.2 *Herschel* and the Far-Infrared Legacy

Science progresses best when observations force us to alter our preconceptions.

–Vera Rubin

The history of FIR astronomy has been a constant march forward as new technologies come to light allowing for bigger and colder telescopes to be launched. Each new telescope and instrument provides an important foundation of knowledge and experience to drive the next generation of instruments. In order to provide context for the *Herschel*–SPIRE FTS, I will briefly discuss its predecessors and how each made a meaningful contribution to the scientific goals of FIR astronomy.

1.2.1 Infrared and Far-Infrared Telescopes

The Infrared Astronomical Satellite (IRAS) mission was a collaborative work between the United States (NASA), the Netherlands (NIVR), and the United Kingdom (SERC) space agencies to provide an unbiased sky survey at wavelengths ranging from 8–120 μm [30]. The IRAS telescope had a liquid helium-cooled primary mirror that was only 60 cm in diameter [31, 32]. The telescope was launched in January 1983 and completed its mission later that year in November with the depletion of its liquid cryogens. The spatial resolution of IRAS ranged from 0.5 arcminutes at 0.5 μm up to 2 arcminutes at 100 μm [32].

During its relatively short lifetime, IRAS providing coverage of more than 96% [31] of the sky. The IRAS survey provided a catalogue of $\sim$ 250 000 point-like FIR sources and $\sim$ 20 000 extended FIR sources [31]. These early catalogues revealed excess FIR emission surrounding stars [33, 34] and the presence of physical processes that occur in the ISM [35]. The success of IRAS marks a significant milestone in FIR astronomy. Providing the first full-sky survey at IR wavelengths [31], it generated the interest necessary for the field to grow and paved the way for future missions.

In 1995 the Infrared Space Observatory (ISO) began its two and a half year mission [36]. Like IRAS, ISO also carried a 60 cm cooled primary mirror [36]. ISO provided an upgrade on IRAS in many respects, achieving an improved spectral sensitivity on the order of 10^3 [36, 37] covering wavelengths from 2.5–240 μm. The spatial resolution of ISO ranged from 1.5 to 90 arcseconds [36].

Through ISO, a much greater understanding of star formation, the ISM, and distant galaxies was achieved [37]. One of the highlighting discoveries was the detection of water vapour in the Orion Nebula [37]. Similar to the IRAS mission, ISO provided an expansive catalogue of 30 000 FIR science observations [37].

Continuing on into the next decade, the *Spitzer Space Telescope* was launched in August 2003 [38, 39]. The *Spitzer* mission was designed as a two-phase mission with a cold phase and a warm phase [38]. During the cold phase of the mission the 0.85 m diameter mirror was cooled to as low as 5.5 K [38] until the depletion of its cryogens in May 2009 which initiated the warm phase of the mission [40]. During the warm phase, only observations at 3.6 and 4.5 μm are possible [39]. The warm phase of the *Spitzer* mission continues today.

The photometric imaging instrument onboard *Spitzer* covers a wavelength range of 3.6–100 μm achieving a spatial resolution of ~ 2 arcseconds but not quite reaching fully into FIR wavelengths. Its spectrometer observed spectra even further from FIR wavelengths only reaching to 40 μm [39]. Through *Spitzer* a large survey of the galaxy revealed important information concerning newly forming stars furthering the development of our current understanding of star formation [41].

Each of the space telescopes and their instruments discussed have played an important role in answering the scientific goals of FIR astronomy. Even with these contributions, it is apparent that high spatial resolution observations covering the entire FIR band had not yet been achieved. This motivation led to the development of a FIR telescope boasting the largest single piece mirror ever employed by a space observatory [42], the *Herschel* Space Observatory.

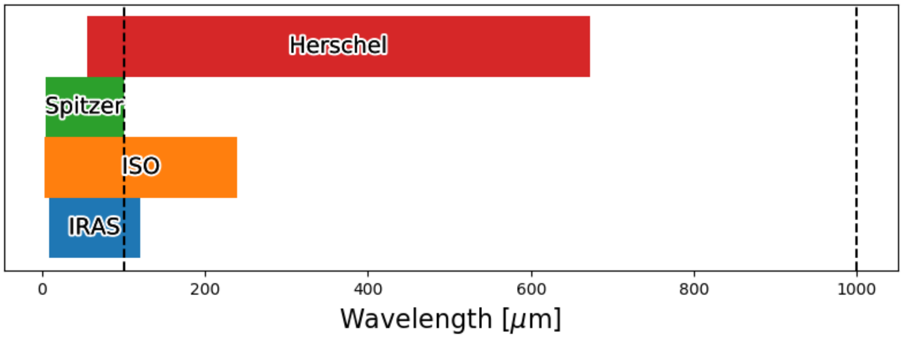

Figure 1.2: The wavelength range covered by each of the FIR/IR telescopes that have been discussed. Black dashed lines mark the FIR region, ~ 100–$1\,000\,\mu$m. The atmosphere is opaque to these FIR wavelengths. During the warm phase of *Spitzer*, only two camera bands centred at 3.6 and 4.5 μm are operational.

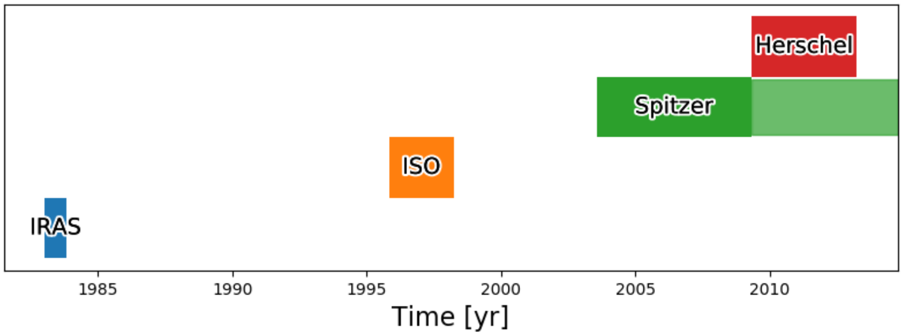

Figure 1.3: The timeline of FIR and IR space telescopes that have been discussed. The lighter shaded green bar shows the warm phase of *Spitzer* which is currently ongoing.

1.2.2 The *Herschel* Space Observatory

The *Herschel* observatory was launched in May 2009 and ended observations in April 2013 with the depletion of its liquid cryogens [43]. The primary mirror of *Herschel* was 3.5 m in diameter [42, 44, 45] which is to date the largest monolithic mirror ever flown in

Table 1.1: A summary of the FIR and IR space observatories discussed. The minimum spatial resolution,θ_{min}, achieved at the shortest wavelength viewed by each telescope is shown with the information provided in the text.

Mission	Duration [months, days]	θ_{min} [arcseconds]	Mirror Diameter [m]	Wavelength Coverage [μm]
IRAS	9, 26	30	0.60	8–120
ISO	28, 22	1.5	0.60	2.5–240
Spitzer	Cold: 68, 20 Warm: Ongoing	2	0.85	Cold: 3.6–100 Warm: 3.6, 4.5
Herschel	49, 2	5	3.5	55-672

space [44]. The cryostat used to cool the three focal plane instruments, the Heterodyne Instrument for the Far Infrared (HIFI), SPIRE, and the Photodetector Array Camera and Spectrometer (PACS) built upon successful technology from the ISO cryostat [45]. Improvements on the design resulted in a projected 3.5-year lifespan for the cryogens (which it surpassed) as an upgrade over the 2.5-year lifespan of ISO. *Herschel* successfully operated far from the Earth in a large-amplitude quasi-halo orbit around the second Lagrangian Point [46] (see Figure 1.4). *Herschel* was the first large-scale space observatory mission to provide broad coverage of FIR wavelengths providing an unprecedented view of the cold and dusty Universe [45, 46].

Herschel was designed in order to further our understanding of distant galaxies and their evolution, the formation of stars and planetary systems, late stages of stellar evolution, and the interaction between successive generations of stars and the ISM [45]. The payload instruments onboard the observatory provided wide area photometric surveys of the Galaxy and extra-galactic targets as well as spectroscopic observations to understand the physics and chemistry of the ISM (both in the Milky Way and in other galaxies) [45]. *Herschel*'s surveys of the Galaxy have uncovered the extensive filament structure of the ISM [47] and traced water molecules throughout star-forming regions [48]. *Herschel*, through its observations of distant galaxies, has also provided a timeline of the role of interstellar dust in

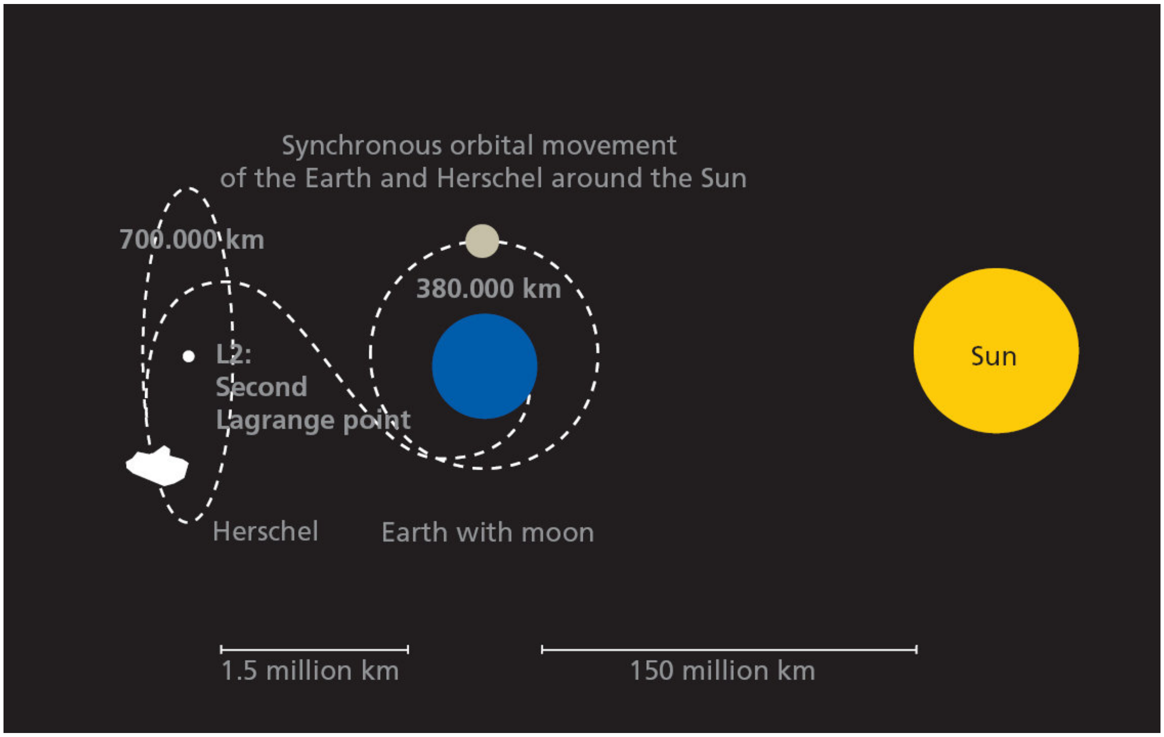

Figure 1.4: The *Herschel* Space Observatory orbit. Courtesy of the European Space Agency, `https://www.esa.int/Science_Exploration/Space_Science/Herschel/Operating_Herschel`. Diagram is not to scale.

galactic evolution [49]. A comprehensive list of publications from *Herschel* observations is maintained by the European Space Agency[1] and new findings continue to be published.

As *Herschel*'s archival phase (following the end of the observation phase) winds to a close, important work is being done to extract all of the information that can be obtained from its observations. This thesis discusses current work that is being done to ensure that the information contained in spectral observations from the *Herschel*–SPIRE instrument is as accessible as possible to astronomers. Spectral observations from the SPIRE instrument are provided by an imaging FTS which is fully discussed in Chapter 2. In the following section, I will provide a brief overview of Fourier transform spectroscopy and the design of FTS instruments.

---

[1] `https://www.cosmos.esa.int/web/herschel/scientific-publications`

1.3 Fourier Transform Spectroscopy

> Nature is not embarrassed by difficulties of analysis.
> –Augustin-Jean Fresnel (1866)

The technique of Fourier analysis was initially developed by Jean Baptiste Joseph Fourier (1768–1830) in his study of heat flow in solids [50] and has since developed into a robust and widely used tool for analyzing periodic functions and signals. In order to understand the utility and physical meaning we can attach to this technique, let us consider a simple example before we begin a more detailed mathematical treatment. It is a fairly simple experiment to see that, through the use of a prism, sunlight is composed of an almost uniform spectrum of many colours or frequencies. A prism is a fairly simple dispersing element, it changes the direction in which light propagates depending on the frequency. If we try this same experiment on another light source, say a sodium vapour lamp, we will instead observe that some frequencies such as yellow and cyan are more prominent than others, in fact, if we have been careful in the structure of our experiment we may even see characteristic dark gaps between bright portions of the spectrum. From this simple experiment we see that, firstly, light is composed of a spectrum of different frequencies, and secondly, that some frequencies may be more prominent, or have greater intensities, than others. It is through Fourier analysis [51] that we obtain a mathematical representation of this phenomenon that allows us to understand the underlying physical processes that occur.

1.3.1 Fourier Analysis

Fourier's theorem essentially states that a function, $f(t)$ of some temporal duration, T_0, (e.g., an electromagnetic wave varying in time) can be represented by an infinite series of harmonic functions with periods that are integer sub-multiples of T_0 (i.e., T_0/n where $n = 1,2,3\ldots$). An example of this Fourier composition of a simple square wave is shown in Figure 1.5. We can see this in the trigonometric form as [52],

$$f(t) = \frac{a_0}{2} + \sum_{n=1}^{\infty} \left[a_n \cos\left(n\omega_0 t\right) + b_n \sin\left(n\omega_0 t\right)\right], \tag{1.12}$$

where

$$\omega_0 = \frac{2\pi}{T_0} \tag{1.13}$$

is the fundamental frequency in the series and a_n and b_n are the amplitudes, or weighting factors, of each sinusoid's *nth* frequency. These coefficients are determined by,

$$a_n = \frac{2}{T_0}\int_t^{t+T_0} f(t)\cos(n\omega_0 t')dt', \quad n = 1,2,3\ldots, \tag{1.14}$$

and

$$b_n = \frac{2}{T_0}\int_t^{t+T_0} f(t)\sin(n\omega_0 t')dt', \quad n = 1,2,3\ldots. \tag{1.15}$$

It is worth noting that in Equation 1.12, the series of $\cos\left(n\omega_0 t\right)$ and $\sin\left(n\omega_0 t\right)$ terms form a mutually orthogonal basis [52].

It is fairly common to see the Fourier series written in exponential form,

$$f(t) = \sum_{n=-\infty}^{\infty} d_n e^{in\omega_0 t}, \tag{1.16}$$

where

$$d_n = \frac{1}{T_0}\int_t^{t+T_0} f(t)e^{-in\omega_0 t'}dt', \tag{1.17}$$

and the weights of each frequency component are split between negative frequencies ($n < 0$) and positive frequencies ($n > 0$), while $n = 0$ provides d_0, the zero frequency offset term. It is important to note that there exist Dirichlet conditions for which a convergent Fourier series representation of $f(t)$ exists [52, 53]. With sufficient number of Fourier components, periodic waveforms that can be generated in a laboratory environment may be described by a Fourier series [54, 55].

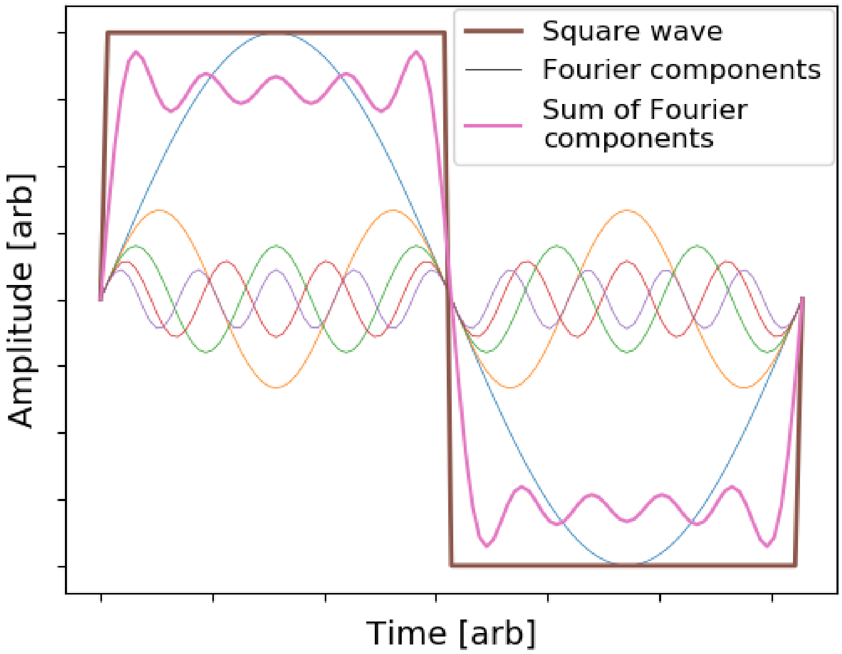

Figure 1.5: The first five terms of the Fourier composition of a square wave. Each discrete frequency sinusoid is shown as a thin waveform and the sum of these components is shown in the thicker brown line. A perfect square wave of the same period is shown by the thickest pink line.

Let us now consider the situation where the spacing between harmonic frequencies becomes infinitesimally small and the limits of the Fourier series extend out to infinity. As we approach this limit Equation 1.16 takes the form,

$$f(t) = \int_{-\infty}^{\infty} F(\nu) e^{i2\pi\nu t} d\nu. \tag{1.18}$$

This is known as the reverse (or inverse) complex Fourier transform (note $2\pi\nu = \omega$). Instead of a set of discrete weighting coefficients or amplitudes for each harmonic frequency, we now have a smooth and continuous spectrum. This spectrum of amplitudes is given by the forward complex Fourier Transform (or simply the complex Fourier Transform),

$$F(\nu) = \int_{-\infty}^{\infty} F(t) e^{-i2\pi\nu t} dt. \tag{1.19}$$

If we return to our prism thought experiment of a polychromatic light source, t takes on units of time, s, and ν takes on units of frequency, Hz. We see that our light source, $f(t)$, is composed of continuous spectrum of frequencies or colours, $F(\nu)$.

1.3.2 The Michelson Interferometer

The Michelson interferometer has been a particularly effective measurement tool that has applications ranging from the historical evidence against the theory of a luminiferous ether [56] to the recent detection of gravitational waves by the Laser Interferometer Graviational-wave Observatory (LIGO) [3]. The Michelson interferometer provides a simple example of an FTS [57]. The experimental design of a Michelson interferometer is shown in Figure 1.6 and the light path is as follows:

1. Collimated light from a source enters the inteferometer.
2. The resulting plane wave, or beam, is split down two separate paths of the interferometer (often called "arms" of the interferometer) by a beamsplitter. Ideally the beam amplitude/intensity is equal in each path of the interferometer.
3. Each beam path strikes a mirror, one is fixed (3a) while the other is movable (3b) along the optical axis. Each beam is reflected back to the beamsplitter.
4. The beams are recombined by the beamsplitter sending the recombined beam through axis output ports. In this case, both the input source (1) and the detector (5) are outputs ports.
5. A detector is placed at the focus of the final optics which records the interference of the combined waves of light. The result is an intensity variation that depends on the phase difference of the interfering waves, known as an interferogram. The phase difference between each beam is the result of an Optical Path Difference (OPD) introduced by the moving mirror (3b).

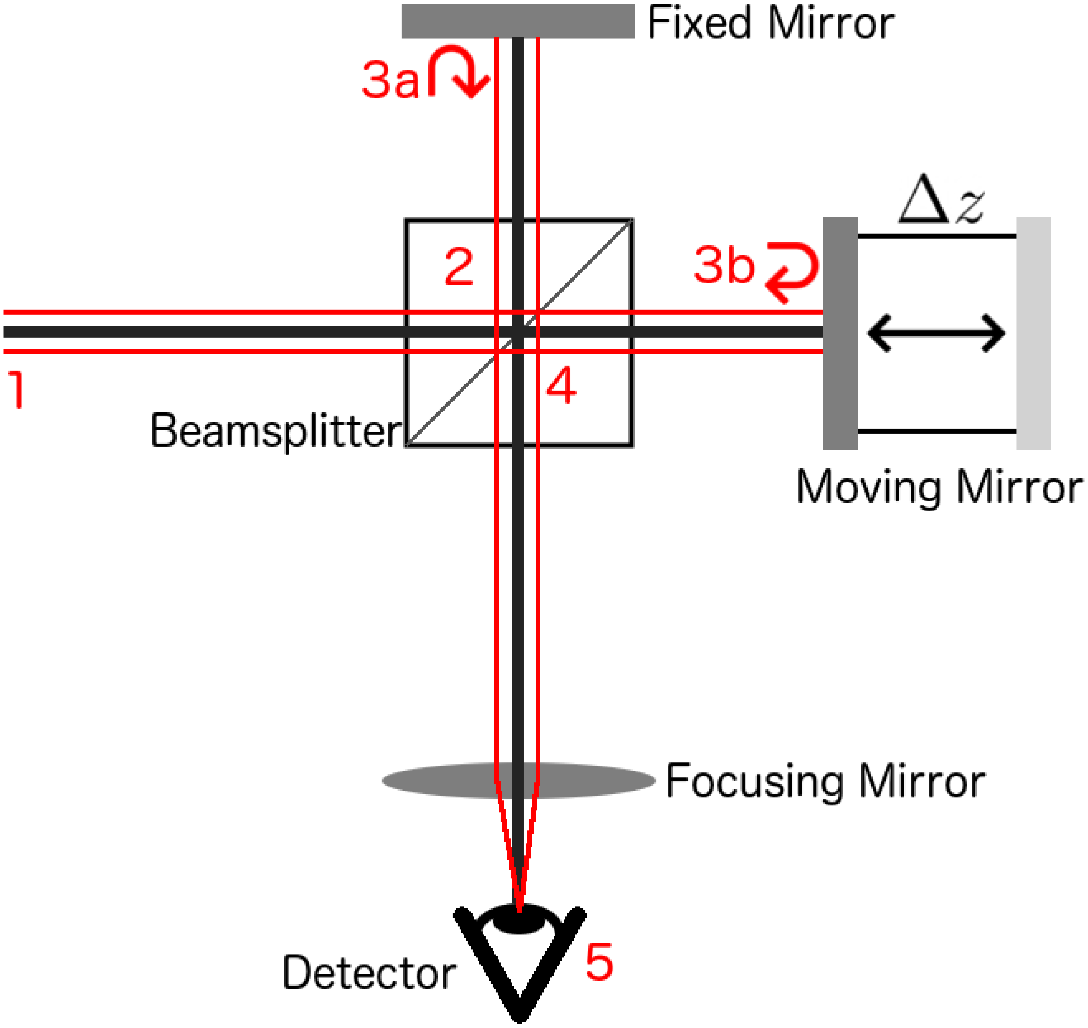

Figure 1.6: Optical diagram of a Michelson interferometer [56, 58]. Adapted from Spencer, L. [55].

Though it is a simple design, the Michelson interferometer has a disadvantage in that one of its outputs is convergent within an input. Improvements to the design have been made by tilting the light path so that it enters and exits the interferometer off-axis from the beamsplitter and stationary mirror [59] or through the use of the Mach-Zehnder (MZ) configuration. A full description of the MZ-FTS is presented in Chapter 2 with the introduction of the SPIRE instrument.

Let us consider a monochromatic source of wavenumber σ_0 [cm^{-1}] illuminating the input of the interferometer. It is worth noting here that in the field of Fourier transform spectroscopy the term wavenumber, and frequency, are often used interchangeably since $\sigma = 1/\lambda = \nu/c$. Once this input beam is divided by the beamsplitter the electric fields describing each beam can be written as,

$$\begin{array}{ll} E_1\left(z_1,t'\right) = E_0 re^{i\rho} r_m e^{i2\pi(\sigma_o z_1 - \nu t')} te^{i\tau} & [\mathrm{V/m}] \\ E_2\left(z_2,t'\right) = E_0 te^{i\tau} r_m e^{i2\pi(\sigma_o z_2 - \nu t')} re^{i\rho} & [\mathrm{V/m}] \end{array}, \tag{1.20}$$

where E_0 is the amplitude of the initial electromagnetic wave with an angular frequency $\omega_0 = 2\pi\sigma_0$, $te^{i\tau}$ is the beamsplitter transmission, $re^{i\rho}$ is the beamsplitter reflection, r_m is the reflection coefficient of each folding mirror, and t' is the travel time. Variables z_1 and z_2 are the optical path lengths of each arm, respectively. The electric field of the waves interfering at the detector, E_D, is simply the superposition of both waves (i.e., $E_D = E_1 + E_2$). Far-Infrared (FIR) detectors typically measure the total intensity, $I_0 = E_D^* E_D$, from both waves once they are recombined. This is given by,

$$I_o(z) = \frac{c\varepsilon_o}{2}\left|E_D\right|^2 = c\varepsilon_o E_0^2 R_m RT\left[1 + \cos\left(2\pi\sigma_o z\right)\right] \quad \left[\mathrm{W/m^2}\right], \tag{1.21}$$

where c is the speed of light, ε_o is the permittivity of free space, $z = z_1 - z_2$ is the OPD, $R_m = r_m^2$ is the reflectance of the mirrors, and $R = r^2$ and $T = t^2$ are the reflectance and transmittance of the beamsplitter, respectively. For an ideal interferometer, the beamsplitter reflects and transmits 50% of incident light and the mirrors are perfect reflectors. It is typical to substitute $B(\sigma_0) = c\varepsilon_o|E_0|^2$ as the intensity of the monochromatic source resulting in the expression,

$$I_o(z) = R_m RTB\left(\sigma_o\right)\left[\cos\left(2\pi\sigma_o z\right)\right] \quad \left[\mathrm{W/m^2}\right]. \tag{1.22}$$

The constant term in Equation 1.21 is typically ignored since it contains no spectral information [57, 55]. We see that as z varies by scanning the movable mirror the detector will observe alternating intensity maxima and minima. Taking the Fourier transform of Equation 1.22, two delta functions are obtained at $\pm\omega_0$ [55]. The spectrum is zero for all frequencies other than that of the source.

Due to the linearity of the Fourier transform, the detector sees a superposition of cosines from Equation 1.22 when viewing a polychromatic source,

$$I(z) = R_m RT \int_{-\infty}^{+\infty} B(\sigma)\cos(2\pi\sigma z)\,d\sigma \quad \left[\mathrm{W/m^2}\right]. \tag{1.23}$$

For an ideal interferometer, when $z = 0$ all frequency components exhibit zero phase difference and constructive interference occurs simultaneously for all wavelengths. This point is commonly referred to as the point of Zero Path Difference (ZPD).

We see that, neglecting the leading constant $R_m RT$ for the moment, Equation 1.23 is the even, or cosine, Fourier transform of the spectrum $B(\sigma)$ [57]. The spectrum is then recovered by the inverse transform,

$$B(\sigma) = \frac{1}{R_m RT}\int_{-\infty}^{+\infty} I(z)\cos(2\pi\sigma z)dz \quad \left[\mathrm{W/m^2}\right]. \tag{1.24}$$

We see here that just as time, t [s], and frequency, ν [Hz], make a Fourier transform pair, so do OPD, $z\,[\mathrm{cm}]$, and wavenumber, $\sigma\,[\mathrm{cm}^{-1}]$.

1.3.3 Instrumental Line Shape

Up to this point our discussion of FTS has been based around an "ideal" instrument. In Equation 1.24 we have considered a system in which OPD can be infinite, for real-world instruments there exists some finite maximum OPD that can be achieved which results in an Instrumental Line Shape (ILS) that deviates from a delta function. It is possible to sample the spectrum in such a way that the true profile of the ILS is not always apparent and the unwary observer may remain unaware of these important considerations.

Consider the interferogram for a monochromatic source:

$$I(z) = \cos(2\pi\sigma_0 z) \quad \left[\mathrm{W/m^2}\right]. \tag{1.25}$$

The interferogram is limited to some finite path where, $-L \leq z \leq +L$. This is the equivalent of multiplying an infinitely long interferogram (Equation 1.25) by a top-hat function,

$$\begin{gathered} I_{obs}(z) = I(z)u\left(\frac{z}{2L}\right) \quad \left[\mathrm{W/m^2}\right], \\ \text{where} \quad u\left(\frac{z}{2L}\right) = \begin{cases} 1 & -L \leq z \leq +L \\ 0 & \text{otherwise} \end{cases} \end{gathered} \tag{1.26}$$

To understand the effect this has on the spectral domain we must consider the convolution theorem for Fourier transforms. For any two functions $f(z)$ and $g(z)$ with the Fourier transform pair function $\mathcal{F}\{f(z)\} = F(\sigma)$ and $\mathcal{F}\{g(z)\} = G(\sigma)$, where $\mathcal{F}$ is the Fourier transform operator. (i.e., $\mathcal{F}\{f(z)\} = \int_{-\infty}^{\infty} f(z)e^{i2\pi\sigma z}\,dz$),

$$\mathcal{F}\{f(z)g(z)\} = F(\sigma) * G(\sigma). \tag{1.27}$$

In Equation 1.27, $F(\sigma) * G(\sigma)$ is the convolution [52] of $F(\sigma)$ and $G(\sigma)$. The convolution theorem shows us that multiplication in one (interferogram) domain is akin to convolution in reciprocal the Fourier (spectral) domain [52].

If we now consider the interferogram observed by the spectrometer in Equation 1.26, the observed spectrum takes the form,

$$B_{obs}(\sigma) = B(\sigma) * 2L\mathrm{sinc}\left(2L\sigma\right) \quad \left[\mathrm{W/m^2}\right], \tag{1.28}$$

where

$$\mathrm{sinc}\left(2L\sigma\right) = \frac{\sin\left(2\pi L\sigma\right)}{2\pi L\sigma} \tag{1.29}$$

is the Fourier transform of the top-hat function $u\left(\frac{z}{2L}\right)$ (Equation 1.26). Due to the finite optical path, the ILS of a real world FTS is a sinc profile. The Full Width at Half Maximum (FWHM) of this sinc profile is given by,

$$\mathrm{FWHM} = 1.207\,\delta\sigma = 1.207\left(\frac{1}{2L}\right) \quad [\mathrm{cm^{-1}}]. \tag{1.30}$$

The width, $\delta\sigma$, of the feature in Equation 1.30 is the resolution width or the distance between statistically independent samples in a spectrum. We see that in order to increase the spectral resolution of an FTS we must increase the maximum possible OPD that is scanned.

The constraints of a physical FTS instrument are described by an ILS function, $O(\sigma)$. The observed spectrum is the ideal spectrum, $B(\sigma)$, convolved with the ILS, $O(\sigma)$ (see Figure 1.7). This ILS deviates from the ideal sinc function through the introduction of off-axis rays entering the interferometer. For the case of the FTS within the SPIRE instrument, which is discussed in Chapter 2, the finite entrance aperture of the central detectors results in a modest deviation in the ILS from the sinc profile. Furthermore, the ILS for the off-axis detectors (see Section 2.1) also exhibit related deviations from the ideal sinc profile. While these effects are noted and understood, the observed effect in SPIRE FTS data is subtle and for the purposes of this thesis and the FF (see Section 2.2) a sinc line profile is sufficient. For the SPIRE FTS instrument, these effects are well characterized by Spencer, L [55] and Naylor, D et al. [60]. Some discussion of these obliquity effects is provided in Appendix D.

In order to reduce the magnitude of sidelobes, or ‘ringing’, in an FTS spectrum, it is common to multiply the measured interferogram by an apodizing function. All analyses of FTS spectra in this thesis will be done without the use of apodization but a full description of the technique can be found in Naylor et al. [61].

1.3.4 Consequences of Digitization

Our considerations of the Fourier relationship between interferogram and spectrum up to this point have only included smooth and continuous functions. The measured data in an FTS instrument is in reality a *sampling* of some theoretically smooth continuous interferogram. Ideally the sampling of the mirror’s movement provides evenly spaced OPD intervals with width δz. The Nyquist-Shannon (or simply Nyquist) sampling theorem states the required conditions for a discrete signal to be mathematically equivalent to the continuous interferogram [62, 63]. The theorem as stated by Claude Shannon is as follows [63]:

> If a function $f(t)$ contains no frequencies higher than W counts per second, it is completely determined by giving its ordinates at a series of points spaced $1/(2W)$ seconds apart.

The consequence of this theorem in the spectral domain limits the spectrum to a maximum frequency equal to $1/(2\delta z)$, or the *Nyquist frequency*, σ_{nyq}. The sampling theory can be thought of as sampling in time or distance [57]. If a spectral feature with a frequency greater than the Nyquist frequency is present in the interferogram, it will be aliased in such a way that a feature of frequency $n\sigma_{\text{nyq}} + \sigma_0$ ($n = 1, 2, 3 \ldots$) will appear in the Nyquist lim-

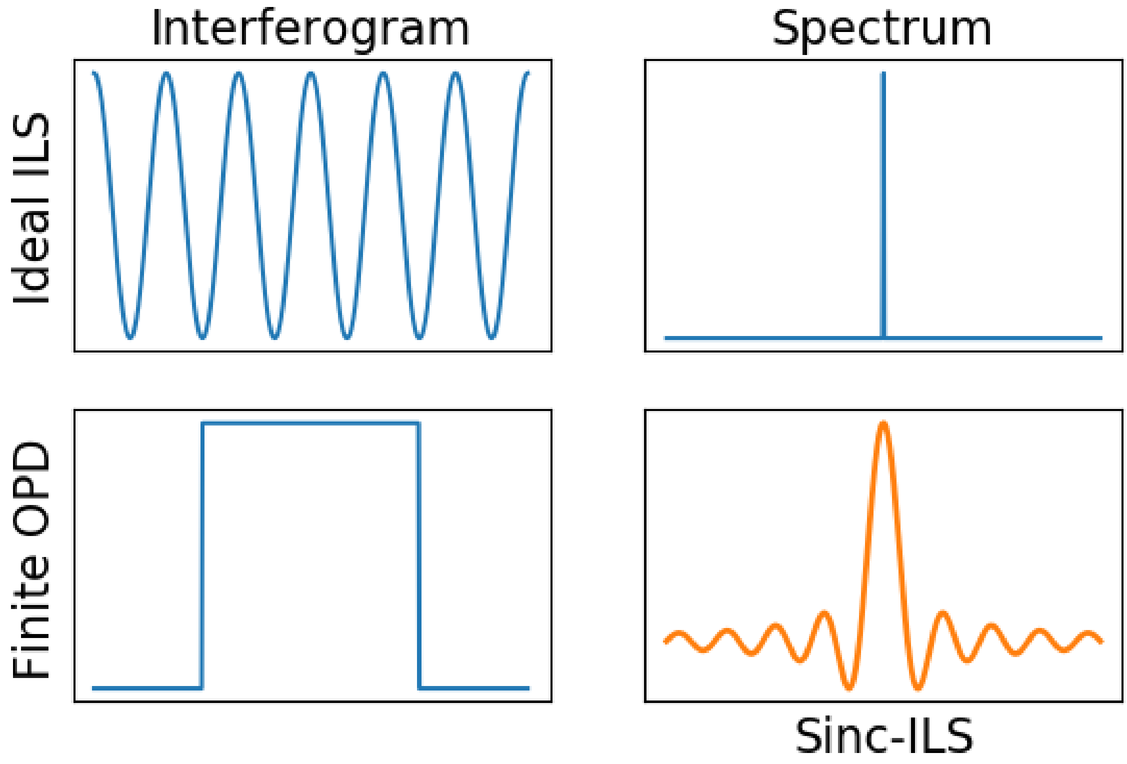

Figure 1.7: The consequences of a limiting OPD on the line profile of an FTS in both the measured interferogram and its Fourier reciprocal spectral domain. For more details see Figure D.1.

ited spectrum as a feature at a frequency of σ_0 [57].

Measuring the interferogram in equal increments of δz allows for the use of the Fast Fourier Transform (FFT) algorithm [64]. The FFT algorithm performs the computation of the discrete Fourier transform of N data points on the order of $N \log_2 N$ operations requiring at least one unique sampling of ZPD. Failure to properly sample ZPD results in unwanted phase errors in the spectrum that can be fixed in post-processing through a measurement of the interferogram that is symmetric about ZPD [57].

We have already considered the effects that a finite maximum OPD, L, has on the ILS in the spectrum. As a consequence of performing the Fourier transform on a discrete signal, independent spectral data points are spaced over a finite interval $\delta\sigma = 1/(2L)$. Again we see that the spectral resolution of an FTS instrument is improved by increasing the maximum possible OPD.

1.4 Conclusions

We have seen that progress in astronomy and astrophysics is limited by our ability to observe the light from distant systems and analyze the information it contains. The cataloguing of astronomical observations has a long history and with each new generation of observational instrument it has become important to extract as much useful data from their observations as possible.

The field of FIR astronomy is uniquely equipped to study star formation in the ISM and distant galaxies. FIR light provides us with a view of the cold dense regions of the ISM where stars in their earliest stages can be observed. From FIR observations of distant galaxies, which account for a significant portion of all the light in the Universe, we are able to measure a timeline of galaxies as they evolve. In spite of the promise of FIR observation, progress in FIR astronomy is limited by the optical sensitivity of the available detector technology, the size and thermal properties of the associated instrumentation and optical components, and the requirement to be outside of Earth's atmosphere.

There exists a legacy of FIR and Infrared (IR) space observatories in which each generation builds on the successful technologies of past generations. Building on the legacy of the IRAS, ISO, and *Spitzer* space telescopes, the *Herschel* space observatory and its instruments provided the first unfettered access to the FIR Universe and was uniquely equipped to further our understanding of star formation and galaxy evolution.

As the SPIRE instrument houses an FTS I briefly reviewed the basics of Fourier Transform Spectroscopy and the requisite instrumentation. Fourier analysis provides a useful method to describe the frequency spectrum of electromagnetic radiation and through FTS instruments the important spectral information contained in the light emitted by a source can be measured. Design limitations and digitization in FTS instruments have important consequences on the Instrumental Line Shape (ILS) of spectral features measured by the FTS which can make the extraction of spectral features difficult for those inexperienced with FTS spectra. In order to aid astronomers working with SPIRE FTS spectra, the SPIRE instrument team has developed an automated method of extracting prominent spectral features from SPIRE FTS observations which is the subject of the following chapter.

The third and fourth chapters of this thesis present my largest contribution to the *Herschel* SPIRE FTS Spectral Feature Finder (FF) project. In the third chapter I introduce and discuss the results of my work to identify the atomic/molecular energy transitions that correspond to the spectral lines found by the FF in SPIRE FTS observations. The fourth chapter presents the extension of the FF to include the spectral observations of off-axis detectors from the SPIRE FTS in sparsely sampled single-pointing observations and discusses these results. In the fifth chapter I summarize the content of this thesis and discuss the possibilities of future work that build on what has been discussed. A brief discussion of the future of space-based FIR observatories as a whole is also included in the fifth and final chapter.

This thesis contains appendices that contain large tables, figures, and supplementary material that would upset the flow of the chapters. A full list of the spectral features, their rest frequencies, upper state energies, and Einstein *A* coefficients is presented in Appendix A. The full results of the line identification routine, as introduced in Chapter 3, applied to all sparse (central and off-axis detectors) and mapping observations is presented as a figure spanning multiple pages in Appendix B. An exemplary set of the FF off-axis postcards introduced in Chapter 4 is presented and briefly discussed in Appendix C. Appendix D provides more complete derivations and simple proofs for some of the mathematical concepts discussed in this thesis.

Chapter 2

The Herschel Spectral and Photometric Imaging Receiver Spectral Feature Finder and Line Catalogue

> Equipped with his five senses, man explores the Universe around him and calls the adventure Science.
>
> –Edwin Hubble (1929)

Today we live in an era of unprecedented coverage of the night sky at multiple wavelengths. In Chapter 1 we have discussed the legacy of progressively longer duration space-based Far-Infrared (FIR) telescope missions. Starting with the short 10 month Infrared Astronomical Satellite (IRAS) mission, some 270 000 Infrared (IR)/FIR sources were observed. Since then, more observations have been taken of several more sources with greater detail and resolution. Figure 2.1 shows the sky coordinates of the 996 *Herschel*–Spectral and Photometric Imaging Receiver (SPIRE) Fourier Transform Spectrometer (FTS) High Resolution (HR) observations that are publicly available today through the Herschel Science Archive (HSA). Single-pointing sparsely sampled observations are marked in blue while mapping observations are marked in magenta (see Section 2.1.1). Observations without reliable velocity estimates are marked with an ‘x’ (see Section 2.2.5). With this modern abundance of observational data, astronomers are now faced with a unique challenge: which, in a multitude of observations, may have the information necessary to further their investigation or improve their model.

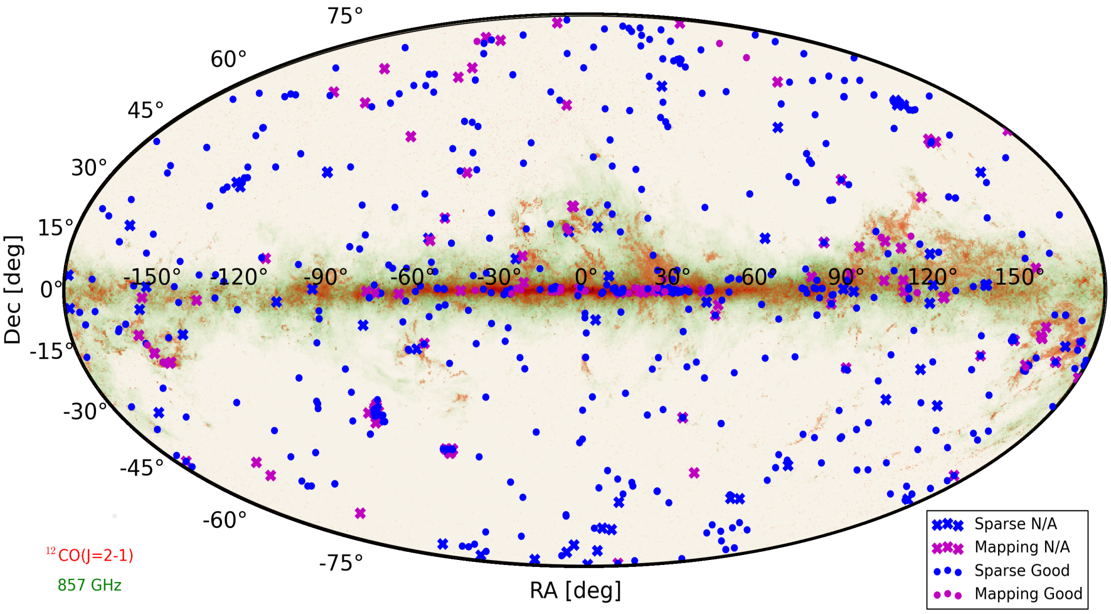

Figure 2.1: The sky coordinates of *Herschel*–SPIRE FTS observations. The background image is a composite of the Planck map from the 857 GHz band (green) [65] and the Planck map of the ^{12}CO $J = 2$–1 galactic emission at 230.5 GHz [66] (red). Courtesy of Scott, J. [67].

In this chapter, I will introduce the work of the SPIRE instrument team to provide a catalogue of all the prominent spectral features contained in every publicly available SPIRE FTS observation. I will begin with a brief overview of the technical design of the SPIRE instrument before introducing the *Herschel* SPIRE FTS Spectral Feature Finder (FF) routine and the SPIRE Automated Feature Extraction Catalogue (SAFECAT). This chapter also details my contributions to the FF project through the development of postcard figures for mapping observation of the FTS and the validation of the velocity estimating routines employed by the FF.

2.1 The Spectral and Photometric Imaging Receiver

One of the three focal-plane instruments onboard the *Herschel* Space Observatory [46] is the Spectral and Photometric Imaging Receiver (SPIRE) [68] which consists of an imaging photometer and an imaging FTS. The SPIRE FTS employs a Mach-Zehnder (MZ) configuration which allows for two separate inputs and outputs through the addition of a second beamsplitter [69]. Figure 2.2 demonstrates the application of the MZ design to the SPIRE FTS, the interferometer has two inputs both illuminating the first beamsplitter (BS 1). One input is illuminated by light from the telescope and the sky while the other is illuminated by the Spectrometer Calibrator (SCAL) [70] internal to the cryostat. SCAL is a thermal source located at a pupil image that allows for the subtraction of background emission from the telescope [70]. OPD (Δz) is achieved as the Spectrometer Mirror Mechanism (SMEC) containing a double rooftop mirror is scanned forward and backward at a constant speed. It should be noted that movement of the SMEC, q, changes OPD by a factor of $4q$. The second beamsplitter (BS 2) recombines both optical paths and sends light towards the two outputs. At each output is a set of feedhorn coupled bolometer arrays that are arranged in a hexagonal pattern and measure the interferogram (Figure 2.3). The two bolometer arrays cover two overlapping wavelength/frequency bands, the Spectrometer Long Wavelength Array (SLW) covers 303–671 μm and the Spectrometer Short Wavelength Array (SSW) covers 194–313 μm. The spectrometer also employs a sequence of metal mesh filters that help define the SLW and SSW bands (not shown in Figure 2.2) [55, 71].

The spectrometer detector arrays provide simultaneous coverage of the full SPIRE band. Figure 2.3 shows the positioning of the detectors in the hexagonal pattern. Detectors with concentric on-sky positions are coloured in blue. The thick red circle demonstrates the combined 2 arcminute unvignetted Field of View (FOV) (right panel). The SSWD5 and SSWF4 detectors (shaded in grey) are dead bolometers and are not used in science observations.

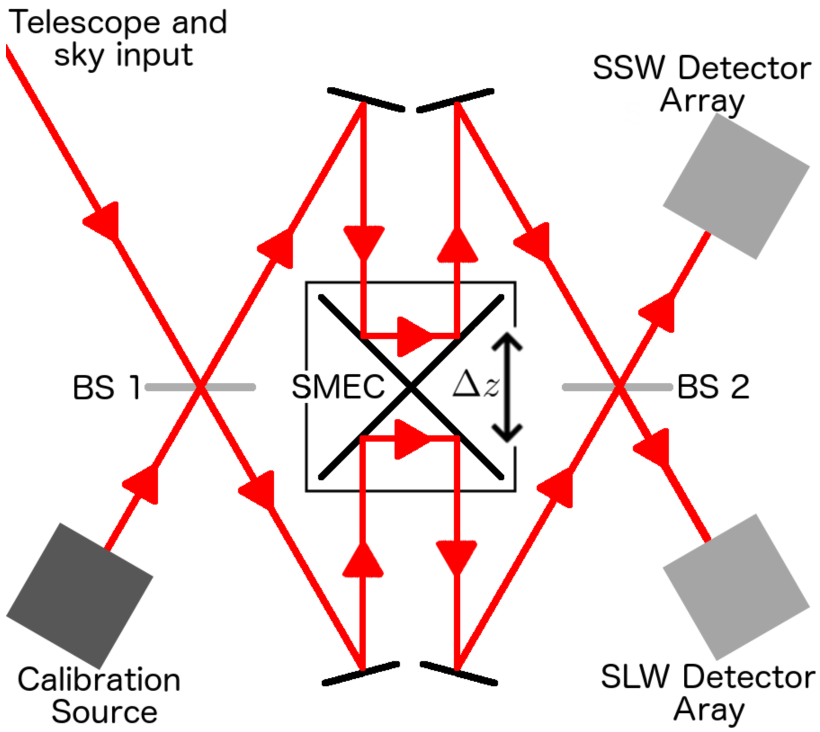

Figure 2.2: The optical design of the SPIRE FTS. Original, Ade et al. [72, 73], adapted from Hargrave, P. et al. [74].

2.1.1 Spectral and Photometric Imaging Receiver observations

The SPIRE FTS has three spectral sampling modes, two pointing modes, and three spatial sampling modes. The following subsection contains a brief description of each. These observational modes are summarized in Table 2.1.

The three spectral sampling modes are the High Resolution (HR), Medium Resolution (MR), and Low Resolution (LR) modes and each corresponds to different OPD scan lengths of the SMEC which has a maximum mechanical scan length of 3.5 cm [6]. LR observations scan the SMEC symmetrically about Zero Path Difference (ZPD) over the shortest distance of the three and are useful for making spectral continuum measurements at a spectral resolution of 25 GHz. The medium resolution option was never used for scientific observations and will not be discussed any further in this thesis. HR observations give

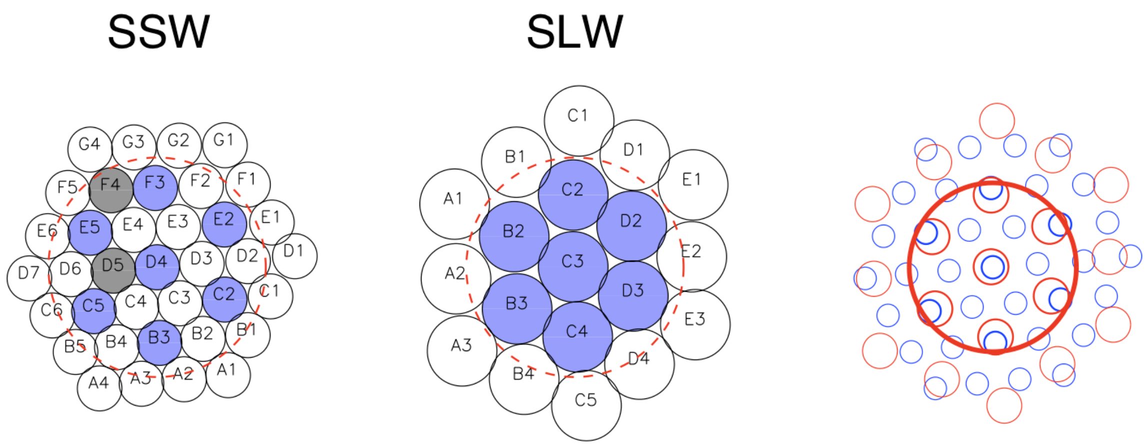

Figure 2.3: A schematic view of both SPIRE FTS detector arrays and their overlap (right). Each circle represents a detector feedhorn. Detector names are also shown. Adapted from Valtchanov, I. [6].

Table 2.1: Observational modes of the SPIRE FTS. Spatial sampling shows the beam spacing between detectors in each array. The pointing and sampling modes required for an observation to be considered sparse are bolded. For more details see the SPIRE observer's manual [6].

Pointing Mode:	**Single-Pointing**	Raster	
Spatial sampling: (SLW, SSW) [arcseconds]	**Sparse** (50.5, 32.5)	Intermediate (25.3, 16.3)	Full (12.7, 8.1)
Spectral Resolution [GHz]:	Low (R$\sim$ 25)	Medium (Unused)	High (R$\sim$ 1.2)

the highest spectral resolution available through the SPIRE FTS, 1.2 GHz, and are most useful for spectral surveys. The majority of my work pertains to HR observations.

The SPIRE FTS observations are classified into two categories, **sparse** observations (non-raster observations with sparse spatial sampling), and **mapping** observations (any other combination of pointing and spatial sampling modes). These two observation types are defined by the pointing mode and the spatial sampling of a SPIRE FTS observation.

The two pointing modes of SPIRE are a single-pointing mode to measure spectra within the instrument's 2 arcminute FOV, and a scanning raster pattern. In the raster pointing mode, the telescope is pointed through various positions making a map that covers an area greater than the instrument FOV [6].

The three spatial sampling options are sparse, intermediate, and full, and are achieved with the SPIRE Beam Steering Mirror (BSM). The BSM is located in the optical path before any incoming radiation is subdivided by further optics [6]. Sparse image sampling does not involve any movement of the BSM during the observation and produces a single footprint of the array at the output port and a spectrum for each of the hexagonally packed detectors. The spacing between the centres of each of the detectors' beams is 32.5 and 50.5 arcseconds in the SSW and SLW bands, respectively. Intermediate image sampling involves the movement of the BSM through a 4-point low frequency jiggle pattern providing a centre beam spacing of 16.3 (SSW) and 25.3 (SLW) arcseconds. Full image sampling moves the BSM through a 16-point jiggle resulting in a complete Nyquist sampling (1/2 beam spacing) of the observation. The beam spacing in the full map is 8.1 (SSW) and 12.7 (SLW) arcseconds. The footprint of each spatial sampling mode is shown in Figure 2.4.

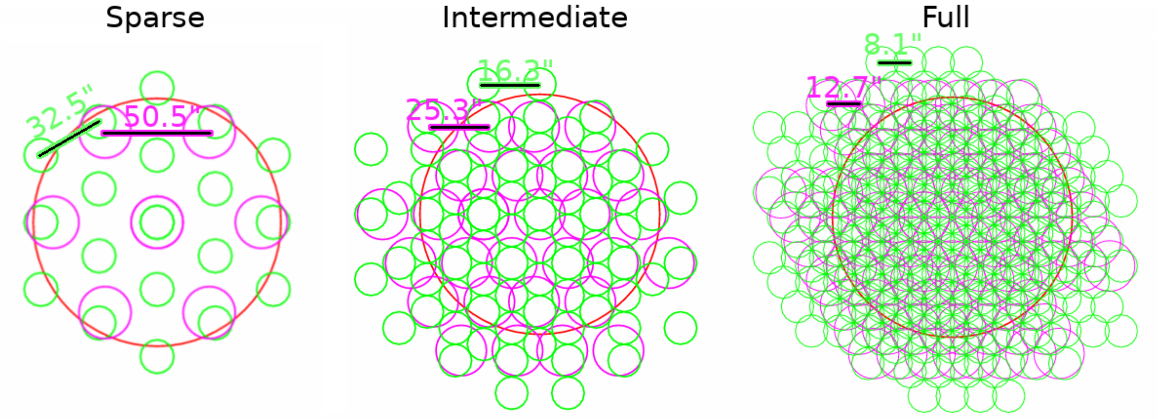

Figure 2.4: Footprints of the SSW detector array (green) and the SLW detector array (magenta) in each image sampling mode. Circles correspond to the FWHM of each detector beam. Adapted from Valtchanov, I. [6].

Sparse observations are simply composed of a spectrum for each detector while mapping observations are more complex. Mapping observations are projected onto a regularly gridded hyperspectral cube that collects the individual spectra from each detector, BSM jiggle position, and raster point into a single list. The result is a two dimensional set of pixels, or spaxels, that each contain a full spectrum. This hyperspectral cube has two spatial axes (sky coordinates) and a depth axis in frequency space.

The flux calibration of sparse observations is divided into two categories based on two key assumptions about the structure of the source in an observation. *Extended source* calibration, refers to the method used for a source that has uniformly extended emission over the entirety of the beam of a given detector. *Point source*, calibration refers to the method employed for a point-like emission centred on the optical axis. Observations processed with the extended calibration result in a spectrum with surface brightness on the intensity axis in units of flux density per steradian, $\mathrm{W\,m^{-2}\,sr^{-1}\,Hz^{-1}}$. The point source calibration of an observation results in a spectrum with an intensity axis of flux density in Janskys ($10^{-26}\,\mathrm{W\,m^{-2}\,Hz^{-1}}$). The use of an incorrect flux calibration for a sparse SPIRE FTS observation is manifest by a discrepancy in flux measurements in the overlapping spectral region of the SLW and SSW bands. It is possible for an observation to exist somewhere between the two extreme geometric cases of point-like and extended sources, due to the multi-moded frequency dependence of the SPIRE FTS beam (see Makiwa et al. [75]). Processing routines detailed by Wu et al. are available to treat these semi-extended sources [76].

We have already discussed that throughout a SPIRE observation the SMEC is scanned forward and backward in order to modulate the interference signal on the detectors. A single observation can employ multiple scans of the SMEC to obtain a time averaged spectrum and interferogram. Owing to this mechanism it is convenient to express the integration time of an observation as a number of repetitions, or full scans of the SMEC.

Each SPIRE FTS observation is assigned an identification number (observation ID). All *Herschel* scientific observations are publicly available through the Herschel Science Archive (HSA)[2]. This web-based platform provides a complete archive of *Herschel* observations that can be searched based on sky coordinates, observation ID, or other keywords listed in the meta data of each observation.

2.1.2 The Herschel Interactive Processing Environment

The Herschel Interactive Processing Environment (HIPE) is an open-source astronomy data analysis package written in Java and Jython (a Java implementation of Python) providing users with access to routines, algorithms, and calibration products developed by the *Herschel* scientific community as well as easy access to the HSA. HIPE is a completely free software package and is available on multiple platforms [77]. HIPE is a script driven development environment and includes several useful SPIRE FTS data processing tools including, sparse and mapping observation processing pipelines, the semi-extended correction tool, the pointing offset correction tool, and the sparse background subtraction tool. Many of the routines presented and discussed in this thesis were developed using the tools available in HIPE

2.2 The *Herschel* Spectral and Photometric Imaging Receive Fourier Transform Spectrometer Feature Finder

The *Herschel* SPIRE FTS Spectral Feature Finder (FF) is an automated process developed within the SPIRE instrument team that finds and fits significant spectral features in all publicly available SPIRE FTS observations, and, where appropriate, provides spectral line catalogue entries associated with the features found. Through the FF, the wealth of spectral

---

[2] `http://archives.esac.esa.int/hsa/whsa/`

data measured by the SPIRE FTS is more accessible to astronomers and provides a useful data mining aid for the HSA. FF products provide a starting point in data analysis for quick inspection of one or multiple SPIRE FTS observations and facilitate the search for spectral features of interest across the entirety of SPIRE FTS observations [7].

2.2.1 My role in the Feature Finder

The FF is a collaborative work produced by researchers within the *Herschel* SPIRE instrument team. For the purposes of this thesis, it becomes important to define my personal contributions to the project. Throughout my work on the FF project I have been involved in testing the agreement between radial velocities measured by the FF and published results, exploring modifications to FF velocity estimations for extragalactic targets, detailed analysis and literature review for niche-case observations, the development of postcard images for mapping observations, and associated documentation for the SAFECAT webpages that are hosted through the HSA.

Postcard images for each observation are displayed in SAFECAT to provide at-a-glance summaries of the information contained in the associated observation catalogue entry. I developed these postcards for SPIRE FTS mapping observations (See Figure 2.5). The first column contains the brightness of each spaxel integrated across the entire frequency band from the SLW (top) and SSW (bottom) hyperspectral cubes. The brightest and dimmest pixels from the SSW array are marked in magenta and green (respectively) as are their complementary pixels in the SLW map. The second column shows the dimmest and brightest spectra as well as the spectra with the greatest number of lines extracted by the FF (red). These spectra from the SLW array are shown in the top panel while those from the SSW array are shown in the bottom panel. The continuum fit results are also shown by the dashed black lines. The third column contains combined maps projecting the SLW cube onto the sky coordinate grid of the SSW cube, the number of lines found by the FF (top) and radial velocity map (bottom) combine the lines found by the FF in the SSW array with its nearest neighbouring SLW pixel. The pixel with the most lines found by the FF is outlined in red with the outline of its corresponding SLW pixel for comparison. Green numbers are placed over each pixel of the velocity map to indicate the number of ^{12}CO features used in measuring the radial velocity (see Section 2.2.5) with an ‘A’ denoting that all 10 in-band rotational transitions were used. The ‘N’ character notes a pixel with a velocity estimate obtained from the ionized nitrogen feature (see [78] and Section 2.2.5 for more details). Spaxels with no reliable velocity estimate are left grey but are outlined in a green border to differentiate them from empty pixels in the spectral cube. Since the vast majority of mapping observations have at least one spaxel with a reliable velocity estimate determined by ^{12}CO features, velocities estimated from external sources are not used within the postcards or FF catalogue for mapping observation (see Section 2.2.5).

The processes by which the FF extracts spectral features from SPIRE FTS observations and the methods by which radial velocities are measured are described in the following sections of this chapter.

My work on velocity verification was to compare the measurements from the ^{12}CO routine (see Section 2.2.5) to values that have been previously published for the sources observed by *Herschel*. These published radial velocity measurements are taken from the Set of Identifications and Bibliography for Astronomical Data (SIMBAD) and NASA/IPAC Extragalactic Database (NED) as well as a list used internally by the Heterodyne Instrument for the Far Infrared (HIFI) instrument team. These collections were queried for targets within a 6 arcsecond radius of the SPIRE FTS central pointing. Queries from the SIMBAD and NED databases were facilitated by the **Astroquery**[3] Python package [79]. FF velocity

---

[3] `https://astroquery.readthedocs.io/en/latest/`

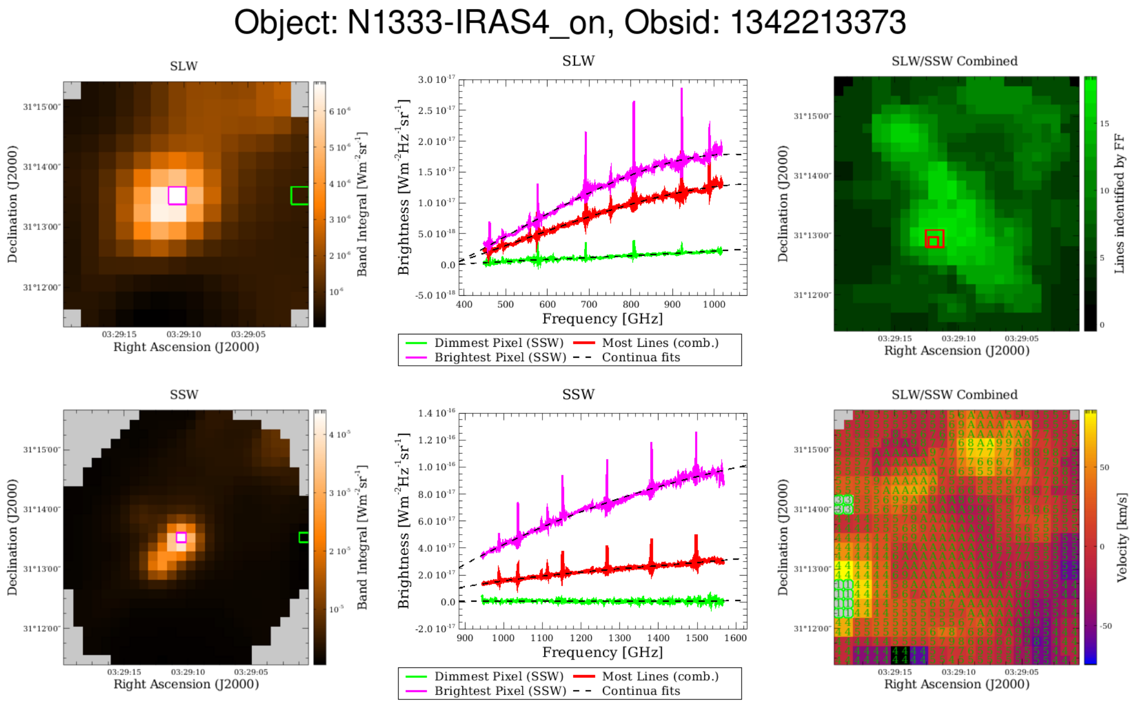

Figure 2.5: A sample mapping postcard from SAFECAT. The first column provides intensity maps for the SLW (top) and SSW (bottom) arrays. The second column displays spectra of interest including brightest spectra, dimmest spectra, and the spectra with the most lines extracted by the FF for SLW (top) and SSW (bottom). The final column shows a map of the number of identified spectral features (top) and associated radial velocities (bottom). A more complete description of the contents is provided in the text.

measurements showed agreement with published values to within 25 km/s for over 90% of the observations studied and to better than 10 km/s for the HIFI list [80]. For reference, the HR frequency spacing of 1.2 GHz corresponds to ∼ 580 km/s and ∼ 306 km/s in the centre of the SLW and SSW bands, respectively. This routine has since been further tested by Scott et al. [78] on simulated spectra.

There exist some niche-case observations of the SPIRE FTS that can result in incorrect velocity measurements that are considered confident by FF radial velocity flagging criteria. I was responsible for investigating these cases. For high redshift galaxies, it is possible for the C II $^2P_{3/2} - ^2P_{1/2}$ fine structure line (rest frequency 1900.5 GHz) to be frequency shifted into the N II search window of the ^{12}CO velocity routine (see Section 2.2.5) causing it to be falsely identified as this N II $^3P_1$–$^3P_0$ feature (rest frequency 1461.1 GHz). A number of radial velocity measurements for SPIRE FTS observations of galactic targets are reported by Wilson et al. [81] which are sometimes used in place of FF estimates to remedy this issue (and flagged accordingly).

Another peculiar observation resulting in an incorrect velocity measurement is that of the Hydrogen recombination maser and laser source, MWC 349 [82, 83]. The postcard of this observation is shown in Figure 2.6. In this observation, the strong H-α recombination lasers are mistakenly taken to be ^{12}CO features by the ^{12}CO velocity routine. This erroneous identification of CO features results in a much larger radial velocity measurement than the actual 14 ± 5 km/s (measured from H-α and H-β recombination lines detected by the FF).

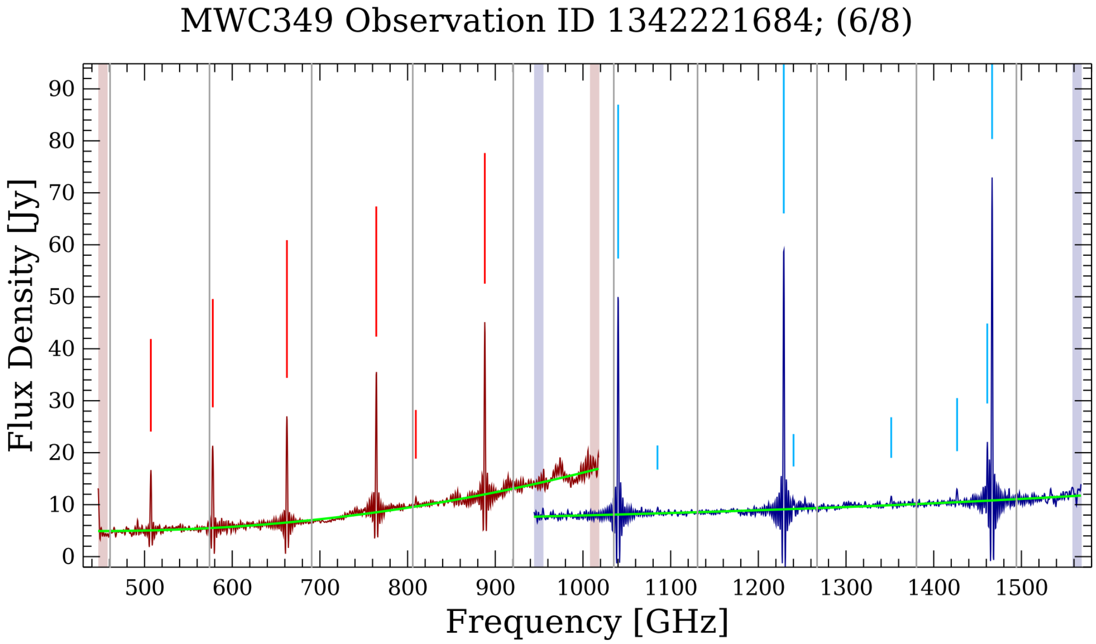

Figure 2.6: The sparse SAFECAT postcard for an observation of MWC 349 demonstrating strong hydrogen infrared laser lines. Vertical grey lines mark the rest frequencies of in band ^{12}CO rotational transitions.

My most substantial additions to the FF involve the identification of the spectral signatures from FF extracted lines and the extension of the FF routine to the off-axis detectors in sparse observations. The identification of FF extracted lines is the subject of Chapter 3, and the extension of the FF routine to the off-axis detectors is detailed in Chapter 4.

2.2.2 Routine inputs

The FF script is designed to work on an FTS spectrum from either SLW or SSW arrays from standard pipeline processed observations from the HSA. This pipeline was developed by Fulton et al. [84] and performs necessary calibrations and corrections to determine the optical spectrum of a source from the interferogram that is measured by the bolometers. The full pipeline process is readily available in HIPE as a Jython script. Input products for the FF are processed by the pipeline with HIPE version 15 and the SPIRE calibration tree, `spire_cal_14_3`. Unapodized spectra are used in the FF.

For HR sparse observations, the FF processes only the central detector of each array (SLWC3 and SSWD4) since most observations of this nature are of point-like sources or sources with little spatial extent. The application of the FF to the off-axis detectors in sparse observations is the subject of Chapter 4. For HR Mapping observations, the FF is run on every spaxel in both SLW and SSW hyper-spectral cubes excluding spaxels in the cube that do not correspond to measured spectra. These spaxels without a spectral measurement are assigned not-a-number (NaN) values when the cube is generated. The FF routine is applied to LR observations following the same sparse and mapping protocols as the HR observations, only the iterative line fitting loop is skipped and only continuum parameters are extracted.

For some SPIRE FTS observations, including observing calibration sources for SPIRE, there exists data products that have received greater attention by experts within the instrument team [85]. Some of these products are available as Highly Processed Data Product (HPDP) that are available through the *Herschel* Science Centre[4]. These HPDPs are used in the FF for HR sparse mode observations when they are available. The improvements in the HPDPs include a correction for semi-extended sources using the Semi-Extended Correction tool in HIPE, subtraction of high background emission using the measurements from the off-axis detectors, and/or a pointing offset correction (for a subset of the calibration targets). This background subtraction is different than the removal of the telescope emission which is done for all SPIRE FTS observations [6]. A full description of the corrections for semi-extended sources and pointing offsets can be found in Wu et al. [76] and Valtchanov et al. [86], respectively.

For extended and semi-extended sources the FF was run with both the point source and the extended source calibration data products. The SPIRE beam diameter is frequency dependent [75], sometimes making it difficult to determine which calibration scheme would provide the better FF result. Correcting for semi-extended sources and determining the proper calibration for ambiguous cases was considered to be beyond the scope of the automated feature finder and thus is not described here. The summary of observational inputs to the feature finder from the entire HSA is summarized in Table 2.2. It should be noted that the use of both calibration scheme products for extended and semi-extended sources results in a double counting of products processed by the FF for some observations. This can be seen in Table 2.2.

2.2.3 Feature Finder routine overview

The Spectral Feature Finder is a scripted program developed in HIPE, version 15, which makes use of several tools contained within the processing environment. Figure 2.7 summarizes the entirety of the FF routine. The routine was developed to process a large number

---

[4] `https://www.cosmos.esa.int/web/herschel/highly-processed-data-products`

Table 2.2: Observational inputs to the FF.

Observation/Product Classification	Quantity
Sparse HR	Total: 818
Point Source	471
Extended Source	147
Semi-Extended	250
HPDP	164
Background Subtracted	86
Mapping HR	Total: 180
Sparse LR	Total: 293
Mapping LR	Total: 106

of observations automatically while having sufficient flexibility to produce reliable results for the diverse observing modes and observation targets. A more detailed description of the routine can be found in Hopwood et al. [7].

Initial fit to the continuum

Before any attempt is made to search for spectral features, the FF fits a polynomial to the continuum. This step is shown by the first orange box in Figure 2.7. All significant features in the spectrum are masked. A "difference spectrum", $\Delta S(\nu_i)$, is generated by taking the difference between adjacent flux values in a subsampled spectrum, $S(\nu_i)$, $\Delta S(\nu_i) = S(\nu_i) - S(\nu_{i-1})$. Any discrete jump in $\Delta S(\nu_i)$ that is greater than 3.5 times the root mean square (rms) of the difference spectrum is considered to be a strong peak in the original spectrum and is masked out. The original spectrum is then fit with a 3$^{\text{rd}}$ order polynomial for an HR spectrum or a 2$^{\text{nd}}$ order polynomial for an LR spectrum to obtain a continuum model. The resulting best fit continuum model is used as a base for all further spectral feature finding within an observation.

Fitting spectral features

At this point the FF has both the input spectrum, $S(\nu_i)$, and modelled continuum, $C(\nu_i)$, available to it as the total model, $M_T(\nu_i)$. The process that finds spectral features iterates

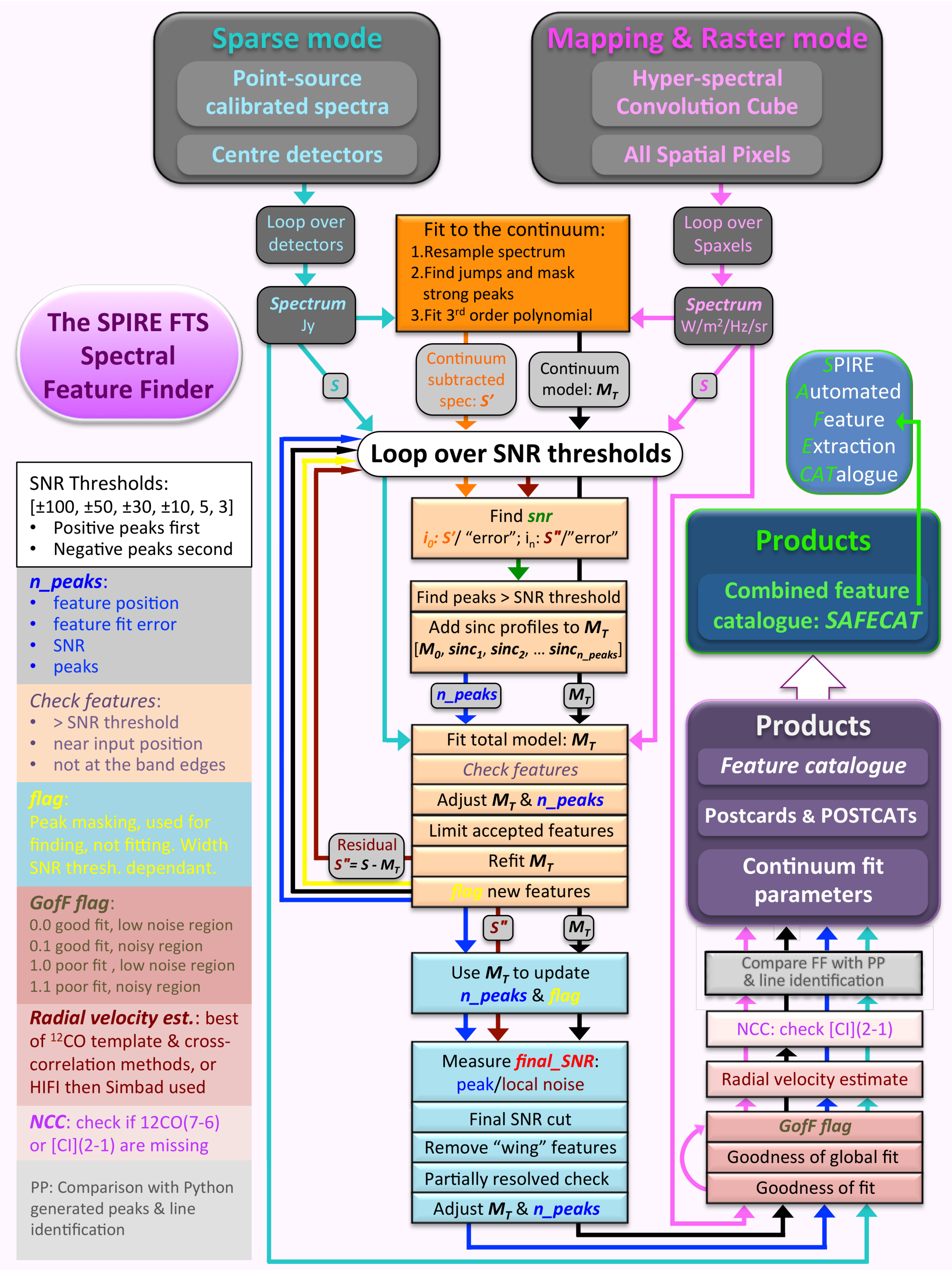

Figure 2.7: The FF flowchart, which demonstrates the main steps of the routine. Developed by Hopwood et al. [7]. A detailed description of the chart is in the text of this chapter and [7].

over a set of decreasing SNR thresholds. This process is represented by the "Loop over SNR thresholds" section of Figure 2.7. The FF employs positive SNRs with negative SNRs as a construct to treat absorption features which have a negative amplitude. The routine first does a positive pass looking for features greater than the SNR thresholds (emission features) then a pass looking for features below the negative of the SNR thresholds (absorption features). Newly fit spectral features are aggregated to the total model as the routine iterates. A description of the routine is given as follows:

1. The continuum model is subtracted from the input spectrum and the input spectrum is then divided by the error spectrum, calculated by the SPIRE FTS pipeline, $\delta S(\nu_i)$, in order to obtain a SNR spectrum.

$$S_{\mathrm{SNR}}(\nu_i) = \frac{S(\nu_i) - C(\nu_i)}{\delta S(\nu_i)} \tag{2.1}$$

2. Regions where S_{SNR} is greater than the iteration threshold are located. The peaks are determined by merging together all peaks in the SNR spectrum within a window that is 10 GHz wide per peak. Multiple peaks that are merged together in this way are considered to pertain to a single spectral feature.

3. A sinc profile is added to the total model, $M_T(\nu_i)$ (which only includes the continuum for the first iteration over SNR thresholds). The width of each sinc function is kept fixed at $1.2/\pi$ GHz since the majority of spectral features in SPIRE FTS HR observations are unresolved (their width is determined only by the ILS) [7].

4. A global fit is performed. The full model containing all spectral features and the continuum model is matched to the input spectrum using a Levenberg-Marquadt least squares fit [87]. Checks are performed to remove features that are likely to be spurious detections. These are detailed in Hopwood et al. [7].

5. At this point, multiple sinc functions may have been fit to partially resolved lines. A

check is performed to reduce the number of multi-sinc fits to these lines [7].

6. The remaining features are assumed to be valid with a stable fitted central frequency. A restriction is imposed to limit all fitted sinc functions to remain within 2 GHz of this initial fitted frequency value.

7. With spurious features removed, the global fit is repeated.

   (a) If the fit succeeds, new features are added to the list of detected features and they are removed from the residual spectrum for following iterations. The frequency width of the mask depends on the SNR threshold and no new features that fall within a previously masked frequency region are accepted.

   (b) If the fit fails, all new features from this iteration are removed and results from the previous iterations remain unchanged for the next iteration at a lower SNR threshold.

8. The residual, $R(\nu_i)$, between the full model, $M_T(\nu_i)$, and the original spectrum is calculated, $R(\nu_i) = S(\nu_i) - M_T(\nu_i)$. This residual is used to search for new peaks in the next iteration, however, the fitting of spectral features is always performed on the original spectrum.

9. Once the loop has cycled through emission features (positive amplitude) down to the lowest SNR threshold, the loop is then repeated searching for absorption features (negative amplitude). By definition absorption features have negative SNRs so the threshold is performed on the absolute negative of the SNR thresholds, in decreasing magnitude.

Frequency masking

A spectral frequency mask centered on a detected feature is used to lesson the number of spurious detections that may occur in the wings of another feature. This mask is built upon and updated after each iteration and its width depends on the SNR threshold. These widths were determined by the expected amplitudes of side lobes in a pure sinc function [7] and a few additional considerations. There is a known asymmetry in the ILS of the SPIRE FTS [60] that deviates the line from the ideal sinc function (see Section 1.3.3) which can result in a small misalignment between the spectral feature and the best-fit model. The velocity dispersion of a source [1] and the noise spectrum of the observation may also cause a broadening in the spectral features in an observation. The known asymmetry and broadening effects can result in prominent spectral residuals in the wings of fitted spectral features [85] which must be understood and managed when determining mask widths. The chosen mask widths are displayed in Table 2.3. Note that in order to avoid false detections in the FF, the -5 and -3 SNR thresholds are omitted when searching for absorption features.

Table 2.3: The iterative SNR thresholds.

Iteration Number	SNR threshold	Mask Width [GHz]
1	±100	8
2	±50	8
3	±30	5
4	±10	4
5	5	2
6	3	2

Limiting spectral feature drift and spurious feature removal

The FF uses masks to set forbidden frequency regimes around each spectral feature and at the edge of the SPIRE detector bands where sensitivity is decreased. These masks do not prevent features from wandering into forbidden regions during the global least squares fitting process and it is possible to end up fitting unwanted side-lobes or noise features. A number of checks are performed after the first global fit in each iteration for new features found to remove those that are likely spurious detections [7].

Estimation of the final SNR

The final residual after the execution of the main loop is used to determine the final reported SNR of each feature. The SNR is calculated as the ratio between the fitted amplitude, A_f, and the standard deviation of the residual spectrum $\boldsymbol{\sigma_A}$, $\mathrm{SNR} = A_f/\boldsymbol{\sigma_A}$. A spectral region in the neighbourhood of the feature is used to determine $\boldsymbol{\sigma_A}$ after a localized baseline subtraction is performed. In order to avoid false positives, features of an absolute SNR below 5 are not reported by the FF.

Neutral Carbon Check

In order to disentangle the neighbouring ^{12}CO(7–6) transition and C I $^3P_2$–$^3P_1$ feature at rest frequencies 806.7 GHz and 809.3 GHz, respectively, a neutral carbon check routine is employed (Scott et al. [88]). This method assumes that both features are coupled in approximately the same radial velocity frame giving a 2.69 GHz separation between the two features (rest frame). This separation, is dependent on the radial velocity of the source (see Section 2.2.5). A C I feature is added to the FF result if it is identified by this check and is flagged accordingly.

2.2.4 Confidence flagging

A quality metric is reported with each feature found by the FF routine. The associated confidence flags are a combination of a goodness of fit parameter and a total fit evaluation parameter. The χ^2 parameter is often used as a fit metric but is only appropriate when the noise of the data is Gaussian in nature. SPIRE FTS data has several incidences of systematic noise from telescope and instrument emission. This noise coupled with the ringing of spectral features themselves (i.e., the sidelobes of the sinc functions) make χ^2 inappropriate as an effective goodness of fit metric. Hopwood et al. [7] describes the formulation of different goodness of fit metrics that are employed by the FF in place of χ^2.

By considering the SPIRE FTS sensitivity and continuum offset error in conjunction with spurious detection in repeated observations of SPIRE FTS featureless calibration sources, “noisy” regions in the frequency range of both the SLW and SSW bands were determined. The noisy regions are defined to be at frequencies < 608.6 GHz and > 944.0 GHz for SLW, and < 1017.8 GHz and > 1504.7 GHz for SSW. The defined noisy regions in conjunction with the goodness of fit parameters make the basis for the FF flags assigned to each fitted feature. These combined flags are presented in Table 2.4.

Table 2.4: Flags used in Feature Finder products. For each velocity flag a ‘?’ is appended to denote a velocity estimate that is not confident when appropriate.

Fitted Feature Flags		Radial Velocity Flags	
Flag	Decription	Flag	Description
0.0	Good fit in a lower noise region	FF(?)	Determined by 12CO
0.1	Good fit in a noisy region	XCORR(?)	Determind by Cross Correlation
1.0	Poor fit in a lower noise region	S?	Value from SIMBAD used [89]
1.1	Poor fit in a noisy region.	H?	Value from HIFI list used
		W17	Determined by Wilson et al. [81]

2.2.5 Velocity Estimates

The spectrum of a source moving with some velocity with respect to the observer experiences a Doppler shift in frequency space. The convention used for this Doppler shift in the FF is as follows:

$$v_{\text{rad}} = \left(\frac{\nu_e}{\nu_o} - 1\right) c = zc \quad [\text{km/s}]\,, \tag{2.2}$$

where v_{rad} is the velocity of the object parallel to the observer’s line of sight. ν_e is the frequency of the emitted radiation, ν_o is the frequency measured by the observer, and c is the vacuum speed of light in km/s. The unitless parameter z is known as the red-shift and is often used as a metric for how much an object is receding from the observer. Note that motion away from the observer is taken to be positive, this is in large part due to Hubble’s observation of the expanding Universe mentioned in the previous chapter [24]. By a large margin, most astronomical objects are moving away from us, shifting their light to lower, or redder, frequencies. It also appears that in almost every case the further away from us an astronomical source is, the faster this object is receding. By measuring the Doppler shift in spectral line frequencies from their rest frequency we obtain a method to determine the radial velocity of the source.

The FF routine employs two analytical methods for determining radial velocity in SPIRE FTS observations, both of which are characterized by Scott. et al. [78]. The first method, referred to as the ^{12}CO method, makes use of the rotational ladder of ^{12}CO that occurs within the SPIRE bands for sources with ^{12}CO rotational features. The frequency differences between spectral features extracted by the FF are compared to the characteristic spacing between ^{12}CO transitions. This process is iteratively repeated for a variety of radial velocities which will either stretch (blueshifted) or compress (redshifted) the spacing between the rotational transitions. Figure 2.8 demonstrates the frequency shift experienced by a simulated spectrum of ^{12}CO features at a radial velocity of 10 000 km/s. Note that the shift towards the left experienced by each feature is dependent on its rest frequency thereby changing the nominal spacing between features. The velocity that provides the maximal number of features with a spacing equal to the expected spacing between ^{12}CO transitions is then taken to be the radial velocity of an observation. This routine also checks for strong emission within the neighbourhood of the N II $^3P_1 - ^3P_0$ fine structure line (rest frequency 1641.1 GHz) that is commonly found in SPIRE FTS observations, and uses the shift of the strongest feature in the search region from the N II rest frequency to obtain a velocity estimate. This N II check is used when a reliable velocity estimate from the ^{12}CO features is not obtained. This ^{12}CO method has been shown to be highly effective and requires minimal processing. [78]. Observations with radial velocity estimates determined by this method are flagged with either of the “FF” or “FF?” radial velocity flags denoting a confident or less confident result from the routine, respectively.

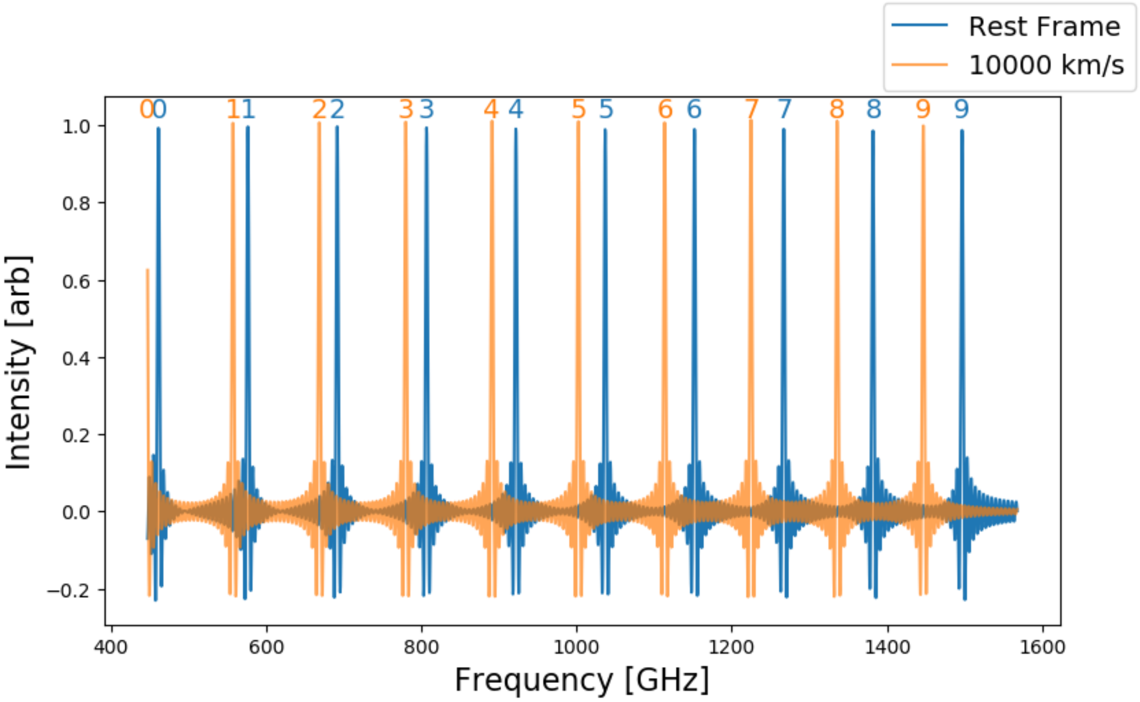

Figure 2.8: The Doppler shift experienced by a simulated spectrum of ^{12}CO features at a radial velocity of 10 000 km/s.

The second analytical method for determining radial velocity employs a template spectrum of molecular and atomic fine structure lines that commonly occur in FIR observations within the SPIRE bands. The full extent of the template spectral line list is discussed in Chapter 3. The radial velocity estimate is obtained by generating an "idealized" spectrum of delta functions centred at the line frequencies of features detected by the FF that are not considered to be a poor fit in a noisy region (FF Flag 1.1) and have a $|\mathrm{SNR}| > 10$, $F(\nu_i)$. This spectrum is then compared to the template spectrum, $T(\nu_i)$ at different radial velocities. The ideal spectrum is frequency shifted through a -100 to $+1400$ km/s radial velocity range in steps of 20 km/s with the new frequency axis at each velocity, v_n, being calculated as,

$$\nu_i' = \left(1 + \frac{v_n}{c}\right)\nu_i. \quad \text{[GHz]} \tag{2.3}$$

Note that in Equation 2.3 the observed lines by the SPIRE FTS at a lower frequency (redshifted) are being blueshifted back to their rest frequency. With the shifted spectrum, the cross-correlation at any given velocity is,

$$C(v) = \frac{1}{\sigma_F \sigma_T} \frac{1}{N} \sum_{i}^{N} T_v(\nu_i') F_v(\nu_i'), \tag{2.4}$$

where σ_F and σ_T are the standard deviations of the spectrum and template, respectively, and N is the number of samples in the frequency grid of both template and spectra. The velocity that maximizes the cross-correlation function provides the radial velocity estimate for the observation that is included in SAFECAT, noting that not all atmoic/molecular species are expected to co-exist within the same radial velocity frame. As with the other FF products, this estimate is intended as a starting point for further study. The cross-correlation function, $C(v)$, is sensitive to equally spaced features such as the ^{12}CO rotational ladder that cause degenerate peaks. In order to combat this issue, the velocity of the five most prominent maxima in $C(v)$ are used for an initial line identification matching features identified by the FF to the template. The velocity of the peak that provides the greatest number of matches to the template is considered to be the radial velocity of the source. When no reliable velocity estimate is obtained from the cross-correlation and line matching, a check for the N II feature in SSW spectra and ^{12}CO(7-6) feature in SLW spectra similar to the N II check in the ^{12}CO method is used. These features are used since they are assumed to be the brightest features within SPIRE FTS observations containing few spectral features.

Figure 2.9 demonstrates the cross correlation between the template and the line spectrum of extracted features from a SPIRE FTS observation. The most prominent peaks in the cross-correlation function are shown by red 'x' markers. The strongest peak corresponds to a velocity of -60 km/s where all 16 lines extracted by the FF are successfully matched to template lines. Observations with radial velocities determined by this cross-correlation method are assigned either the "XCORR" or "XCORR?" radial velocity flag. Again the '?' denotes a less confident result from the routine. Due to the higher processing requirements of this routine, it was only used for sparse observations.

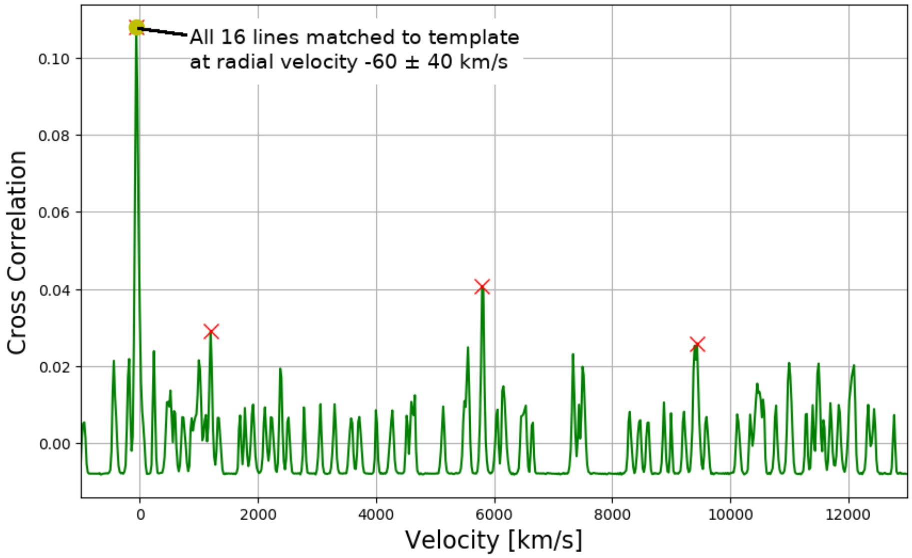

Figure 2.9: The cross correlation between Feature Finder extracted features and the template.

On the occasion that no radial velocity can be obtained with either the ^{12}CO or cross-correlation methods, a value provided from a list of velocity estimates from the Heterodyne Instrument for the Far Infrared (HIFI) instrument team is used instead. The HIFI list of radial velocities is a collection of targets and corresponding radial velocities used internally by the HIFI team (Lisa Benamati, private communication). The CO and cross-correlation methods have been compared to the HIFI provided values for sources where an estimate from both are available and show excellent agreement: either the difference is less than 20 km/s or the fractional difference is within 20% if the velocity estimate is > 100 km/s [78]. Observations with a radial velocity reported from the HIFI list are flagged ‘H?’.

Many sources observed by the SPIRE FTS have documented radial velocities obtained from measurements with other telescopes. Many of these measurements can be found in online databases such as the NED [90] and SIMBAD [89] and can be easily accessed in bulk through the python package **Astroquery** [79]. Each of these databases were queried for objects within 6 arcseconds of the SPIRE central pointing for each observation when no better velocity estimate was obtained. From the queried radial velocities, the closest target to the SPIRE FTS pointing is chosen and reported in the FF with a 'S?' radial velocity flag. It is important to note that observations of SPIRE FTS targets by other instruments at different wavelengths may not necessarily probe the same objects. Reported radial velocities that are not determined from SPIRE FTS observations (e.g., radial velocities from SIMBAD, NED, or the HIFI list) are never considered confident and have a '?' character in their flag.

Another source of radial velocity estimates used in the FF comes from the work of Wilson et al. [81]. This work contains radial velocity measurements for 207 extragalactic targets measured in SPIRE FTS observations. The radial velocity measurements presented in this work are sometimes used for objects that are within 6 arcseconds of the SPIRE central pointing. When the radial velocity measurement recorded in the feature finder is from this source it is given the "W17" flag. A summary of all the velocity flags employed by the FF is provided in Table 2.4.

2.2.6 The Spectral and Photometric Imaging Receive Automated Feature Extraction Catalogue

Significant features measured by the SPIRE FTS extracted by the FF are combined into the the SPIRE Automated Feature Extraction Catalogue (SAFECAT)[5]. The catalogue contains a row entry for every feature extracted by the FF with absolute SNR greater than 5 and includes all sparse (point and extended-source calibrations) and mapping observations in its current release. The columns of SAFECAT provide information about the observation itself and the results from the FF. Observational information contains columns with the observation identifier (Obs. ID), operation date, observing mode (single-pointing, raster), appropriate calibration (point or extended-source), spatial sampling mode (sparse, inter-

---

[5] `https://www.cosmos.esa.int/web/herschel/spire-spectral-feature-catalogue`

mediate, or full), whether an HPDP has been used, the detector the spectral feature was detected in, the row and column of corresponding spaxel (-1 for sparse observations), and the sky coordinates of the spaxel (mapping) or nominal pointing (sparse). Results from the FF are presented in columns that contain the fitted feature frequency and associated error, SNR of the fitted peaks to local noise in the full residual (of the total model), the FF flag, the velocity estimate and associated error, the velocity flag indicating which method was used, and a neutral carbon flag indicating features that were detected or modified by the neutral carbon check routine.

In total SAFECAT contains 167 735 spectral features from 1 159 SPIRE FTS observations [7]. A more detailed breakdown of these features is shown in Table 2.5 showing the number of observations divided amongst pointing modes and spatial sampling (first row). The final two rows demonstrate the number of lines broken into the same categories.

Table 2.5: The number of features detected by the Feature Finder broken down into various categories.

	Mapping	Sparse	
		Point	Extended/Semi-Extended
Observations	178	818	388
SLW lines	67 397	6 262	2 486
SSW lines	84 344	5 566	1 1470

2.3 Conclusions

In this Chapter, the *Herschel*–SPIRE instrument has been introduced and we have described the optical design of its FTS. Over its mission, the SPIRE FTS underwent 996 unique publicly available spectral observations that contain a wealth of spectral lines. The FF provides a useful data-mining aid for astronomers to search through SPIRE FTS observations in bulk and it provides a powerful starting point for further analysis.

The technical details concerning SPIRE and the FF necessary to provide context for the remaining chapters of this thesis have also been presented in this chapter. As we continue our discussion it is my hope that the reader will learn more about the unique ways in which the SPIRE FTS is able to accomplish the scientific goals of FIR astronomy described in Chapter 1 and how the FF is an important archival tool for astronomers looking to SPIRE FTS data to further our understanding in the field.

The FF provides astronomers with the frequency, SNR of prominent spectral features ($|\mathrm{SNR}| \geq 5$), and internal flagging conventions (Table 2.4). The FF also provides radial velocity estimates for SPIRE FTS observations. Radial velocity is measured using either a routine that makes use of the characteristic spacing between all 10 in-band ^{12}CO rotational transitions or the cross correlation between FF extracted lines and a template of spectral features that are commonly found in SPIRE observations. Both routines are introduced in this chapter.

Throughout my studies, I have had the opportunity to assist in the development of the FF that will be discussed throughout this thesis. I have contributed to the development of FF postcards for mapping observations, the validation of the ^{12}CO radial velocity estimating routine, and studied outlying problem cases for the velocity estimate routines. These mapping postcards provide a summary of the information extracted by the FF including a velocity map of the source measured by the ^{12}CO rotational ladder in observations where it is evident. My largest contributions to the project are the subjects of the following chapters in this thesis.

Chapter 3

Line Identification with the SPIRE Spectral Feature Finder

> In every branch of knowledge the progress is proportional to the amount of facts on which to build, and therefore to the facility of obtaining data.
>
> –James Clerk Maxwell (1851)

In Chapter 2, I reviewed the bulk of the *Herschel* SPIRE FTS Spectral Feature Finder (FF) routine and my contributions to the project. In this chapter, I will describe the methods I used to identify the atomic/molecular species and energy state transitions that correspond to the spectral features extracted by the FF routine. Through this work, the SPIRE Automated Feature Extraction Catalogue (SAFECAT) will not only provide the frequencies and Signal to Noise Ratios (SNRs) of significant spectral features but also provide initial information concerning the atomic/molecular composition. The line identification is the final step in the FF's goal of providing an accessible data mining aid for the Herschel Science Archive (HSA) by including a list of the atomic and molecular features that occur in an observation. Line identification comprises the final stage of generating products to be included in SAFECAT and is represented by the final grey box in the FF flowchart (See Figure 2.7). This chapter discusses the formulation of a template of spectral lines that commonly occur in Far-Infrared (FIR) observations, the matching of that template to the output of the main FF execution, and how the line identification is used to search for low SNR lines that the FF may have missed and have thus not been included in the catalogue. The effectiveness and utility of this routine is also discussed.

3.1 Template

The SPIRE instrument team has developed a template of 307 molecular and atomic fine structure lines based on 15 atomic/molecular species that are commonly found in SPIRE FTS observations. This template is used to identify the atomic/molecular species of each spectral feature extracted by the FF. The template is predominantly composed of spectral features from the Centre d'Analyse Scientifique de Spectres Instrumentaux et Synthétiques (CASSIS) software [91] (`http://cassis.irap.omp.eu/?page=presentation`), a collaborative work from the Heterodyne Instrument for the Far Infrared (HIFI) and SPIRE teams. Also included in the template are a number of spectral features from the FF team that are often found in SPIRE FTS spectra. The template makes use of the publicly available information contained in the following spectral databases: the National Institute of Standards and Technology (NIST)/Lovas Atomic/molecular Spectra Database [92, 93], the Cologne Database for Molecular Spectroscopy (CDMS) [94], and the NASA Jet Propulsion Laboratory (JPL) sub-millimetre, millimetre and microwave spectral line catalogue [95]. Quick access to these catalogues was aided by the National Radio Astronomy Observatory (NRAO) developed online tool, Splatalogue [96]. The atoms and molecules contained in the catalogue are summarized in Table 3.1 and a full list of the spectral information in the template can be found in Appendix A. The types of spectral features described in the table describe the transition between energy states that give rise to the feature. Vibro-rotational refers to molecules that have rotational features included in the template from multiple vibrational bands. In this thesis, fine structure lines refer to spectral features that result from the splitting of an energy state due to electron and/or nuclear spin orientations [97].

A visual representation of the template is shown in Figure 3.1. All lines occur at FIR wavelengths and the false colour scale is chosen so that the most red line is the lowest

Table 3.1: Summary of the template used in line identification. The full list including rest frequencies can be found in Appendix A.

Molecule/Atom	Type	Lines	Molecule/Atom	Type	Lines
C I	Fine Structure	2	$^{13}C^{17}O$	Rotational	4
C II	Fine Structure	1	$^{13}C^{18}O$	Rotational	2
N II	Fine Structure	1	N_2H^+	Rotational	7
CH^+	Rotational	2	HCO^+	Rotational	9
p-H_2O	Rotational	9	$H^{13}CO^+$	Rotational	5
o-H_2O	Rotational	10	$HC^{18}O^+$	Rotational	1
HDO	Rotational	1	p-H_2CO	Rotational	35
$H_2{}^{18}O$	Rotational	2	o-H_2CO	Rotational	40
HCN	Vibro-Rotational	23	p-H_2S	Rotational	7
$H^{13}CN$	Vibro-Rotational	14	o-H_2S	Rotational	13
HNC	Rotational	8	CS	Vibro-Rotational	19
CO	Rotational	13	^{13}CS	Vibro-Rotational	12
^{13}CO	Rotational	14	SiO	Vibro-Rotational	19
$C^{17}O$	Rotational	9	SO	Rotational	15
$C^{18}O$	Rotational	10			

frequency and the most violet is the highest frequency.

The line identification routine is applied to all High Resolution (HR) SPIRE FTS observations that have lines identified by the FF and have a reported radial velocity estimate. The template is matched to the features extracted by the FF routine by first shifting the frequencies of the FF features to the rest frame (Equation 2.2), then all template lines that are within 0.3 GHz (1/4 the resolution of an HR observation) of a FF feature are matched to that feature. When multiple template features are matched to a single FF extracted line each is differentiated by a letter flag ranging from a–z and the most likely candidate of the features is marked with an asterisk.

In order to determine the most likely candidate, a check against all other identified features is performed. Consider two states of an atom or molecule, m and n; this pair of states could be electronic, rotational, or vibrational and the transition between them results

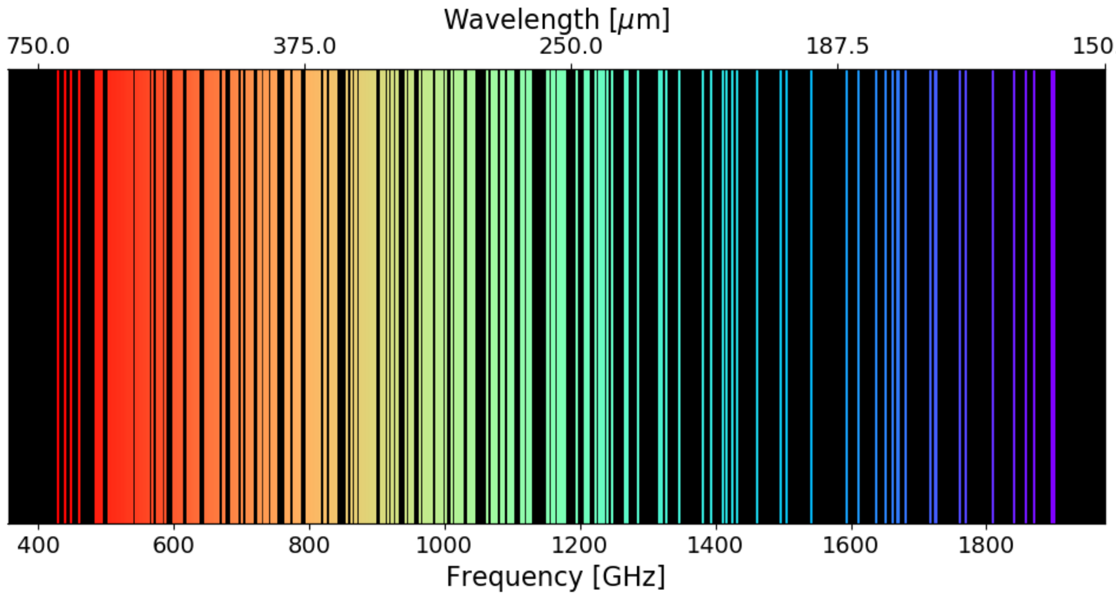

Figure 3.1: The template line list used for line identification. The template contains a combination of 307 molecular and atomic fine structure spectral features at their rest frame frequencies.

in an observed spectral line. The intensity of a spectral line depends on the population of the lower state of a transition [97]. Under Local Thermodynamic Equilibrium (LTE) conditions the population of these states, N_n and N_m are governed by a Boltzmann distribution [14, 97],

$$\frac{N_n}{N_m} = \frac{g_n}{g_m} e^{-\Delta E/kT}, \tag{3.1}$$

where T is the excitation temperature that governs the population of states, and g_n and g_m are the degeneracy of the n and m states, respectively. In Equation 3.1, ΔE is the energy from the transition of states, $\Delta E = h\nu$, where h is Planck's constant and ν is the rest frequency of the associated radiation. This relationship is shown for the first 70 rotational states of CO at 5 and 30 K in Figure 3.2. The relationship between energy states shows us that, under LTE conditions, closely spaced spectral lines pertaining to a single atom or molecule have similar intensities. Many emission lines from interstellar molecules arise from systems that are not under LTE [14], but it is useful to assume that when spectral features from a particular atom/molecule are found in a spectrum, other features pertaining to that same atom/molecule that are within the spectrometer band, and LTE regime, are likely to be present as well. In order to flag the most likely candidate when multiple template lines are matched to a single FF line, the full FF output is checked for other possible instances of lines that correspond to the same atom/molecule as that species. The atomic/molecular candidate with the most other lines present in the spectrum is chosen as the most likely candidate and is marked with an asterisk. If multiple candidates have the same number of occurrences, both are marked with an asterisk.

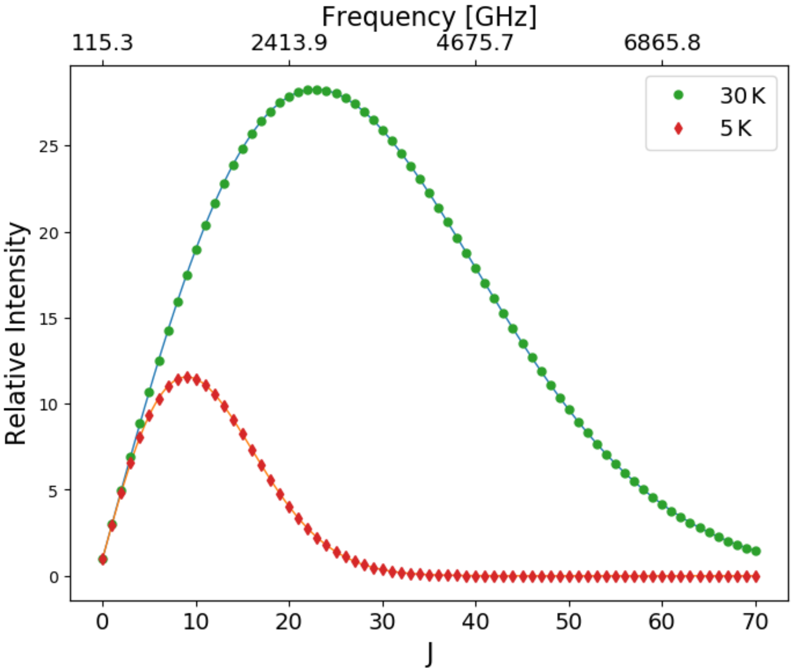

Figure 3.2: The intensity, relative to the ground state, of rotational transitions of CO at 5 and 30 K, assuming LTE (see Equation 3.1). The frequency of spectral features transitioning to the lower state are shown by the top horizontal axis.

The line identification routine outputs the following column entries for each spectral feature found by the FF in addition to those already contained in SAFECAT (See Chapter 2):

- the frequency of the spectral line found by the FF shifted to rest frame based on the radial velocity estimate,

- the rest frame frequency of the template line matched to the feature from the FF,
- the molecular or atomic species of the matched template line,
- the quantum numbers associated with the template line, and
- a comment flag; when multiple template features are associated with a single FF each is assigned a letter from a–z.

3.1.1 Template notation

In this thesis, there are a variety of different quantum numbers used to distinguish spectral features. The conventions used are similar to CDMS and NIST with a few modifications. Atomic and molecular names follow standard convention where isotope numbers are denoted by preceding superscripts and the number of a particular atom contained in a molecule is marked by a subscript. For fine structure lines, the ionization level of the atom is marked with Roman numerals, with I denoting a neutral atom, e.g., N II represents the first ionization level of Nitrogen for a fine structure line [14]. The following conventions for quantum numbers are used:

- for molecules in which the vibrational band is not explicitly stated (denoted by the vibrational quantum number, v [97]) it is zero (e.g., p-H_2O);
- vibrational bands can be denoted with a range (e.g., v=0-4) signifying that a rotational transition occurs at a single vibrational band within that range (e.g., SiO, v=0-10 12 1 – 11 1 at 517.2597 GHz is from the first vibrational band: SiO, v=1 12 1 – 11 1);
- quantum numbers of the format, $J'(K'_a,K'_c)$–$J(K_a,K_c)$, as in water molecules, are arranged such that J is the total angular momentum quantum number while K_a and K_c are the limiting prolate and limiting oblate case quantum numbers for the projection of total angular momentum along the axis of symmetry (e.g., p-H_2O, 6(2,4)–7(1,7));

- quantum numbers containing a transition of a single number to another single number (e.g., J'–J), are rotational transitions with the number, J, representing the total angular momentum quantum number [14] (e.g., CO, v=0 4–3);
- quantum numbers of the format, $\mathrm{J}'\ \mathrm{F}'$ – J F, indicate J as the total angular momentum quantum number and F as the total angular momentum quantum number *including* nuclear spin [97] (e.g., SiO, v=0-10 12 1 – 11 1).

The fine structure transitions included in the template arise from spin-orbit coupling [97] and are described by the quantum numbers S, L, and J. The variable S describes the coupling of the spin angular momenta, s_i, for all electrons in the atom,

$$\mathrm{S} = \sum_{i}^{N} s_i, \tag{3.2}$$

and L describes coupling of the orbital angular momenta, l_i, of all electrons in the atom,

$$\mathrm{L} = \sum_{i}^{N} l_i, \tag{3.3}$$

where J=L+S is the total angular momentum of the state [97, 67]. Rather than represent L as a number, it is fairly common in spectroscopic notation to instead use a letter, where L$= 0,1,2,3,4,5,\ldots$ is noted L$=$ S, P, D, F, G, H,... [97]. Fine structure transitions in this thesis follow the notation, $^{(2\mathrm{S}'+1)}\mathrm{L}'_{\mathrm{J}'}$–$^{(2\mathrm{S}+1)}\mathrm{L}_{\mathrm{J}}$. This notation is best seen in an example. The electronic configuration of carbon is $1s^2 2s^2 2p^2$ (where lower case letters follow the same convention for l as the upper case letters) only the electrons in the $2p$ shell need to be considered since s shells correspond to an orbital angular momentum of zero. Each of the two electrons in the p shell have orbital angular momenta $l_1 = l_2 = 1$. Accounting for their magnetic quantum number, L can take 3 possible values 2 (D), 1 (P), or 0 (S) [67]. The spin orientations of these two electrons are either parallel, S=1, or antiparallel S=0. The ^{3}P state is triplet with fine structure states denoted $^3P_0$, $^3P_1$, and $^3P_2$ corresponding to J=0, 1, 2. The $^3P_1$–$^3P_0$ and $^3P_2$–$^3P_1$ transitions occur in the SPIRE FTS band and are included in the template [22].

For convenience in figures, quantum numbers are separated from their atom by square braces e.g., H_2O [4(3,2)–3(3,2)]. Superscripts and subscripts for the quantum numbers are also foregone in figures (e.g., $^3P_2$ is instead written 3P2). Fine structure lines are commonly denoted with square braces around the atom, e.g., [N II]; in this thesis they are omitted since square braces are instead used to separate atom/molecular species from quantum numbers in figures.

3.1.2 Scientific importance of template lines

The primary science objectives of *Herschel*, and by extension the SPIRE FTS, are tied to measurements of the physical processes that occur in the Interstellar Medium (ISM) [46]. The spectral features that are included in the template are chosen based on their overall prominence in SPIRE FTS spectra and their utility as a probe of ISM processes. These molecular and atomic fine structure lines provide effective tools for measuring thermodynamic processes, the kinetic motion of shocks, and ionization processes in the ISM.

CO is the most abundant molecule in the Universe following H_2 [98] and is the most important coolant in dense molecular clouds [14]. Due to its dipole moment, CO has several rotational transitions that radiate at FIR wavelengths. CO is easily excited into rotational energy states as it collides with H_2 in the cool ISM and it relaxes to ground state quickly [14]. The lowest transition in the ^{12}CO ladder ($J = 1$–0) is separated by an energy equivalent to 5.5 K meaning the molecule is an effective coolant down to this temperature [14]. From my discussion of Equation 1.8 I showed that star formation out of necessity occurs in cold dense regions of the ISM, thus CO provides an important tool for probing star-forming regions [22, 98]. The abundance of CO in an observation is also used frequently as a measure of the total molecular gas present [98]. The SPIRE FTS was designed to cover rotational transitions of ^{12}CO from $J = 4$–3 to $J = 13$–12.

Measurements of CO rotational transitions can be useful for probing the molecule's column density in a source and its LTE temperature (see Equation 3.1) through rotation (or population) diagrams [22, 99]. The ^{12}CO molecule also has two other common stable isotopologues, ^{13}C^{16}O and ^{12}C^{18}O. These other isotopologues are readily found in the ISM but are much less abundant and are often found to be optically thin, meaning the observer receives the emission through the surrounding medium [14]. Measurements of these optically thin isotopologues can be used to estimate the total CO assuming typical [CO/^{13}CO] and [CO/C^{18}O] ratios in an observation where CO emission is self-absorbed [22]. It should be noted that these isotopic ratios are observed to vary throughout the ISM and can be indicative of star formation rates [100]. Goto et al. [101] describe the CO isotope ratios in nearby molecular clouds that deviate from the local ISM ratios by as much as a factor of 2.8. Since the CO isotopologues often occur at different optical depths (when both isotopologues are not optically thin) they can be used together to probe the physical processes at different depths into a molecular cloud.

Water (H_2O) is an important molecule for life on Earth and is an asymmetric rotor. A multiplicity of lines from gas-phase water vapour occur in the SPIRE FTS band and are commonly observed. Like CO, these rotational transitions provide an important coolant in the ISM [22]. SPIRE measurements of water vapour are particularly useful for studying ultraluminous infrared galaxies [102] and can be used as a tracer of star formation in the ISM [103].

Fine structure lines from C I and N II are important coolants for the gas phase of the ISM [22]. They are of particular import as they probe entirely different energy regimes than the molecules that have been discussed. The CO molecule has a binding energy of $\sim 11.10\,\mathrm{eV}$ [104] while the first ionization of carbon occurs at $11.26\,\mathrm{eV}$ [105]. From these two energies we see that, in the presence of a source of ionizing radiation, there exists a thin shell of neutral carbon just between the cool molecular CO region and the warm ionized region immediately adjacent to the source. The C I transitions that are commonly found in SPIRE spectra provide an important probe of this thin region (corresponding to a difference of $0.16\,\mathrm{eV}$) around ionization sources such as stars [67]. The ionization energy of Nitrogen is $14.53\,\mathrm{eV}$ [105] providing an even deeper probe that is able to access the warm ionization region of a source. The utility of lines from molecules, atoms, and ionized atoms are not limited to nearby ionization regions. Recently, Lapham et al. [106], have shown the utility of C I, N II, and CO features measured by the SPIRE FTS to probe the properties of distant galaxies.

The other molecules included in the template are CH^+, HCN, HNC, N_2H^+, HCO^+, H_2CO, H_2S, CS, SiO, and SO. Features from these molecules are commonly found in SPIRE FTS observations and provide similar utility to those mentioned above but often to a lesser extent. These features also tend to appear much more faintly in SPIRE FTS observations but have been detected on several occasions which we will see further on in the chapter.

3.2 Low Signal to Noise Ratio Lines

In Chapter 2, we have seen that the FF does not report features with an absolute SNR less than 5. Let us imagine a situation where a molecular or atomic species containing multiple lines in the SPIRE FTS band has some features detected at an SNR near this limit.

Equation 3.1 and Figure 3.2 tell us that other features pertaining to this molecule are likely to be present in the SPIRE FTS observation with similar SNR, and in some cases may actually fall below this cutoff and not be included in the SAFECAT. An example of this is shown in Figure 3.3. Strong ^{12}CO emission is evident in the observation of this post-Asymptotic Giant Branch (AGB) star [1] but the $J = 5$–4 transition is not picked up by the FF since it occurs at an SNR of 4.35.

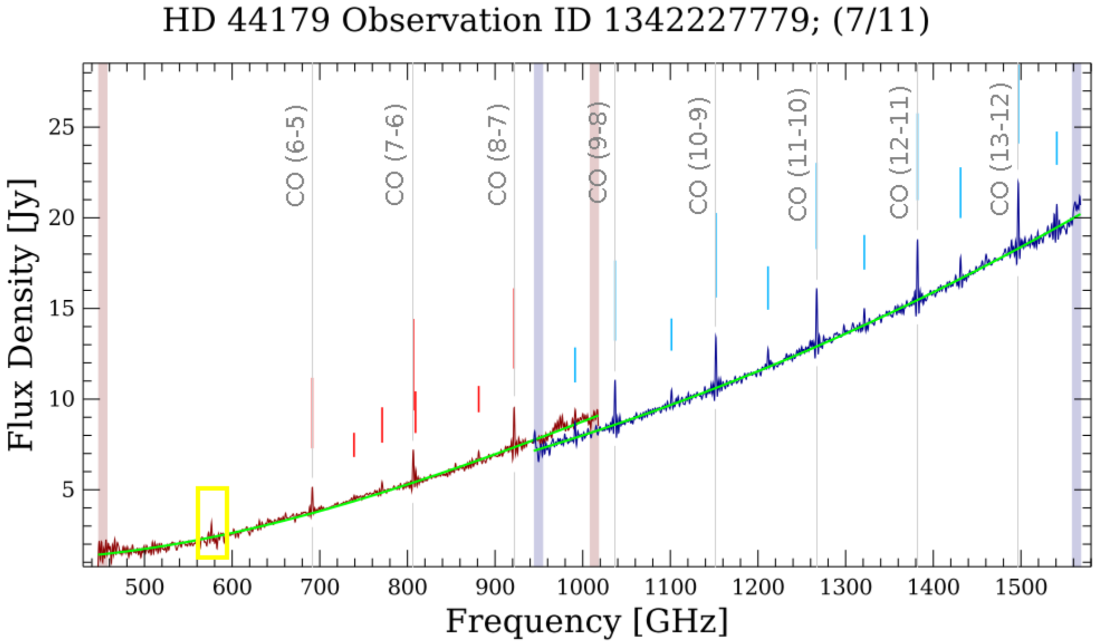

Figure 3.3: The postcard from a sparse observation of the post-AGB star HD 44179. Prominent ^{12}CO rotational transitions are marked with vertical lines and the $J = 5$–4 transition that is not extracted by the FF is highlighted by the yellow box.

The line identification obtained by matching with the template provides a useful tool for extracting these low SNR lines that are missed by the FF. The low SNR search routine addresses these missing low SNR features by iterating through the atoms/molecules identified in an observation looking for transitions that are expected to be found in the spectrum but are not contained in the FF results. These missing transitions are then re-input into the FF as an initial guess in order to obtain the missing lines for SAFECAT. This low SNR searching process is shown in Figure 3.4, in which spectral features are represented by the small squares. The following list is a step-by-step description of the routine:

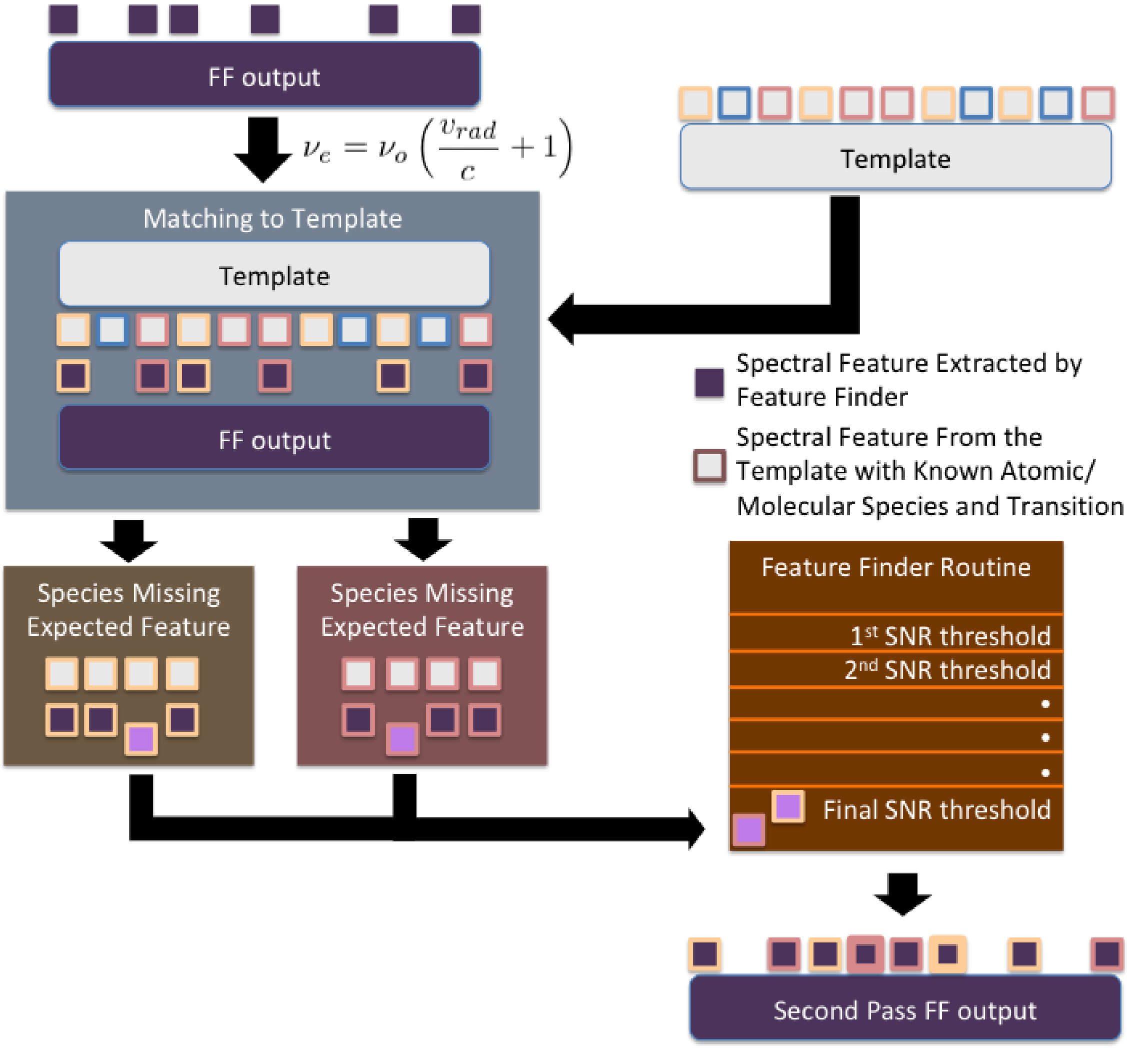

Figure 3.4: Flow chart describing how line identification with the template is used to find low SNR lines that may have been missed in the first pass of the FF. A full step-wise description of the algorithm is presented in this section.

1. Features output by the FF (shown as purple squares in the flow chart) are shifted into the rest frame.

2. FF features are compared to the template (shown in grey) in which the atom/molecule and transition for each feature is known (shown by the colour outlining the boxes that

represent spectral features). This allows for the atoms/molecules and transitions of the FF features to be identified.

3. The low SNR search routine iterates through the identified molecules in the FF features and looks to the template to determine if any transitions are missing (shown by the lighter coloured squares). These expected but missing features are added to a list.
4. The FF routine is repeated on the SPIRE FTS observation from the HSA. During the final iteration of SNR thresholds, which is changed to include features $5 > |\mathrm{SNR}| \geq 2$, frequencies shifted to the velocity frame from the list of missing features are injected as initial guesses for the central line frequency of features to be fit by sinc functions. These features are assumed to be of low SNR.
5. The new list of features output by the FF is subjected to the nominal checks for removing features in the FF [7] with the exception of the flags around prominent features (for missing but expected features that may lie close to a another high SNR line).
6. Remaining features that are contained in the list of missing but expected features are recorded and flagged (shown with the thicker outline).
7. Features found by the low SNR search routine are appended to the output from the line identification routine with a '!' character in the comment section.

As a result of this routine, spectral features down to a SNR of two that are expected to be present but are not included in the FF are aggregated to the catalogue. The SNR threshold of two was empirically chosen as a cutoff to prevent the inclusion of spurious detections.

This low SNR search routine has also been found to pick out higher SNR lines above the absolute SNR cutoff of five. This can occur for features that are within the side lobes of strong features and are nominally considered spurious features and removed from the catalogue. Hopwood et al. [85], studied multiple observations of calibration sources for the Herschel SPIRE FTS (see the following section) and mark a detected feature in the planetary nebula NGC 7027 at 802 GHz. This feature is not found by the FF in any FTS observations of the source since it occurs within the mask width of the bright CO(7-6) feature (rest frequency 806.65 GHz). The low SNR search routine picks out this feature at 802.46 GHz while looking for missing HCO^+ features in multiple observations of NGC 7027. This feature is found at SNRs as high as 22 (observation ID 1342245075).

3.3 Calibration Sources

Over the *Hershcel* mission, the SPIRE FTS observed several secondary calibrators in order to monitor the spectral-line calibration and line shape, the continuum calibration and shape, the frequency calibration, and to validate the spectral resolution. These sources were also used to determine the instrument pointing stability with repeated observations over the instrument's lifetime [85]. These calibration sources range in object type and structure in order to include point-like sources, sources with extended emission, planets, and asteroids. Of these calibration sources, those that are rich in spectral features provide excellent test cases for the line identification and low SNR search routines since they provide several observations of targets with a known spectral signature. Hopwood et al. [85] discusses these sources in detail and the process by which Highly Processed Data Products (HPDPs) were obtained for them. Hopwood et al. also provide measurements of the spectral lines for many of these sources that are compared to the results from the line identification and low SNR search routines discussed in this chapter.

The calibration sources and observations selected to test these routines are summarized in Table 3.2. All of the analyzed observations are point-source calibrated or semi-extended sparse observations that have HPDPs available. Figure 3.6 shows the results of these rou-

Table 3.2: Summary of the line-rich calibration observations used to validate the line identification and low SNR search routines.

Source	RA	Dec.	Type	HR Obs.
NGC 7027	21:07:01.59	+42:14:10.2	Planetary nebula	31
AFGL 4106	10:23:19.47	-59:32:04.9	Post-red supergiant	29
CRL 618[a]	04:45:53.64	+36:06:53.4	Protoplanetary nebula	22
CW Leo[b]	09:47:57.41	+13:16:43.6	Variable star	7
VY CMa	07:22:58.33	-25:46:03.5	Red supergiant	8
AFGL 2688[c]	21:02:18.78	+36:41:41.2	Protoplanetrary nebula	17

[a] Also known as AFGL 618

[b] Also known as irc+10216

[c] Also known as CRL 2688

tines for the planetary nebula NGC 7027 for all 31 observations. Lines that are not identified by matching to the template are marked in light red while those found by the second pass of the FF during the low SNR search routine are outlined in red. Each point on the plot represents a spectral feature and they are coloured based on the integration time of each observation (repetitions refers to full scans of the FTS, see Chapter 2). The absolute SNR cutoff of five is shown by the dashed black line, most features found by the second pass of the FF are below this threshold as expected. The summary of the results from applying these routines to the six calibration sources is presented in Table 3.3. Photometer maps from the SPIRE Photometer Short Wavelength (PSW) array with the footprints of FTS observations over-plotted are shown for each source. The sources CRL 618 and AFGL 2688 both have CRL (Cambridge Research Laboratory Sky-Survey) and AFGL (Air Force Geophysical Laboratory) naming conventions; the choice for when one name is used over the other in this thesis is dependent on the observational target's name as submitted by the original investigators of an observation and the convention used in publications from the SPIRE instrument team (See Hopwood et al. [85]).

Table 3.3: Results of the line identification and low SNR search routines for all observations of the selected calibration sources. Sections 3.3.1–3.3.6 describe each of these sources.

Source	Lines found by the FF	Lines Matched	Lines Added
NGC 7027	832	616	89
AFGL 4106	375	338	62
CRL 618	1205	832	149
CW Leo	705	374	56
VY CMa	620	291	60
AFGL 2688	978	602	43

3.3.1 NGC 7027

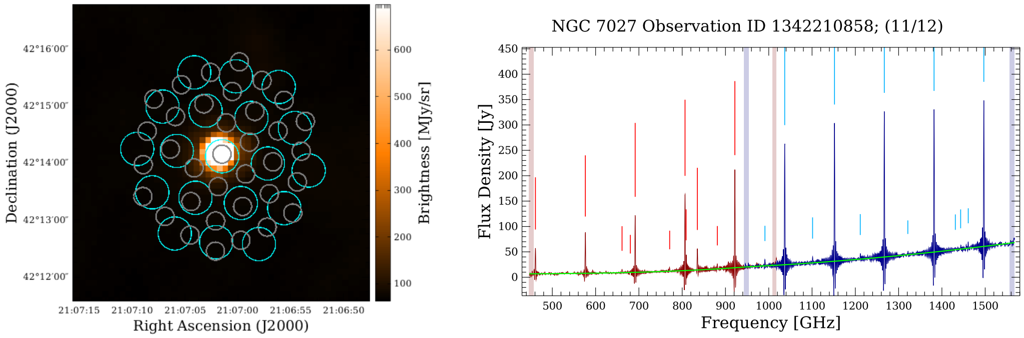

Figure 3.5: Photometer map of the calibration source NGC 7027 (left) from the SPIRE Photometer Short Wavelength (PSW) array (250 μm) with the footprints of the spectrometer SLW (cyan) and SSW (grey) arrays. The Feature Finder postcard from the central detectors of an observation of the source is also shown (right).

NGC 7027 is a young FIR luminous planetary nebula [107] consisting of a central H II ionization region with molecular bipolar outflow [108] and a surrounding CO envelope [109]. Line identification with the template is able to successfully identify 74% of the lines extracted by the FF and obtain an additional 31 features from the low SNR search for this source. Figure 3.6 summarizes the results of both the identification and low SNR search routines for this source. Note the strong CO emission for the source (marked by vertical grey lines) and that the low SNR search routine is particularly effective at finding ^{13}CO features missed by the first pass of the FF.

The presence of ^{13}CO emission from rotational transitions ranging between $J = 5$–4

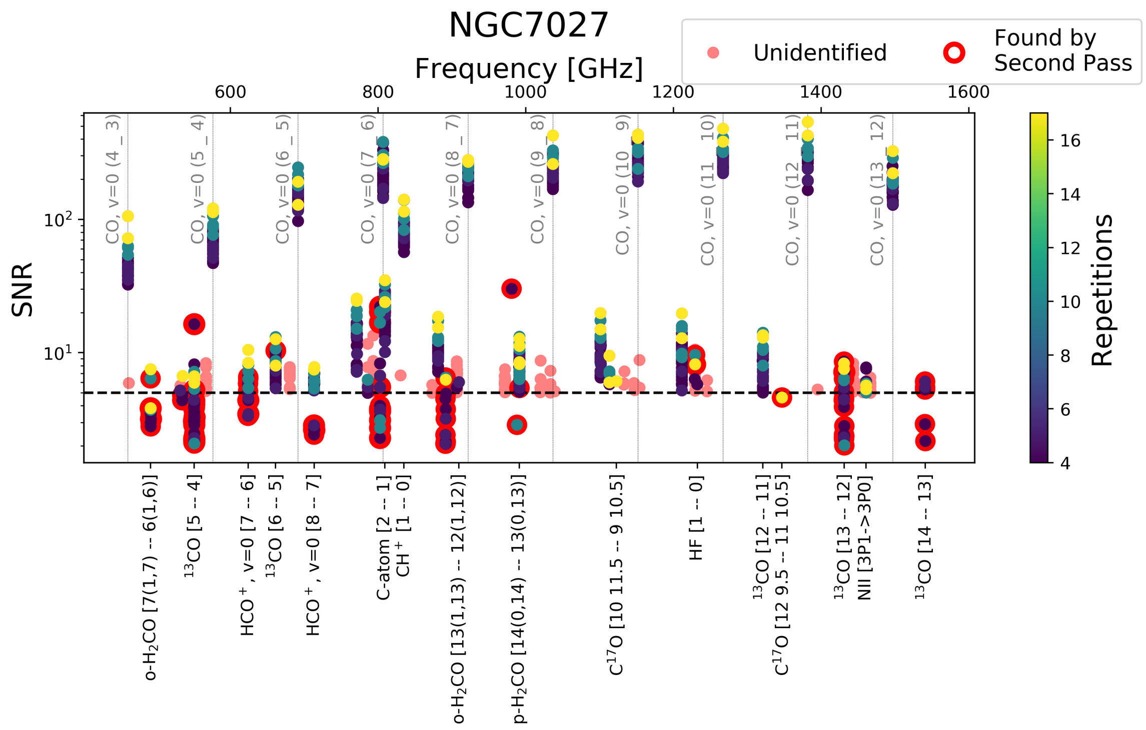

Figure 3.6: The line identification results for the calibration source NGC 7027 (see Table 3.2).

and $J = 13$–12, with the exception of the $J = 10$–9 transition, is confirmed in Hopwood et al. [85]. The presence of all 10 in-band ^{12}CO rotational features is also confirmed in this source. The presence of the HCO$^+$ $J = 6$–5, $J = 7$–6, $J = 8$–7, $J = 10$–9, and $J = 13$–12 rotational features that are often missed by the FF, but are found by the low SNR search, are also confirmed. FF lines that have been matched with the template that are not reported by Hopwood et al. are a combination of CH$^+$, p-H$_2$O, HF, and HNC features. The N II fine structure line is also detected in this source.

3.3.2 AFGL 4106

AFGL 4106 is notably fainter than other SPIRE FTS calibrators but was included to ensure that at least one calibration source was available on every observing day of the mission [85]. It is an evolved massive star (post-red supergiant) that is encased in a dust shell

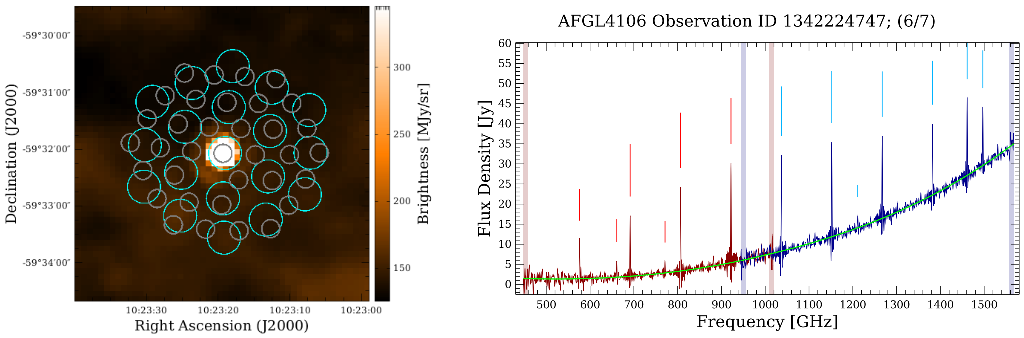

Figure 3.7: Photometer map (left) and postcard (right) for the calibration source AFGL 4106. Format similar to Figure 3.5.

and is known to be part of a binary system [110]. The star is surrounded by a bow-shaped emission complex related to its mass loss [111]. The template also fits this source well allowing for the identification of 90% of the spectral features extracted by the FF and the addition of another 28 lines from the low SNR search. Figure 3.8 summarizes the results of both the identification and low SNR search routines for this source.

Observations of AFGL 4106 are known to have significant emission from the surrounding galactic cirrus [85] which results in fairly prominent occurrences of the N II fine structure line. In Section 4.3.1 I provide a brief study of the emission surrounding the central source and how the ionized nitrogen feature can be used to decouple the two.

Hopwood et al. [85] confirm the presence of all 10 in-band ^{12}CO features and ^{13}CO rotational features from $J = 5$–4 to $J = 11$–10. The identification and low SNR routine have identified a p-H_2O feature and the N II fine structure line that are not reported by Hopwood et al. [85].

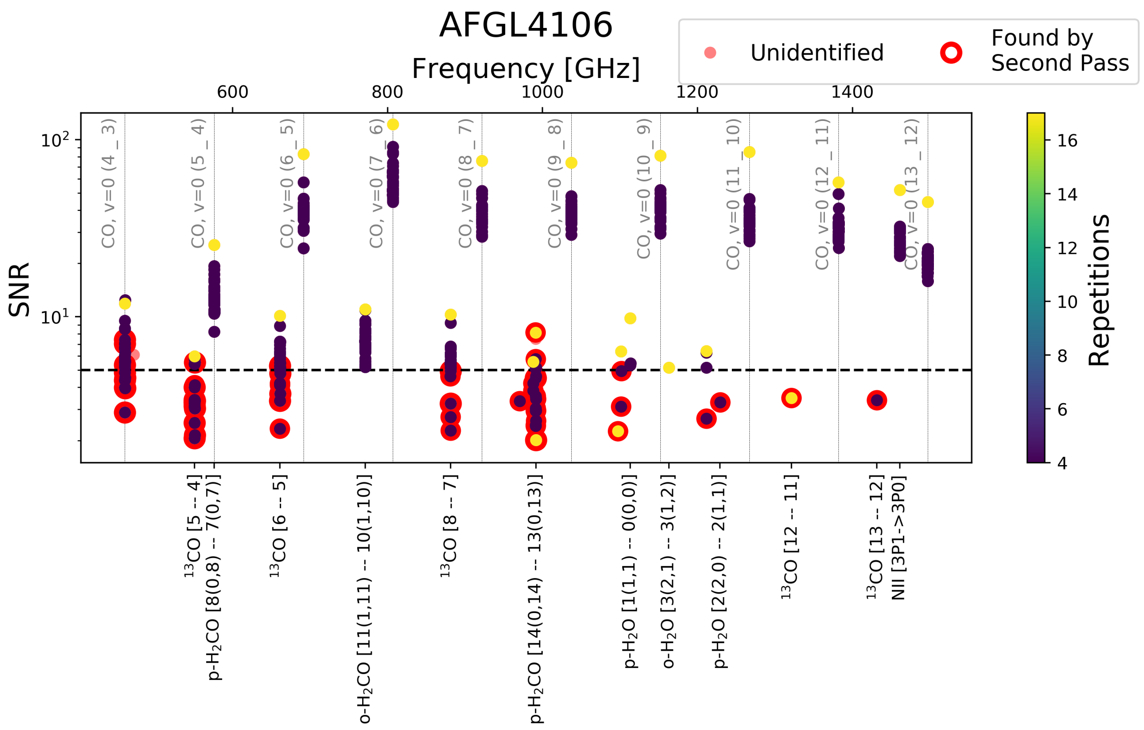

Figure 3.8: The line identification results for the calibration source AFGL 4106 (see Table 3.2).

3.3.3 CRL 618

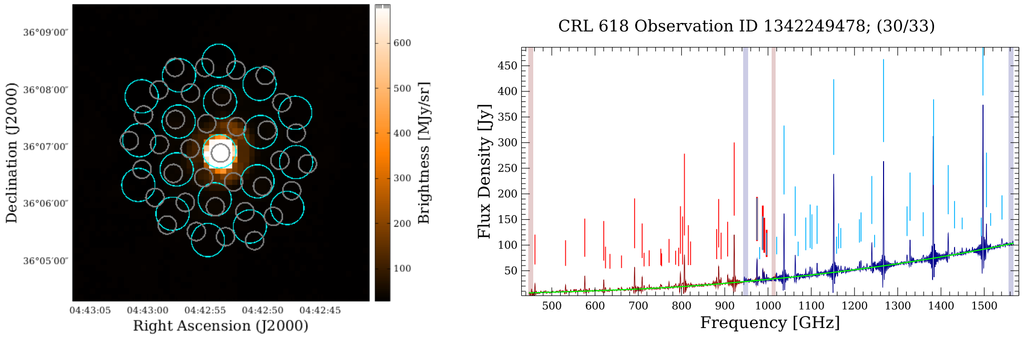

Figure 3.9: Photometer map (left) and postcard (right) for the calibration source CRL 618. Format similar to Figure 3.5.

CRL 618 (also known as AFGL 618) is a young protoplanetary nebula entering its post-AGB phase only $\sim$ 100 years ago and has a compact H II region surrounding the star [112]. The nebula also has bipolar outflow and a roughly circular outer halo [113]. As with the previous two sources, the template is fairly effective for identifying the features found by the FF. The line identification routine is able to match 69% of the features found by the FF to the template and an additional 21 lines are found by the low SNR search. These results are displayed in Figure 3.10.

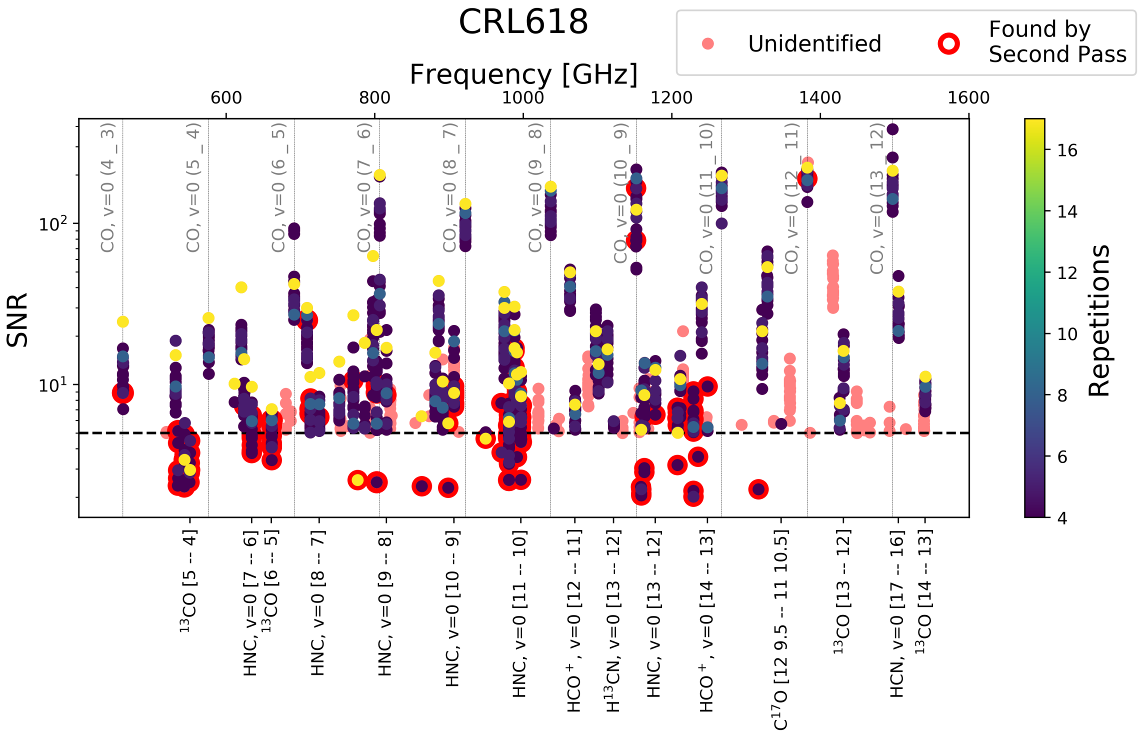

Figure 3.10: The line identification results for the calibration source CRL 618 (see Table 3.2).

CRL 618 contains a significantly more diverse set of molecules than the previous two sources we have discussed having HCN, HNC, and H_2O confirmed by Hopwood et al. [85]. The full list of transitions found by the line identification and low SNR search that agree with the findings of Hopwood et al. [85] are shown in Table 3.4. All of the features identified by Hopwood et al. have been identified by the routine in at least one observation of the SPIRE FTS. Line identification through template matching and the low SNR search found a combination of HCO^+, $H^{13}CN$, $C^{18}O$, and H_2CO features in addition to those reported by Hopwood et al.

Table 3.4: The lines reported by Hopwood et al. [85] for CRL 618. The rest frequency, ν_0, of each line is also shown.

	SLWC3			SSWD4	
Species	Transition	ν_0 [GHz]	Species	Transition	ν_0 [GHz]
^{12}CO	4–3	461.04	^{12}CO	9–8	1036.91
^{12}CO	5–4	576.27	^{12}CO	10–9	1151.99
^{12}CO	6–5	691.47	^{12}CO	11–10	1267.01
^{12}CO	7–6	806.65	^{12}CO	12–11	1381.10
^{12}CO	8–7	921.80	^{12}CO	13–12	1496.92
^{13}CO	5–4	550.93	^{13}CO	9–8	991.33
^{13}CO	6–5	661.07	^{13}CO	10–9	1101.35
^{13}CO	7–6	771.18	^{13}CO	11–10	1211.33
^{13}CO	8–7	881.00	^{13}CO	12–11	1321.27
^{13}CO	9–8	991.33	^{13}CO	13–12	1431.154
HCN	6–5	531.71	HCN	11–10	974.488
HCN	7–6	620.30	HCN	12–11	1062.97
HCN	8–7	708.88	HCN	14–13	1239.88
HCN	9–8	797.45	HCN	15–14	1328.29
HCN	11–10	974.49	HCN	16–15	1416.67
HNC	5–4	453.27	HCN	17–16	1505.04
HNC	6–5	543.90	HNC	11–10	996.77
HNC	7–6	634.51	HNC	12–11	1087.28
HNC	8–7	725.11	HNC	13–12	1177.75
HNC	9–8	815.68	HNC	15–14	1358.61
HNC	11–10	996.77	HNC	16–15	1448.98
H_2O	2(1,1)–2(0,2)	752.03	H_2O	2(0,2)–1(1,1)	987.92
H_2O	2(0,2)–1(1,1)	987.92	H_2O	3(1,2)–3(0,3)	1097.37
			H_2O	1(1,1)–0(0,0)	1113.34
			H_2O	3(2,1)–3(1,2)	1162.93
			H_2O	2(2,0)–2(1,1)	1228.80

It should be noted in Figure 3.10 there are instances of the low SNR search finding ^{12}CO $J = 10$–9 at a very high SNR. These features are indeed found by the first pass of the FF but are not successfully matched to the template. When shifted to rest frame, these features have fitted frequencies that are more than 0.3 GHz from the template line. These features are marked as missing but expected features by the low SNR search. These features are included in the list of missing features that are searched for in the second pass of the FF and fit in the final SNR iteration. The refitting of these features effectively widens the 0.3 GHz matching window by the central frequency fitting constraints in the main loop of the FF. This effective widening of the matching window can be seen for the ^{12}CO $J = 10$–9 transition in this source and for several other transitions in the calibration sources discussed in the following subsections.

3.3.4 CW Leo

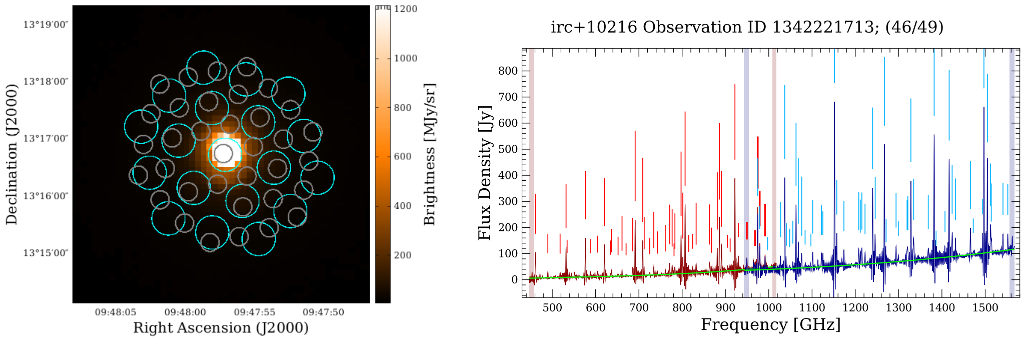

Figure 3.11: Photometer map (left) and postcard (right) for the calibration source CW Leo. Format similar to Figure 3.5.

CW Leo is a carbon-rich variable star in its AGB phase [114]. The star is undergoing significant mass loss and resides within a dense molecular circumstantial envelope [115] with a fairly complicated structure [116]. The line identification routine is able to successfully match 53% of the spectral features extracted by the FF and an additional seven lines are found by the second pass of the FF searching for low SNR features. The results from applying both routines is presented in Figure 3.12 in which a large number of unmatched lines are shown.

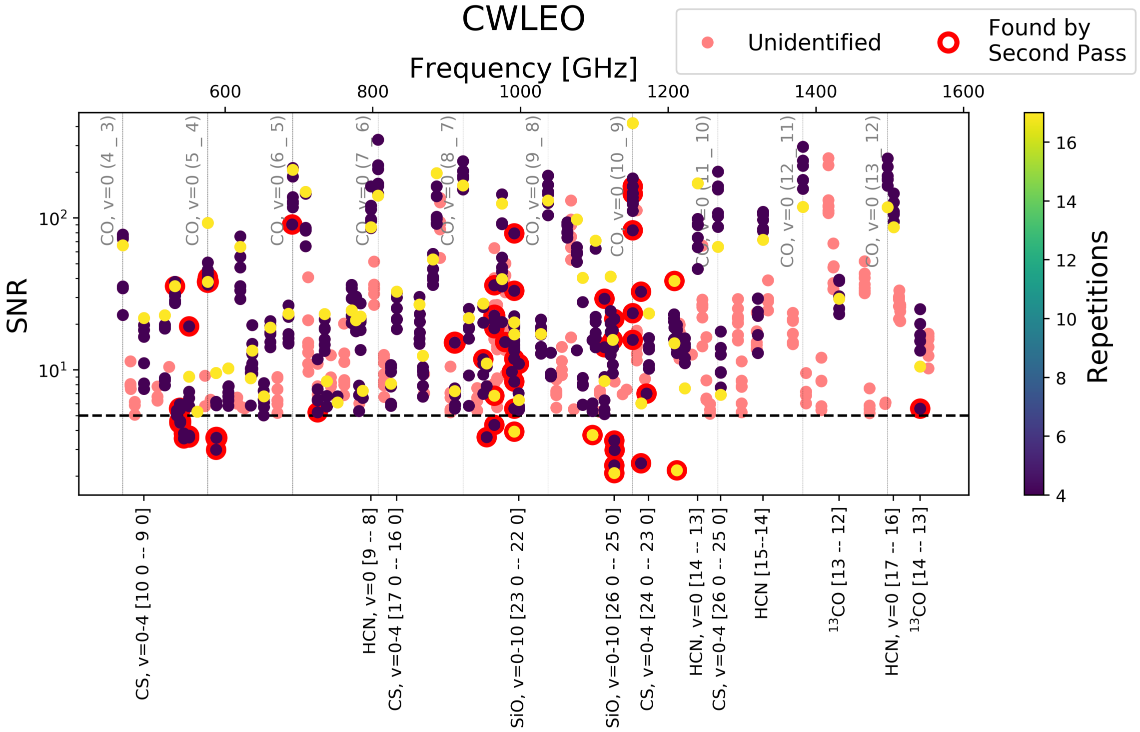

Figure 3.12: The line identification results for the calibration source CW Leo (see Table 3.2).

CW Leo is a known source of SiS and HCl [117, 118] lines that are not included in the template as they are less ubiquitous in SPIRE FTS observations. These features, along with a D_2O feature at 890.3 GHz, account for the majority of FF lines that are not identified by the template. Figure 3.13 shows the continuum subtracted spectrum of an observation of CW Leo (observation ID 1342253661) with all features that have been successfully matched with the template removed. Red lines and annotations mark SiS lines reported by Decin et al. [117] and are found to agree with their expected frequencies within 0.3 GHz. Those marked by an asterisk are reported in Decin et al. [117] to be blended with other low SNR features and can be detected by the FF further from their expected frequency. These blended features match with their expected frequencies within 2.52 GHz. The HCl feature discovered by Cernicharo et al. [118] is marked in Cyan. Remaining spectral features that are found by the FF but do not correspond to any of the above atomic/molecular species are marked with dashed magenta lines and are possibly some combination of emission from SO^+, NH_3, and SiC molecules.

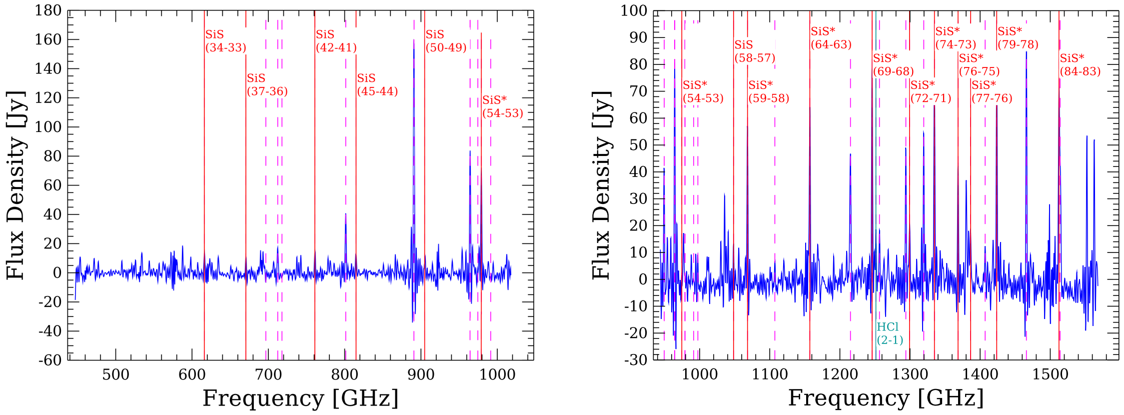

Figure 3.13: A SPIRE FTS observation (SLW left, SSW right) of CW Leo (observation ID 1342253661) with spectral features identified with the template removed. SiS features reported by Decin et al. are marked and labelled in red with an HCl feature marked in cyan. The HCl feature was reported by Cernicharo et al. [118]. Features detected by the FF that are not identified are noted by the dashed magenta lines.

3.3.5 VY CMa

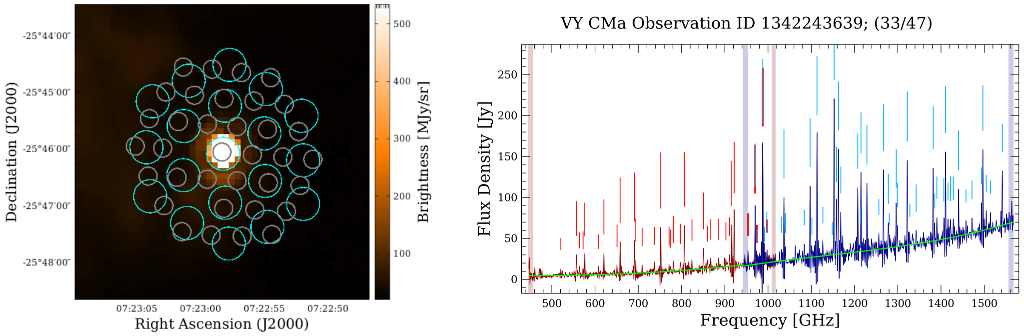

Figure 3.14: Photometer map (left) and postcard (right) for the calibration source VY CMa. Format similar to Figure 3.5.

VY CMa is a highly luminous ($\sim 10^5$ times more luminous than the sun) red supergiant star [119] surrounded by a circumstellar envelope that creates a reflection nebula at optical wavelengths [120]. Similar to CW Leo it is experiencing mass-loss [121] and is a known source of SiS features [120] in the SPIRE FTS band. The line identification routine is able to successfully match 47% of the features found by the FF to the template and add another eight lines to the catalogue through the low SNR search. These results are shown in Figure 3.15.

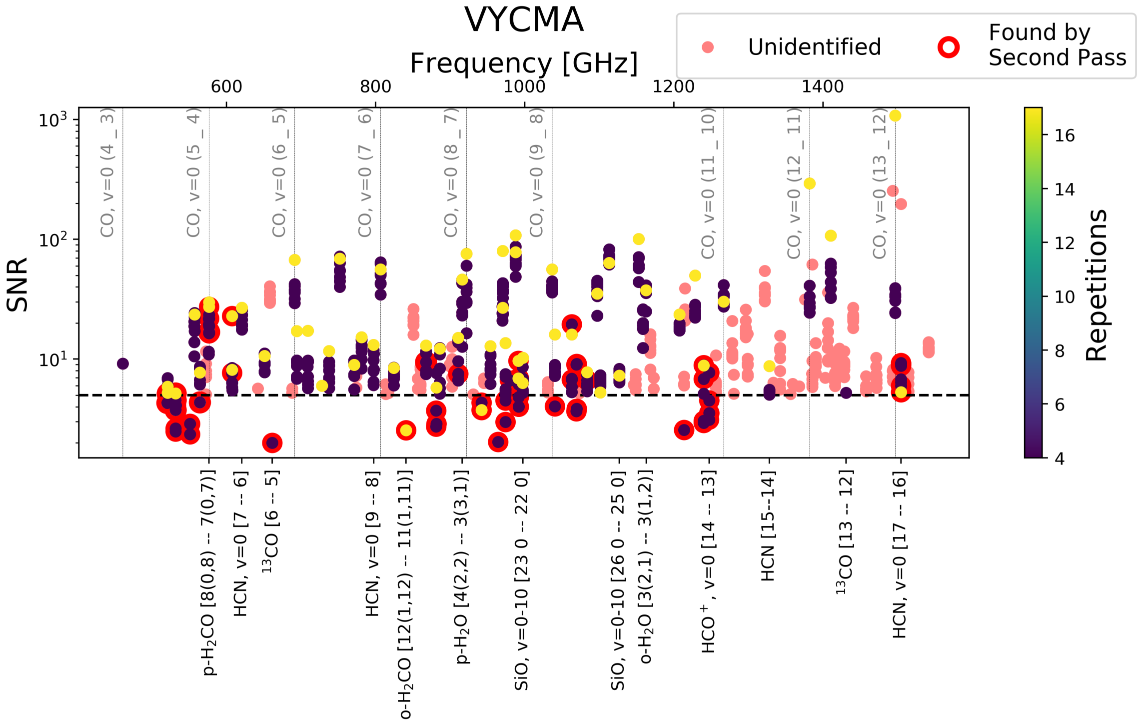

Figure 3.15: The line identification results for the calibration source VY CMa (see Table 3.2).

From Figure 3.15, we see that a large portion of the lines that remain unidentified by the template occur in the SSW band between 1100 and 1500 GHz. Many possible molecular species and transitions for these features are reported by Matsuura et al. [120] which are predominantly comprised of SiS and water lines from higher vibrational bands than those included in the template.

3.3.6 AFGL 2688

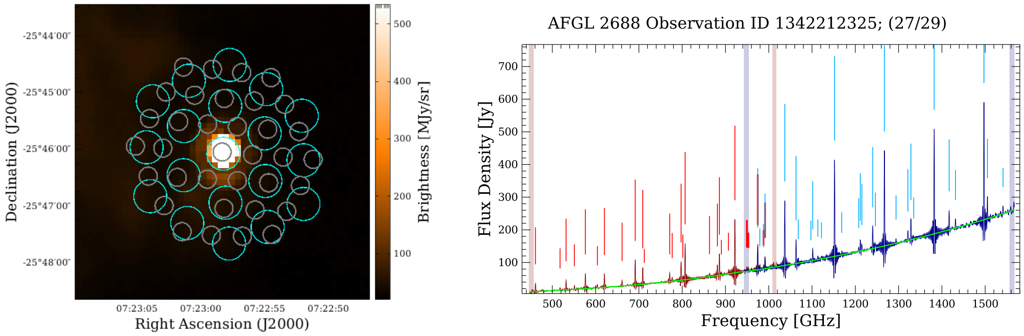

Figure 3.16: Photometer map (left) and postcard (right) for the calibration source AFGL 2688. Format similar to Figure 3.5.

AFGL 2688 is a very young protoplanetary nebula having left the AGB phase $\sim$ 100 years ago [122]. There is a fast molecular wind extending from the central star heating the surrounding molecular gas [85, 122]. Line identification with the template successfully matches 62% of the lines extracted by the FF to the template and the low SNR search finds an additional 17 features shown in Figure 3.17.

There are a large number of observations of this source with a high SNR unidentified feature detected between 1414.77–1414.90 GHz. This feature could possibly correspond to the H_2O, v=1 17(4, 14)–16(5, 11) transition at 1414.86 GHz or a SiC feature at 1414.99 GHz which are not included in the template.

The presence of HCN, ^{12}CO, and ^{13}CO rotational features in SPIRE FTS observations of this source are confirmed in Hopwood et al. [122]. Isotpologues of these molecules are also found by matching FF lines to the template as well as CS, H_2O, and H_2CO features.

A summary of the molecular and atomic lines identified in each calibration source is displayed in Table 3.5. CO features are commonly found in all of these six calibration sources as well as water lines. The expected SiO features in VY CMa and CW Leo can also

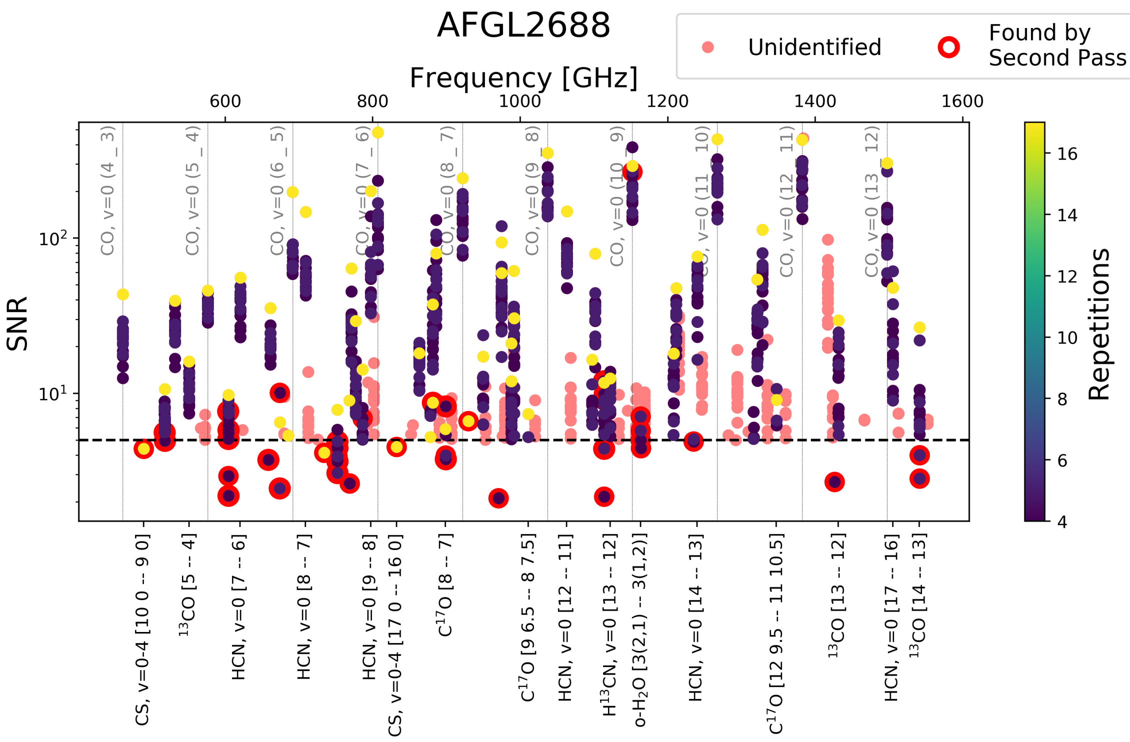

Figure 3.17: The line identification results for the calibration source AFGL 2688 (see Table 3.2).

be seen.

3.4 Application to the Full Catalogue

In Chapter 2 I have discussed the different observing modes and the products processed by the FF. Sparse observations are treated nominally as has been previously explained, however, mapping observations are treated as if each spaxel is a separate single pointing observation. Line identification with the template and the low SNR search are conducted on each spaxel of the SLW and SSW cubes independently using the velocity estimate from the combined arrays that is obtained from the ^{12}CO routine (see Section 2.2.5).

Table 3.5: Atomic/molecular species identified in the six calibration sources. The number of lines extracted by the Feature Finder, n_{FF}, are also shown as well as the number of lines found in the low SNR search, n_{SP}.

	NGC 7027	AFGL 4106	CRL 618	CW Leo	VY CMa	AFGL 2688
n_{FF}	832	375	1205	374	620	978
n_{SP}, SNR≥ 5	25	10	77	37	29	15
n_{SP}, SNR< 5	64	52	72	19	31	28
CO	310	277	208	70	65	168
^{13}CO	287	177	198	74	28	178
C^{17}O	5	0	16	3	0	24
C^{18}O	0	0	38	4	8	42
N II	12	28	0	0	0	0
C I	39	0	0	0	0	0
H_2O	11	11	151	25	128	85
$H_2^{18}O$	6	1	4	7	8	0
H_2CO	32	31	54	37	40	37
HCO$^+$	80	0	181	0	16	0
H^{13}CO$^+$	0	0	0	2	9	0
CH$^+$	31	0	0	0	0	0
CS	1	1	2	0	0	6
^{13}CS	0	0	0	0	0	3
HCN	1	0	254	103	70	205
H^{13}CN	0	0	17	7	8	130
HNC	1	0	130	11	0	0
HF	1	0	0	0	0	0
H_2S	0	0	3	0	0	
SO	0	0	1	0	0	1
SiO	0	0	1	56	139	0
N_2H^+	0	0	0	7	0	0

3.4.1 Sparse observations

The effectiveness of the template matching at identifying the features extracted by the FF is demonstrated in Figure 3.18. The green bins in Figure 3.18 show the ratio between the number of lines extracted by the FF that remain unidentified by the template matching and the total number of lines from observations with reliable velocity estimates. This ratio is determined over larger frequency ranges than the bins of the histogram in order to guide the eye to regions of high or low success in line identification. A similar figure is generated for mapping observations in the following section.

High concentrations of successfully identified ^{12}CO transitions can be seen. This is unsurprising since these features tend to occur at high SNR resulting in more reliable FF fitting results. The rest frequencies of the 10 in-band rotational ^{12}CO transitions are displayed in Table 3.6.

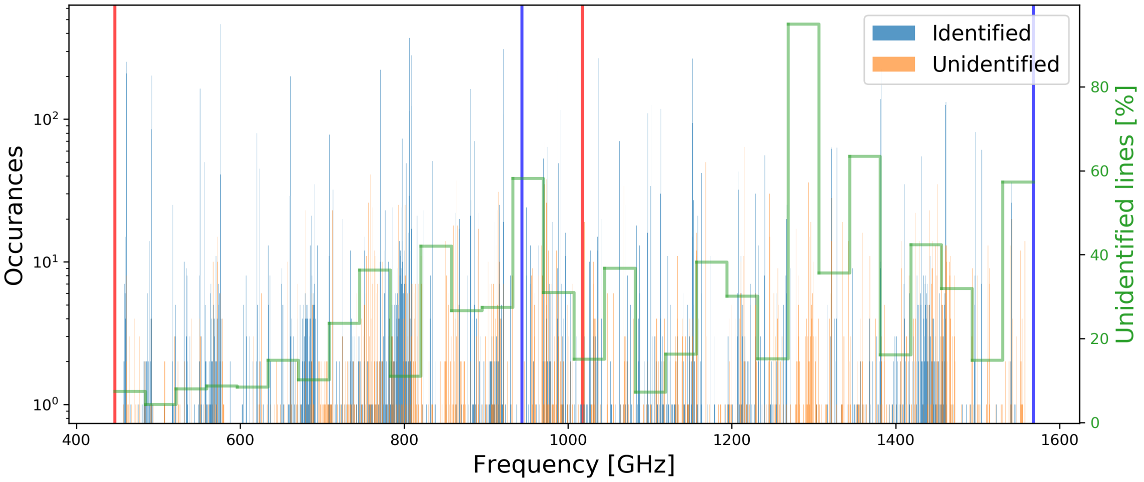

Figure 3.18: The results of line identification through matching with the template line list shown as a histogram over frequency for sparse observations. The edges of the SLW (red) and SSW (blue) bands are marked by thick vertical lines. The histogram bin width is 0.3 GHz matching the resolution of the line identification routine. Larger bins in green guide the eye to frequency regions of high or low success in identifying features.

Only 60 of the lines extracted by the FF (0.3%) are from sources without reliable ve-

Table 3.6: The rotational transitions of ^{12}CO in rest frame. Transition numbers represent the *J* quantum number.

SLW		SSW	
Transition	Frequency [GHz]	Transition	Frequency [GHz]
4–3	461.041	9–8	1036.912
5–4	576.268	10–9	1151.985
6–5	691.473	11-10	1267.014
7–6	806.652	12–11	1381.995
8–7	921.800	13–12	1496.923

locity estimates. Of the lines with velocity estimates, 77.3% are successfully matched to the template and an additional 1 833 features are found by the low SNR search. 506 of the features found by the low SNR search have an absolute SNR greater than 5. There is a large number of features in the 1261–1325 GHz region that are unable to be matched with the template. Table 3.7 shows several spectral features in this region that are not included in the template. Many of these transitions are reported as possible matches to spectral features in SPIRE FTS observations of the calibration source VY CMa (see Matsuura et al. [120]).

3.4.2 Mapping observations

A similar histogram as in the previous section is presented in Figure 3.19 to show the effectiveness of the line identification routine for mapping observations. Mapping observations provide a significantly larger data set of lines extracted by the FF than sparse observations (see Table 2.5) and the majority of the observed sources are large extended emission regions (see Figure 2.5).

I found that 14.1% of lines from mapping observations are from spaxels that do not have a radial velocity estimate, this is significantly more than the number of lines without corresponding velocity estimates from sparse observations. The lack of reliable velocity estimates is likely a combination of the structure of mapping sources and the absence of

Table 3.7: Spectral features not included in the template that occur in the frequency region centred at 1288 GHz where many Feature Finder lines from sparse observations are not identified by the template.

Molecule	Transition	Rest frequency [GHz]
H_2O	7(4,3)–6(5,2)	1278.27
H_2O	8(2,7)–7(3,4)	1296.41
H_2O v2=3	6(5,2)–7(4,3)	1286.83
HDO	2(1,2)–1(0,1)	1277.68
HDO	2(2,0)–2(1,1)	1291.64
HDO	8(2,6)–8(2,7)	1293.37
SiS	71–70	1280.45
SiS	72–71	1298.24
SO	26(2,6)–25(2,6)	1287.66
SO	30(2,9)–29(2,8)	1287.75
SO	30(3,0)–29(2,9)	1287.78
H_2S	9(6,4)–9(5,5)	1283.11
H_2S	6(2,4)–6(1,5)	1298.79
$C^{34}S$ v=1	27–26	1289.17
CS	26–25	1270.94
H_2CO	17(2,15) – 16(2,4)	1269.48
$HC^{15}N$	15–14	1289.73

cross-correlation velocity estimates. Mapping observations tend to be of sources with complex emission structure and there may exist dark spaxels that do not contain sufficient spectral information for a reliable velocity estimate (see Figure 3.20). It should also be noted that the cross-correlation method for determining radial velocities has not been applied to mapping observations (see Chapter 2).

Of the lines from spaxels with reliable velocity estimates, 95.2% are successfully matched to the template by the line identification routine and an additional 342 lines are found by the low SNR search. 167 of the lines found by the low SNR search have an absolute SNR greater than 5. As in the result from sparse observations, the 1261–1325 GHz region has no identified lines, however, only two features are extracted by the FF from mapping observations in this region. There are a large number of unidentified features towards the edge

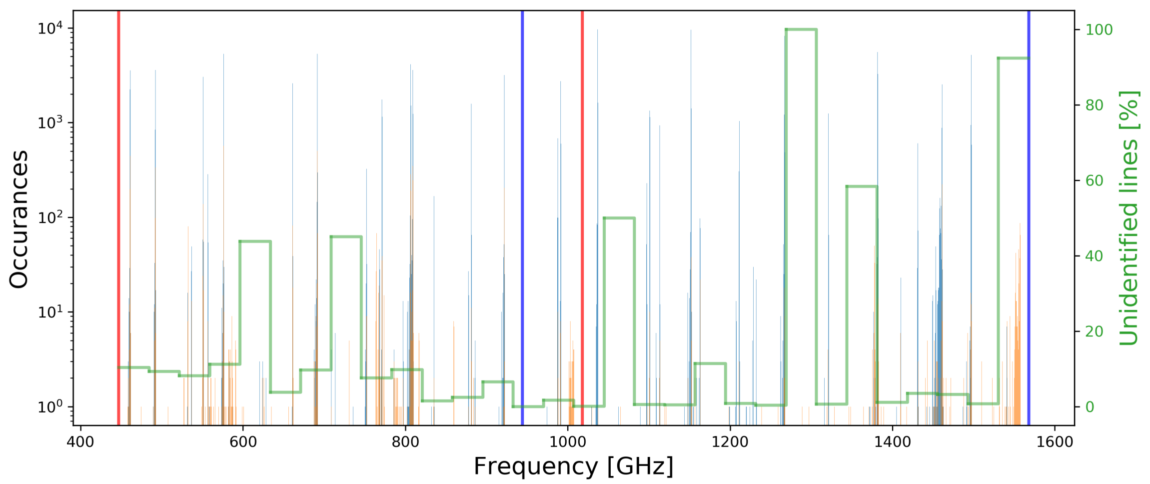

Figure 3.19: The results of line identification through matching with the template line list shown as a histogram over frequency for mapping observations. Notations are similar to Figure 3.18

of the SSW band (1531–1568 GHz) where a series of H_2CO features that are not included in the template occur. Table 3.8 shows these H_2CO features that occur in this region with some other lines that are also not included in the template.

Table 3.8: Spectral features not included in the template that occur in the frequency region centred at 1549 GHz where many Feature Finder lines from mapping observations are not identified by the template.

Molecule	Transition	Rest frequency [GHz]
H_2O	6(3,3)–5(4,2)	1541.97
H_2CO	21(5,17) – 20(5,16)	1530.39
H_2CO	22(0,22) – 21(0,21)	1530.78
H_2CO	21(3,19) – 20(3,18)	1531.51
H_2CO	21(4,18) – 20(4,17)	1532.95
H_2CO	21(4,7) – 20(4,16)	1534.57
H_2CO	21(1,20) – 20(1,19)	1540.68
H_2CO	21(3,18) – 20(3,17)	1540.68
$HC^{15}N$	18 – 17	1547.10
$H^{13}CN$	18 – 17	1552.19
HNC	17–16	1539.33

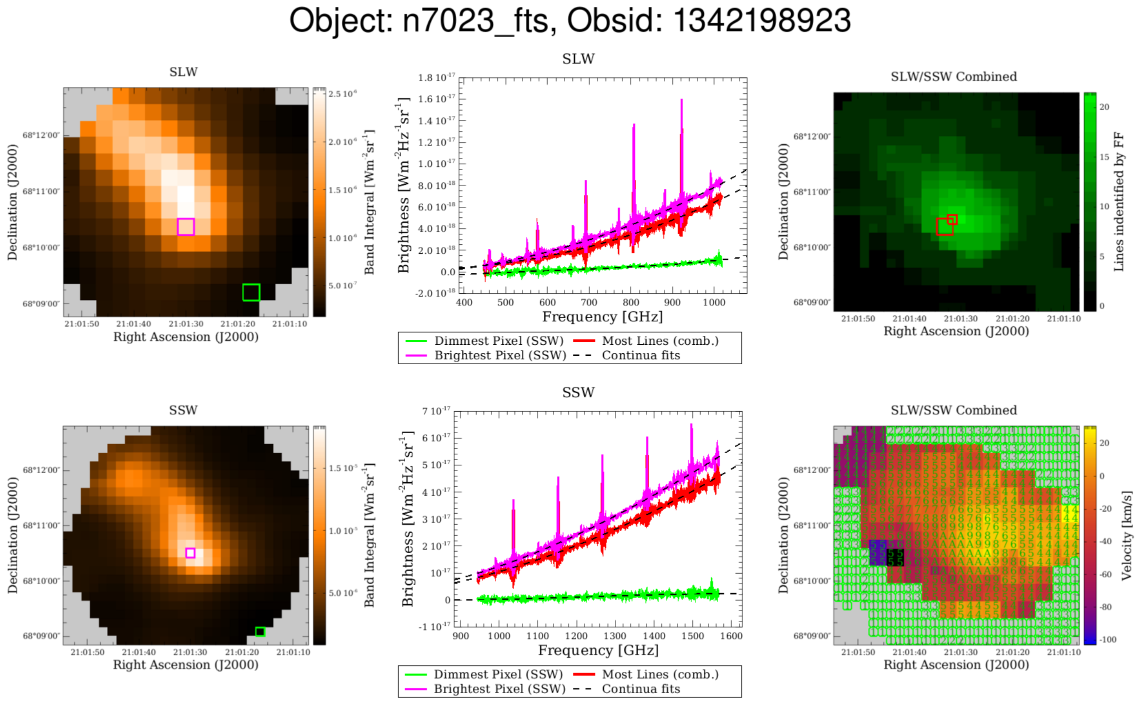

Figure 3.20: A mapping postcard of the nebula NGC 7023. This observation demonstrates the usual structural differences between sparse and mapping observations (compare to Figure 2.5) and that multiple spaxels of a complex emission structure often do not contain sufficient spectral content to measure the radial velocity with the ^{12}CO method.

3.4.3 Dual pointing observations

Over the course of the *Herschel* mission, two observations of the SPIRE FTS were taken with special settings at two Beam Steering Mirror (BSM) positions [7]. The first observation, ID 1342227785, is of the calibration source CRL 618 and the other, ID 1342227778, is of the calibration source AFGL 4106. The FTS observation pipeline successfully processes these observations as mapping mode observations and they exist in the HSA as spectral cubes with spatial coverage slightly better than sparse observations but slightly worse than intermediately sampled observations. In both cases in the FF, the single FTS observation is treated as two separate sparse observations. In the scope of the FF for sparse observations at the time, this was appropriate since only central detectors were used for sparse observations, however, this thesis details the application of the FF to all of the detectors in a sparse observation (See Chapter 4) and it becomes more appropriate to treat these as mapping observations. The mapping postcards for these sources are shown in Figure 3.21. The spaxel with the most lines in the observation of AFGL 4106 appears to largely be spurious detections. Note that the foreground emission from the galaxy is brighter than the source itself in the SLW band.

The application of the line identification and low SNR search routines first requires both observations to be processed as mapping observations in the FF obtaining a radial velocity estimate for each spaxel. After this process, both observations are ready to be processed as normal mapping observations. The results of the routines on these observations are summarized in Figure 3.22. Features that are successfully identified by matching to the template are marked in blue while those that are not matched are marked in red. Features from spaxels that do not have a reliable velocity estimate are marked with triangular markers in a fainter red. Note the high quantities of N II features found in AFGL 4106.

3.5 Conclusions

The line identification routine has successfully matched 12 052 lines from sparse observations (77.3% of FF lines from observations with reliable velocity estimates) and 124 065 lines from mapping observations (95.2% of FF lines from spaxels with reliable velocity estimates). The low SNR search has added 1 516 missing lines from sparse observations and 342 lines from mapping observations to the catalogue. Though the line identification does not give a complete picture of every prominent atomic and/or molecular feature contained in SAFECAT, the template selected is representative of typical sources observed by the SPIRE FTS instrument as is evidenced by the 95% line matching in mapping observations.

The low SNR search routine, by design, is searching for features at low SNRs, where spurious detections of features are common and should be viewed with a degree of skep-

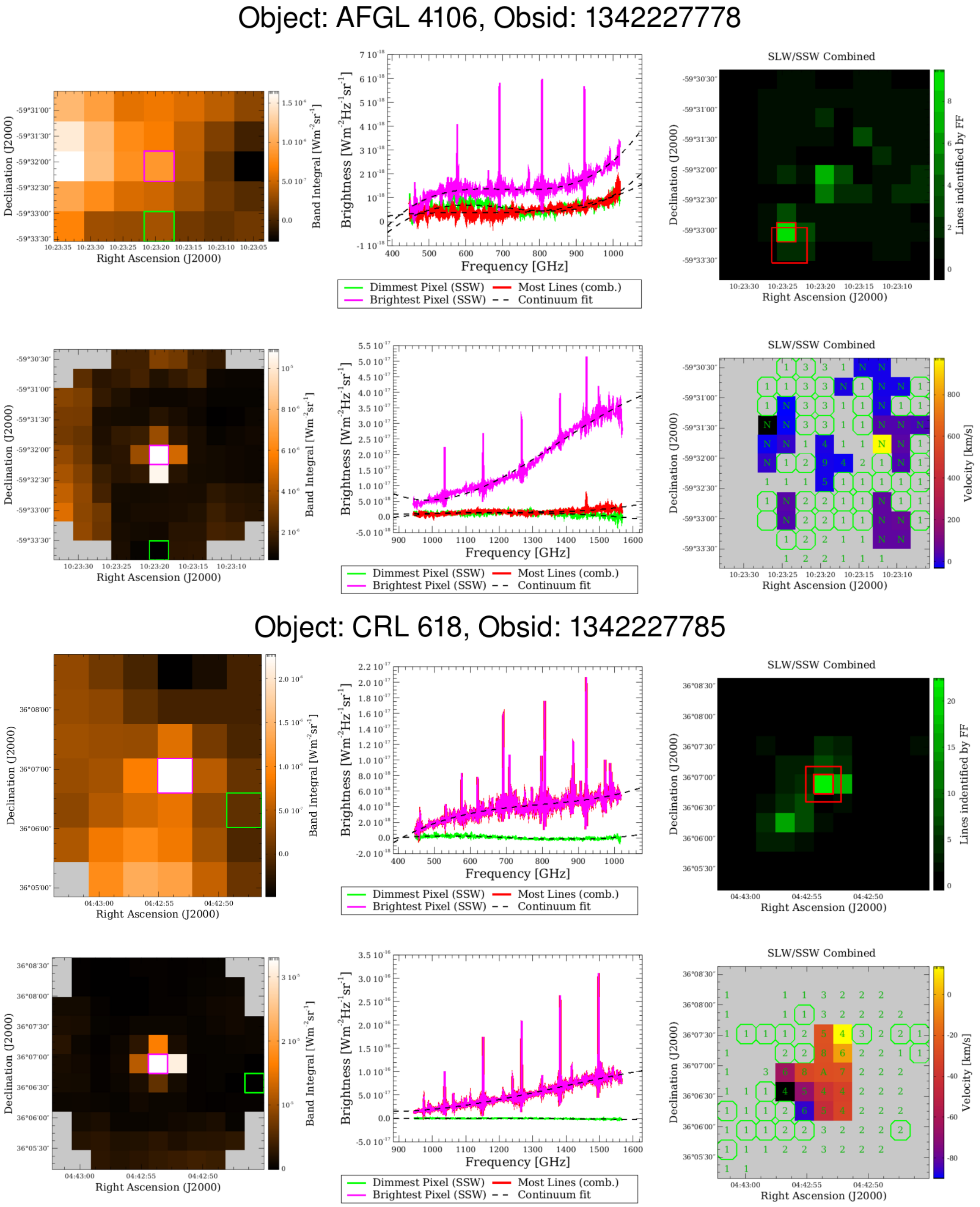

Figure 3.21: The mapping postcards for the dual pointing observations of AFGL 4106 (top) and CRL 618 (bottom).

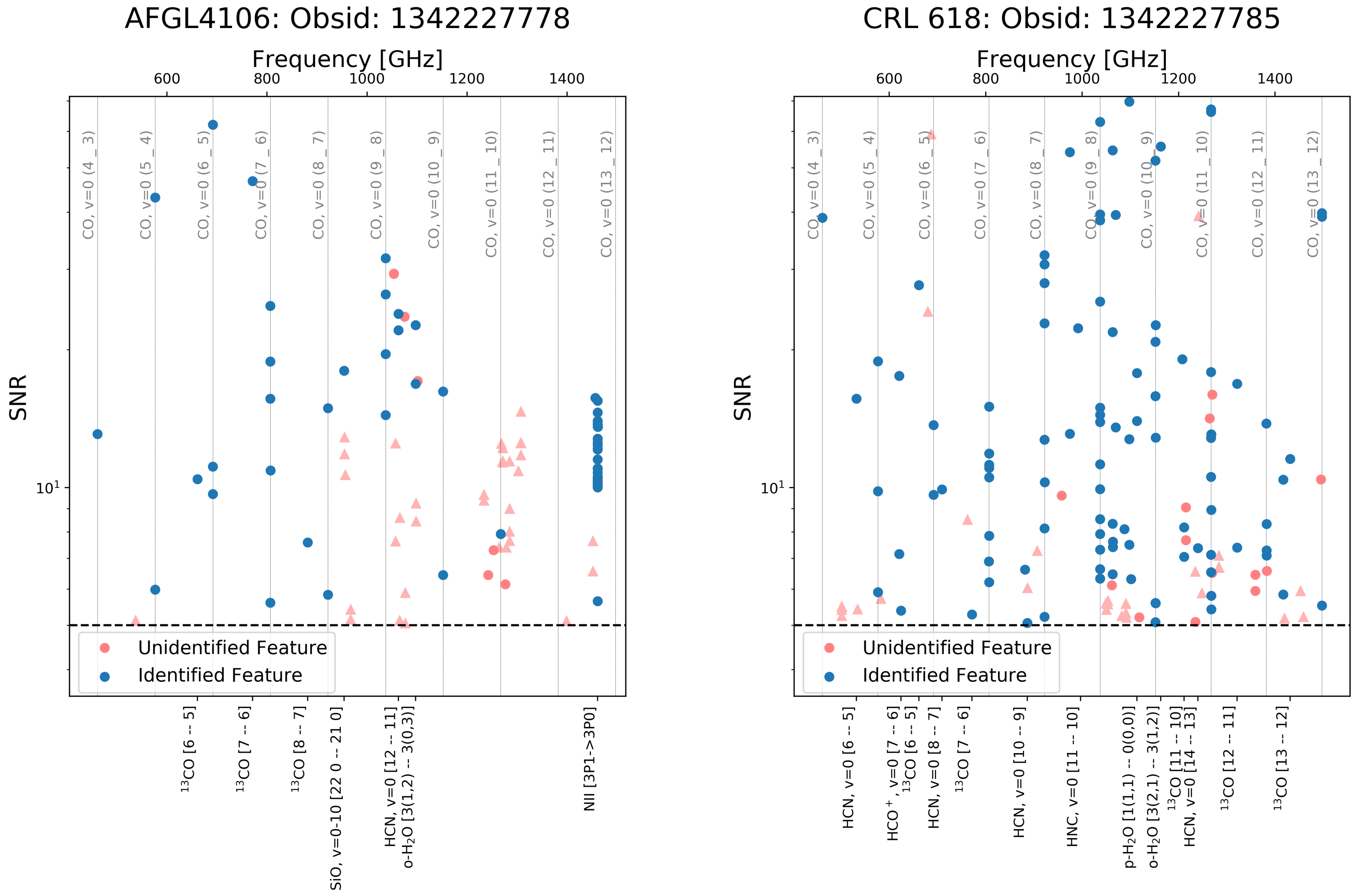

Figure 3.22: The line identification results from the dual pointing observations of the calibration sources AFGL 4106 and CRL 618. Fainter red triangles mark features found by the FF that are from spaxels without reliable velocity estimates. All 10 in-band rotational CO transitions are marked by vertical grey lines.

ticism. A significant portion of features found by the low SNR search are considered a poor fit by the FF flagging criteria. Of the lines found by the low SNR search, 75.9% from sparse observation and 87.1% from mapping observations are flagged as poor fits. Though caution should be used when considering these features, this routine fills a known weakness of the FF routine and aids in increasing the frequency spacing tolerance in the identification routine when an expected prominent feature is found by the FF more than 0.3 GHz from its rest frequency.

The results from the line identification provide a useful addition to the FF catalogue for determining the resources in a given SPIRE FTS observation that can be used to measure the system. Appendix B presents the results of the line identification routine after its application to all publicly available SPIRE FTS observations. These results include features identified in the spectra from off-axis detectors of the FTS which is the subject of the following chapter. The identification of all 15 atomic/molecular species in the template is shown broken down by observing mode in Figure 4.14 in the following chapter.

Chapter 4

Application of the Feature Finder to Off-Axis Detectors

> Many of the truths we cling to depend greatly on our own point of view.
> – Obi-Wan Kenobi
>
> –George Lucas, dir. *Star Wars Episode IV: A New Hope*.
>
> Twentieth Century Fox, 1977.

In Chapter 2 we have seen that the majority of the *Herschel* Spectral and Photometric Imaging Receiver (SPIRE) Fourier Transform Spectrometer (FTS) observations are single-pointing and sparsely sampled. Current public releases of the *Herschel* SPIRE FTS Spectral Feature Finder (FF) catalogue only present extracted features from the central detectors of the Spectrometer Long Wavelength Array (SLW) and Spectrometer Short Wavelength Array (SSW) arrays, SLWC3 and SSWD4. This leaves the wealth of spectral information from the other 52 active detectors untouched. In the development of the FF, we identified 397 sparse observations that were of semi-extended or extended sources which would be expected to contain significant emission observed by off-axis detectors. It has been my responsibility to extend the FF routine to include observations from off-axis detectors in sparse observations for the next public release of the FF catalogue.

In this chapter, I will discuss the application of the FF to the off-axis detectors in sparse observations of the SPIRE FTS and the justification for their inclusion in the the SPIRE Automated Feature Extraction Catalogue (SAFECAT). The application of line identification and the extraction of low SNR features, as introduced in Chapter 3, to off-axis detectors of the SPIRE FTS is also presented in this chapter. Discussion of these routines in this chapter is in compliment to what is presented in Chapter 3. I have included a brief study comparing the effectiveness of both methods used by the FF to measure radial velocity in off-axis detectors. The FF has been applied to the off-axis detectors of all sparse observations contained in the catalogue (with the exception of the dual pointing observations from the previous chapter) and the extended calibration has been used to determine their spectra regardless of whether the source in the central detector is extended or point-like emission. It is also important to note that the SPIRE FTS has a 2 arcminute unvignetted Field of View (FOV, see Figure 2.3) and that the outer ring of detectors on both the SLW and SSW array have a reduction in the light that they receive. The flux calibration for these detectors is thus less reliable [6]. Other obliquity effects on line shape and centre are corrected in the nominal SPIRE FTS processing pipeline [123].

4.1 Importance of Off-Axis Detectors

We have already discussed that there exist 397 observations in the Herschel Science Archive (HSA) that are expected to have significant emission in off-axis detectors of the FTS which represent 45.7% of unique sparse observations. An example of both an extended and semi-extended source is shown in Figure 4.1, with the SPIRE FTS footprint shown. The extended source, SH104 IRS2, shows bright emission extended throughout the off-axis detectors of the FTS while the semi extended source shows a bright point-like source slightly off-centre of the detector arrays with diffuse emission extending out from it. In both cases, significant spectral content is expected to be observed by off-axis detectors. There is also a known potential for pointing errors in SPIRE FTS observations that can sometimes result in an observation straying as much as 1 arcminute from the requested pointing (See Figure 4.2) [86]. In cases in which the pointing error is large, it is possible for the desired source to appear in an off-axis detector of the FTS.

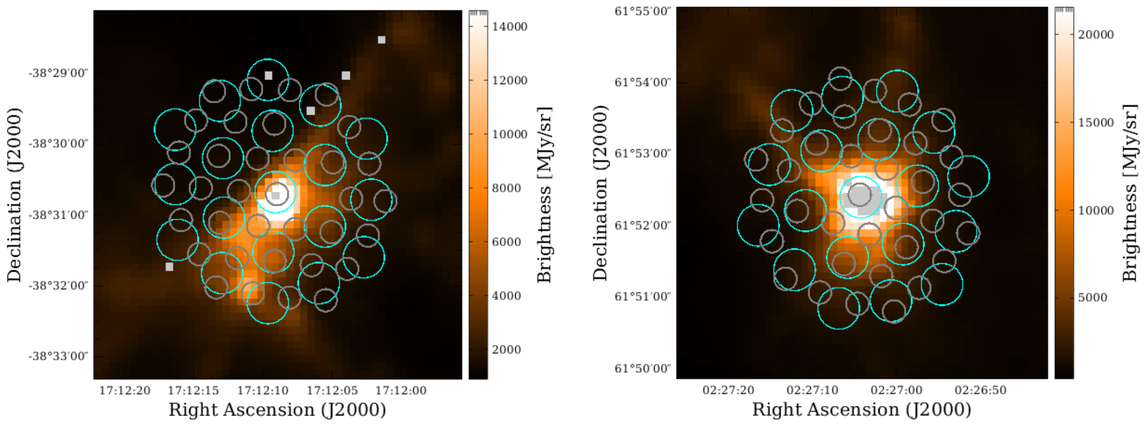

Figure 4.1: SPIRE observations of an extended source, the emission nebula RCW 120 (left), and a semi-extended source, the molecular cloud W3 (right), with the FTS footprint shown (grey: SSW, cyan:SLW) superimposed on SPIRE Photometer Short Wavelength (PSW) maps (250 μm) of the sources. Note that grey pixels in the photometer map are either dead or saturated pixels that are assigned a not-a-number value in the SPIRE photometer processing pipeline.

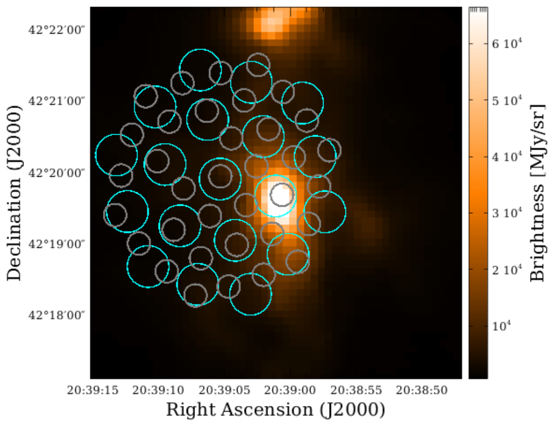

Figure 4.2: SPIRE observations of the star forming region DR 21. The figure is centred on the requested pointing seen by the bright source in the SPIRE PSW (250 μm) map but due to the pointing error (see Valtchanov et al. [86]), the source occurs in an off-axis detector of the FTS.

The number of SPIRE FTS observations that are expected to have significant emission in off-axis pixels can be easily estimated by comparing the integrated intensity across the entire SPIRE band. I have found that 26.4% of sparse observations have at least one off-axis SLW spectrum that is brighter than that of the central detector. For the SSW array, 25.1% of observations have a brighter off-axis detector than the central detector. These results are shown in Figure 4.3 and are summarized in Table 4.1, where F_{OA} is the integrated intensity of the spectrum from an off-axis detector and F_{cent} is the integrated intensity of the spectrum from the central detector of the corresponding array. The final column of Table 4.1 presents the number of spectra from off-axis detectors within the defined region compared against the total of all off-axis spectra.

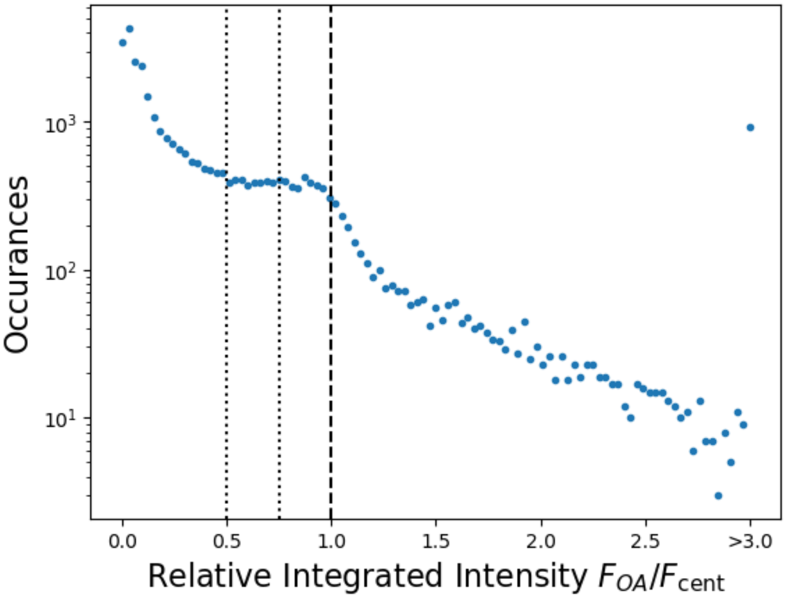

Figure 4.3: The integrated intensity of off-axis detectors compared to their respective central detectors in sparse SPIRE FTS observations. Vertical black lines show the regions summarized in Table 4.1.

There is also a particularly interesting example of the important information contained in off-axis detectors of the SPIRE FTS. Recently the first astronomical detection of the Noble gas molecule, $^{36}\text{ArH}^{+}$, was discovered by Barlow et al. [124]. This detection comes from a SPIRE observation of the Crab nebula supernova remnant and was found in the off-axis detectors, SSWA2, SSWB1, SSWB2, SSWB3, and SSWD4 [124].

Table 4.1: The number of off-axis spectra and observations with significant emission. Flux ratio ranges in the first column are cumulative.

	SLW		SSW		Combined
F_{OA}/F_{cent}	Spectra	Observations	Spectra	Observations	Total Ratio of Spectra
> 0.50	4 275	415	6 091	305	32.4%
> 0.75	2 880	304	4 193	257	22.6%
≥ 1	1 738	216	2 221	205	13.1%

Understanding the spectral content of off-axis detectors also becomes important when performing background subtraction for SPIRE Fourier Transform Spectrometer (FTS) observations as is done by Hopwood et al. [85] when examining calibration sources. Spectral information from off-axis pixels can be used to remove surrounding emission/absorption from a point source measured in the central detector, similar to aperture photometry [125]. If there are spectral features in off-axis detectors that are not present in the central detector, or that occur at a significantly different radial velocity, it may result in unwanted artifacts in the subtracted central spectrum.

Though most sparse observations are of sources that are point-like, extension of the FF to off-axis detectors is justified due to the extended nature of many sources, the FTS pointing error, and to provide comprehensive information for background subtraction of the central detector.

4.2 Postcards

In Chapter 2 we have briefly discussed the formation of mapping postcards and their role in the FF. The goal of FF postcards is to provide an at-a-glance summary of the information provided by the FF for any given observation. Figure 4.4 shows the application of the sparse postcards for the central detectors of SPIRE FTS observations to all detectors in a sparse observation. Figures of this nature are far too large and complicated to serve as postcards. These postcards do not provide any obvious information concerning the structure of the observed source or the velocity estimates that can be obtained on a per-detector basis from the SPIRE FTS. An approach similar to the mapping postcards was used instead for developing sparse postcards to present information from off-axis detectors.

The postcards developed to highlight off-axis spectral content extend the previously developed sparse postcards for central detectors and have been designed to follow a similar format to the mapping postcards. An example of these off-axis postcards is shown in Figure 4.5. It should be noted that the object names reported in SPIRE observations are submitted by the observer and do not necessarily conform to any naming standards. Throughout this thesis, it will also become apparent that they certainly do not keep to a consistent convention. For the convenience of generating postcards in mass quantities, the reported names in postcards are those that are directly recorded in the metadata of HSA observations as provided by the original observation investigators.

The first of the four columns of the postcard displays the sparse postcard that was generated in the nominal FF process (top) and the SPIRE FTS footprint over the PSW photometer map (bottom). The sparse postcard shows the spectra from each central detector (SLWC3 in red, SSWD4 in blue) and vertical shaded regions mark the 10 GHz wide edges of each band, which are nominally avoided by the FF in line searching. Features extracted by the FF are marked by vertical sticks whose size is proportional to the SNR of the line. The fitted continuum polynomial is also shown in green. For the photometer map, the figure itself is centred on the requested pointing of the observation and cropped to a 4 arcminute square. The colourbar of the photometer map is scaled to reflect the image content and empty pixels which are assigned a not-a-number (NaN) value are coloured in grey. The SPIRE footprint is shown with its actual pointing for each detector, the SLW array is out-

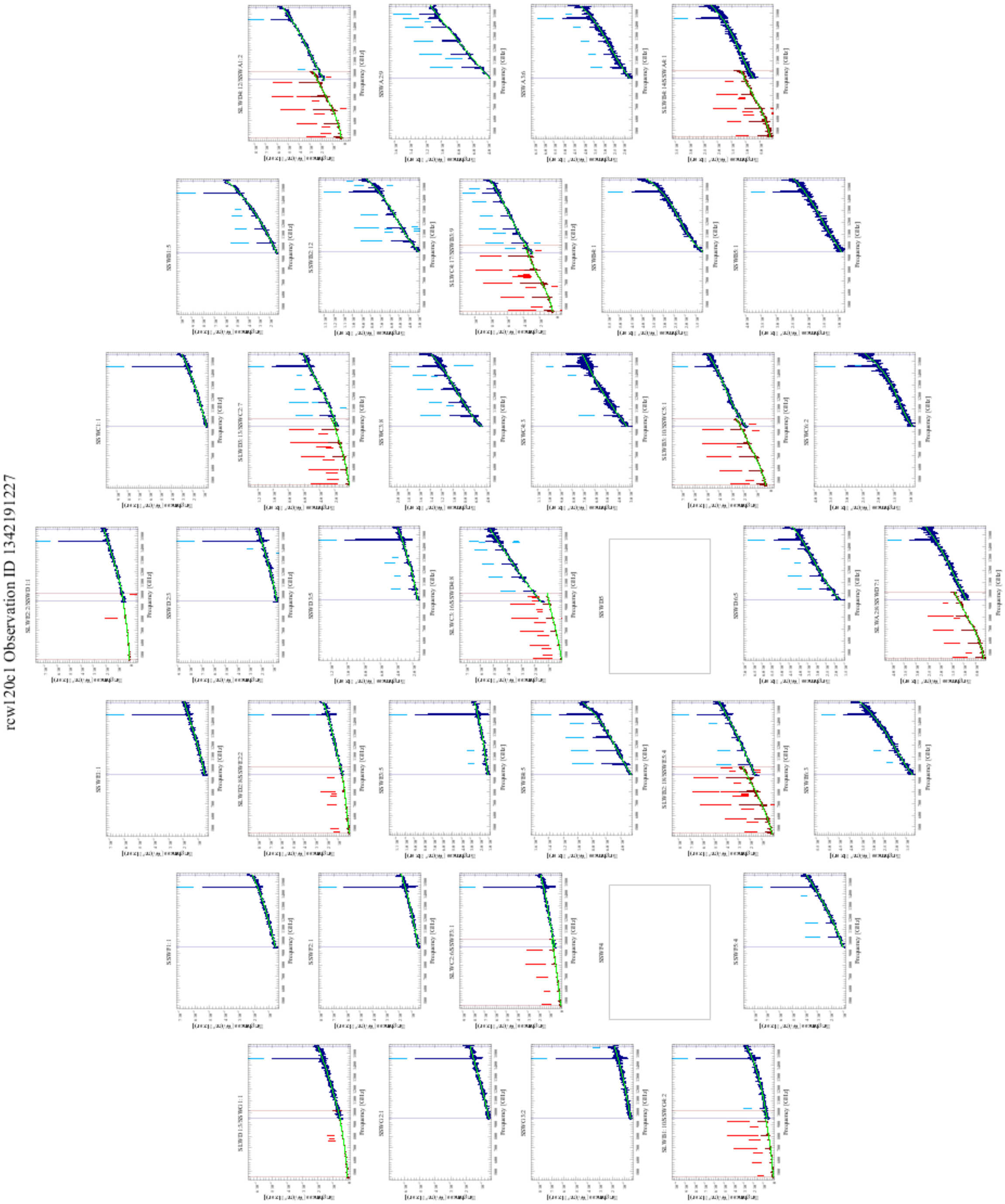

Figure 4.4: The postcards designed for central detectors in sparse observations applied to each detector in the SSW array for an observation of RCW 120 (see Figure 4.1). For SSW detectors that have a coaligned SLW detector, both spectra are shown on the same plot (the SLW spectrum in red and the SSW spectrum in blue).

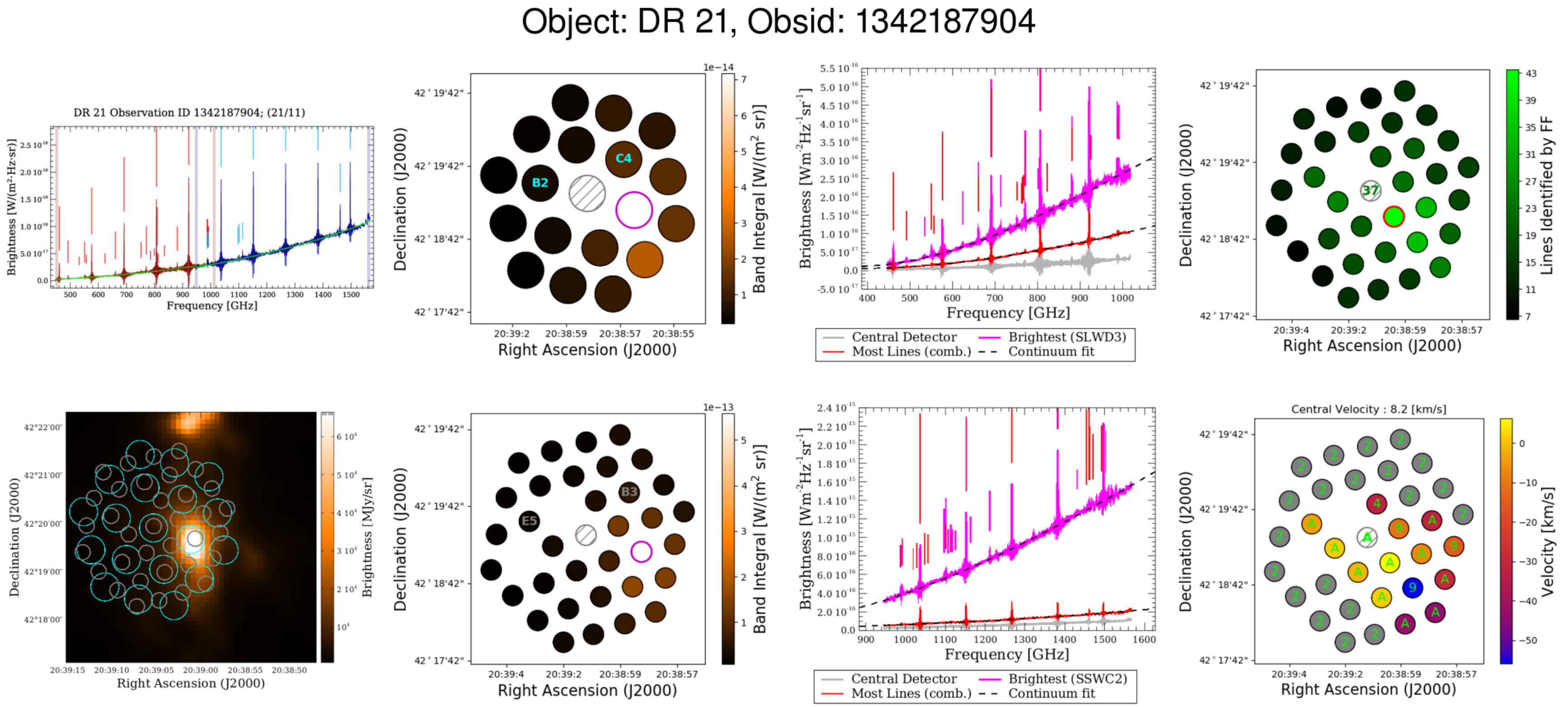

Figure 4.5: The off-axis postcard for the star forming region DR 21 (see Figure 4.2). The top panel in the first column provides the on-axis FF postcard, with the photometer 250 μm map and FTS footprint in the bottom panel. The second column provides intensity maps for the off-axis detectors from the SLW (top) and SSW (bottom) arrays. The third column displays spectra of interest including brightest off-axis spectra, and the off-axis spectra with the most lines extracted by the FF for SLW (top) and SSW (bottom). The final column shows a map of the number of identified spectral features (top) and associated radial velocities (bottom). A detailed description of each panel in the postcard is given in the body of this section.

lined in cyan and the SSW array is outlined in grey. The circles represent the Full Width at Half Maximum (FWHM) of the detector beam at the centre of the band corresponding to each array, ~ 25 arcseconds for SLW and ~ 19 arcseconds for SSW. In cases where no SPIRE photometer map is available for the pointing of the FTS observation, a stock image stating that no photometer map was found is shown instead. There are 97 SPIRE FTS observations for which no photometer map could be found.

The second column contains the footprint of each detector array on sky (SLW top, SSW bottom). In order to determine the orientation of the detector arrays, the SLWC3 and SLWB2 detectors are labelled in cyan while the overlapping SSW detectors SSWB3 and SSWE5 are marked in grey. Each detector is coloured based on the integrated intensity across their entire band for the given observation, with the extended calibrated spectrum used for this calculation. The central detector is not included in the determination of the colourbar dynamic ranges and it is marked by the grey hashed-out circle to illustrate this. Note the two dead detectors in the SSW array which also help in determining the orientation of the FTS on sky. The brightest detector from each array is outlined in magenta. This intensity map of the FTS footprint with the photometer map provides information about the structure of the source which should correspond to the spectral content of off-axis detectors.

The third column presents a few spectra of interest from the SLW array (top) and the SSW array (bottom). The spectra from the brightest off-axis detectors are plotted in magenta (based on the band integrated intensity and marked in the corresponding panels to the left) and the spectra from the detectors with the most lines are plotted in red (marked in the upper panel to the right). The spectrum from the central pixel is also plotted in the figure background, in grey, and intentionally does not influence the axis limits, the central spectrum is only provided for comparison and is better viewed in the central detector postcard (top left panel). Again the extended calibrated spectrum is chosen for this plot. The spectra with the largest number of lines is determined by combining the lines extracted from each SSW spectrum with those from its nearest neighbouring SLW spectrum, the number of features is then determined as the total number of features from both. As is the case for central detector postcards, the lines extracted by the FF are marked by vertical sticks with sizes proportional to the SNR of the feature. Emission features are marked above the spectra while absorption features are marked below.

The fourth and final column contains the number of lines extracted by the FF (top) and the velocity measurements (bottom) from off-axis detectors. In each case, the lines identified in the SSW detectors are paired to the nearest SLW detector and used for velocity estimates and the total number of lines displayed in each SSW detector. The SSW off-axis detector with the most number of lines found by the FF is outlined in red. The number of spectral features found by the FF for the central detector is written in green on the central detector. The velocity estimates are obtained from the ^{12}CO velocity estimate routine and follow similar annotations to those in mapping postcards. The green numbers mark the number of ^{12}CO features used in the velocity estimate with the character ‘A’ denoting that all 10 in-band ^{12}CO features are used. When the N II feature is used for the velocity estimate an ‘N’ character is used instead. Detectors for which no reliable velocity estimate can be obtained are coloured in grey. The radial velocity estimate from the central pixel is also shown in the title of the velocity panel and the radial velocity flag is printed in green over the central pixel.

Figures 4.6 and 4.7 both provide an example of an extended source and a semi-extended source that both have significant numbers of spectral features observed by off-axis detectors. More off-axis postcards, including cases in which off-axis detectors do not contain significant spectral information, are presented and discussed in Appendix C.

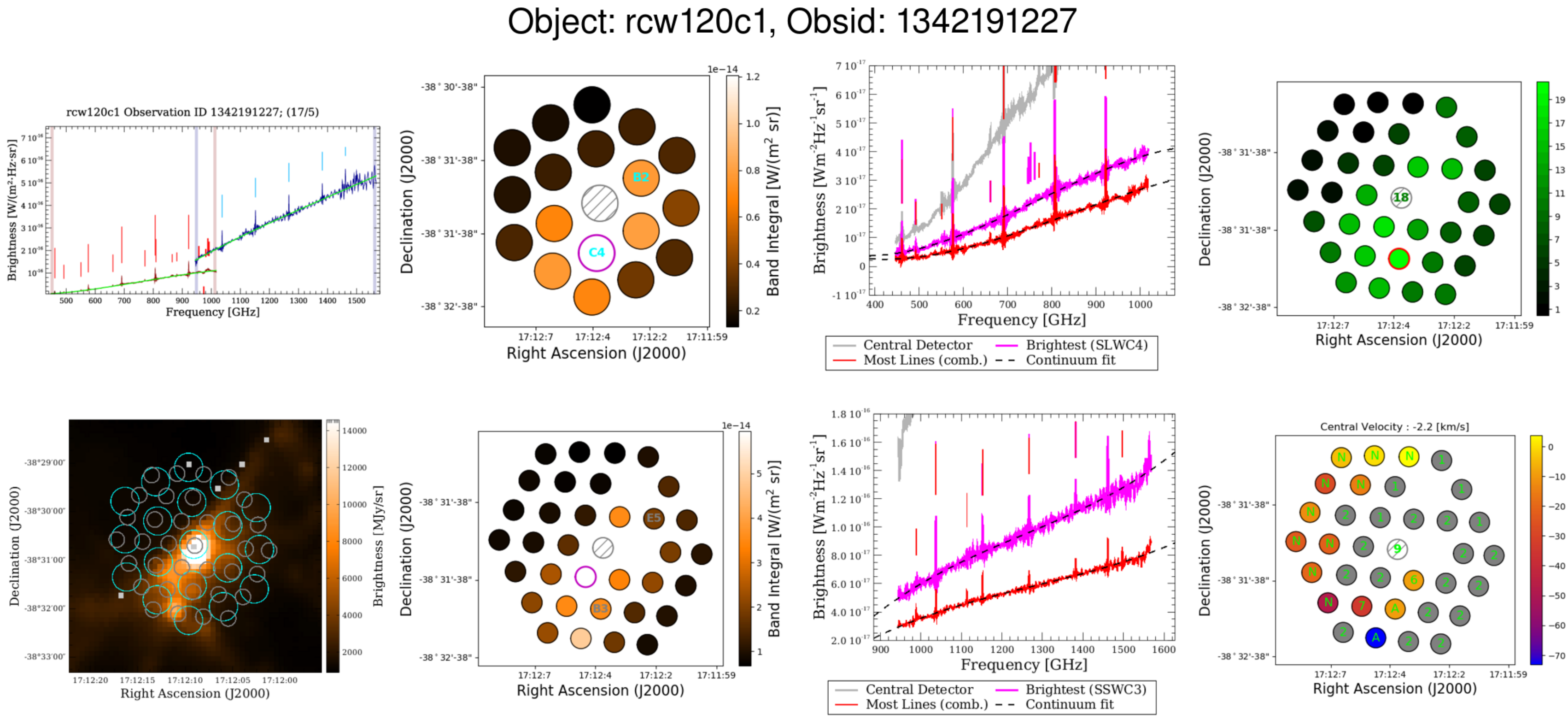

Figure 4.6: Example off-axis postcard for the extended source RCW 120.

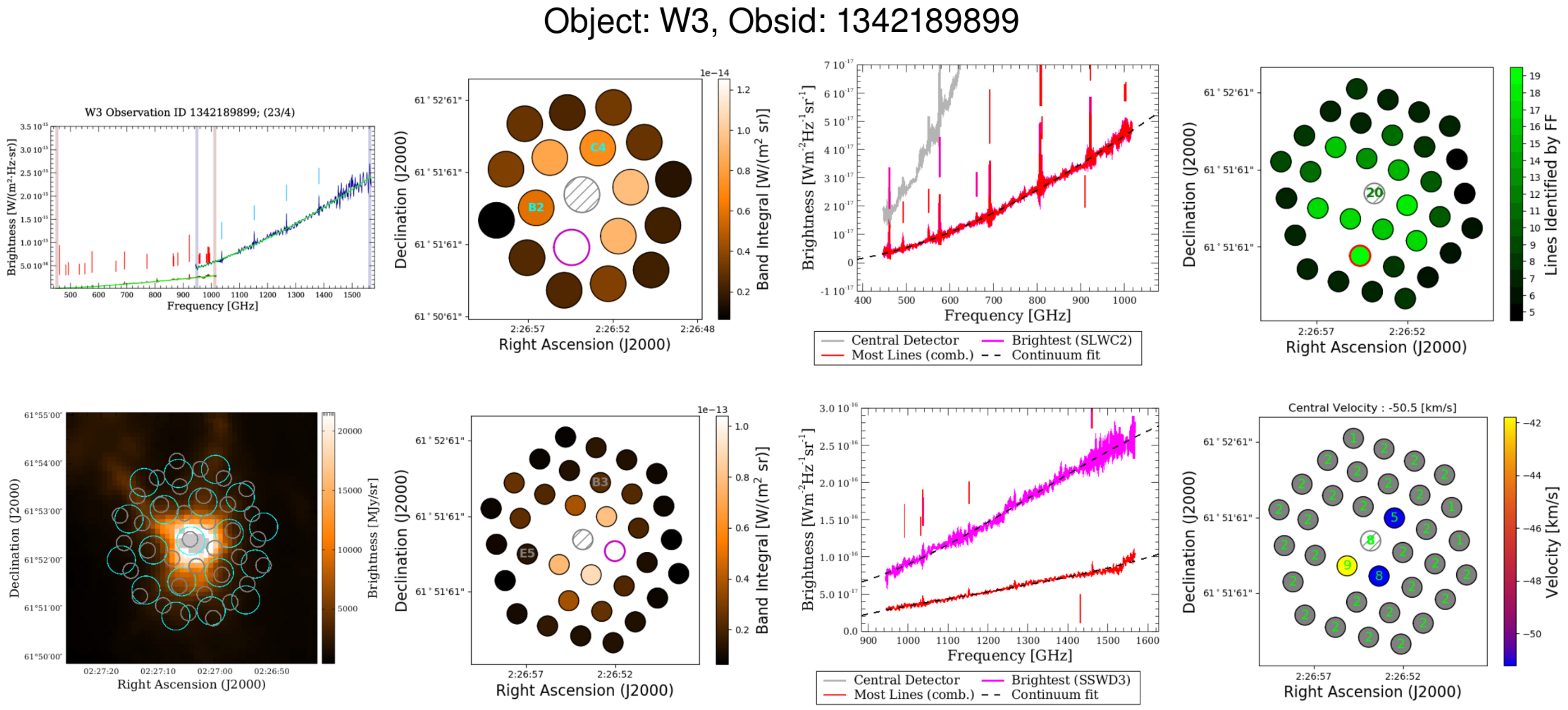

Figure 4.7: Example off-axis postcard for the semi-extended source W3.

4.3 Application of the Feature Finder

Applying the standard FF routine to the off-axis detectors of all 814 sparse observations yielded a total of 29 130 additional lines with an absolute SNR greater than 6.5. Note that there are four less sparse observations since the two dual pointing observations which were previously processed as four sparse observations have been processed as two mapping observations in Section 3.4.3. The results from the FF are broken down per detector in Figure 4.8. As expected the majority of lines discovered are close to the central detector of each array. Since a large portion of the spectra from off-axis detectors are significantly dimmer than the spectra from central detectors, only emission features extracted by the FF with an absolute SNR greater than 6.5 are included in the catalogue. Absorption features with an absolute SNR less than 10 are also removed from the catalogue. Nominally a cutoff of absolute SNR = 5 is employed for emission features in spectra from the central detectors while a cutoff of 10 is used for absorption features. This removal of spurious detections discards 36.3% of the spectral features originally found in off-axis detectors.

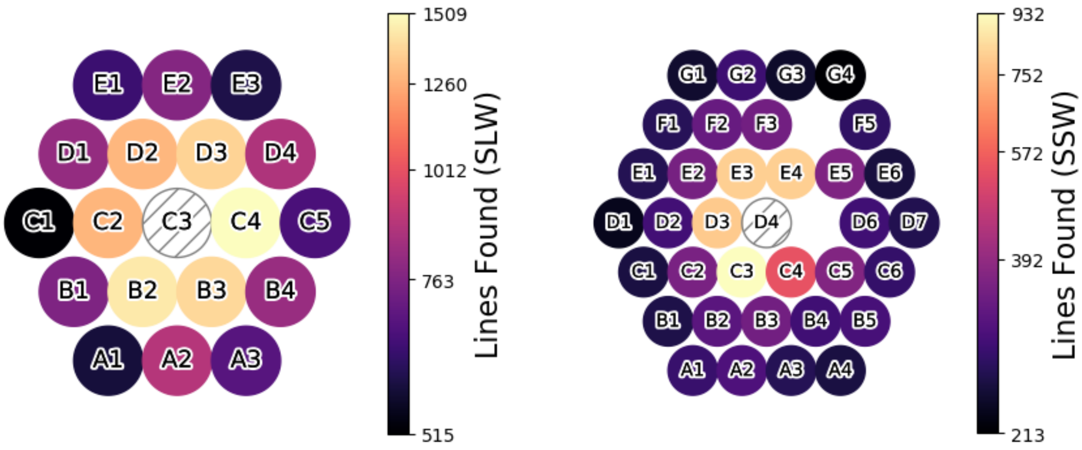

Figure 4.8: The number of lines detected in each off-axis detector over all 818 sparse observations of the SPIRE FTS.

The number of features found at different frequencies in the SPIRE FTS band is shown in Figure 4.9. We see that the N II $^3P_1$–$^3P_0$ feature (marked by the vertical red line) is frequently detected in off-axis detectors accounting for over 10% of the total detected features. ^{12}CO features are also fairly common, as expected. Figure 4.15 shows a similar histogram for the SNR of spectral features from off-axis sources in comparison to lines from mapping sources and central detectors. Triangular symbols mark the detection of features from the low SNR search routine after line identification has been performed. This is detailed in the following section.

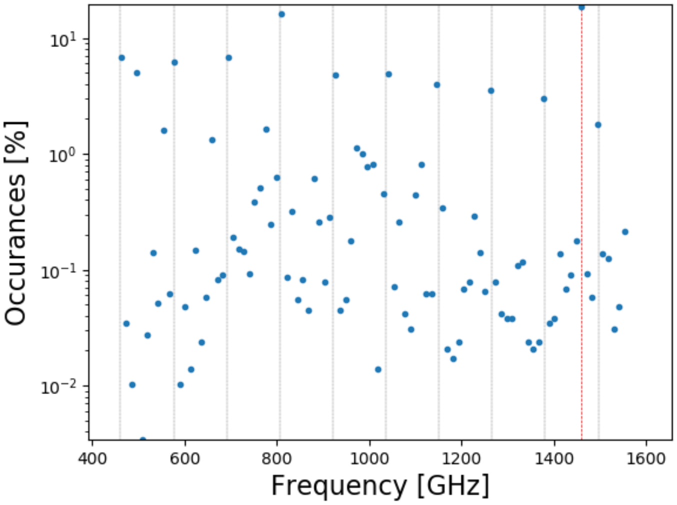

Figure 4.9: The number of lines detected by off-axis detectors at different frequencies. Histogram bin widths are 11.6 GHz wide. The rest frequencies of ^{12}CO are marked by vertical grey lines while the N II $^3P_1$–$^3P_0$ transition is marked by the red line.

Of the spectra from off-axis detectors with features found by the FF, 3 590 of 27 673 (13.0%) have reliable velocity estimates based on the ^{12}CO features. These velocity estimates are further discussed in Section 4.4.1.

4.3.1 Ionized nitrogen emission

We have seen in Section 3.1.2 that the N II $^3P_1$–$^3P_0$ feature originates from higher energy systems than the molecular lines that are commonly found in SPIRE FTS observations. There are several sparse observations that have a FIR bright central source with strong molecular emission and N II across the entire field viewed by the FTS. Figure 4.10 shows an example of this N II emission surrounding the calibration source, AFGL 4106 (see Section 3.3). In this case, the N II emission is useful for decoupling the dusty star measured by the central detector from the surrounding Galactic cirrus which has a radial velocity that differs by as much as ~ 60 km/s.

The N II $^3\mathrm{P}_1$–$^3\mathrm{P}_0$ transition has an energy difference corresponding to 70.1 K [92] and it is an effective coolant down to these temperatures in the Interstellar Medium (ISM) [22]. Typical methods of measuring metallicity in astronomical observations depend on bright optical features creating a strong bias to dust-free regions and have been known to underestimate the total metallicity of an observation [126, 127]. As this feature is so ubiquitous in FIR observations, it will play an important role in future FIR missions as well [126].

4.3.2 NGC 891

NGC 891 is a well studied spiral galaxy that is viewed edge-on and is thought to be fairly similar to our own galaxy [128, 129]. The galaxy contains layers of diffuse ionized gas that extend from the plane out to 4.5 kpc [130]. SPIRE observations of this galaxy have been used to measure its heating and cooling processes [129]. These SPIRE FTS observations have also been used to study the relationship between CO luminosity and Far-Infrared (FIR) luminosity, and the correlation between molecular gas density and star formation rates [131].

There are two SPIRE observations of this galaxy that demonstrate the utility of the information provided by the FF from off-axis detectors of the FTS. Figure 4.11 shows selections from the postcards from both observations. The Galaxy traces a diagonal line through the centre of the FTS footprint and the velocity of the N II $^3P_1$–$^3P_0$ line shows the

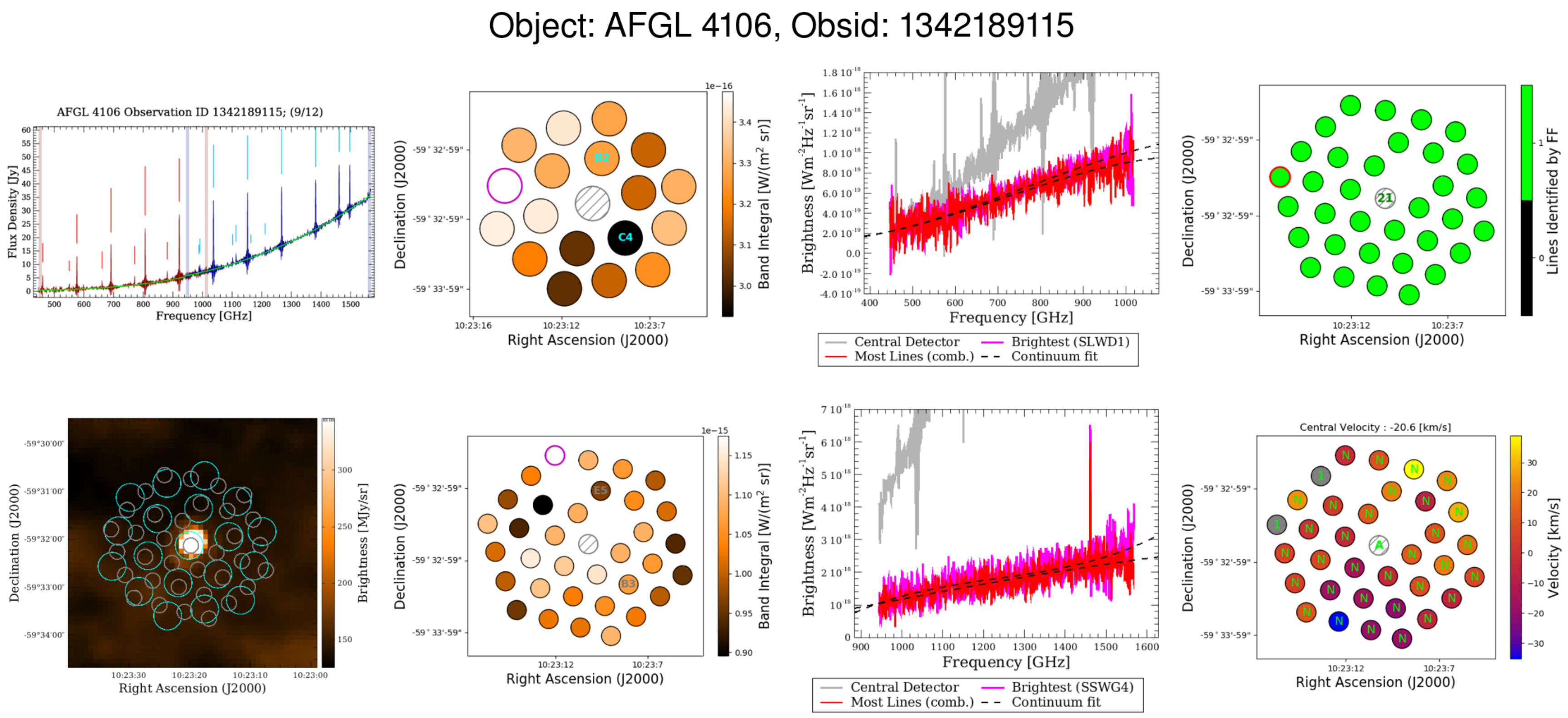

Figure 4.10: The off-axis postcard for an observation of the post-red supergiant AFGL 4106. The dusty molecular cloud surrounding the star is observed by the central detector while ionized nitrogen from the surrounding Galactic cirrus can be seen in the off-axis detectors.

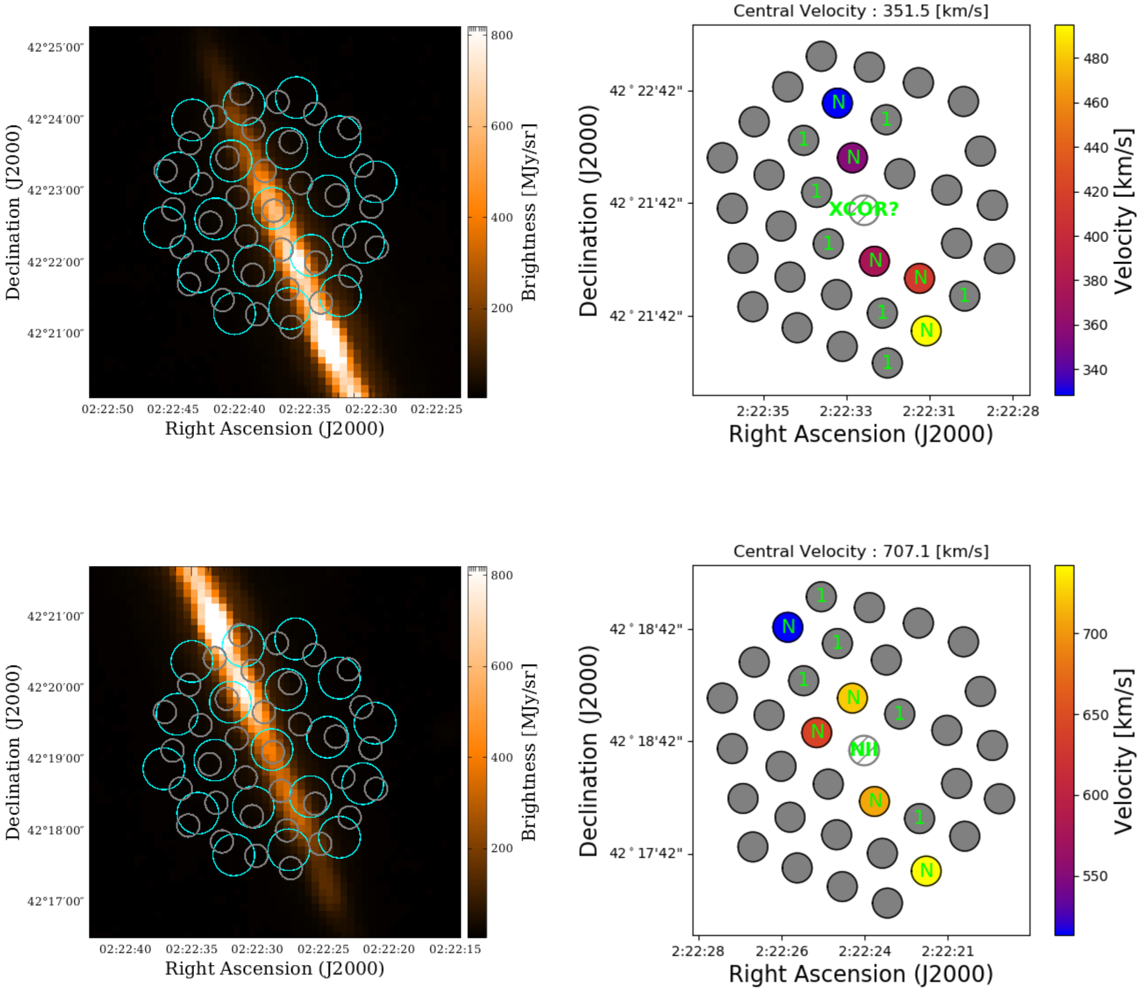

Figure 4.11: Two SPIRE FTS observations (top: Observation ID 134224766, bottom: 1342224765) of the galaxy NGC 891. The photometer map and FTS footprints from their postcards are shown (left) as well as their velocity maps (right). These results are provided by the FF radial velocity estimate routine (see [78]), modified by the author to process off-axis detector data within sparse observations.

velocity gradient corresponding to the rotation of the galaxy. The velocity of the central bulge as measured by the N II $^3P_1$–$^3P_0$ feature in the SSWF1 detector is 513 ± 20 km/s which is in agreement with the radial velocity reported in the NASA/IPAC Extragalactic Database (NED) [132]. Correcting to the rest velocity of the central bulge, the radial velocity of the south edge is measured by the SSWB5 detector (in observation ID 1342224765) to be 229 ± 28 km/s and the radial velocity of the north edge is measured by SSWF2 detector (in observation ID 134222476) to be -185 ± 28. This rotation is in agreement with measurements of the ionized gas by Keppel et al. [133] in this galaxy (see also [134, 135]).

4.4 Line Identification

The line identification routine of the FF was also extended to include off-axis detectors in sparse observations. This section presents and summarizes the results of both the line identification and low SNR search routine for off-axis detectors in sparse observations.

4.4.1 Velocity Estimates

In order to apply the line identification routine described in Chapter 3, velocity estimates specific to each off-axis detector in an observation were used (see Section 4.2). We have already seen cases above (Figure 4.10) where the radial velocity of a given detector may not necessarily match that of an off-axis detector. Only 13.0% of off-axis detectors from all sparse observations contain sufficient spectral information to determine a confident radial velocity estimate using ^{12}CO/N II features. In order to provide more off-axis detectors with radial velocity estimates for line identification, the cross-correlation method outline in Section 2.2.5 is employed for the spectra from off-axis detectors that do not have ^{12}CO velocity estimates.

There are 3 110 cases where a velocity estimate is provided by both the ^{12}CO and cross-correlation routines in off-axis spectra of the FTS. This allows us to further the validation of both routines performed by Scott et al. [78] with the results from off-axis detectors of the FTS. I found that 92.4% of velocities recorded by both routines are in agreement to within 20 km/s, which is similar to the agreement in central detectors [78]. I also found that the majority of outlying cases are a result of erroneous identification of the N II $^3P_1$–$^3P_0$ feature. When an observation is particularly line sparse, both methods look for this single line for a velocity estimate. It is expected for large discrepancies between each routine, to exist for these sources as the ^{12}CO routine is known to erroneously identify the N II $^3P_1$–$^3P_0$ transition to measure the radial velocity instead of an alternate atomic/molecular species [78].

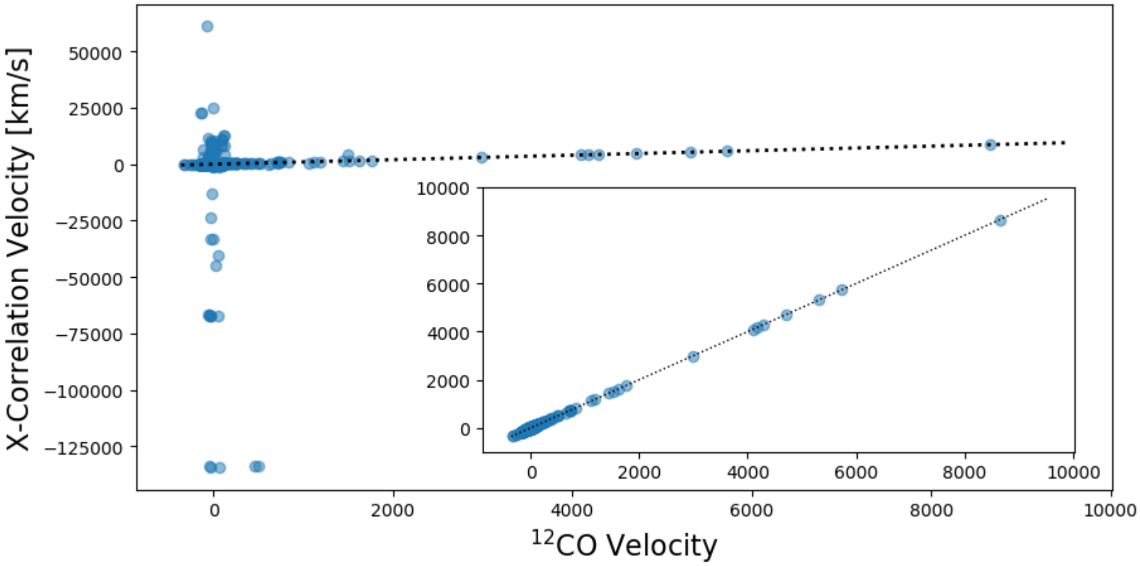

Figure 4.12: The agreement between the velocity measurements made by the ^{12}CO and cross-correlation methods (see Section 2.2.5) for off-axis detectors in sparse observations. The agreement of all 3 110 off-axis observations are shown in the main plot while the inset plot shows 92.4% of the velocity estimates, these agree within 20 km/s. In both cases, the dotted black line marks 1:1 agreement.

The agreement of these two routines is shown in Figure 4.12. The majority of off-axis velocity measurements can be seen to cluster around velocities less than 1 000 km/s. I found that 99.1% of velocities measured in off-axis detectors by both routines are of velocities lower than 500 km/s. This result is unsurprising since SPIRE FTS observations of high redshift targets usually contain a bright source in the central pixel with little to no signal in off-axis detectors. By employing both the ^{12}CO and cross-correlation routines, the number of spectra from off-axis detectors with reliable velocity estimates is increased from 3 590 to 9 211 (33.3%). In total, there are 4 129 lines, 14.4% of all lines extracted from off-axis detectors, that are from spectra in observations without reliable velocity estimates for the given detector.

4.4.2 Results

The line identification routine successfully matches 23 179 spectral features (93.1% of lines with velocity estimates) with their corresponding atomic/molecular transitions. These results are summarized in Figure 4.13. As in Chapter 3, the green bins in Figure 4.13 show the ratio between the number of lines extracted by the FF that remain unidentified by the template matching and the total number of lines from off-axis detectors with reliable velocity estimates. Similar to the histograms in both Figures 3.18 and 3.19 we see that the line identification routine is effective at identifying rotational CO features (see Table 3.6) and the N II $^3P_1$–$^3P_0$ transitions (rest frequency 1461.13 GHz).

The identification of all 15 atomic/molecular species in SPIRE FTS spectra from mapping, off-axis detectors in sparse observations, and central detectors in sparse observations is shown in Figure 4.14. Note that isotopologues and ionization states have all been grouped together for each species.

Figure 4.15 compares the FF results for off-axis detectors to the rest of the catalogue. The SNR histogram of the features from off-axis detectors is shown on the top plot in blue while the results from the central detector of sparse observations and the results from mapping observations are shown in orange on the middle plot and in violet on the final plot,

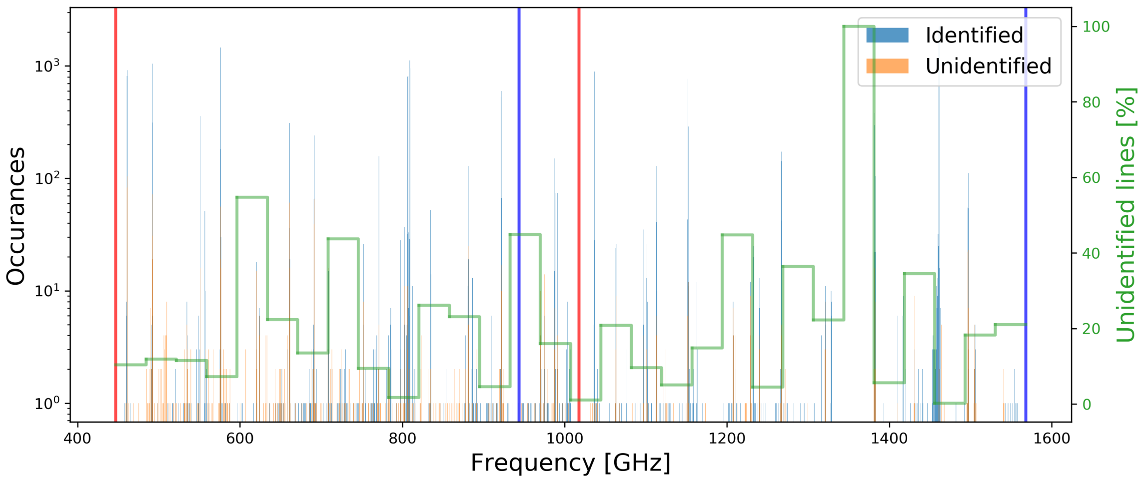

Figure 4.13: Identified and unidentified features extracted by the FF from off-axis detectors in sparse observations of the SPIRE FTS. Similar to Figures 3.18 and 3.19 the frequency bin width matches the 0.3 GHz template matching tolerance in the line identification routine. Larger green bins showing the number of unidentified features are used to guide the eye.

respectively. The absolute SNR cut-off for each case is shown by the dashed black line, note that for off-axis detectors, the absolute SNR cutoff was chosen to be SNR 6.5 due to a higher concentration of spurious detections from the more faint signals typically found in the off-axis detectors in sparse observations. Features discovered by the low SNR search routine described in Chapter 3 are shown by triangular-shaped markers. A total of 1 757 features from off-axis detectors in sparse observations have been added to the catalogue by this routine, 565 of these have an absolute SNR greater than 5.

Comparing Figure 4.13 to Figures 3.18 and 3.19, the composition of off-axis spectra appear to be more similar to mapping observation than the spectra from central detectors in sparse observations. Spectra from off-axis emission does not share the clusters of lines centred at ∼ 800 GHz and ∼ 1288 GHz. In general, the template line list is also more successful at identifying features extracted from these spectra than for central detectors. Of features from off-axis detectors, 93.1% are successfully identified while only 77.3% of features from central detectors are successfully matched with the template. Since the majority of off-axis emission is expected to come from extended sources similar to the usual targets

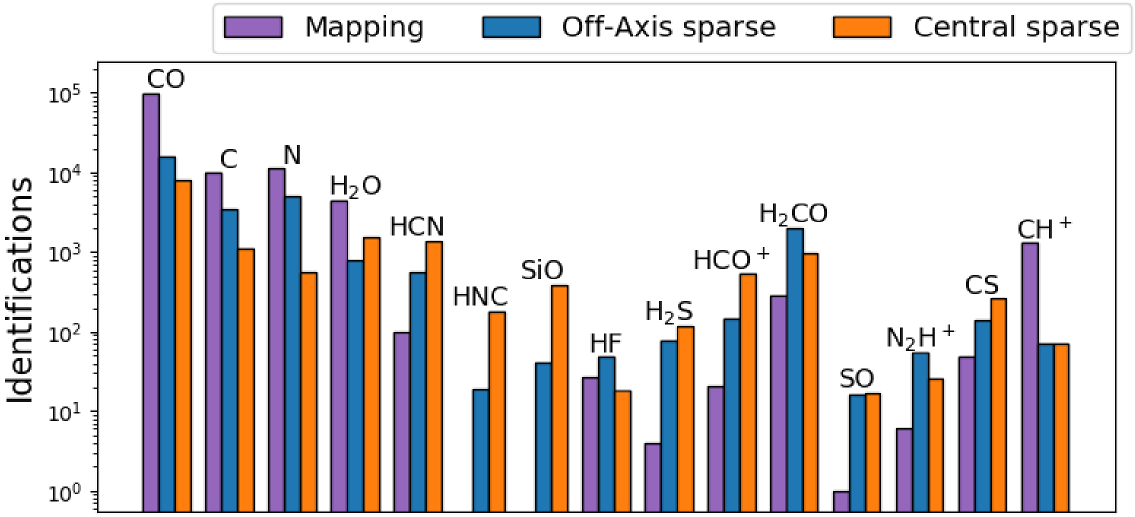

Figure 4.14: The line identification of all 15 atomic/molecular species contained in the template for mapping and sparse SPIRE observations.

of mapping observations, perhaps this is unsurprising.

The application of the line identification routine and low SNR search routine to the entirety of sparse (spectra from central and off-axis detectors) and mapping observations is presented in Appendix B. This figure shows the number of identifications for each individual spectral feature contained in the template.

4.5 Conclusions

There is a wealth of spectral data observed by the off-axis detectors that the FF is well equipped to extract and catalogue. The FF found a total of 37 869 spectral features from the off axis detectors within sparse single-pointing observations, 36.3% of these features are emission features with a SNR less than 6.5 or absorption features with absolute SNR less than 10. These features are not included in the FF catalogue in order to avoid the inclusion of spurious detections leaving 29 130 features to be ingested to the catalogue with the next public release. Postcard images were developed for each sparse observation to summarize

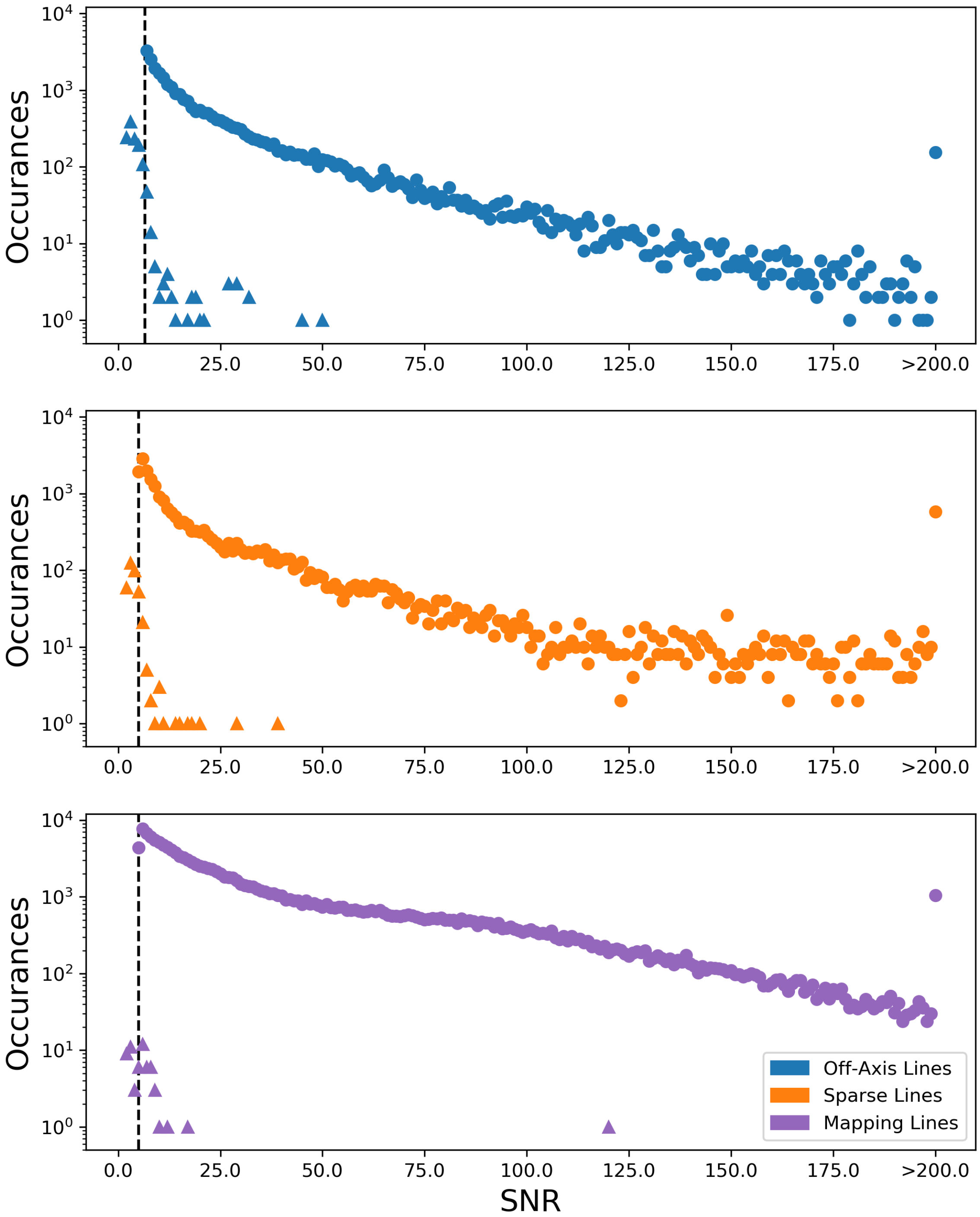

Figure 4.15: The SNR of lines extracted by the Feature Finder and the low SNR for off-axis detectors of sparse observations (top), central detectors of sparse observations (middle), and from mapping observations (bottom) are shown in blue, orange, and violet, respectively. Lines found by the FF employ round markers while those found by the low SNR search routine use triangular markers. The absolute SNR cutoff in each case is shown by the dotted black line. Axis in each case have been set to the same scale for easy comparison.

the features found by the FF and the radial velocity estimates (as shown in Figures 4.5, 4.6, 4.7, and Appendix C).

The N II fine structure line is the most commonly found feature in off-axis detectors. This chapter has shown the utility of this feature to disentangle a source from background emission (Figure 4.10) and measure the rotation of a nearby galaxy, NGC 891 (Figure 4.11). ^{12}CO features are also commonly found in off-axis detectors. Together, these features are used to provide radial velocity estimates for 3 590 off-axis spectra.

Spectra from off-axis detectors provide another test case to further compare the two radial velocity measuring routines employed by the FF [78]. Using off-axis spectra that provided a confident velocity estimate from both the ^{12}CO and cross-correlation methods I found that these two methods agree to within 20 km/s for 92.5% of these observations.

Line identification is able to successfully match 23 179 features extracted by the FF to template lines. An additional 1 757 features are found by the low SNR search routine to be included in the catalogue. These results appear to be more in line with the identification of features from mapping observations than from the central detectors of these sparse observations.

Chapter 5

Conclusions and Future Work

> If you don't know everything, you must go on with what you do know. – Rand al'Thor
>
> –Robert Jordan (A Crown of Swords, 1996)

In this thesis, I have presented my findings from identifying the energy transitions in molecules and atoms that give rise to the spectral features detected by the Spectral and Photometric Imaging Receiver (SPIRE) Fourier Transform Spectrometer (FTS) that have been extracted by the *Herschel* SPIRE FTS Spectral Feature Finder (FF) routine and the extension of this routine to the off-axis detectors in sparse single-pointing SPIRE FTS observations. In this final chapter, I will summarize these findings as well as the context provided for them in Chapters 1 and 2. I will also discuss the future of the FF and the next steps to further the investigation that I have presented.

Included in this chapter is a brief overview of future FIR space telescope missions and technologies that are in development to further the field of FIR astronomy. This discussion will be from my perspective as a researcher who has aided in the close of the previous generation's archival phase and will focus on how these projects build on what has been learned from *Herschel* and SPIRE.

5.1 Conclusion

In the initial chapter of this thesis I have introduced key areas of study in the field of FIR astronomy and some of its primary goals. A significant portion of all of the radiation incident on the Earth from extra-solar sources in the Universe occurs at IR and FIR wavelengths. FIR astronomy is perfectly suited for studying the cold and dense regions of space where stars form and allows us to study the evolution of distant galaxies. In this chapter, I also introduced the technical details involved in Fourier transform spectroscopy as a tool to study the spectral composition of light.

Throughout this thesis, we have seen that the SPIRE instrument measures the emission from important atoms and molecules for studying the processes in the ISM that make it possible for stars to form. Through the identification of CO, H_2O, C I, and N II spectral features extracted by the FF detailed in Chapter 3, the SPIRE Automated Feature Extraction Catalogue (SAFECAT) provides an excellent resource for astronomers looking to study star formation. The line identification routine provides the atomic/molecular information for over 150 000 spectral features observed by the SPIRE FTS which all can be used to study the physical processes that occur in the ISM and distant galaxies.

In the initial chapter of this thesis, we begin to see that the ability of a telescope to resolve the difference between multiple sources is much more difficult at FIR wavelengths than shorter wavelengths. Much larger telescopes for FIR observations are required to achieve the same spatial resolution available to optical telescopes (Section 1.1.3). We have seen in Chapter 4 that, while limited in its spatial resolution, SPIRE is capable of decoupling objects from surrounding emission via spectral resolution. We will also see in the following section that current research is underway exploring new methods to overcome this obstacle.

In Chapter 2, the SPIRE FTS and the FF project are discussed as well as my contributions to the project. This discussion also establishes the FF as a powerful data mining aid to accompany SPIRE FTS observations contained in the Herschel Science Archive (HSA). Chapter 3 demonstrates the successful identification of the majority of spectral features extracted by the FF. This identification is the result of matching FF extracted spectral features to a template line list containing 307 spectral features that are important to FIR astronomy and are commonly found in SPIRE FTS observations. I have also shown that the information provided by this line identification routine can be used to extract low Signal to Noise Ratio (SNR) features that are nominally not included in the FF catalogue.

In Chapter 4, we have seen that the off-axis detectors of sparsely sampled single-pointing observations of the SPIRE FTS contain a wealth of spectral information despite the majority of sources being point-like. The application of the FF to the spectra from these off-axis detectors uncovers more than 29 000 spectral features to be aggregated to SAFECAT. Of these, some 25 000 features have radial velocity estimates (i.e., ~85% of spectra) and more than 23 000 spectral features have been matched with atomic/molecular signatures.

5.2 Future Work

The findings presented in this thesis provide an important basis for both the FF and future FIR observing missions. In this section, we will discuss the next steps that will be taken to conclude the bulk of the FF project and the future direction of FIR observational instruments. This discussion of future missions includes one of the three European Space Agency (ESA) candidates for the upcoming medium-size mission (M5), the Space Infrared Telescope for Cosmology and Astrophysics (SPICA). Also discussed is the application of spatial-interferometry to FIR wavelengths.

5.2.1 Next steps for the Feature Finder

The FF catalogue is currently in its second release [7] and does not yet include the results presented in this thesis. These results are expected to be included in SAFECAT by the end of 2019. The implementation of these results will require some infrastructure work with the HSA in order to include the newly discovered features and atomic/molecular source information to SAFECAT, and the ingestion of the presented postcards to the HSA legacy archive that houses FF products. This will also involve the editing of current FF documentation to include the technical details presented in this thesis.

The contributions to the FF project detailed in this thesis provide several avenues of study to demonstrate the utility of the FF as a whole. The results of the line identification routine provide an excellent tool for comparing the chemical composition of different sources observed by the SPIRE FTS in large quantities. These results could easily be used to compare observations that are categorized as point-like, extended, or a very large-scale source (from a mapping observation) to determine expected atomic and molecular features for each case. The velocity measurements from off-axis detectors provide an excellent tool to probe for unexpected sources observed within the SPIRE FTS Field of View (FOV) which occur at different radial velocities than the observational target.

The success of the FF is wholly dependent on its use by astronomers. Currently, several papers are pending publication in the Monthly Notices of the Royal Astronomical Society to present the technical details of the FF routine and SAFECAT. In this thesis a few examples of the utility of the FF have been presented, such as determining the rotation of NGC 891 (see Figure 4.11) and the decoupling of AFGL 4106 from the surrounding galactic cirrus (see Figure 4.10), but these are far from an exhaustive analysis. There is a substantial unexplored area for thorough demonstrations of the utility that the FF provides.

5.2.2 The Space Infrared Telescope for Cosmology and Astrophysics

The Space Infrared Telescope for Cosmology and Astrophysics (SPICA) mission proposed for the upcoming M5 ESA mission is a massive step forward to improve on what *Herschel* has revealed [136, 137]. *SPICA* will be a collaborative mission between the Japan Aerospace Exploration Agency (JAXA), ESA, and NASA Jet Propulsion Laboratory (JPL) [137] with a target launch date of 2032 [138]. In our discussion of *Herschel* in Chapter 1 we did not discuss that, unlike the Infrared Astronomical Satellite (IRAS), Infrared Space Observatory (ISO), and *Spitzer* missions, the 3.5 m diameter primary mirror of the *Herschel* space observatory was not actively cooled [46]. The *Herschel* mirror was passively cooled to the operational range of 80–90 K making thermal emission from the telescope itself the most dominant source of radiation to the cryogenic instruments [139]. In all SPIRE observations the telescope emission had to be accurately modelled and removed [139].

The SPICA mission provides a massive upgrade on previous FIR missions by providing a mirror that is both large (2.6 m in diameter) and actively cooled to cryogenic temperatures (less than 8 K) [136]. The SPICA design for a large cryogenic telescope provides an improvement in spectral sensitivity more than two orders of magnitude better than that of *Herschel* while still maintaining a similar spatial resolution [126, 136].

In this thesis we have discussed the N II $^3P_1$–$^3P_0$ fine-structure line that is commonly found at high SNR in SPIRE FTS spectra. Chapter 3 has demonstrated that this feature is particularly useful for measuring the properties of the ISM and galaxies. The prominence of this feature in SPIRE FTS spectra has motivated the design of SPICA spectrometers which aim to measure this spectral line out to a redshift of $z = 3$ (see Equation 2.2) [126].

Herschel's view of the filamentary structure of the ISM has sparked research into how these structures form from the magnetic field present in the ISM and how they relate to star formation [140]. One of the main science goals of the SPICA mission is to further our understanding of how magnetic fields affect star formation in the ISM through imaging polarimetry at FIR wavelengths [126].

Building on the great advancements in our understanding of star formation and distant galaxies made by *Herschel*, SPICA will provide superbly sensitive observations of the FIR Universe while maintaining excellent spatial resolution. The SPICA mission is the next great step in the FIR astronomy legacy leading us closer to a full understanding of stellar birth and galactic evolution.

5.2.3 Far-infrared Interferometry Missions

In Chapter 1 we have seen that in order to obtain the sub-arcsecond angular resolution necessary to differentiate between newly forming planetary bodies ~ 1 AU from a stellar object even the largest conceivable mirror that can be launched into space is insufficient [26]. We have seen in Chapter 2 that even with the unprecedented 3.5 m diameter primary mirror of *Herschel*, the SPIRE FTS could only obtain a spatial resolution of 9.5 arcseconds in fully sampled mapping observations. In ground-based radio astronomy, the technique of spatial interferometry has been used to overcome this issue of angular resolution at long wavelengths [141]. In order to achieve the necessary resolution to observe planetary systems, understand the evolution of black holes in their host galaxies, and observe the formation of the first stars, a space-based FIR interferometry mission is needed [26, 142].

Spatial interferometry is a technique by which a formation of smaller-mirrored telescopes are used in place of a single large telescope. Through this technique, the angular resolution of the telescope is limited by the distance, or baseline, between multiple receivers rather than the size of the primary mirror of a single telescope [141]. The utility of this technique is best understood through an example. The massive Arecibo radio telescope has a primary reflector that is $\sim 300\,\mathrm{m}$ in diameter [143]. Using Equation 1.11, Arecibo would obtain an angular resolution of ~ 0.013 arcseconds at 345 GHz. The Atacama Large Millimeter/submillimeter Array (ALMA) (a radio interferometer) achieves a similar angular resolution at this frequency using up to fifty smaller telescopes with 12 m diameter mirrors at a baseline of $\sim 244\,\mathrm{m}$ [144].

Currently both NASA and ESA have included the implementation of FIR interferometry in their decadal plans [145, 26] and have proposed missions called the Space Infrared Interferometric Telescope (SPIRIT) [146, 147] and the Far Infrared Interferometer (FIRI) [26]. These proposals are in their early phases and a great deal of ground-based proof of concept testing is underway [142, 148]. A space-based FIR spatial interferometer mission can provide a significantly greater spatial resolution than the largest *Herschel*-like telescope. This increase in spatial resolution is necessary to answer some of the key questions facing FIR astronomy concerning the formation of stellar systems and galaxy evolution.

5.3 Final Remarks

The contributions to *Herschel*–SPIRE via the FF and SAFECAT detailed in this thesis provide easier access to a wealth of publicly available data comprised of spectroscopic observations in the FIR within the Herschel Science Archive (HSA). This work provides an important bridge to the next generation of FIR instruments. These contributions to the *Herschel* SPIRE FTS Spectral Feature Finder (FF) provide an important data mining aid as we seek to learn all that we can from the *Herschel*–SPIRE instrument.

References

[1] Dale A Ostlie and Bradley W Carroll. *An introduction to modern stellar astrophysics*. Addison-Wesley USA, 1996.

[2] D. A. Gurnett, W. S. Kurth, E. C. Stone, A. C. Cummings, S. M. Krimigis, R. B. Decker, N. F. Ness, and L. F. Burlaga. The Systematic Increase of the Electron Density and Other Related Effects as Voyager 1 Moves Outward into the Interstellar Space. *AGU Fall Meeting Abstracts*, December 2018.

[3] Alex Abramovici, William E Althouse, Ronald WP Drever, Yekta Gürsel, Seiji Kawamura, Frederick J Raab, David Shoemaker, Lisa Sievers, Robert E Spero, Kip S Thorne, et al. Ligo: The laser interferometer gravitational-wave observatory. *science*, 256(5055):325–333, 1992.

[4] Abd al-Rahman al Sufi. *Kitab suwar al-kawakib (Book of the constellations of the fixed stars)*. 964.

[5] David H Clark and F Richard Stephenson. *The historical supernovae*. Elsevier, 2016.

[6-9] Floyd P. Shine On You Crazy Diamond.

[6] Ivan Valtchanov. *The Spectral and Photometric Imaging Receiver Handbook*. Herschel Science Centre, European Space Astronomy Centre, European Space Agency, 2.5 edition, 3 2014. The author is also document editor and custodian.

[7] Rosalind Hopwood, Ivan Valtchanov, Locke D Spencer, Jeremy Scott, Chris S Benson, N Marchili, N Hładczuk, E T Polehamption, N Lu, G Makiwa, D A Naylor, G Noble, and M J Griffin. The *Herschel* SPIRE Fourier transform spectrometer spectral feature finder and the spectral feature catalogue. *Monthly notices of the Royal Astronomical Society*, 2019. in prep.

[8] Andrew W Blain, Ian Smail, RJ Ivison, J-P Kneib, and David T Frayer. Submillimeter galaxies. *Physics Reports*, 369(2):111–176, 2002.

[9] Frank J. Low. Low-temperature germanium bolometer. *J. Opt. Soc. Am.*, 51(11):1300–1304, Nov 1961.

[10] Harold L Johnson. Astronomical measurements in the infrared. *Annual Review of Astronomy and Astrophysics*, 4(1):193–206, 1966.

[11] Frank J Low and Harold L Johnson. Stellar photometry at 10 mu. *The Astrophysical Journal*, 139:1130, 1964.

[12] Frank J Low, George H Rieke, and Robert D Gehrz. The beginning of modern infrared astronomy. *Annu. Rev. Astron. Astrophys.*, 45:43–75, 2007.

[13] Robert C Kennicutt Jr and Neal J Evans. Star formation in the Milky Way and nearby galaxies. *Annual Review of Astronomy and Astrophysics*, 50:531–608, 2012.

[14] John Edward Dyson and David Arnold Williams. *The physics of the interstellar medium*. CRC Press, 1997.

[15] Rudolf Clausius. XVI. on a mechanical theorem applicable to heat. *The London, Edinburgh, and Dublin Philosophical Magazine and Journal of Science*, 40(265):122–127, 1870.

[16] L Mestel and L Spitzer Jr. Star formation in magnetic dust clouds. *Monthly Notices of the Royal Astronomical Society*, 116(5):503–514, 1956.

[17] Telemachos Ch Mouschovias. Magnetic braking, ambipolar diffusion, cloud cores, and star formation-natural length scales and protostellar masses. *The Astrophysical Journal*, 373:169–186, 1991.

[18] Richard B Larson. Turbulence and star formation in molecular clouds. *Monthly Notices of the Royal Astronomical Society*, 194(4):809–826, 1981.

[19] James Hopwood Jeans. I. the stability of a spherical nebula. *Philosophical Transactions of the Royal Society of London. Series A, Containing Papers of a Mathematical or Physical Character*, 199(312-320):1–53, 1902.

[20] Nicholas A Devereux and Judith S Young. The rate and efficiency of high-mass star formation along the hubble sequence. *The Astrophysical Journal*, 371:515–524, 1991.

[21] Marc Sauvage and Trinh X Thuan. On the use of far-infrared luminosity as a star formation indicator in galaxies. *The Astrophysical Journal*, 396:L69–L73, 1992.

[22] Gibion Makiwa. *Physics of the interstellar medium using Herschel/SPIRE*. PhD thesis, University of Lethbridge, 2014.

[23] Edwin Powell Hubble. A relation between distance and radial velocity among extra-galactic nebulae. *Proceedings of the national academy of sciences*, 15(3):168–173, 1929.

[24] Edwin Powell Hubble. *The observational approach to cosmology*. Clarendon Press Oxford, 1937.

[25] Igor D Karachentsev, Valentina E Karachentseva, Walter K Huchtmeier, and Dmitry I Makarov. A catalog of neighboring galaxies. *The Astronomical Journal*, 127(4):2031, 2004.

[26] Frank P Helmich and RJ Ivison. FIRI–a far-infrared interferometer. *Experimental Astronomy*, 23(1):245–276, 2009.

[27] B T Soifer and Judith L Pipher. Instrumentation for infrared astronomy. *Annual Review of Astronomy and Astrophysics*, 16(1):335–369, 1978.

[28] Lord Rayleigh. XXXI. investigations in optics, with special reference to the spectroscope. *The London, Edinburgh, and Dublin Philosophical Magazine and Journal of Science*, 8(49):261–274, 1879.

[29] Gisela N Ortiz-León, Sergio A Dzib, Marina A Kounkel, Laurent Loinard, Amy J Mioduszewski, Luis F Rodríguez, Rosa M Torres, Gerardo Pech, Juana L Rivera, Lee Hartmann, et al. The gould's belt distances survey (GOBELINS). III. the distance to the Serpens/Aquila molecular complex. *The Astrophysical Journal*, 834(2):143, 2017.

[30] F M Olnon, E Raimond, G Neugebauer, R J van Duinen, H J Habing, H H Aumann, D A Beintema, N Boggess, J Borgman, P E Clegg, et al. IRAS catalogues and atlases-atlas of low-resolution spectra. *Astronomy and Astrophysics Supplement Series*, 65:607–1065, 1986.

[31] C A Beichman, G Neugebauer, Chester T J, F C Gillet, P Clegg, D Langford, A Pouw, W Irace, and Houck J. Infrared astronomical satellite explanatory supplement. Prepared under the auspices of The Joint IRAS Science Working Group, 1988.

[32] J A Bamberg and N H Zaun. Design and performance of the cryogenic focal plane optics assembly for the infrared astronomical satellite (IRAS). In *Cryogenic Optical Systems and Instruments I*, volume 509, pages 94–102. International Society for Optics and Photonics, 1985.

[33] H H Aumann, F C Gillett, C A Beichman, T De Jong, J R Houck, F J Low, Gerry Neugebauer, Russell G Walker, and Paul R Wesselius. Discovery of a shell around Alpha Lyrae. *The Astrophysical Journal*, 278:L23–L27, 1984.

[34] C A Beichman, R E Jennings, J P Emerson, B Baud, S Harris, Michael Rowan-Robinson, H H Aumann, T N Gautier, F C Gillett, H J Habing, et al. The formation of solar type stars-IRAS observations of the dark cloud Barnard 5. *Astrophysical Journal*, 278:L45, 1984.

[35] C A Beichman. The infrared universe revealed by IRAS. *Astrophysical Letters and Communications*, 27:67–88, 1988.

[36] M F Kessler, J A Steinz, M E Anderegg, J Clavel, G Drechsel, P Estaria, J Faelker, J R Riedinger, A Robson, B G Taylor, et al. The infrared space observatory (ISO) mission. *Astronomy and Astrophysics*, 315:L27–L31, 1996.

[37] Catherine Cesarsky and Alberto Salama. *ISO Science Legacy: A Compact Review of ISO Major Achievements*, volume 119. Springer Science & Business Media, 2006.

[38] Michael W Werner, T L Roellig, F J Low, George H Rieke, M Rieke, W F Hoffmann, E Young, J R Houck, B Brandl, G G Fazio, et al. The *Spitzer* space telescope mission. *The Astrophysical Journal Supplement Series*, 154(1):1, 2004.

[39] Spitzer Science Center. *Spitzer Space Telescope Observer's Manual*. California Institute of Technology, 8.0 edition, 8 2007.

[40] William A Mahoney, Lisa J Garcia, Joseph Hunt Jr, Douglas B McElroy, Vince G Mannings, David S Mittman, JoAnn C O'Linger, Marc Sarrel, and Elena Scire. *Spitzer* warm mission transition and operations. In *Observatory Operations: Strategies, Processes, and Systems III*, volume 7737, page 77371W. International Society for Optics and Photonics, 2010.

[41] Ed Churchwell, Brian L Babler, Marilyn R Meade, Barbara A Whitney, Robert Benjamin, Remy Indebetouw, Claudia Cyganowski, Thomas P Robitaille, Matthew Povich, Christer Watson, et al. The *Spitzer*/GLIMPSE surveys: a new view of the milky way. *Publications of the Astronomical Society of the Pacific*, 121(877):213, 2009.

[42] Emmanuel Sein, Yves Toulemont, Frederic Safa, Michel Duran, Pierre Deny, Daniel de Chambure, Thomas Passvogel, and Goeran L Pilbratt. A 3.5 m diameter SiC telescope for *Herschel* mission. In *IR Space Telescopes and Instruments*, volume 4850, pages 606–618. International Society for Optics and Photonics, 2003.

[43] Micha Schmidt and Frank Keck. The end of life operations of the *Herschel* space telescope. In *SpaceOps 2014 Conference*, page 1935, 2014.

[44] Dominic Doyle, Göran Pilbratt, and Jan Tauber. The *Herschel* and *Planck* space telescopes. *Proceedings of the IEEE*, 97(8):1403–1411, 2009.

[45] Göran L Pilbratt. *Herschel* mission overview and key programmes. In *Space Telescopes and Instrumentation 2008: Optical, Infrared, and Millimeter*, volume 7010, page 701002. International Society for Optics and Photonics, 2008.

[46] G L Pilbratt, J R Riedinger, T Passvogel, G Crone, D Doyle, U Gageur, A M Heras, C Jewell, L Metcalfe, S Ott, et al. Herschel Space Observatory–an ESA facility for far-infrared and submillimetre astronomy. *Astronomy & Astrophysics*, 518:L1, 2010.

[47] Sergio Molinari, B Swinyard, John Bally, Mike Barlow, J P Bernard, P Martin, T Moore, Alberto Noriega-Crespo, René Plume, Leonardo Testi, et al. Clouds, filaments, and protostars: the *Herschel* Hi-GAL Milky Way. *Astronomy & Astrophysics*, 518:L100, 2010.

[48] E F Van Dishoeck, L E Kristensen, A O Benz, E A Bergin, P Caselli, J Cernicharo, Fabrice Herpin, M R Hogerheijde, D Johnstone, René Liseau, et al. Water in star-forming regions with the *Herschel* Space Observatory (WISH). I. overview of key program and first results. *Publications of the Astronomical Society of the Pacific*, 123(900):138, 2011.

[49] H S Hwang, D Elbaz, G Magdis, E Daddi, M Symeonidis, B Altieri, A Amblard, P Andreani, V Arumugam, R Auld, et al. Evolution of dust temperature of galaxies through cosmic time as seen by *Herschel*. *Monthly Notices of the Royal Astronomical Society*, 409(1):75–82, 2010.

[50] Jean Baptiste Joseph baron Fourier. *Théorie analytique de la chaleur*. F. Didot, 1822. Title translation: The Analytical Theory of Heat.

[51] John Herivel. *Joseph Fourier: the man and the physicist*. Clarendon Press, 1975.

[52] Kenneth Franklin Riley, Michael Paul Hobson, and Stephen John Bence. *Mathematical methods for physics and engineering: a comprehensive guide*. Cambridge university press, 2006.

[53] Peter Gustav Lejeune Dirichlet and Philipp Ludwig Seidel. *Die Darstellung ganz willkürlicher Functionen durch Sinus-und Cosinusreihen: von Lejeune Dirichlet (1837), und Note über eine Eigenschaft der Reihen, welche discontinuirliche Functionen darstellen, von Philipp Ludwig Seidel (1847)*, volume 116. W. Engelmann, 1900.

[54] Rao B Visvesvara et al. *Signals and systems*. PHI Learning Pvt. Ltd., 2008.

[55] Locke Dean Spencer. *Imaging Fourier Transform Spectroscopy from a Space Based Platform–The Herschel/SPIRE Fourier Transform Spectrometer*. PhD thesis, University of Lethbridge, 2009.

[56] Albert A Michelson and Edward W Morley. On the relative motion of the earth and of the luminiferous ether. *Sidereal Messenger, vol. 6, pp. 306-310*, 6:306–310, 1887.

[57] Sumner P Davis, Mark C Abrams, and James W Brault. *Fourier transform spectrometry*. Elsevier, 2001.

[58] E. Hecht. *Optics*. Pearson education. Addison-Wesley, 2002.

[59] F Grandmont, L Drissen, Julie Mandar, S Thibault, and Marc Baril. Final design of SITELLE: a wide-field imaging Fourier transform spectrometer for the Canada-France-Hawaii Telescope. In *Ground-Based and Airborne Instrumentation for Astronomy IV*, volume 8446, page 84460U. International Society for Optics and Photonics, 2012.

[60] David Naylor, Gibion Makiwa, Ian Veenendaal, Jeremy Scott, and Locke Spencer. Line asymmetry in *Herschel* SPIRE FTS spectra. In *Fourier Transform Spectroscopy*, pages FM2D–2. Optical Society of America, 2016.

[61] David A Naylor and Margaret K Tahic. Apodizing functions for Fourier transform spectroscopy. *JOSA A*, 24(11):3644–3648, 2007.

[62] Harry Nyquist. Certain topics in telegraph transmission theory. *Transactions of the American Institute of Electrical Engineers*, 47(2):617–644, 1928.

[63] Claude Elwood Shannon. Communication in the presence of noise. *Proceedings of the IEEE*, 86(2):447–457, 1998.

[64] James W Cooley and John W Tukey. An algorithm for the machine calculation of complex Fourier series. *Mathematics of computation*, 19(90):297–301, 1965.

[65] N Aghanim, Y Akrami, M Ashdown, J Aumont, C Baccigalupi, M Ballardini, AJ Banday, RB Barreiro, N Bartolo, S Basak, et al. Planck 2018 results. iii. high frequency instrument data processing and frequency maps. *arXiv preprint arXiv:1807.06207*, 2018.

[66] Peter A R Ade, N Aghanim, M I R Alves, C Armitage-Caplan, M Arnaud, M Ashdown, F Atrio-Barandela, J Aumont, Carlo Baccigalupi, A J Banday, et al. *Planck* 2013 results. XIII. Galactic CO emission. *Astronomy & Astrophysics*, 571:A13, 2014.

[67] Jeremy Scott. Estimating radial velocity and improving line identification within the *Herschel* SPIRE automated spectral feature catalogue. Master's thesis, University of Lethbridge, 2015.

[68] Matthew Joseph Griffin, A Abergel, As Abreu, Peter AR Ade, P André, J-L Augueres, T Babbedge, Y Bae, T Baillie, J-P Baluteau, et al. The *Herschel*–SPIRE instrument and its in-flight performance. *Astronomy & Astrophysics*, 518:L3, 2010.

[69] L Mach. Ueber einen interferenzrefraktor. *Zeitschrift für Instrumentenkunde*, 12:89–93, 1892. Title translation: About an interference refractor.

[70] Peter Hargrave, Tim Waskett, Tanya Lim, and Bruce Swinyard. Performance of flight-model on-board calibration sources on *Herschel*–SPIRE. In *Millimeter and Submillimeter Detectors and Instrumentation for Astronomy III*, volume 6275, page 627514. International Society for Optics and Photonics, 2006.

[71] Bruce Miles Swinyard, Peter A R Ade, Matthew J Griffin, Kjetil Dohlen, Jean-Paul Baluteau, Dominque Pouliquen, Diddier Ferand, Pascal Dargent, Guy Michel, Jerome Martignac, et al. FIRST-SPIRE spectrometer: a novel imaging FTS for the submillimeter. In *UV, optical, and IR space telescopes and instruments*, volume 4013, pages 196–207. International Society for Optics and Photonics, 2000.

[72] Peter A R Ade, Peter A Hamilton, and David A Naylor. An absolute dual beam emission spectrometer. In *Fourier Transform Spectroscopy*, page FWE3. Optical Society of America, 1999.

[73] Bruce Swinyard, Matt Griffin, Peter Ade, Kjetil Dohlen, Dominique Pouliquen, Dider Ferrand, Pascal Dargen, Jean-Paul Baluteau, Guy Michel, Jerome Martignac, et al. The imaging Mach-Zehnder FTS for the FIRST SPIRE instrument. In *Fourier Transform Spectroscopy*, page FTuB1. Optical Society of America, 2001.

[74] B. M. Swinyard, E. T. Polehampton, R Hopwood, I Valtchanov, N Lu, T Fulton, D Benielli, P Imhof, N Marchili, J-P Baluteau, et al. Calibration of the *Herschel* SPIRE Fourier transform spectrometer. *Monthly Notices of the Royal Astronomical Society*, 440(4):3658–3674, 2014.

[75] Gibion Makiwa, David A Naylor, Marc Ferlet, Carl Salji, Bruce Swinyard, Edward Polehampton, and Matthijs H. D. van der Wiel. Beam profile for the *Herschel*–SPIRE fourier transform spectrometer. *Applied Optics*, 52(16):3864–3875, 2013.

[76] Ronin Wu, Edward T Polehampton, Mireya Etxaluze, Gibion Makiwa, David A Naylor, Carl Salji, Bruce M Swinyard, Marc Ferlet, Matthijs H. D. van der Wiel, Anthony J Smith, et al. Observing extended sources with the *Herschel* SPIRE Fourier transform spectrometer. *Astronomy & Astrophysics*, 556:A116, 2013.

[77] Stephan Ott, Herschel Science Centre, and European Space Agency. The *Herschel* data processing system–HIPE and pipelines-up and running since the start of the mission. *arXiv preprint arXiv:1011.1209*, 2010.

[78] Jeremy Scott, Rosalind Hopwood, Ivan Valtchanov, Locke D Spencer, Chris S Benson, N Marchili, N Hładczuk, E T Polehamption, N Lu, G Makiwa, D A Naylor, G Noble, and M J Griffin. Estimating radial velocity within the SPIRE FTS spectral feature finder. *Monthly notices of the Royal Astronomical Society*, 2019. in prep.

[79] Thomas P Robitaille, Erik J Tollerud, Perry Greenfield, Michael Droettboom, Erik Bray, Tom Aldcroft, Matt Davis, Adam Ginsburg, Adrian M Price-Whelan, Wolfgang E Kerzendorf, et al. Astropy: A community Python package for astronomy. *Astronomy & Astrophysics*, 558:A33, 2013.

[80] Chris S Benson, Locke D Spencer, Jeremy P Scott, Rosalind Hopwood, and Ivan Valtchanov. On-sky validation of the *herschel*/spire automated feature finder using source radial velocity estimates. In *Optical Nanostructures and Advanced Materials for Photovoltaics*, pages JW4A–20. Optical Society of America, 2016.

[81] Derek Wilson, Asantha Cooray, Hooshang Nayyeri, Matteo Bonato, Charles M Bradford, David L Clements, Gianfranco De Zotti, Tanio Díaz-Santos, Duncan Farrah, Georgios Magdis, et al. Stacked average far-infrared spectrum of dusty star-forming galaxies from the Herschel/SPIRE Fourier transform spectrometer. *The Astrophysical Journal*, 848(1):30, 2017.

[82] C Thum, J Martin-Pintado, A Quirrenbach, and H E Matthews. Infrared lasers in the circumstellar disk of MWC 349. *Astronomy and Astrophysics*, 333:L63–L66, 1998.

[83] Jesús Martín-Pintado. Recombination line masers in YSOs. In *Symposium-International Astronomical Union*, volume 206, pages 226–233. Cambridge University Press, 2002.

[84] Trevor R Fulton, Jean-Paul Baluteau, George Bendo, Dominique Benielli, Rene Gastaud, Matt Griffin, Steve Guest, Peter Imhof, Tanya L Lim, Nanyao Lu, et al. The

data processing pipelines for the *Herschel*/SPIRE imaging Fourier transform spectrometer. In *Space Telescopes and Instrumentation 2010: Optical, Infrared, and Millimeter Wave*, volume 7731, page 773134. International Society for Optics and Photonics, 2010.

[85] R Hopwood, E.T. Polehampton, I Valtchanov, B.M. Swinyard, T Fulton, N Lu, N Marchili, M.H.D. van der Wiel, D Benielli, P Imhof, et al. Systematic characterization of the *Herschel* SPIRE Fourier transform spectrometer. *Monthly Notices of the Royal Astronomical Society*, 449(3):2274–2303, 2015.

[86] Ivan Valtchanov, Rosalind Hopwood, Edward Polehampton, Dominique Benielli, Trevor Fulton, Peter Imhof, Tomasz Konopczyński, Tanya Lim, Nanyao Lu, Nicola Marchili, et al. Relative pointing offset analysis of calibration targets with repeated observations with *Herschel*–SPIRE fourier-transform spectrometer. *Experimental Astronomy*, 37(2):207–223, 2014.

[87] Donald W Marquardt. An algorithm for least-squares estimation of nonlinear parameters. *Journal of the society for Industrial and Applied Mathematics*, 11(2):431–441, 1963.

[88] Jeremy Scott, Locke D Spencer, Rosalind Hopwood, Ivan Valtchanov, D A Naylor, T R Fulton, and E T Polehamption. Neutral carbon detection in the SPIRE FTS spectral feature finderr. *Monthly notices of the Royal Astronomical Society*, 2019. in prep.

[89] Marc Wenger, François Ochsenbein, Daniel Egret, Pascal Dubois, François Bonnarel, Suzanne Borde, Françoise Genova, Gérard Jasniewicz, Suzanne Laloë, Soizick Lesteven, et al. The SIMBAD astronomical database–the cds reference database for astronomical objects. *Astronomy and Astrophysics Supplement Series*, 143(1):9–22, 2000.

[90] George Helou, BF Madore, M Schmitz, MD Bicay, X Wu, and J Bennett. The NASA/IPAC extragalactic database. In *Databases & On-Line Data in Astronomy*, pages 89–106. Springer, 1991.

[91] E Caux, S Bottinelli, C Vastel, and JM Glorian. CASSIS, a software package to analyse high spectral resolution observations. In *The Molecular Universe*, volume 280, 2011.

[92] A Kramida, Yu Ralchenko, J Reader, and NIST ASD Team. NIST atomic spectra database (version 5.6.1). National Institute of Standards and Technology, Gaithersburg, https://physics.nist.gov/asd, 2018.

[93] Frank J Lovas. NIST recommended rest frequencies for observed interstellar molecular microwave transitions–2002 revision. *Journal of Physical and Chemical Reference Data*, 33(1):177–355, 2004.

[94] Christian P Endres, Stephan Schlemmer, Peter Schilke, Jürgen Stutzki, and Holger SP Müller. The cologne database for molecular spectroscopy, CDMS, in the virtual atomic and molecular data centre, VAMDC. *Journal of Molecular Spectroscopy*, 327:95–104, 2016.

[95] H M Pickett, R L Poynter, E A Cohen, M L Delitsky, J C Pearson, and H S P Müller. Submillimeter, millimeter, and microwave spectral line catalog. *Journal of Quantitative Spectroscopy and Radiative Transfer*, 60(5):883–890, 1998.

[96] Anthony J Remijan, A Markwick-Kemper, et al. Splatalogue: Database for astronomical spectroscopy. In *Bulletin of the American Astronomical Society*, volume 39, page 963, 2007.

[97] J Michael Hollas. *Modern spectroscopy*. John Wiley & Sons, 2004.

[98] Jonathan Tennyson. *Astronomical spectroscopy: an introduction to the atomic and molecular physics of astronomical spectra*, volume 2. World Scientific, 2010.

[99] Paul F Goldsmith and William D Langer. Population diagram analysis of molecular line emission. *The Astrophysical Journal*, 517(1):209, 1999.

[100] Timothy A Davis. Systematic variation of the 12CO/13CO ratio as a function of star formation rate surface density. *Monthly Notices of the Royal Astronomical Society*, 445(3):2378–2384, 2014.

[101] Miwa Goto, Tomonori Usuda, Naruhisa Takato, Masa Hayashi, Seiichi Sakamoto, W Gaessler, Yutaka Hayano, Masanori Iye, Yukiko Kamata, Tomio Kanzawa, et al. Carbon isotope ratio in 12CO/13CO toward local molecular clouds with near-infrared high-resolution spectroscopy of vibrational transition bands. *The Astrophysical Journal*, 598(2):1038, 2003.

[102] E González-Alfonso, J Fischer, K Isaak, A Rykala, G Savini, M Spaans, P van der Werf, R Meijerink, FP Israel, AF Loenen, et al. *Herschel* observations of water vapour in Markarian 231. *Astronomy & Astrophysics*, 518:L43, 2010.

[103] José Cernicharo and Jacques Crovisier. Water in space: the water world of ISO. In *ISO Science Legacy*, pages 29–69. Springer, 2005.

[104] B deB Darwent. Bond dissociation energies in simple molecules. Technical report, National Standard Reference Data System, 1970.

[105] William M Haynes. *CRC handbook of chemistry and physics*. CRC press, 84 edition, 2003.

[106] Ryen Carl Lapham and Lisa M Young. SPIRE spectroscopy of early-type galaxies. *The Astrophysical Journal*, 875(1):3, 2019.

[107] Kevin Volk and Sun Kwok. A self-consistent photoionization-dust continuum-molecular line transfer model of NGC 7027. *The Astrophysical Journal*, 477(2):722, 1997.

[108] Zhen-Yuan Huang, Tatsuhiko I Hasegawa, Sun Kwok, Sebastien Muller, Naomi Hirano, Jeremy Lim, C Muthu Mariappan, Aran Lyo, et al. Detection of multiple bipolar flows in NGC 7027 with submillimeter array. *The Astrophysical Journal*, 722(1):273, 2010.

[109] F Herpin, Javier R Goicoechea, J R Pardo, and José Cernicharo. Chemical evolution of the circumstellar envelopes of carbon-rich post-asymptotic giant branch objects. *The Astrophysical Journal*, 577(2):961, 2002.

[110] F J Molster, L B F M Waters, N R Trams, Hans Van Winckel, Leen Decin, J Th Van Loon, C Jager, Th Henning, H-U Kaufl, A De Koter, et al. The composition and nature of the dust shell surrounding the binary AFGL 4106. *arXiv preprint astro-ph/9908065*, 1999.

[111] Jacco Th van Loon, FJ Molster, Hans Van Winckel, and LBFM Waters. The circumstellar envelope of AFGL 4106. *arXiv preprint astro-ph/9907183*, 1999.

[112] S Kwok and RC Bignell. Radio structure of the proto-planetary nebula GL 618. *The Astrophysical Journal*, 276:544–550, 1984.

[113] C Sánchez Contreras, V Bujarrabal, A Castro-Carrizo, J Alcolea, and A Sargent. 1” resolution mapping of the molecular envelope of the protoplanetary nebula CRL 618. *The Astrophysical Journal*, 617(2):1142, 2004.

[114] Patricia A Whitelock. Asymptotic giant branch variables in the galaxy and the local group. *Astrophysics and Space Science*, 341(1):123–129, 2012.

[115] Elvire De Beck, Robin Lombaert, M Agúndez, F Daniel, Leen Decin, J Cernicharo, HSP Müller, M Min, Pierre Royer, Bart Vandenbussche, et al. On the physical structure of IRC+ 10216-ground-based and herschel observations of CO and C2H. *Astronomy & Astrophysics*, 539:A108, 2012.

[116] Jeremy Lim et al. Molecular shells in IRC+ 10216: Evidence for nonisotropic and episodic mass-loss enhancement. *The Astrophysical Journal*, 678(1):303, 2008.

[117] Leen Decin, J Cernicharo, M J Barlow, Pierre Royer, Bart Vandenbussche, R Wesson, E T Polehampton, Elvire De Beck, M Agúndez, JADL Blommaert, et al. Silicon in the dust formation zone of IRC+ 10216. *Astronomy & Astrophysics*, 518:L143, 2010.

[118] J Cernicharo, Leen Decin, MJ Barlow, M Agúndez, Pierre Royer, Bart Vandenbussche, R Wesson, ET Polehampton, Elvire De Beck, JADL Blommaert, et al. Detection of anhydrous hydrochloric acid, HCl, in IRC+ 10216 with the *Herschel* SPIRE and PACS spectrometers-detection of HCl in IRC+ 10216. *Astronomy & Astrophysics*, 518:L136, 2010.

[119] Yoon Kyung Choi, Tomoya Hirota, Mareki Honma, Hideyuki Kobayashi, Takeshi Bushimata, Hiroshi Imai, Kenzaburo Iwadate, Takaaki Jike, Seiji Kameno, Osamu Kameya, et al. Distance to VY Canis Majoris with VERA. *Publications of the Astronomical Society of Japan*, 60(5):1007–1012, 2008.

[120] Mikako Matsuura, J A Yates, M J Barlow, B M Swinyard, Pierre Royer, J Cernicharo, Leen Decin, R Wesson, E T Polehampton, J A D L Blommaert, et al. *Herschel* SPIRE and PACS observations of the red supergiant VY CMa: analysis of the molecular line spectra. *Monthly Notices of the Royal Astronomical Society*, 437(1):532–546, 2013.

[121] Dinesh Shenoy, Roberta M Humphreys, Terry J Jones, Massimo Marengo, Robert D Gehrz, L Andrew Helton, William F Hoffmann, Andrew J Skemer, and Philip M Hinz. Searching for cool dust in the mid-to-far infrared: The mass-loss histories of the hypergiants μ Cep, VY CMa, IRC+ 10420, and ρ Cas. *The Astronomical Journal*, 151(3):51, 2016.

[122] F Herpin, Javier R Goicoechea, J R Pardo, and José Cernicharo. Chemical evolution of the circumstellar envelopes of carbon-rich post-asymptotic giant branch objects. *The Astrophysical Journal*, 577(2):961, 2002.

[123] Locke D Spencer, David A Naylor, Gibion Makiwa, Trevor R Fulton, Edward T Polehampton, Ivan Valtchanov, Rosalind Hopwood, Matthijs van der Wiel, Jeremy Scott, Courteney Hamilton, et al. Frequency scale calibration of the *Herschel*/SPIRE imaging Fourier transform spectrometer. In *Fourier Transform Spectroscopy*, pages JM3A–8. Optical Society of America, 2015.

[124] M J Barlow, B M Swinyard, P J Owen, J Cernicharo, Haley Louise Gomez, RJ Ivison, O Krause, T L Lim, Mikako Matsuura, S Miller, et al. Detection of a noble gas molecular ion, 36ArH+, in the crab nebula. *Science*, 342(6164):1343–1345, 2013.

[125] Chris Pearson, Tanya Lim, Chris North, George Bendo, Luca Conversi, Darren Dowell, Matt Griffin, Terry Jin, Nicolas Laporte, Andreas Papageorgiou, et al. SPIRE point source photometry: within the *Herschel* interactive processing environment (HIPE). *Experimental Astronomy*, 37(2):175–194, 2014.

[126] Roelfsema and the *SPICA* consortium. *SPICA* M5 proposal. ESA call for medium-size mission proposals, 2017. A technical document describing the proposed *SPICA* mission. Has been selected as one of the final three candidates.

[127] P Santini, R Maiolino, B Magnelli, L Silva, A Grazian, B Altieri, P Andreani, H Aussel, S Berta, A Bongiovanni, et al. The dust content of high-z submillimeter galaxies revealed by *Herschel*. *Astronomy & Astrophysics*, 518:L154, 2010.

[128] Cristina C Popescu, Richard J Tuffs, Nikolaos D Kylafis, and Barry F Madore. Far infrared mapping of NGC 891. *Astronomy & Astrophysics*, 414(1):45–52, 2004.

[129] T M Hughes, K Foyle, M R P Schirm, T J Parkin, Ilse De Looze, C D Wilson, G J Bendo, Maarten Baes, Jacopo Fritz, A Boselli, et al. Insights into gas heating and cooling in the disc of NGC 891 from *Herschel* far-infrared spectroscopy. *Astronomy & Astrophysics*, 575:A17, 2015.

[130] R-J Dettmar. The distribution of the diffuse ionized interstellar medium perpendicular to the disk of the edge-on galaxy NGC 891. *Astronomy and Astrophysics*, 232:L15–L18, 1990.

[131] Daizhong Liu, Yu Gao, Kate Isaak, Emanuele Daddi, Chentao Yang, Nanyao Lu, and Paul van der Werf. High-J CO versus far-infrared relations in normal and starburst galaxies. *The Astrophysical Journal Letters*, 810(2):L14, 2015.

[132] Gérard de Vaucouleurs, Antoinette de Vaucouleurs, G Harold Jr, Ronald J Buta, Georges Paturel, Pascal Fouqué, et al. *Third reference catalogue of bright galaxies*, volume 3. Springer Science & Business Media, 2013.

[133] Jean W Keppel, Ralf-Juergen Dettmar, John S Gallagher III, and Morton S Roberts. Extraplanar ionized gas and kinematics in the edge-on galaxy NGC 891. *The Astrophysical Journal*, 374:507–515, 1991.

[134] R Sancisi and R J Allen. Neutral hydrogen observations of the edge-on disk galaxy NGC 891. *Astronomy and Astrophysics*, 74:73–84, 1979.

[135] R A Swaters, R Sancisi, and JM Van Der Hulst. The HI halo of NGC 891. *The Astrophysical Journal*, 491(1):140, 1997.

[136] Bruce Swinyard and Takao Nakagawa. The space infrared telescope for cosmology and astrophysics: SPICA a joint mission between JAXA and ESA. *Experimental Astronomy*, 23(1):193, 2009.

[137] Takao Nakagawa, Hideo Matsuhara, and Yasuhiro Kawakatsu. The next-generation infrared space telescope SPICA. In *Space Telescopes and Instrumentation 2012: Optical, Infrared, and Millimeter Wave*, volume 8442, page 84420O. International Society for Optics and Photonics, 2012.

[138] David Rodgers, Fabrice Cipriani, and Denis Payan. Overview of spacecraft charging activities europe-wide. 2018.

[139] Rosalind Hopwood, Trevor Fulton, Edward T Polehampton, Ivan Valtchanov, Dominique Benielli, Peter Imhof, Tanya Lim, Nanyao Lu, Nicola Marchili, Chris P Pearson, et al. *Herschel* SPIRE FTS telescope model correction. *Experimental Astronomy*, 37(2):195–205, 2014.

[140] Sergio Molinari, B Swinyard, John Bally, Mike Barlow, J-P Bernard, P Martin, T Moore, Alberto Noriega-Crespo, René Plume, Leonardo Testi, et al. Clouds, filaments, and protostars: the *Herschel* Hi-GAL Milky Way. *Astronomy & Astrophysics*, 518:L100, 2010.

[141] Anthony Richard Thompson, James M Moran, George Warner Swenson, et al. *Interferometry and synthesis in radio astronomy*. Wiley New York et al., 1986.

[142] William F Grainger, Roser Juanola-Parramon, Peter AR Ade, Matt Griffin, Flo Liggins, Enzo Pascale, Giorgio Savini, and Bruce Swinyard. Demonstration of spectral and spatial interferometry at THz frequencies. *Applied optics*, 51(12):2202–2211, 2012.

[143] Marshall H Cohen. Genesis of the 1000-foot Arecibo dish. *Journal of Astronomical History and Heritage*, 12(2):141–152, 2009.

[144] A Remijan, A Biggs, P A Cortes, B Dent, J Di Francesco, E Fomalont, A Hales, S Kameno, B Mason, N Philips, K Saini, F Stoehr, B Vila Vilaro, and E Villard. *ALMA Cycle 7 Technical Handbook*. Alma Science Centre, National Radio Astronomy Observatory, doc. 7.3, ver 1.1 edition, 6 2019. ISBN 978-3-923524-66-2.

[145] David Leisawitz. NASAâĂŹs far-IR/submillimeter roadmap missions: SAFIR and SPECS. *Advances in Space research*, 34(3):631–636, 2004.

[146] C John, Leisawitz David, et al. The SPIRIT and SPECS far-infrared/submillimeter interferometry missions. *The Institute of Space and Astronautical Science repot. SP*, 14:219, 2000.

[147] David Leisawitz, Matthew R Bolcar, Richard G Lyon, Stephen F Maher, Nargess Memarsadeghi, Stephen A Rinehart, and Evan J Sinukoff. Developing wide-field spatio-spectral interferometry for far-infrared space applications. In *Optical and Infrared Interferometry III*, volume 8445, page 84450A. International Society for Optics and Photonics, 2012.

[148] Locke D Spencer, David A Naylor, Giorgio Savini, Peter A R Ade, and Brad G Gom. Space-based far-infrared interferometry technology development through a laboratory-based spatial/spectral interferometry testbed instrument. In *Space Telescopes and Instrumentation 2014: Optical, Infrared, and Millimeter Wave*, volume 9143, page 91434G. International Society for Optics and Photonics, 2014.

Appendix A

Spectral Feature Template

The full list of spectral features that compose the template used for line identification (see Chapter 3). The template line list is comprised of 307 features from molecular and atomic fine-structure transitions. The transition name, rest frequency ν_0, corresponding energy of the upper state E_u, and Einstein A coefficient A_{ij} for each transition is given. The values presented in this table are taken from a collection of databases: the National Institute of Standards and Technology (NIST)/Lovas Atomic/molecular Spectra Database [92][93], the Cologne Database for Molecular Spectroscopy (CDMS) [94], and the NASA Jet Propulsion Laboratory (JPL) sub-millimetre, millimetre and microwave spectral line catalogue [95]. These lines are visually represented in Figure 3.1. For notes on the quantum numbers see Section 3.1.

Table A.1: The template line list used to identify features extracted by the FF

Atom/Molecule	Quantum Numbers	ν_0 [GHz]	E_u [K]	A_{ij} [s^{-1}]
C I	$^3P_1$–$^3P_0$	492.1607	23.6	8×10^{-8}
C I	$^3P_2$–$^3P_1$	809.3420	62.5	2.7×10^{-7}
C II	$^3P_{3/2}$–$^3P_{1/2}$	1900.5369	91.2	2.3×10^{-6}
N II	$^3P_1$–$^3P_0$	1461.1314	70.1	2.1×10^{-6}
CH^+	1 – 0	835.1375	40.1	0.0064
CH^+	2 – 1	1669.2813	120.2	0.061
p-H_2O	6(2,4) – 7(1,7)	488.4911	867.3	1.3×10^{-5}
p-H_2O	2(1,1) – 2(0,2)	752.0332	136.9	0.007
p-H_2O	4(2,2) – 3(3,1)	916.1716	454.3	0.00057
p-H_2O	5(2,4) – 4(3,1)	970.3150	598.8	0.00089
p-H_2O	2(0,2) – 1(1,1)	987.9267	100.8	0.0058
p-H_2O	1(1,1) – 0(0,0)	1113.3430	53.4	0.018
p-H_2O	4(2,2) – 4(1,3)	1207.6388	454.3	0.028
p-H_2O	2(2,0) – 2(1,1)	1228.7887	195.9	0.019
o-H_2O	1(1,0) – 1(0,1)	556.9360	26.7	0.0034
o-H_2O	5(3,2) – 4(4,1)	620.7008	697.8	0.00011

Continued on next page

Table A.1 – continued from previous page

Atom/Molecule	Quantum Numbers	ν_0 [GHz]	E_u [K]	A_{ij} [s^{-1}]
o-H_2O	3(1,2) – 3(0,3)	1097.3647	215.2	0.016
o-H_2O	3(1,2) – 2(2,1)	1153.1268	215.2	0.0027
o-H_2O	3(2,1) – 3(1,2)	1162.9116	271.0	0.023
o-H_2O	5(2,3) – 5(1,4)	1410.7319	642.4	0.043
o-H_2O	2(2,1) – 2(1,2)	1661.0076	159.9	0.031
o-H_2O	2(1,2) – 1(0,1)	1669.9047	80.1	0.056
o-H_2O	3(0,3) – 2(1,2)	1716.7696	162.5	0.05
HDO	1 1 1 – 0 0 0	893.6387	42.9	0.0083
$H_2{}^{18}O$	1(1,0) – 1(0,1)	547.6764	60.5	0.0033
$H_2{}^{18}O$	1(1,1) – 0(0,0)	1101.6983	52.9	0.018
HF	1 – 0	1232.4762	59.1	0.024
HCN, v=0	6 – 5	531.7164	89.3	0.0072
HCN, v=0	7 – 6	620.3040	119.1	0.012
HCN, v=0	8 – 7	708.8770	153.1	0.017
HCN, v=0	9 – 8	797.4333	191.4	0.025
HCN, v=0	10 – 9	885.9707	233.9	0.034
HCN, v=0	11 – 10	974.4872	280.7	0.046
HCN, v=0	12 – 11	1062.9807	331.7	0.06
HCN, v=0	13 – 12	1151.4491	386.9	0.076
HCN, v=0	14 – 13	1239.8902	446.5	0.096
HCN, v=0	15 – 14	1328.3084	510.2	0.039
HCN, v=0	16 – 15	1416.6830	578.2	0.048
HCN, v=0	17 – 16	1505.0299	650.4	0.17
HCN, v=0	18 – 17	1593.3415	726.9	0.2
HCN, v=0	19 – 18	1681.6155	807.6	0.24
HCN, v=0	20 – 19	1769.8498	892.5	0.28
HCN, v=0	21 – 20	1858.0422	981.7	0.33
HCN, v2=1	6 -1 – 5 1	531.6484	1113.7	0.0068
HCN, v2=1	6 1 – 5 -1	534.3399	1114.2	0.0069
HCN, v2=3	6 -1 – 5 1	532.9930	3130.3	0.0065
HCN, v2=3	6 -3 – 5 3	535.2362	3174.3	0.005
HCN, v2=3	6 1 – 5 -1	538.5339	3131.3	0.0067
HCN, v3=1	6 – 5	528.0899	3105.6	0.007
$H^{13}CN$, v=0	6 – 5	517.9698	87.0	0.0066
$H^{13}CN$, v=0	7 – 6	604.2679	116.0	0.011
$H^{13}CN$, v=0	8 – 7	690.5521	149.2	0.016
$H^{13}CN$, v=0	9 – 8	776.8203	186.4	0.023
$H^{13}CN$, v=0	10 – 9	863.0706	227.9	0.032

Continued on next page

Table A.1 – continued from previous page

Atom/Molecule	Quantum Numbers	ν_0 [GHz]	E_u [K]	A_{ij} [s^{-1}]
H^{13}CN, v=0	11 – 10	949.3011	273.4	0.042
H^{13}CN, v=0	12 – 11	1035.5096	323.1	0.055
H^{13}CN, v=0	13 – 12	1121.6941	376.9	0.07
H^{13}CN, v=0	14 – 13	1207.8529	434.9	0.088
H^{13}CN, v=0	19 – 18	1638.1891	786.7	0.22
H^{13}CN, v=0	20 – 19	1724.1510	869.5	0.26
H^{13}CN, v=0	21 – 20	1810.0731	956.4	0.3
H^{13}CN, v=0	22 – 21	1895.9534	1047.3	0.35
H^{13}CN, v2=1	6 -1 – 5 1	517.8180	1102.7	0.0063
H^{13}CN, v2=1	6 1 – 5 -1	520.3939	1103.2	0.0064
HNC, v=0	6 – 5	543.8976	91.4	0.008
HNC, v=0	7 – 6	634.5108	121.8	0.013
HNC, v=0	8 – 7	725.1073	156.6	0.019
HNC, v=0	9 – 8	815.6847	195.8	0.028
HNC, v=0	10 – 9	906.2405	239.3	0.038
HNC, v=0	11 – 10	996.7723	287.1	0.051
HNC, v=0	13 – 12	1177.7547	395.8	0.085
CO, v=0	4 – 3	461.0408	55.3	6.1×10^{-6}
CO, v=0	5 – 4	576.2679	83.0	1.2×10^{-5}
CO, v=0	6 – 5	691.4731	116.2	2.1×10^{-5}
CO, v=0	7 – 6	806.6518	154.9	3.4×10^{-5}
CO, v=0	8 – 7	921.7997	199.1	5.1×10^{-5}
CO, v=0	9 – 8	1036.9124	248.9	7.3×10^{-5}
CO, v=0	10 – 9	1151.9855	304.2	0.0001
CO, v=0	11 – 10	1267.0145	365.0	0.00013
CO, v=0	12 – 11	1381.9951	431.3	0.00017
CO, v=0	13 – 12	1496.9229	503.1	0.00022
CO, v=0	14 – 13	1611.7935	580.5	0.00027
CO, v=0	15 – 14	1726.6025	663.4	0.00034
CO, v=0	16 – 15	1841.3455	751.7	0.0004
^{13}CO	4 – 3	440.7652	52.9	5.4×10^{-6}
^{13}CO	5 – 4	550.9263	79.3	1.1×10^{-5}
^{13}CO	6 – 5	661.0672	111.1	1.9×10^{-5}
^{13}CO	7 – 6	771.1841	148.1	3×10^{-5}
^{13}CO	8 – 7	881.2728	190.4	4.5×10^{-5}
^{13}CO	9 – 8	991.3293	237.9	6.4×10^{-5}
^{13}CO	10 – 9	1101.3496	290.8	8.9×10^{-5}
^{13}CO	11 – 10	1211.3296	348.9	0.00012

Continued on next page

Table A.1 – continued from previous page

Atom/Molecule	Quantum Numbers	ν_0 [GHz]	E_u [K]	A_{ij} [s^{-1}]
^{13}CO	12 – 11	1321.2655	412.3	0.00015
^{13}CO	13 – 12	1431.1530	481.0	0.00019
^{13}CO	14 – 13	1540.9883	555.0	0.00024
^{13}CO	15 – 14	1650.7673	634.2	0.0003
^{13}CO	16 – 15	1760.4860	718.7	0.00036
^{13}CO	17 – 16	1870.1404	808.5	0.00043
C^{17}O	4 1.5 – 3 2.5	449.3947	53.9	2×10^{-7}
C^{17}O	5 – 4	561.7128	80.9	1.1×10^{-5}
C^{17}O	6 – 5	674.0094	113.2	2×10^{-5}
C^{17}O	7 – 6	786.2808	151.0	3.2×10^{-5}
C^{17}O	8 – 7	898.5230	194.1	4.8×10^{-5}
C^{17}O	9 6.5 – 8 7.5	1010.7311	242.6	4.2×10^{-8}
C^{17}O	10 11.5 – 9 10.5	1122.9025	296.5	9.2×10^{-5}
C^{17}O	11 8.5 – 10 9.5	1235.0315	355.8	3.1×10^{-8}
C^{17}O	12 9.5 – 11 10.5	1347.1148	420.4	2.8×10^{-8}
C^{18}O	4 – 3	439.0888	52.7	5.3×10^{-6}
C^{18}O	5 – 4	548.8310	79.0	1.1×10^{-5}
C^{18}O	6 – 5	658.5533	110.6	1.9×10^{-5}
C^{18}O	7 – 6	768.2516	147.5	3×10^{-5}
C^{18}O	8 – 7	877.9219	189.6	4.5×10^{-5}
C^{18}O	9 – 8	987.5604	237.0	6.4×10^{-5}
C^{18}O	10 – 9	1097.1629	289.7	8.8×10^{-5}
C^{18}O	11 – 10	1206.7255	347.6	0.00012
C^{18}O	12 – 11	1316.2441	410.8	0.00015
C^{18}O	13 – 12	1425.7149	479.2	0.00019
^{13}C^{17}O	4 1.5 – 3 2.5	429.1170	51.5	1.8×10^{-7}
^{13}C^{17}O	5 2.5 – 4 3.5	536.3678	77.2	1.1×10^{-7}
^{13}C^{17}O	12 9.5 – 11 10.5	1286.3764	401.4	2.4×10^{-8}
^{13}C^{17}O	13 10.5 – 12 11.5	1393.3680	468.3	2.2×10^{-8}
^{13}C^{18}O	5 4.5 – 4 4.5	523.4842	75.4	2.1×10^{-7}
^{13}C^{18}O	6 5.5 – 5 5.5	628.1411	105.5	2.4×10^{-7}
N_2H^+, v=0	6 – 5	558.9665	93.9	0.012
N_2H^+, v=0	7 – 6	652.0956	125.2	0.019
N_2H^+, v=0	8 – 7	745.2099	161.0	0.026
N_2H^+, v=0	9 – 8	838.3073	201.2	0.038
N_2H^+, v=0	10 – 9	931.3857	245.9	0.052
N_2H^+, v=0	11 – 10	1024.4430	295.1	0.069
N_2H^+, v=0	12 – 11	1117.4771	348.7	0.09

Continued on next page

Table A.1 – continued from previous page

Atom/Molecule	Quantum Numbers	ν_0 [GHz]	E_u [K]	A_{ij} [s^{-1}]
HCO^+, v=0	6 – 5	535.0616	89.9	0.013
HCO^+, v=0	7 – 6	624.2084	119.8	0.02
HCO^+, v=0	8 – 7	713.3412	154.1	0.03
HCO^+, v=0	9 – 8	802.4582	192.6	0.043
HCO^+, v=0	10 – 9	891.5573	235.4	0.06
HCO^+, v=0	11 – 10	980.6365	282.4	0.08
HCO^+, v=0	12 – 11	1069.6939	333.8	0.1
HCO^+, v=0	13 – 12	1158.7272	389.4	0.13
HCO^+, v=0	14 – 13	1247.7350	449.3	0.17
$H^{13}CO^+$	6 – 5	520.4599	87.4	0.011
$H^{13}CO^+$	7 – 6	607.1746	116.6	0.018
$H^{13}CO^+$	8 – 7	693.8763	149.9	0.028
$H^{13}CO^+$	9 – 8	780.5628	187.3	0.04
$H^{13}CO^+$	10 – 9	867.2324	229.0	0.055
$HC^{18}O^+$	6 – 5	510.9096	85.8	0.011
p-H_2CO	6(2,4) – 7(0,7)	485.2276	120.7	1.5×10^{-6}
p-H_2CO	7(0,7) – 6(0,6)	505.8337	97.4	0.0038
p-H_2CO	7(2,6) – 6(2,5)	509.1462	144.9	0.0036
p-H_2CO	7(4,4) – 6(4,3)	509.8296	286.2	0.0026
p-H_2CO	7(4,3) – 6(4,2)	509.8302	286.2	0.0026
p-H_2CO	7(2,5) – 6(2,4)	513.0763	145.4	0.0037
p-H_2CO	8(0,8) – 7(0,7)	576.7083	125.1	0.0057
p-H_2CO	8(2,7) – 7(2,6)	581.6118	172.8	0.0055
p-H_2CO	8(6,3) – 7(6,2)	582.0708	548.7	0.0026
p-H_2CO	8(4,5) – 7(4,4)	582.7229	314.1	0.0044
p-H_2CO	8(4,4) – 7(4,3)	582.7242	314.1	0.0044
p-H_2CO	8(2,6) – 7(2,5)	587.4537	173.5	0.0056
p-H_2CO	9(0,9) – 8(0,8)	647.0818	156.2	0.0081
p-H_2CO	9(2,8) – 8(2,7)	653.9701	204.2	0.008
p-H_2CO	9(6,4) – 8(6,3)	654.8382	580.2	0.0047
p-H_2CO	9(4,6) – 8(4,5)	655.6399	345.6	0.0068
p-H_2CO	9(4,5) – 8(4,4)	655.6437	345.6	0.0068
p-H_2CO	9(2,7) – 8(2,6)	662.2091	205.3	0.0083
p-H_2CO	10(0,10) – 9(0,9)	716.9384	190.6	0.011
p-H_2CO	10(2,9) – 9(2,8)	726.2083	239.1	0.011
p-H_2CO	10(4,7) – 9(4,6)	728.5831	380.6	0.0098
p-H_2CO	10(4,6) – 9(4,5)	728.5916	380.6	0.0098
p-H_2CO	10(2,8) – 9(2,7)	737.3427	240.7	0.012

Continued on next page

Table A.1 – continued from previous page

Atom/Molecule	Quantum Numbers	ν_0 [GHz]	E_u [K]	A_{ij} [s^{-1}]
p-H_2CO	11(0,11) – 10(0,10)	786.2849	228.3	0.015
p-H_2CO	11(2,10) – 10(2,9)	798.3134	277.4	0.015
p-H_2CO	11(2,9) – 10(2,8)	812.8314	279.7	0.016
p-H_2CO	12(0,12) – 11(0,11)	855.1513	269.4	0.019
p-H_2CO	12(2,11) – 11(2,10)	870.2735	319.2	0.019
p-H_2CO	12(2,10) – 11(2,9)	888.6291	322.4	0.021
p-H_2CO	13(0,13) – 12(0,12)	923.5878	313.7	0.024
p-H_2CO	13(2,12) – 12(2,11)	942.0766	364.4	0.025
p-H_2CO	13(2,11) – 12(2,10)	964.6681	368.7	0.027
p-H_2CO	14(0,14) – 13(0,13)	991.6601	361.3	0.03
p-H_2CO	14(2,12) – 13(2,11)	1040.8651	418.6	0.034
p-H_2CO	15(2,14) – 14(2,13)	1085.1676	465.1	0.038
o-H_2CO	7(1,7) – 6(1,6)	491.9684	91.1	0.0034
o-H_2CO	7(5,2) – 6(5,1)	509.5621	376.7	0.0019
o-H_2CO	7(5,3) – 6(5,2)	509.5621	376.7	0.0019
o-H_2CO	7(3,5) – 6(3,4)	510.1558	188.7	0.0032
o-H_2CO	7(3,4) – 6(3,3)	510.2378	188.7	0.0032
o-H_2CO	7(1,6) – 6(1,5)	525.6658	97.6	0.0042
o-H_2CO	8(1,8) – 7(1,7)	561.8993	118.1	0.0052
o-H_2CO	8(5,4) – 7(5,3)	582.3821	404.6	0.0036
o-H_2CO	8(5,3) – 7(5,2)	582.3821	404.6	0.0036
o-H_2CO	8(3,6) – 7(3,5)	583.1446	216.7	0.0051
o-H_2CO	8(3,5) – 7(3,4)	583.3086	216.7	0.0051
o-H_2CO	8(1,7) – 7(1,6)	600.3306	126.4	0.0063
o-H_2CO	9(1,9) – 8(1,8)	631.7028	148.4	0.0075
o-H_2CO	9(7,3) – 8(7,2)	654.4633	717.1	0.0033
o-H_2CO	9(7,2) – 8(7,1)	654.4634	717.1	0.0033
o-H_2CO	9(5,5) – 8(5,4)	655.2121	436.1	0.0058
o-H_2CO	9(5,4) – 8(5,3)	655.2121	436.1	0.0058
o-H_2CO	9(3,7) – 8(3,6)	656.1647	248.2	0.0075
o-H_2CO	9(3,6) – 8(3,5)	656.4646	248.2	0.0075
o-H_2CO	9(1,8) – 8(1,7)	674.8098	158.8	0.0091
o-H_2CO	10(1,10) – 9(1,9)	701.3704	182.1	0.01
o-H_2CO	10(5,6) – 9(5,5)	728.0535	471.0	0.0087
o-H_2CO	10(5,5) – 9(5,4)	728.0536	471.0	0.0087
o-H_2CO	10(3,8) – 9(3,7)	729.2126	283.2	0.011
o-H_2CO	10(3,7) – 9(3,6)	729.7250	283.3	0.011
o-H_2CO	10(1,9) – 9(1,8)	749.0719	194.8	0.013

Continued on next page

Table A.1 – continued from previous page

Atom/Molecule	Quantum Numbers	ν_0 [GHz]	E_u [K]	A_{ij} [s^{-1}]
o-H_2CO	11(1,11) – 10(1,10)	770.8961	219.1	0.014
o-H_2CO	11(5,7) – 10(5,6)	800.9075	509.5	0.012
o-H_2CO	11(3,9) – 10(3,8)	802.2824	321.7	0.014
o-H_2CO	11(3,8) – 10(3,7)	803.1116	321.8	0.015
o-H_2CO	11(1,10) – 10(1,9)	823.0828	234.3	0.017
o-H_2CO	12(1,12) – 11(1,11)	840.2757	259.4	0.018
o-H_2CO	12(3,10) – 11(3,9)	875.3662	363.7	0.019
o-H_2CO	12(3,9) – 11(3,8)	876.6491	363.9	0.019
o-H_2CO	12(1,11) – 11(1,10)	896.8051	277.3	0.022
o-H_2CO	13(1,13) – 12(1,12)	909.5077	303.1	0.023
o-H_2CO	13(3,11) – 12(3,10)	948.4538	409.2	0.025
o-H_2CO	13(1,12) – 12(1,11)	970.1992	323.9	0.028
o-H_2CO	14(1,14) – 13(1,13)	978.5924	350.0	0.028
o-H_2CO	14(3,12) – 13(3,11)	1021.5331	458.3	0.031
o-H_2CO	14(3,11) – 13(3,10)	1024.2886	458.6	0.031
o-H_2CO	14(1,13) – 13(1,12)	1043.2229	374.0	0.034
o-H_2CO	15(3,13) – 14(3,12)	1094.5899	510.8	0.038
o-H_2CO	16(3,14) – 15(3,13)	1167.6085	566.8	0.047
p-H_2S	5(3,3) – 6(0,6)	493.0849	351.6	1.1×10^{-7}
p-H_2S	3(3,1) – 3(2,2)	568.0506	166.0	0.00038
p-H_2S	4(2,2) – 4(1,3)	665.3937	245.1	0.00074
p-H_2S	2(0,2) – 1(1,1)	687.3034	54.7	0.00092
p-H_2S	3(2,2) – 3(1,3)	747.3019	138.7	0.00067
p-H_2S	3(1,3) – 2(0,2)	1002.7787	102.8	0.0038
p-H_2S	4(1,3) – 4(0,4)	1018.3473	213.1	0.0014
o-H_2S	2(2,1) – 2(1,2)	505.5652	59.6	0.00024
o-H_2S	7(5,2) – 7(4,3)	555.2540	707.9	0.00073
o-H_2S	5(3,2) – 5(2,3)	611.4416	359.7	0.00073
o-H_2S	4(4,1) – 4(3,2)	650.3742	261.7	0.00055
o-H_2S	3(1,2) – 3(0,3)	708.4704	117.0	0.00059
o-H_2S	2(1,2) – 1(0,1)	736.0341	35.3	0.0013
o-H_2S	4(3,2) – 4(2,3)	765.9379	230.5	0.001
o-H_2S	3(0,3) – 2(1,2)	993.1018	83.0	0.0037
o-H_2S	5(2,3) – 5(1,4)	993.1018	330.3	0.002
o-H_2S	6(4,3) – 6(3,4)	1025.8844	497.3	0.0026
o-H_2S	4(2,3) – 4(1,4)	1026.5112	193.8	0.0014
o-H_2S	2(2,1) – 1(1,0)	1072.8365	59.6	0.0041
o-H_2S	3(1,2) – 2(2,1)	1196.0121	117.0	0.0028

Continued on next page

Table A.1 – continued from previous page

Atom/Molecule	Quantum Numbers	ν_0 [GHz]	E_u [K]	A_{ij} [s^{-1}]
CS, v=0-4	10 1 – 9 1	486.2010	1958.7	0.0024
CS, v=0-4	10 0 – 9 0	489.7509	129.3	0.0025
CS, v=0-4	11 1 – 10 1	534.7840	1984.4	0.0032
CS, v=0-4	11 0 – 10 0	538.6890	155.1	0.0033
CS, v=0-4	12 0 – 11 0	587.6165	183.3	0.0043
CS, v=0-4	13 0 – 12 0	636.5324	213.9	0.0055
CS, v=0-4	14 0 – 13 0	685.4359	246.8	0.0069
CS, v=0-4	15 0 – 14 0	734.3259	282.0	0.0086
CS, v=0-4	16 0 – 15 0	783.2015	319.6	0.01
CS, v=0-4	17 0 – 16 0	832.0617	359.6	0.013
CS, v=0-4	18 0 – 17 0	880.9056	401.8	0.015
CS, v=0-4	19 0 – 18 0	929.7321	446.5	0.018
CS, v=0-4	20 0 – 19 0	978.5404	493.4	0.02
CS, v=0-4	21 0 – 20 0	1027.3295	542.7	0.024
CS, v=0-4	22 0 – 21 0	1076.0984	594.4	0.027
CS, v=0-4	23 0 – 22 0	1124.8461	648.4	0.031
CS, v=0-4	24 0 – 23 0	1173.5718	704.7	0.035
CS, v=0-4	25 0 – 24 0	1222.2744	763.3	0.04
CS, v=0-4	26 0 – 25 0	1270.9529	824.3	0.045
^{13}CS, v=0,1	11 0 – 10 0	508.5347	146.5	0.0028
^{13}CS, v=0,1	12 0 – 11 0	554.7257	173.1	0.0037
^{13}CS, v=0,1	13 0 – 12 0	600.9065	201.9	0.0047
^{13}CS, v=0,1	15 0 – 14 0	693.2337	266.2	0.0072
^{13}CS, v=0,1	16 0 – 15 0	739.3785	301.7	0.0088
^{13}CS, v=0,1	17 0 – 16 0	785.5096	339.4	0.011
^{13}CS, v=0,1	18 0 – 17 0	831.6261	379.3	0.013
^{13}CS, v=0,1	19 0 – 18 0	877.7272	421.5	0.015
^{13}CS, v=0,1	20 0 – 19 0	923.8120	465.8	0.017
^{13}CS, v=0,1	21 0 – 20 0	969.8797	512.4	0.02
^{13}CS, v=0,1	22 0 – 21 0	1015.9294	561.1	0.023
SiO, v=0-10	12 1 – 11 1	517.2597	1930.5	0.0075
SiO, v=0-10	12 0 – 11 0	520.8811	162.5	0.0076
SiO, v=0-10	13 0 – 12 0	564.2490	189.6	0.0097
SiO, v=0-10	14 0 – 13 0	607.6076	218.8	0.012
SiO, v=0-10	15 0 – 14 0	650.9561	250.0	0.015
SiO, v=0-10	16 0 – 15 0	694.2939	283.3	0.018
SiO, v=0-10	17 0 – 16 0	737.6202	318.7	0.022
SiO, v=0-10	18 0 – 17 0	780.9346	356.2	0.026

Continued on next page

Table A.1 – continued from previous page

Atom/Molecule	Quantum Numbers	ν_0 [GHz]	E_u [K]	A_{ij} [s^{-1}]
SiO, v=0-10	19 0 – 18 0	824.2359	395.8	0.03
SiO, v=0-10	20 0 – 19 0	867.5236	437.4	0.036
SiO, v=0-10	21 0 – 20 0	910.7969	481.1	0.041
SiO, v=0-10	22 0 – 21 0	954.0551	526.9	0.048
SiO, v=0-10	23 0 – 22 0	997.2976	574.8	0.054
SiO, v=0-10	24 0 – 23 0	1040.5236	624.7	0.062
SiO, v=0-10	25 0 – 24 0	1083.7324	676.7	0.07
SiO, v=0-10	26 0 – 25 0	1126.9233	730.8	0.079
SiO, v=0-10	27 0 – 26 0	1170.0955	786.9	0.088
SiO, v=0-10	28 0 – 27 0	1213.2484	845.2	0.098
SO, v=0	7(7) – 6(7)	487.7083	71.0	1.7×10^{-5}
SO, v=0	4(3) – 1(2)	504.6763	28.7	1.6×10^{-5}
SO, v=0	12(11) – 11(10)	514.8537	167.6	0.0018
SO, v=0	12(12) – 11(11)	516.3358	174.2	0.0018
SO, v=0	12(13) – 11(12)	517.3545	165.8	0.0018
SO, v=0	8(8) – 7(8)	527.9412	87.5	1.8×10^{-5}
SO, v=0	13(12) – 12(11)	558.0876	194.4	0.0023
SO, v=0	13(13) – 12(12)	559.3197	201.1	0.0023
SO, v=0	13(14) – 12(13)	560.1786	192.7	0.0023
SO, v=0	9(9) – 8(9)	568.7414	106.1	1.9×10^{-5}
SO, v=0	14(13) – 13(12)	601.2584	223.2	0.0029
SO, v=0	14(14) – 13(13)	602.2930	230.0	0.0029
SO, v=0	14(15) – 13(14)	603.0216	221.6	0.0029
SO, v=0	10(10) – 9(10)	609.9601	126.7	2×10^{-5}
SO, v=0	5(4) – 2(3)	611.5524	38.6	1.5×10^{-5}

Appendix B

Spectral Feature Finder Line Identification Results

The line identification routine, as described in Chapter 3, is presented broken down by molecule and transitional states in this appendix. This line identification has been applied to all publicly available SPIRE FTS observations including the spectra from off-axis detectors in sparse observations, the central detectors in sparse observations, and in mapping observations.

In the following figures, a histogram of the number of identifications of each specific transition is marked by the orange bars. The larger blue bars mark the sum of all these individual transitions for each atomic/molecular species. Each atom/molecule is ordered by the normalized number of detections. White space is used to ensure each figure maintains the same bin width and vertical scale. It is also used to ensure that the lines identified in a single atomic/molecular species are not broken up over multiple figures.

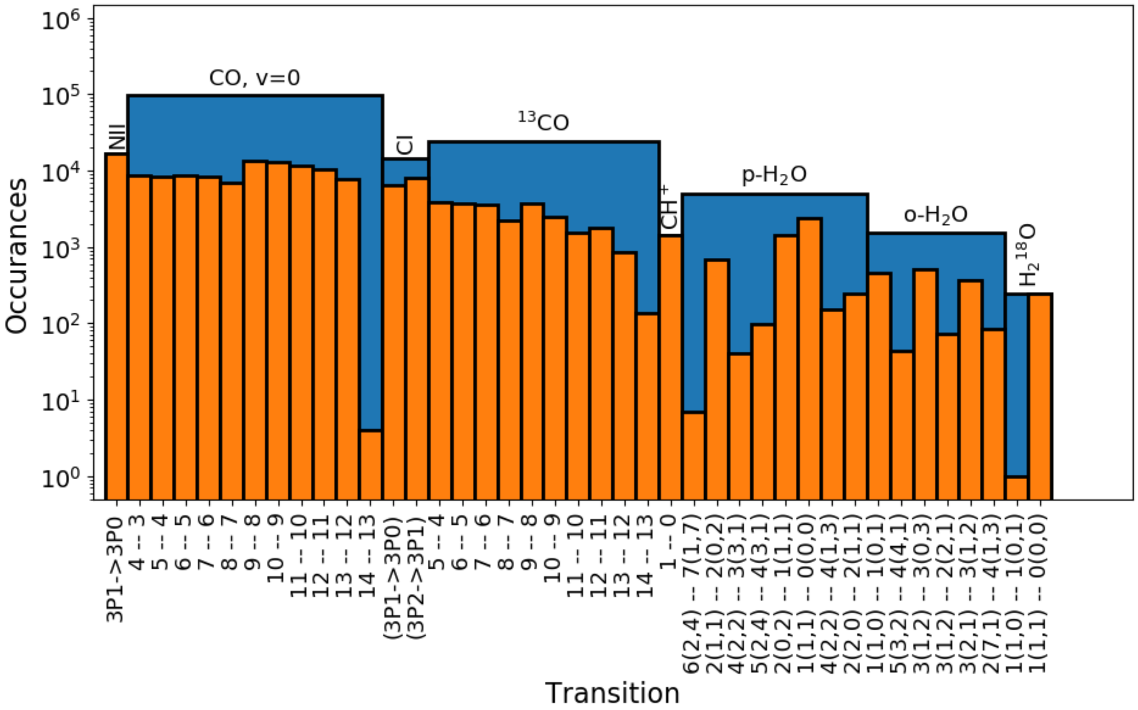

Figure B.1: Figure detailed in the text of the appendix.

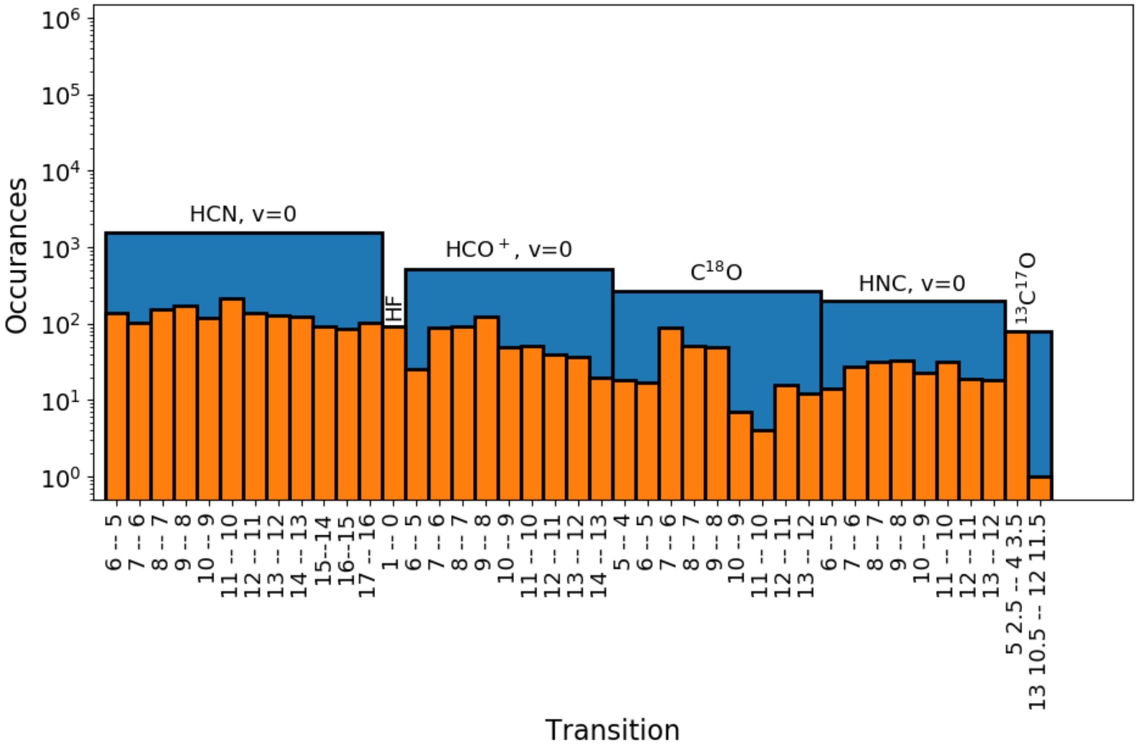

Figure B.2: Figure detailed in the text of the appendix.

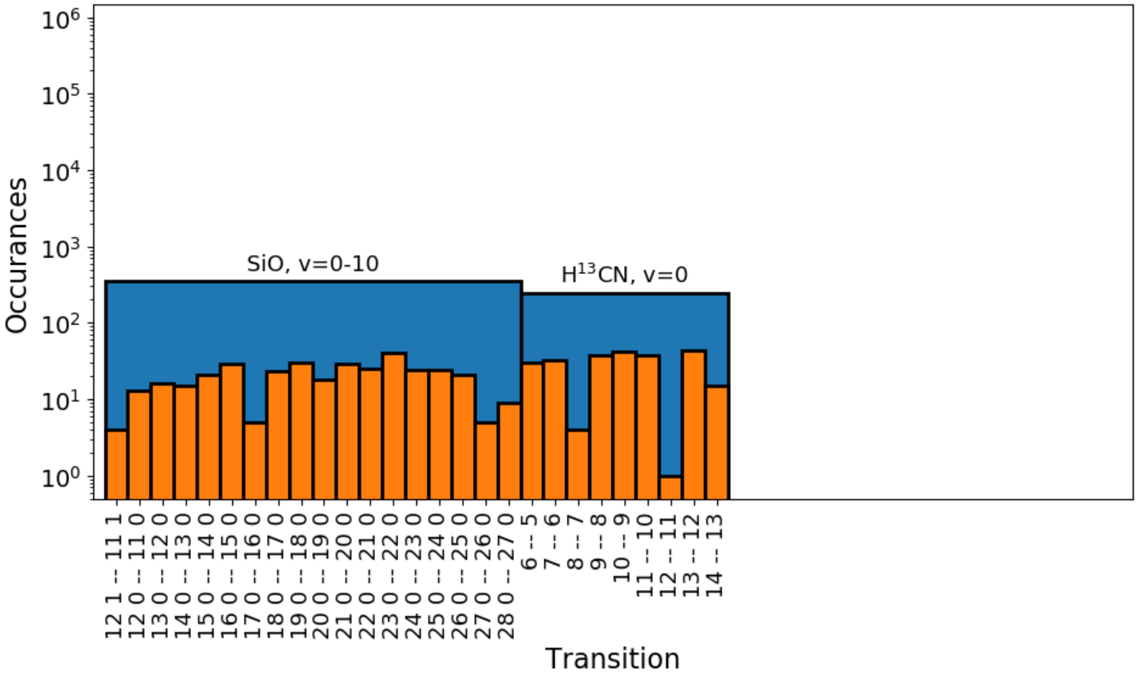

Figure B.3: Figure detailed in the text of the appendix.

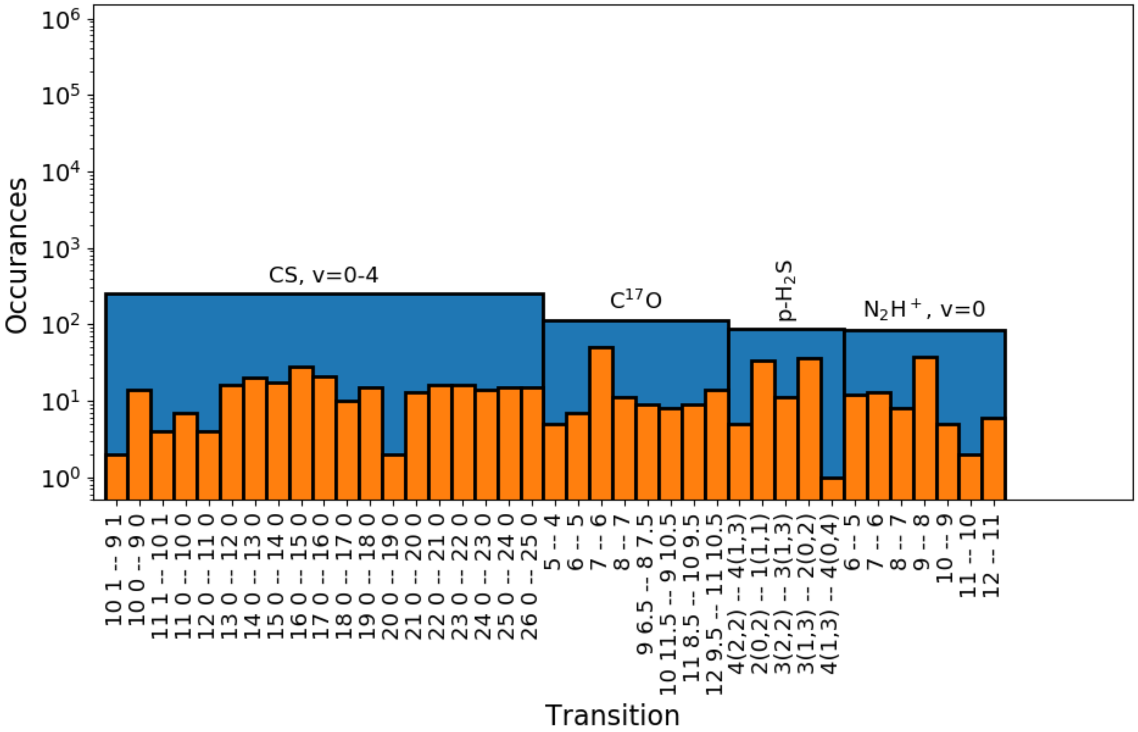

Figure B.4: Figure detailed in the text of the appendix.

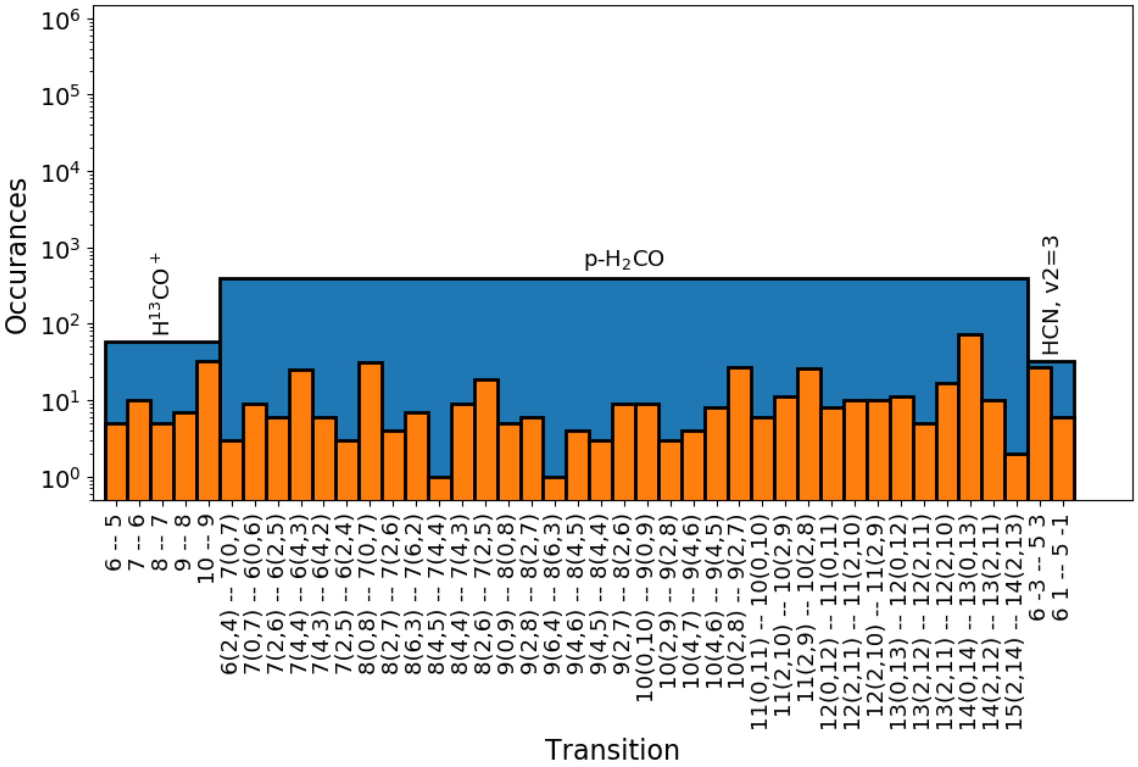

Figure B.5: Figure detailed in the text of the appendix.

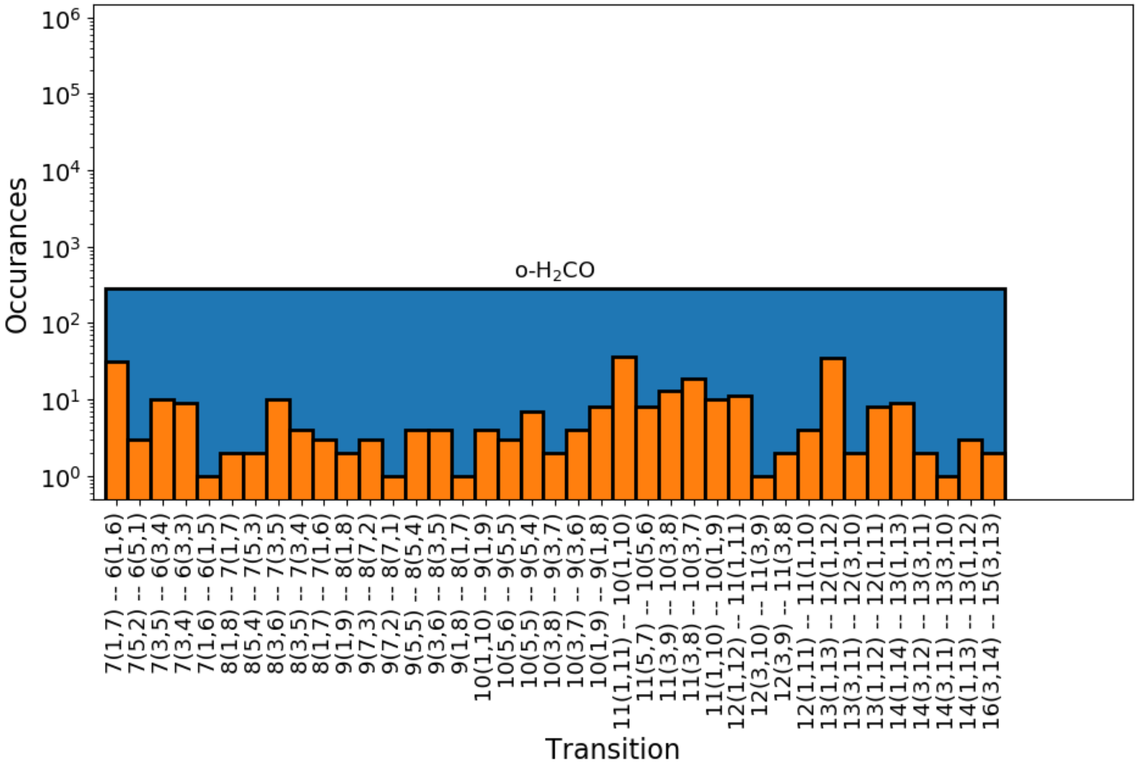

Figure B.6: Figure detailed in the text of the appendix.

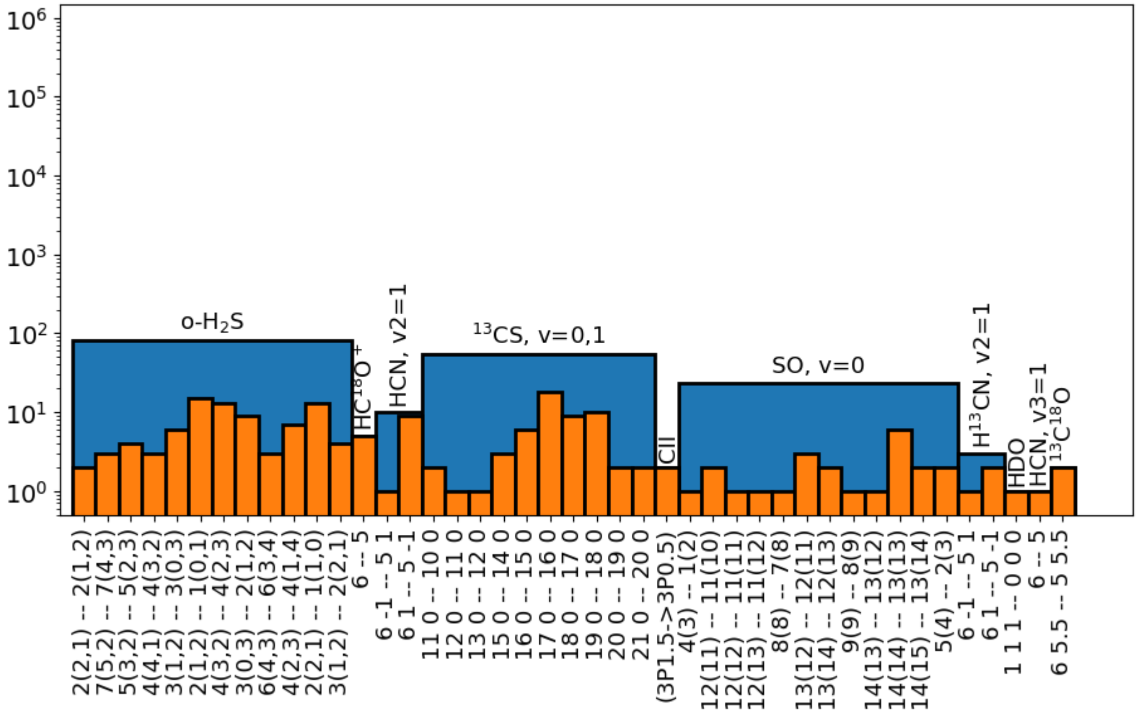

Figure B.7: Figure detailed in the text of the appendix.

Appendix C

Off-Axis Postcard Examples

Postcards that emphasize the FF results from off-axis detectors in sparsely sampled single-pointing observations from SPIRE FTS are described in Chapter 4. In this appendix, I will briefly discuss a few example postcards and off-axis results from observations of the SPIRE FTS.

C.1 NGC 6334, Observation ID 1342214829

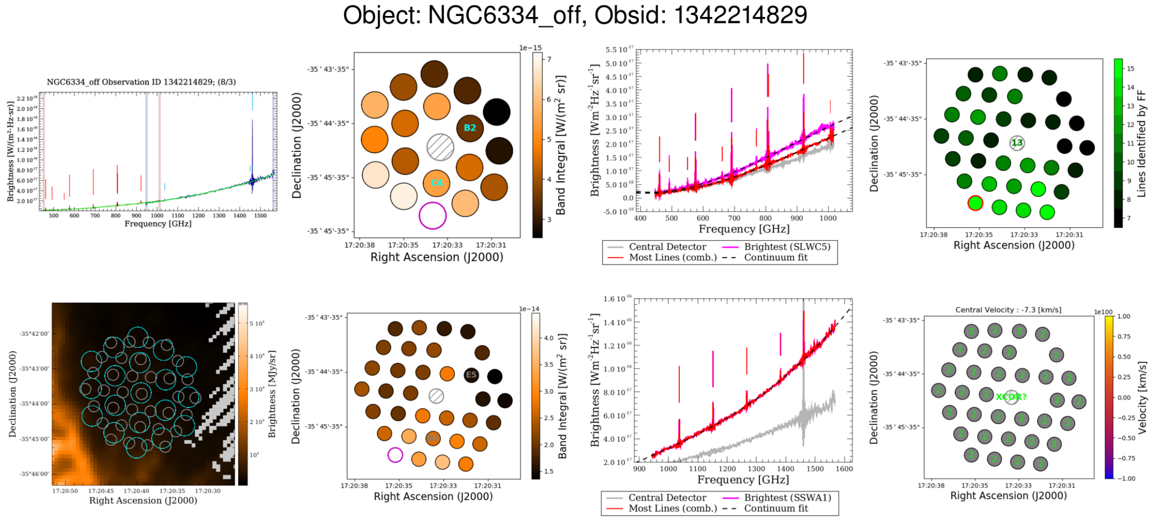

Figure C.1: Off-Axis postcard for the SPIRE FTS observation of the source NGC 6334

Observation ID 1342214828 is of an ionized hydrogen region [89] at sky coordinates: Right Ascencion (RA) 17:20:39.15, Declination (Dec) -35:43:43.80 and provides an excellent example of an observation with more spectral content in the off-axis detectors than the central detectors. There is a single publication involving this source reported on the HSA.

C.2 NGC 3256, Observation ID 1342201201

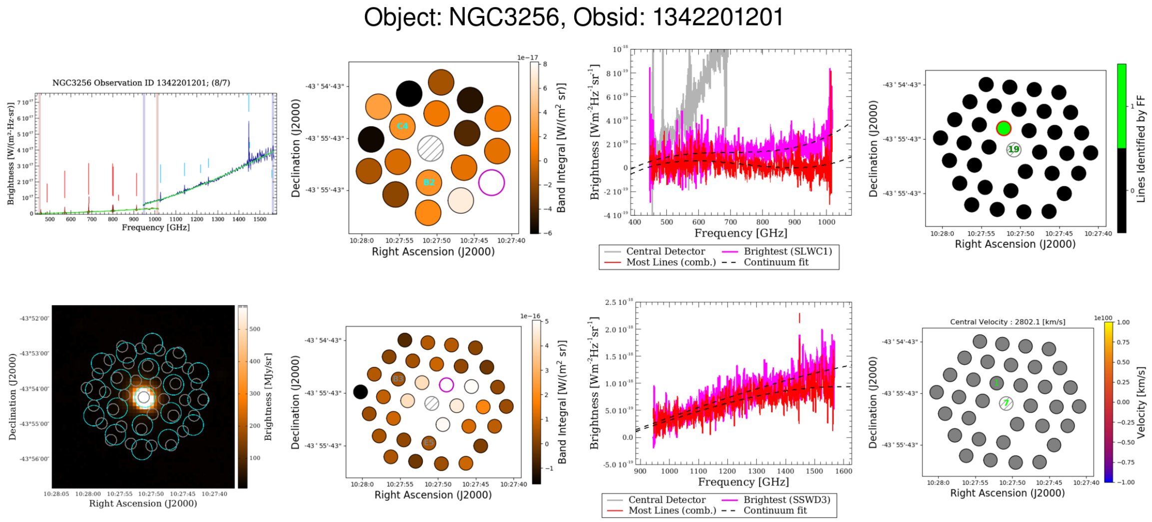
Object: NGC3256, Obsid: 1342201201

Figure C.2: Off-Axis postcard for the SPIRE FTS observation of the source NGC 3256

Observation ID 1342201201 is of interacting galaxies [89] at sky coordinates: RA 10:27:51.18, Dec -43:54:14.21. This observation provides an example of a point-like source with significant emission in the central pixel but no spectral features in off-axis detectors. The single line extracted by the FF from off-axis detectors may be a spurious detection. There are 15 publications concerning this observation reported on the HSA.

C.3 NGC 3256, Observation ID 1342214845

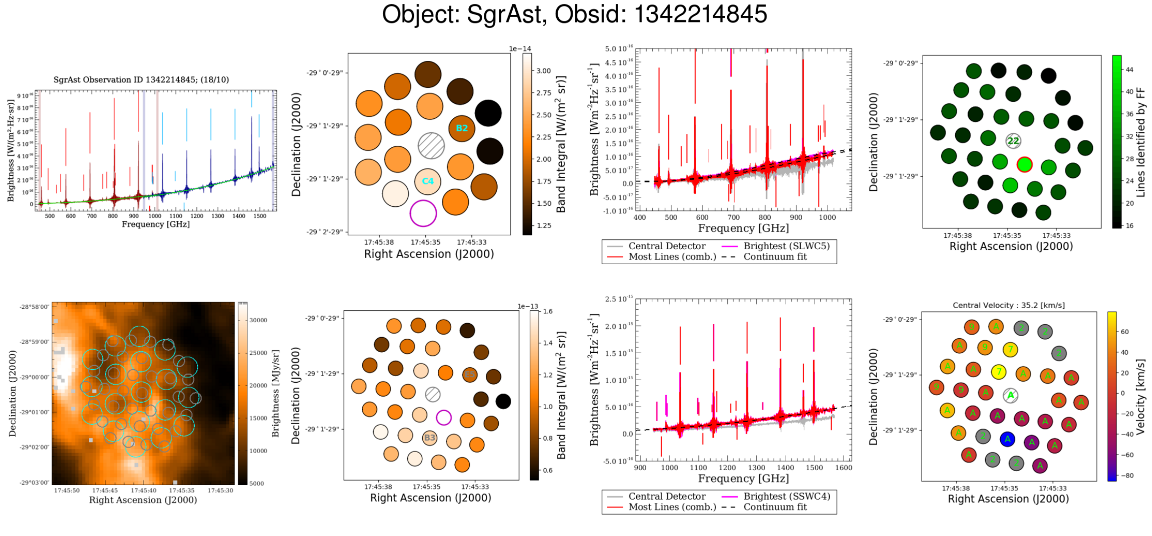
Object: SgrAst, Obsid: 1342214845

Figure C.3: Off-Axis postcard for the SPIRE FTS observation of the Galactic centre

Observation ID 1342214845 is of the galactic centre, Sagittarius A* [89], at sky coordinates: RA 17:20:39.15, Dec -35:43:43.80. In this observation, there is bright line-filled emission across the entirety of the FTS footprint which provides a velocity map for almost the entirety of the observation. There is a single publication related to this observation reported on the HSA.

C.4 RCW 82 IRS 2, Observation ID 1342204903

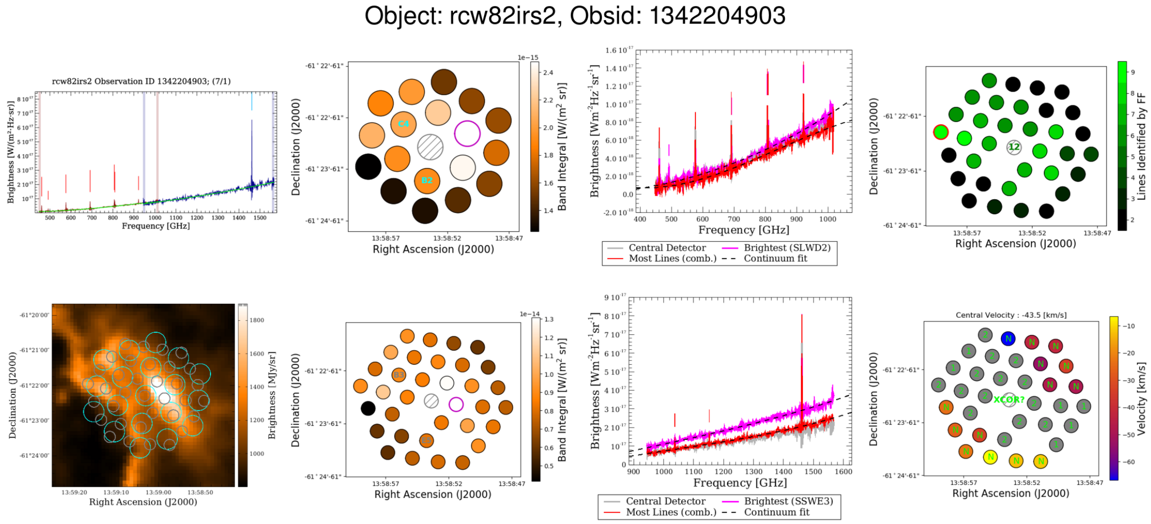

Figure C.4: Off-Axis postcard for the SPIRE FTS observation of the source RCW 82 IRS 2.

Observation ID 1342204903 is of an IR source at the sky coordinates: RA 13:59:3.31, Dec -61:22:17.25. RCW 82 is an ionized hydrogen region centred nearby [89]. The SPIRE FTS observation has a high degree of emission in off-axis detectors from the extended source with a prominent N II feature in several spectra. Molecular emission is seen in what appears to be the rotational CO ladder however a reliable velocity is not obtained by the ^{12}CO radial velocity estimating routine. There are no known publications involving this observation recorded in the HSA.

C.5 IC443C, Observation ID 1342216885

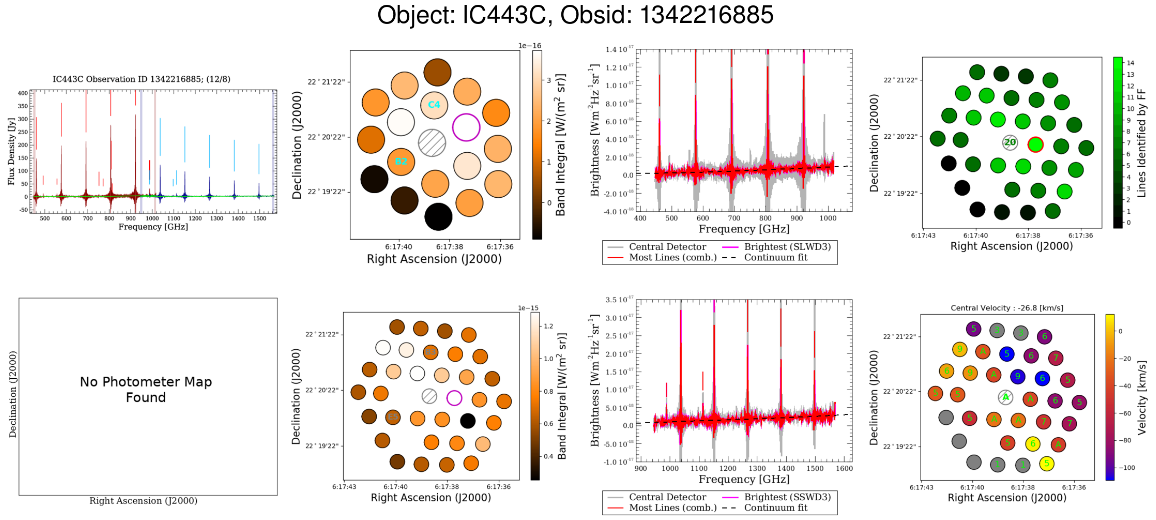

Figure C.5: Off-Axis postcard for the SPIRE FTS observation of the source RCW 82 IRS 2.

Observation ID 1342216885 is of a supernova remnant [89] and is at the sky coordinates: RA 06:17:52.45, Dec +22:21:28.7. Extended molecular emission about the central source is apparent and velocity estimates from the ^{12}CO routine are often capable of finding all 10 in-band CO features for some off-axis detectors. This observation provides an example of mapping postcard in which no photometer map of the source can be found.

Appendix D

Useful Derivations

D.1 Stars and star formation

D.1.1 Equilibrium of a single monatomic cloud

The following treatment follows a similar path to that of Dyson [14].

We begin with a spherically symmetric gas cloud, a single spherical shell of thickness dr in the cloud at some radius r. The mass of the shell is

$$dM(r) = 4\pi r^2 \rho(r) dr \quad [\text{kg}], \tag{D.1}$$

where $\rho(r)$ is the density of the gas as a function of radius r. We will take the only forces on the cloud to be its internal pressure, self-gravity and surface pressure from an external medium. For equilibrium to hold we require that the gravitational force on the shell, due to a mass $M(r)$, must be balanced by some differential pressure across the shell, $dP(r)$. As the pressure must push against the gravitational collapse, the pressure must decrease outward. We now write the equilibrium condition,

$$4\pi r^2 \, dP(r) = \frac{-GM(r)\, dM(r)}{r^2} \quad [\text{N}]. \tag{D.2}$$

Introducing the enclosed volume, $V(r) \equiv \frac{4}{3}\pi r^3$ we can write

$$3V(r)\, dP(r) = \frac{-GM(r)\, dM(r)}{r} \quad [\text{J}]. \tag{D.3}$$

We now integrate from the centre of the cloud where the pressure is P_{c0} to the edge of radius R_c and where the pressure is equal to the external pressure P_s,

$$3\int_{P_{c0}}^{P_s} V(r) dP(r) = -\int_0^{M_c} \frac{GM(r)\, dM}{r} \quad [\text{J}], \tag{D.4}$$

where M_c is the total mass of the cloud.

We can further our analysis by integrating the left hand side of the equation by parts to give

$$3\int_{P_{c0}}^{P_s} V(r) dP(r) = 3V_c P_s - 3\int_0^{V_c} P\, dV \quad [\text{J}], \tag{D.5}$$

where V_c as the total volume of the cloud.

Using the internal energy of a monatomic cloud per unit volume and the ideal gas law,

$$\varepsilon_I = \frac{3}{2}\frac{NkT}{V} = \frac{3}{2}P \quad [\mathrm{N\,m^{-2}}], \tag{D.6}$$

we can rewrite the above integral

$$\int_0^{V_c} P\,dV = \frac{2}{3}\int_0^{V_c} \varepsilon_I\,dV = \frac{2}{3}\mathcal{T} \quad [\mathrm{J}], \tag{D.7}$$

where $\mathcal{T}$ is the thermal energy content of the cloud.

The right hand side of Equation D.4 is the gravitational self-energy, Ω, allowing us to finally write the equilibrium condition:

$$3V_cP_s = 2\mathcal{T} + \Omega \quad [\mathrm{J}]. \tag{D.8}$$

D.2 Fourier analysis

D.2.1 Convolution theorem proof

Consider two arbitrary function $f(x)$ and $g(x)$ and their Fourier transform pairs $F(k)$ and $G(k)$. The convolution of the Fourier transform pairs is,

$$H(z) = \int_{-\infty}^{\infty} F(k)G(z-k)\,dk. \tag{D.9}$$

The inverse Fourier transform of $H(z)$ is,

$$h(x) = \int_{-\infty}^{\infty} dz e^{i2\pi zx}\left[\int_{-\infty}^{\infty} F(k)G(z-k)\,dk\right] \tag{D.10}$$

$$= \int_{-\infty}^{\infty} dk F(k)\left[\int_{-\infty}^{\infty} G(z-k)e^{i2\pi zx}\,dz\right]. \tag{D.11}$$

Substituting $u = z - k$ we obtain

$$H(k) = \int_{-\infty}^{\infty} dk F(k)\left[\int_{-\infty}^{\infty} G(u)e^{i2\pi(u+k)x}\,dz\right] \tag{D.12}$$

$$= \int_{-\infty}^{\infty} F(k)e^{i2\pi kx}\,dk \int_{-\infty}^{\infty} G(u)e^{i2\pi ux}\,du \tag{D.13}$$

$$= f(x)g(x). \tag{D.14}$$

Thus we see that,

$$\mathcal{F}^{-1}\{F(k) * G(k)\} = f(x)g(x) \tag{D.15}$$

$$\mathcal{F}\{f(x)g(x)\} = F(k) * G(k) \tag{D.16}$$

D.2.2 Fourier transform of a top-hat function

For a top-hat function of width $2L$,

$$u\left(\frac{z}{2L}\right) = \begin{cases} 1 & -L \leq z \leq +L \\ 0 & \text{otherwise} \end{cases}. \tag{D.17}$$

The Fourier transform of $u\left(\frac{z}{2L}\right)$ is as follows,

$$\begin{aligned}
U(\sigma) &= \int_{-\infty}^{\infty} u\left(\frac{z}{2L}\right) e^{-i2\pi z\sigma}\, dz && \text{(D.18)}\\
&= \int_{-L}^{L} e^{-i2\pi z\sigma}\, dz && \text{(D.19)}\\
&= \frac{1}{-i2\pi\sigma}\left(e^{-i2\pi z\sigma}\Big|_{-L}^{L}\right) && \text{(D.20)}\\
&= \frac{1}{-i2\pi\sigma}\left(e^{-i2\pi\sigma L} - e^{i2\pi\sigma L}\right) && \text{(D.21)}\\
&= \frac{2L}{\pi\sigma 2L}\left(\frac{e^{i2\pi\sigma L} - e^{-i2\pi\sigma L}}{2i}\right) && \text{(D.22)}\\
&= \frac{2L}{2\pi L\sigma}\sin(2\pi L\sigma) && \text{(D.23)}\\
&= 2L\mathrm{sinc}(2L\sigma) && \text{(D.24)}
\end{aligned}$$

D.2.3 An introduction to obliquity effects

More complication to the line profile of an FTS instrument is introduced by the finite width of the entry aperture. The ideal situation of two plane waves interfering breaks down in a laboratory environment where a large aperture is required to get a measurable amount of radiation to the detector introducing a range of angles off of the optical axis. The path differences for the collimated beams of light extend over a range of values defined by $z\cos\alpha$, where α is the angle at which the light is off of the optical axis. The infinitesimal interference fringe intensity for a particular frequency at an OPD of z and obliquity angle α is

$$dI = \cos(2\pi\sigma z\cos\alpha)\, d\Omega, \tag{D.25}$$

where $d\Omega$ is an infinitesimal increment of solid angle at oblique angle α [57]. With the second order small angle approximation (i.e. $\cos\alpha \approx 1 - \alpha^2/2$) Equation D.25 can be written

$$dI = \cos\left(2\pi\sigma z\left[1 - \frac{\alpha^2}{2}\right]\right) d\Omega \quad \left[\mathrm{W/m^2}\right]. \tag{D.26}$$

The solid angle of a circular aperture at the focus of the mirror that collimates the input to the interferometer is related to the angle alpha by

$$\frac{\alpha^2}{2} = \frac{\Omega}{2\pi}. \tag{D.27}$$

Integrating Equation D.26 over an aperture that extends to Ω_m,

$$\begin{aligned} I(z) &= \int_0^{\Omega_m} dI(z) = \int_0^{\Omega_m} \cos\left(2\pi\sigma z\left[1-\frac{\Omega}{2\pi}\right]\right) d\Omega \quad \left[\mathrm{W/m^2}\right] \\ I(z) &= \Omega_m \mathrm{sinc}\left(\frac{\sigma z \Omega_m}{2\pi}\right)\cos\left(2\pi\sigma z\left[1-\frac{\Omega_m}{4\pi}\right]\right) \quad \left[\mathrm{W/m^2}\right]. \end{aligned} \tag{D.28}$$

Equation D.28 demonstrates two effects produced by the finite aperture. The first is a change of scale in both z and σ by a factor of $(1-\Omega_m/4\pi)$. The second effect is a σ dependent sinc function envelope on the interferogram.

The result of both the limiting OPD and finite aperture size of the instrument gives a characteristic ILS, $O(\sigma)$, where the spectrum is convolved with $\mathrm{sinc}(2L\sigma)$ and a top hat function (See Equation 1.26) with a width of $\sigma_0\Omega_m/2\pi$,

$$O(\sigma) = \left[\Omega_m \frac{2\pi}{\sigma_0\Omega_m} u\left(\frac{2\pi\sigma}{\sigma_0\Omega_m}\right)\right] * \left[2L\mathrm{sinc}(2L\sigma)\right]. \tag{D.29}$$

For a demonstration of these effects see Figure D.1

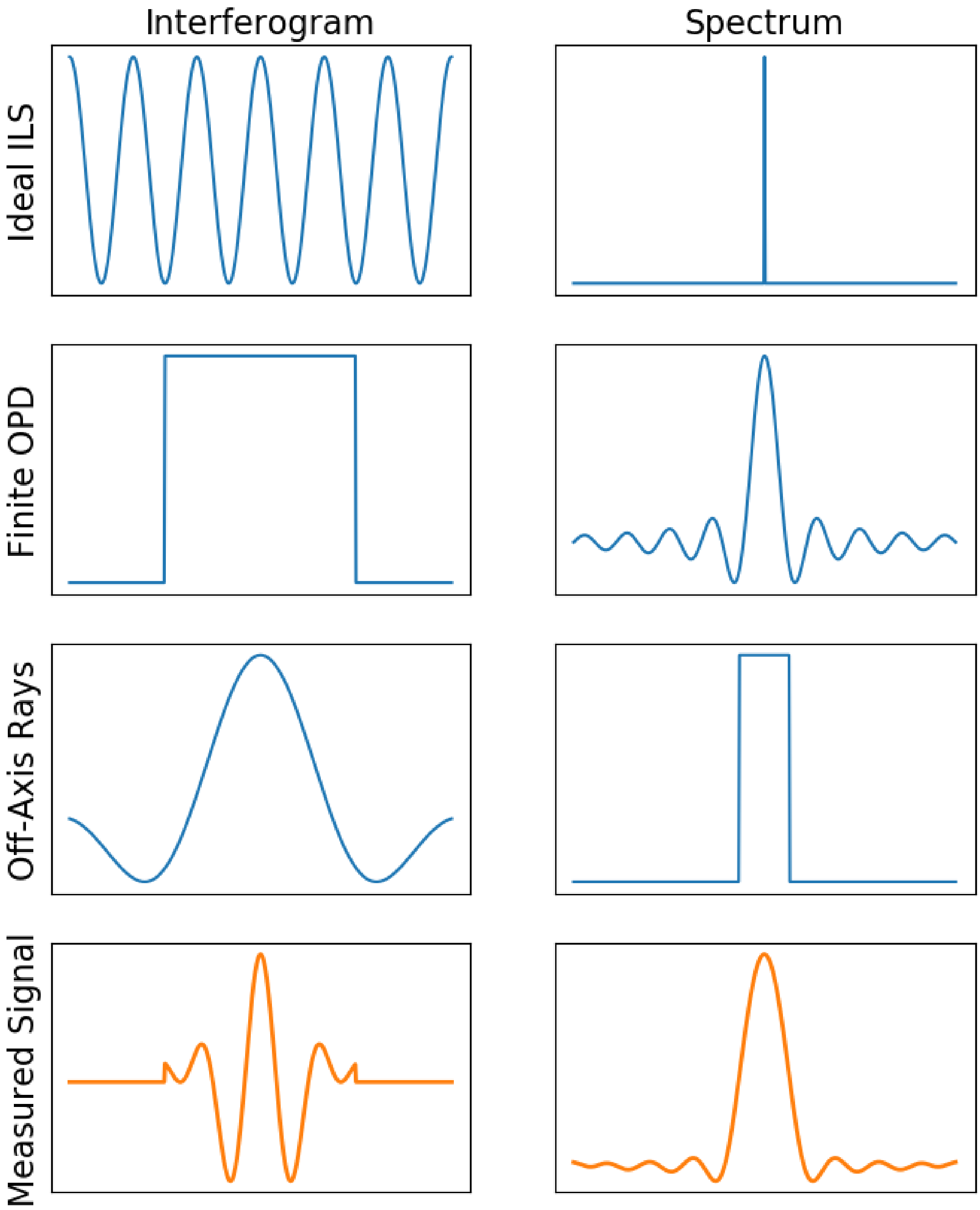

Figure D.1: The consequences of a limiting OPD and off-axis light entering the interferometer on the ideal line profile of an FTS in both the measured interferogram and its Fourier reciprocal spectral domain. The full measured signal is shown in orange on the bottom panels.

Appendix E

Low SNR Search Routine Code

Presented in this appendix is an example of the Jython scripts written for the Herschel Interactive Processing Environment (HIPE) to find low Signal to Noise Ratio (SNR) features from the line identification routine as detailed in Chapter 3. This script makes use of existing function from the *Herschel* SPIRE FTS Spectral Feature Finder (FF) [7]. This particular script is designed to work on mapping observations of the SPIRE FTS.

```
#this script looks for low SNR features that the FF may have missed
from herschel.share.unit import *
from java.lang.Math import PI
import os
c = Constant.SPEED_OF_LIGHT.value/1000.0

type = 'mapping' #point, ext, mapping
if type == 'mapping':
    pathFF = mainP + 'FFv2_release_25Sep2018/HR%s/featureCatalogues/' %(type)
else:
    pathFF = mainP + 'FFv2_release_25Sep2018/HR%sProducts/featureCatalogues/'
        %(type)
    pathCont = mainP +
        'FFv2_release_25Sep2018/HR%sProducts/continuumSpectrum/' %(type)
    pathContParms = mainP +
        'FFv2_release_25Sep2018/HR%sProducts/continuumParameters/' %(type)

if type == 'ext':
    suf = 'ext'
elif type == 'point':
    suf = 'pnt'

#specProbs = []
mainP = "/home/cbenson/remote/TBdrive/FF_lineID/"
outTabDir = mainP + 'line_id/Mapping/SecondPass02/'
inputPath = mainP + 'line_id/Mapping/Output2/'
#Tolerance [GHz] for ano
eps2 = 0.4 #higher than intitial ID since we're looking at lower snr lines,
    harder to fit properly
```

```
gOfFRng = 3 #range used by GofF to take the stats


#pathFF = mainP + 'FFv2_release_25Sep2018\\HR\\'
#where function file is located
functionsF = mainP+'featureFinderFunctionsV22_v4_CB1.py'
execfile(functionsF)
estimateRedshift = 2

snrCut = 2.0 #final cut using final noise estimate from full residual
snrCap = 500. #Highest SNR allowed for the initial guess
snrRange = [4.0,25.0] #(GHz) range either side of feature for final noise
    estimate
avoid = 10 #(GHz) excludes the ends of the bands by this width
mergeRadius = 20.0 #(GHz) merge radius for preliminary features found
flagWidths = [8.0, 8.0, 6.0, 4.0, 2.0, 2.0] #(GHz) HALF the width of region
    flagged for feature found
snrThresholds = [100.0, 50.0, 30.0, 10.0, 5.0, 2.0] #SNR thresholds for
    finding to loop over
flagWidths+=flagWidths
snrThresholds+=snrThresholds
signs = ['pos']*len(snrThresholds)
signs+= ['neg']*len(snrThresholds)
extraConstraints = False
subtractBaseline=False

resampleResolution = 5.0 #(GHz) for continuum fitting only
jumpThreshold = 3.5 #minimum jump (in RMS) to flag for continuum fitting only
baselineOrder = 3 #order of poly used for final SNR estimate
fwhm=None
polyOrder=3
##Set checkCutResults to a snrThreshold if you want to check the
    corresponding
##mid-cut residual and totalModel *produced for 1st detector in 1st obsid
    only*
checkCutResults = False
#checkCutResults = snrThresholds[3]
##1. Check the initial peak position
testCheckFit = 0
##2. Check both spectral max and min
testMaxMinAmp = 0
##3. Set to attempt an estimate of the source redshift
##Set to: 0 to turn off; 1 to use redshift1 function; 2 to use redshift2
    function
estimateRedshift = 2
##4. & 5. Set to test notoriously blended lines with two sinc profiles
testNeutralC = 0

```

```
ALLFreqs =
    Double1d([461.0407682,576.2679305,691.4730763,806.6518060,921.7997000,\
            1036.9123930,1151.9854520,1267.0144860,1381.9951050,1496.9229090])
#array with the difference patern for 12CO lines
refArray = ALLFreqs - ALLFreqs[0]

##################
#maxFitThresh = 30.0 #SNR above which the check will be performed
maxFitThresh = 5.0 #SNR above which the check will be performed
sampleRange = 3.0
window = 20.0


#Pick a method for resampling: 'gaussian', 'trapezoidal', or 'euler'
resampScheme = 'trapezoidal'

if testMaxMinAmp:
    testCheckFit = 1
if testNeutralC:
    testCheckFit = 1
    SLWFreqs =
        Double1d([461.0407682,576.2679305,691.4730763,806.6518060,921.7997000])
    SSWFreqs = Double1d([1036.9123930,1151.9854520,1267.0144860,1381.9951050,\
                        1496.9229090])

##SET THE MAXIMUM NUMBER OF ITERATIONS FOR THE SPECTRUM FITTER
maxIter=None
maxIter = 500

limitValue = 2. #To prevent features racing off or jumping outside of the
    frequency bands
checkValue = 2. #To remove features moved too far

apod = False

##############################################################################
###                          3. Gof\\ToFE options                        ###
##############################################################################

#Now turned on as default#

###GoF
testGofFfinal = 1
testGofFcut = 0
testGofFcutLines=0

###ToFE
testFitEvidence = 1
```

```
limitFitEvidence = True
plotFitEvidence = False
verboseFitEvidence = False
useWeights = False


####################################### Functions ##########################################

#removes isotope numbers from a molecule, for checking isotopologues
def formatMol(mol):
    newStrM = ''
    isoNum = False
    cc = -1
    for char in mol:
        cc+=1
        if isoNum:
            if char.isdigit():
                continue
            else:
                isoNum = False
        if char == '-':
            #following characters may be istope number, terminates with another-
            if isoNum:
                isoNum = False
            else:
                isoNum = True
        elif char.islower():
            if cc+1 < len(mol):
                if mol[cc+1]=='-':
                    continue
                else:
                    newStrM += char
            else:
                newStrM += char
        elif char == ',':
            break
        else:
            newStrM += char
    return newStrM

#returns the count of a given atom in a molecule
def atomCount(mol, atom):
    if mol.find(atom) == -1:
        numAtom = 0
    else:
        numAtom = mol[mol.find(atom)+1]
```

```
        if numAtom.isdigit():
            numAtom = int(numAtom) + (mol.count(atom)-1)
        else:
            numAtom = 1
    return numAtom

#Removes the continuum from a spectrum
def continuumSub(specIn, cont):
    #fitter = SpectrumFitter(specIn, False)
    #contCoeff = [cont.meta['p0'].value, cont.meta['p1'].value, \
    #            cont.meta['p2'].value, cont.meta['p3'].value]
    #fitter
    specOut = specIn.copy()
    specOut.setFlux(specOut.flux-cont.flux)
    specOut.setDescription('Continuum subtracted spectrum')
    return specOut



######################################## Main Execution
    #####################################

templateSm = asciiTableReader(mainP +
    'line_id/data/CSV_smallerLinelist.csv',\
                              tableType='ADVANCED', columnNames=True)
molecs = []
#develop a list of individual molecules (to later find all transitions)
for mol in templateSm['Species'].data:
    if mol not in molecs:
        molecs.append(mol)
#Determine Isotopologues for each molecule
isotopDic = {}
for mol in molecs:
    #extract atomic onformation ignoring isotope numbers and versions
    newStrM = formatMol(mol)
    #A dict to give isotopologues for each molecule
    isotopDic[mol] = []

    #iterate through other molecules
    for mol2 in molecs:
        if mol2 == mol:
            continue
        newStrM2 = formatMol(mol2)
        if newStrM2 == newStrM:
            isotopDic[mol].append(mol2)
    #Deuterium is a bit of a pain, add HDO to H2O and vice versa
    if newStrM == 'H2O':
        isotopDic[mol].append('HDO')
```

```
    if newStrM == 'HDO':
        isotopDic[mol].append('p-H2O')
        for isotop in isotopDic['p-H2O']:
            if isotop == 'HDO':
                continue
            isotopDic[mol].append(isotop)

#Get the observation list
obsidL = []
for fl in os.listdir(inputPath):
    oid = fl.split('_')[0]
    if oid not in obsidL:
        obsidL.append(oid)
#obsidL = []
#for lineIdFile in os.listdir(mainP+'\\line_id\\outputPoint\\'):
#   if ('restFrame.csv' not in lineIdFile):
#       continue
#   else:
#       obsidL.append(lineIdFile.split('_')[0])
hpdpObs = []
hpdpFileNames = []
for fln in os.listdir(mainP+'line_id/HPDP/'):
    oid = fln.split('_')[0]
    hpdpObs.append(oid)
    hpdpFileNames.append(fln)

#open up the line ID results and the FF results
for obsid in obsidL:
    System.gc()
    obsid = str(obsid)
    #if obsid != "1342188670":
    #   continue
    '''
    try:
        lineID_f = mainP + 'line_id\\CalOut\\%s_restFrame_cal_ed.csv' %(obsid)
        lineIdRes = asciiTableReader(lineID_f, tableType='ADVANCED',
            skipRows=3)
    except TaskException:
        try:
            lineID_f = mainP + 'line_id\\CalOut\\%s_restFrame_cal_ed.csv'
                %(obsid)
            lineIdRes = asciiTableReader(lineID_f, tableType='ADVANCED',
                skipRows=3)
        except:
            continue
    '''
    if (obsid == '1342227778') or (obsid[:3] == '100') or (obsid[:3] ==
        '200'):
```

```
        #We'll worry about this later
        continue
    else:
        lineID_f = inputPath + '%s_restFrame_map.csv' %(obsid)
        if os.path.isfile(lineID_f) == False:
            if os.path.isfile(inputPath + '%s_restFrame_map.csv' %obsid):
                continue #no lines in this file
        lineIdRes = asciiTableReader(lineID_f, tableType='ADVANCED',
            skipRows=3)
        outFF = simpleFitsReader(pathFF+'%s_featuresFound_%s.fits' %(obsid,
            suf))
        #load in continuum
        contPTab = simpleFitsReader(pathCont+obsid+'_continuum_%s.fits' %suf)
        contParms =simpleFitsReader(\
        pathContParms+obsid+'_fittedContinuumParameters_%s.fits' %suf)

    calibObs = outFF['data'].meta['calibration'].value

    if obsid in hpdpObs:
        obs_h = simpleFitsReader(\
        mainP+'line_id/HPDP/'+hpdpFileNames[hpdpObs.index(obsid)])
        hpdp = True
    else:
        obs_h = getObservation(obsid, useHsa=True)
        hpdp = False

    #Number of snrThresholds to iterate over
    N = len(snrThresholds)
    #Copy over the ID'd line table to add more
    newLineTab = lineIdRes.copy()

    ######Start with SLW spectrum
    nSLW = len(lineIdRes['c5'].data.where(\
                     lineIdRes['c5'].data == 'SLWC3').toInt1d())
    if nSLW != 0:
        det = 'SLWC3'
        #grab the correct spectrum
        if hpdp:
            specIn = obs_h['0000']['SLWC3']
        else:
            specIn = obs_h.refs["level2"].product.refs["HR_spectrum_%s"%type]\
            .product["0000"]["SLWC3"]
        #Modifications to the spectrum
        cont = contPTab['0000']['SLWC3']
        specOut = continuumSub(specIn, cont)
        continuumParams = [contParms["data"]["p0"].data[0],
            contParms["data"]["p1"].data[0], contParms["data"]["p2"].data[0],
            contParms["data"]["p3"].data[0]]
```

```
        #list of identified molecules
        molecs = []
        detIs = lineIdRes['c5'].data.where(lineIdRes['c5'].data == 'SLWC3')
        for rr in detIs.toInt1d():
            mol = lineIdRes['c3'].data[rr]
            if mol not in molecs:
                molecs.append(mol)
        #already ID'd feature frequencies
        features = lineIdRes['c1'].data[detIs]
        missedFeatures = []
        missedMolTrans = []

        #first look for any missing lines
        for mol in molecs:
            inds = templateSm['Species'].data.where(templateSm['Species'].data == mol)
            #find how many you expect in the band
            lowF = specOut['wave'].data[0] + avoid
            highF = specOut['wave'].data[-1] - avoid
            lineFreqs = templateSm['Frequency'].data[inds]/1000
            filter1 = lineFreqs.where(lineFreqs>=lowF)
            filter2 = lineFreqs[filter1].where(lineFreqs[filter1]<=highF)
            bandFreqs = lineFreqs[filter1][filter2]
            #now iterate through expected lines find any missing ones
            for freq in bandFreqs:
                #identify any missing lines
                if freq not in lineIdRes['c2'].data:
                    #applying the appropriate redshift
                    vel = outFF["data"].meta['radVelEstimate'].value
                    shiftF = freq/(vel/c + 1)
                    #skip if line has been shifted out the band
                    if (shiftF > highF) or (shiftF < lowF):
                        continue
                    #some tolerance, if a liner within .3 GHZ is identified we will skip it
                    templF = lineIdRes['c1'].data[detIs]
                    closestF = templF[min(range(len(templF)), key=lambda i: abs(templF[i]-shiftF))]
                    if abs(closestF-shiftF) <= 0.3:
                        continue
                    #add on the missing one
                    features.append(shiftF)
                    missedFeatures.append(shiftF)
                    rowI = templateSm['Frequency'].data.where(\
                    templateSm['Frequency'].data/1000 == freq)
                    molStr = mol + templateSm['QuantumNumbers'].data[rowI][0]
                    #if molStr not in molStr:
```

```
                   missedMolTrans.append(molStr)

        flags = {'SLWC3':{'p1':Double1d(),'fL':Double1d(),'fR':Double1d()},\
                'SSWD4':{'p1':Double1d(),'fL':Double1d(),'fR':Double1d()}}

        #now run the feature finder, at the lowest snr cut add the expected missing features
        featuresFound, snrs, snrsIter, cutFeatures, cutSnrs, cutSnrsIter, thresholds, \
        cutThresholds, finalModelArray, finalResidualArray, fitter, continuumModel,\
        sincModels, cutSincModels, featuresErr, cutFeaturesErr, initialContinuumArray, \
        peaks, cutPeaks, cutContinuumValues, outputInitialFeatureFreq, \
        cutOutputInitialFeatureFreq, indexFeatures, cutIndexFeatures,\
        threshSincs,threshResiduals,threshTotalModels,\
        gOfFthreshold, linesForGofFthresholds, allSnrForGofFthresholds,\
        expectedFreq, zEstimate, \
        flags, cutSnrs2, cutSnrs3,\
            residualDet,residualDet2,residualDet3 = \
                 catalogueFeatures(specIn,snrThresholds,signs,\
                            jumpThreshold,det,flags,\
                            resampleResolution=resampleResolution,\
                            flagWidths=flagWidths, \
                            polyOrder=polyOrder, snrCut=snrCut, snrRange=snrRange,\
                            mergeRadius=mergeRadius, subtractBaseline=True, \
                            baselineOrder=baselineOrder, checkCutResults = checkCutResults,\
                            avoid=avoid, snrCap=snrCap, testGofFcut=testGofFcut,\
                            testCheckFit=testCheckFit,\
                            testNeutralC=testNeutralC,\
                            estimateRedshift=estimateRedshift,\
                            testGofFcutLines=testGofFcutLines,\
                            maxIter=maxIter,limitValue=limitValue,\
                            checkValue=checkValue,\
                            apod=apod, extraFeats=missedFeatures)

        if len(featuresFound) == 0:
            #specProbs.append(obsid)
            continue
        #The goodness of fit Flags
        #Get the continuum from the results
        param = continuumModel.getFittedParameters()
        paramError = continuumModel.getFittedStdDev()
        poly = PolynomialModel(polyOrder)
        poly.setParameters(param)
```

```
        con1 = poly(specIn.wave)
        #continuum[0][det].flux = con1
        specInSub = specIn.copy()
        specInSub.flux = specInSub.flux-con1
        gOfFdet = gOfF(cutFeatures,specInSub,cutSincModels,rng=gOfFRng)
        gOfFflagsOut = getGofFflags(gOfFdet)

        if limitFitEvidence:
            if len(Double1d(cutFeatures)) > 35:
                print ’Number of features found for %s %s is > 35, so skipping fitEvidence’%(obsid,det)
                odds = Double1d((Double1d(cutFeatures)).size)-99.0
                result = odds
            else:
                result, odds = fitEvidence(specIn,Double1d(cutFeatures),normalise=True, plotIt=plotFitEvidence, verbose=verboseFitEvidence, useWeights=useWeights, polyOrder=polyOrder)
        else:
            result, odds = fitEvidence(specIn,Double1d(cutFeatures),normalise=True, plotIt=plotFitEvidence, verbose=verboseFitEvidence, useWeights=useWeights, polyOrder=polyOrder)
        combinedFlags = getCombinedFlags(gOfFdet, result)
        ###find the closest features to the missing ones
        mm = -1
        for missedF in missedFeatures:
            mm += 1
            fitF_i = min(range(len(cutFeatures)), key=lambda i: abs(cutFeatures[i]-missedF))
            foundSnr = snrs[fitF_i]
            featFlag = combinedFlags[fitF_i]
            if foundSnr < 2:
                continue
            if abs(missedF-cutFeatures[fitF_i]) <= eps2:
                #get info to build the row to append
                measF = cutFeatures[fitF_i]
                restF = (vel/c + 1)*measF
                #get back the molecule and the transition
                molStr = ’’
                transStr = ’’
                molT = True
                for char in missedMolTrans[mm]:
                    if molT:
                        molStr += char
                        if molStr in molecs:
                           molT = False
                    else:
```

```
                    transStr += char
            #get template frequency
            tempRows1 =
                templateSm['Species'].data.where(templateSm['Species'].data
                == molStr)
            tempRows2 =
                templateSm['QuantumNumbers'].data[tempRows1].where(\
                        templateSm['QuantumNumbers'].data[tempRows1] ==
                            transStr)
            tempFreq =
                templateSm['Frequency'].data[tempRows1][tempRows2][0]/1000
            print 'New line Id, %s, at SNR %f' %(missedMolTrans[mm],
                foundSnr)
            if newLineTab['c8'].data[0] == 0:
                newLineTab.addRow([restF, measF, tempFreq, molStr,
                    transStr, 'SLWC3', featFlag, foundSnr, -12])
            else:
                newLineTab.addRow([restF, measF, tempFreq, molStr,
                    transStr, 'SLWC3', featFlag, foundSnr, '!'])

####Repeat the process for SSW
nSSW = len(lineIdRes['c5'].data.where(\
                   lineIdRes['c5'].data == 'SSWD4').toInt1d())
det = 'SSWD4'
if nSSW != 0:
   #grab the correct spectrum
    if hpdp:
        specIn = obs_h['0000']['SSWD4']
    else:
        specIn = obs_h.refs["level2"].product\
        .refs["HR_spectrum_%s"%type].product["0000"]["SSWD4"]
    #Modifications to the spectrum
    cont = contPTab['0000']['SSWD4']
    specOut = continuumSub(specIn, cont)
    #The second entry is for SSWD4
    continuumParams = [contParms["data"]["p0"].data[1],
        contParms["data"]["p1"].data[1], contParms["data"]["p2"].data[1],
        contParms["data"]["p3"].data[1]]

    #list of identified molecules
    molecs = []
    detIs = lineIdRes['c5'].data.where(lineIdRes['c5'].data == 'SSWD4')
    for rr in detIs.toInt1d():
        mol = lineIdRes['c3'].data[rr]
        if mol not in molecs:
            molecs.append(mol)
    #already ID'd feature frequencies
    features = lineIdRes['c1'].data[detIs]
```

```
        missedFeatures = []
        missedMolTrans = []

        #first look for any missing lines
        for mol in molecs:
            inds = templateSm['Species'].data.where(templateSm['Species'].data
                == mol)
            #find how many you expect in the band
            lowF = specOut['wave'].data[0] + avoid
            highF = specOut['wave'].data[-1] - avoid
            lineFreqs = templateSm['Frequency'].data[inds]/1000
            filter1 = lineFreqs.where(lineFreqs>=lowF)
            filter2 = lineFreqs[filter1].where(lineFreqs[filter1]<=highF)
            bandFreqs = lineFreqs[filter1][filter2]
            #now iterate through expected lines find any missing ones
            for freq in bandFreqs:
                #identify any missing lines
                if freq not in lineIdRes['c2'].data:
                    #applying the appropriate redshift
                    vel = outFF["data"].meta['radVelEstimate'].value
                    shiftF = freq/(vel/c + 1)
                    #skip if line has been shifted out the band
                    if (shiftF > highF) or (shiftF < lowF):
                        continue
                    #some tolerance, if a liner within .3 GHZ is identified we
                        will skip it
                    templF = lineIdRes['c1'].data[detIs]
                    closestF = templF[min(range(len(templF)), key=lambda i:
                        abs(templF[i]-shiftF))]
                    if abs(closestF-shiftF) <= 0.3:
                        continue
                    #add on the missing one
                    features.append(shiftF)
                    missedFeatures.append(shiftF)
                    rowI = templateSm['Frequency'].data\
                    .where(templateSm['Frequency'].data/1000 == freq)
                    molStr = mol + templateSm['QuantumNumbers'].data[rowI][0]
                    #if molStr not in molStr:
                    missedMolTrans.append(molStr)

        flags = {'SLWC3':{'p1':Double1d(),'fL':Double1d(),'fR':Double1d()},\
                'SSWD4':{'p1':Double1d(),'fL':Double1d(),'fR':Double1d()}}

        #now run the feature finder, at the lowest snr cut add the expected
            missing features
        featuresFound, snrs, snrsIter, cutFeatures, cutSnrs, cutSnrsIter,
            thresholds, \
        cutThresholds, finalModelArray, finalResidualArray, fitter,
```

```
            continuumModel,\
        sincModels, cutSincModels, featuresErr, cutFeaturesErr,
            initialContinuumArray, \
        peaks, cutPeaks, cutContinuumValues, outputInitialFeatureFreq, \
        cutOutputInitialFeatureFreq, indexFeatures, cutIndexFeatures,\
        threshSincs,threshResiduals,threshTotalModels,\
        gOfFthreshold, linesForGofFthresholds, allSnrForGofFthresholds,\
        expectedFreq, zEstimate, \
        flags, cutSnrs2, cutSnrs3,\
             residualDet,residualDet2,residualDet3 = \
                  catalogueFeatures(specIn,snrThresholds,signs,\
                              jumpThreshold,det,flags,\
                              resampleResolution=resampleResolution,\
                              flagWidths=flagWidths, \
                              polyOrder=polyOrder, snrCut=snrCut,
                                  snrRange=snrRange,\
                              mergeRadius=mergeRadius, subtractBaseline=True, \
                              baselineOrder=baselineOrder, checkCutResults =
                                  checkCutResults,\
                              avoid=avoid, snrCap=snrCap,\
                              testGofFcut=testGofFcut,\
                              testCheckFit=testCheckFit,\
                              testNeutralC=testNeutralC,\
                              estimateRedshift=estimateRedshift,\
                              testGofFcutLines=testGofFcutLines,\
                              maxIter=maxIter,limitValue=limitValue,\
                              checkValue=checkValue,\
                              apod=apod, extraFeats=missedFeatures)
        if len(featuresFound) == 0:
            #specProbs.append(obsid)
            continue
        #The goodness of fit Flags
        #Get the continuum from the results
        param = continuumModel.getFittedParameters()
        paramError = continuumModel.getFittedStdDev()
        poly = PolynomialModel(polyOrder)
        poly.setParameters(param)
        con1 = poly(specIn.wave)
        #continuum[0][det].flux = con1
        specInSub = specIn.copy()
        specInSub.flux = specInSub.flux-con1
        gOfFdet = gOfF(cutFeatures,specInSub,cutSincModels,rng=gOfFRng)
        gOfFflagsOut = getGofFflags(gOfFdet)

        if limitFitEvidence:
            if len(Double1d(cutFeatures)) > 35:
                print 'Number of features found for %s %s is > 35, so skipping
                    fitEvidence'%(obsid,det)
```

```
                odds = Double1d((Double1d(cutFeatures)).size)-99.0
                result = odds
            else:
                result, odds = fitEvidence(specIn,Double1d(cutFeatures),normalise=True, plotIt=plotFitEvidence, verbose=verboseFitEvidence, useWeights=useWeights, polyOrder=polyOrder)
        else:
            result, odds = fitEvidence(specIn,Double1d(cutFeatures),normalise=True, plotIt=plotFitEvidence, verbose=verboseFitEvidence, useWeights=useWeights, polyOrder=polyOrder)
        combinedFlags = getCombinedFlags(gOfFdet, result)
        ###find the closest features to the missing ones
        mm = -1
        for missedF in missedFeatures:
            mm += 1
            fitF_i = min(range(len(cutFeatures)), key=lambda i: abs(cutFeatures[i]-missedF))
            foundSnr = snrs[fitF_i]
            featFlag = combinedFlags[fitF_i]
            if foundSnr < 2:
                continue
            if abs(missedF-cutFeatures[fitF_i]) <= eps2:
                #get info to build the row to append
                measF = cutFeatures[fitF_i]
                restF = (vel/c + 1)*measF
                #get back the molecule and the transition
                molStr = ''
                transStr = ''
                molT = True
                for char in missedMolTrans[mm]:
                    if molT:
                        molStr += char
                        if molStr in templateSm['Species'].data:
                           molT = False
                    else:
                        transStr += char
                #get template frequency
                tempRows1 = templateSm['Species'].data.where(templateSm['Species'].data == molStr)
                tempRows2 = templateSm['QuantumNumbers'].data[tempRows1].where(\
                            templateSm['QuantumNumbers'].data[tempRows1] == transStr)
                tempFreq = templateSm['Frequency'].data[tempRows1][tempRows2][0]/1000
```

```
              print 'New line Id, %s, at SNR %f' %(missedMolTrans[mm],
                  foundSnr)
              if newLineTab['c8'].data[0] == 0:
                  newLineTab.addRow([restF, measF, tempFreq, molStr,
                      transStr, 'SSWD4', featFlag, foundSnr, -12])
              else:
                  newLineTab.addRow([restF, measF, tempFreq, molStr,
                      transStr, 'SSWD4', featFlag, foundSnr, '!'])
    #save the new output file
    asciiTableWriter(table=newLineTab,
        file=outTabDir+'%s_restFrame_added.csv' %(obsid))
```